Title

Enhanced Atmospheric Water Harvesting in Metal-Organic Frameworks

Author

Zheng, Zhiling

Publication Date

2023

Peer reviewed|Thesis/dissertation

Enhanced Atmospheric Water Harvesting in Metal-Organic Frameworks

by

Zhiling Zheng

A dissertation submitted in partial satisfaction of the

requirements for the degree of

Doctor of Philosophy

in

Chemistry

in the

Graduate Division

of the

University of California, Berkeley

Committee in charge:

Professor Omar M. Yaghi, Chair
Professor John Arnold
Professor Jeffrey Reimer

Fall 2023

Abstract

Enhanced Atmospheric Water Harvesting in Metal-Organic Frameworks

by

Zhiling Zheng

Doctor of Philosophy in Chemistry

University of California, Berkeley

Professor Omar M. Yaghi, Chair

The dawn of the 21st century has ushered in a water crisis, intensified by the dual challenges of climate change and burgeoning population growth. Freshwater reservoirs are being strained, and while there are existing water generation technologies, they often come with limitations, either being energy-consuming or geographically confined. In response, atmospheric water harvesting (AWH) has emerged as a potential remedy, providing access to an inexhaustible source of water. Central to this solution is the development of efficient materials capable of capturing water, especially in arid regions where the need is most urgent. Metal-organic frameworks (MOFs), with their unique construction from metal-containing secondary building units (SBUs) linked by organic molecules, present a robust, crystalline, and enduringly porous framework, placing them at the forefront of potential solutions. MOFs' structural and chemical versatility, combined with their ultra-high porosity, makes them ideal candidates for large gas and vapor uptakes, thereby making them invaluable for AWH.

This dissertation focuses on a range of methodologies aimed at enhancing the design, synthesis, and pragmatic applications of MOFs in atmospheric water harvesting. The focus is twofold: discovery strategies and optimization techniques. Key highlights include the pivotal role of reticular design in augmenting MOF water harvesting properties and the synergy between artificial intelligence (AI) and reticular chemistry to accelerate the close-up discovery of water-harvesting MOFs. Furthermore, this work elucidates high-yield, eco-friendly, and scalable synthesis protocols for MOFs, along with device-centric optimizations to harness MOFs' potential in real-world water harvesting scenarios.

Chapter I provides a general introduction to metal-organic frameworks and their potential in water harvesting. MOFs, as emerging candidates, possess numerous advantages, making them ideal sorbents for water harvesting. These include retaining water capacity across multiple uptake-release cycles, exhibiting impressive water sorption capacities under operational

conditions, requiring lower regeneration temperatures, and demonstrating dynamic water sorption properties. Apart from their high crystallinity and permanent porosity, the tunability of MOFs facilitates the design of bespoke materials tailored for specific needs. This chapter emphasizes the role of reticular design in establishing MOFs as a distinctive class of sorbents for atmospheric water harvesting. It also delves into the structure-function relationships of MOFs pertinent to water sorption and discusses the principles for designing novel MOFs for this application.

Chapter II delves into synthesis strategies tailored for the large-scale and eco-friendly production of MOFs suitable for water harvesting. While traditional MOF synthesis primarily targets small-scale laboratory setups, the broader application of MOF technology for water harvesting necessitates overcoming challenges in scalability and productivity. This chapter bridges the gap between laboratory findings and industrial applications. It introduces a green, robust, and high-yield synthesis protocol for MOFs, prioritizing cost-effectiveness and environmental sustainability. Several aluminum-based MOFs were synthesized at the kilogram scale and detailed characterization confirmed the retaining of their crystallinity and water uptake capacities. The chapter also sheds light on key parameters essential for optimizing the green synthesis of MOFs, emphasizing their future scalability in water harvesting applications.

Chapter III shifts the focus from the sorbent material to device optimization. A notable advancement in passive water harvesting is introduced through the design of a device leveraging MOF-303. Characterized by its efficiency and modularity, this device demonstrated its prowess in real-world conditions, particularly in extreme environments in the Death Valley National Park. The chapter underscores the device's potential in combating water scarcity and outlines several key parameters crucial for enhancing its atmospheric water harvesting efficiency.

Chapters IV and V elucidate new strategies to enhance MOF water sorption properties. Specifically, Chapter IV delves into a multivariate approach, transitioning a single-linker MOF to a diverse mixed-linker MOF family. The resulting MOFs benefit from wider tunability in both operational humidity ranges and the regeneration temperature. Additionally, the employed synthesis method is both scalable and environmentally conscious. Chapter V presents a "linker arm" extension strategy, which enhances the water-harvesting capabilities of MOF-303 by elongating the linker "arm", resulting in a significant 50% boost in water uptake. These two examples of strategic innovation underscore the versatility and potential of MOFs in water-harvesting applications.

Chapter VI delves into the transformative potential of AI-guided MOF synthesis, suggesting a departure from traditional research paradigms towards innovative methodologies for discovering new MOFs tailored for water harvesting. The chapter champions the use of AI agents to alleviate labor-intensive lab tasks, thereby allowing researchers to focus on more intricate aspects and achieve enhanced efficiency. The integration of machine learning algorithms aims to curtail human biases in optimizing MOF synthesis conditions. Specifically, a suite of seven ChatGPT-based agents is introduced, demonstrating their capability to streamline numerous lab activities. This confluence of AI and MOF synthesis marked a significant milestone in refining

water-harvesting MOFs, with the overarching AI framework streamlining the synthesis process, mitigating human biases, and maximizing efficiency.

Chapter VII is the concluding chapter of my thesis. In it, I share my reflections and insights on the future development of MOFs for atmospheric water harvesting. As we delve deeper into this field and refine our design principles and optimization strategies, I believe that MOFs will undoubtedly play a pivotal role in ensuring water security, sustainability, and prosperity for all.

Table of Contents

Acknowledgements

First and foremost, I would like to thank Professor Omar M. Yaghi for his unconditional guidance and support throughout the course of this work. The trajectory of my career and indeed, the course of my life, underwent a profound transformation the day I first stepped into his office. Our initial encounter was marked by a deeply enriching conversation about science, ambition, and the future. And when, filled with hope and enthusiasm, I expressed my keen interest in being part of his esteemed group, he didn't hesitate for a moment and warmly welcomed me with the words "you're in." Over the ensuing years, Professor Yaghi has granted me literally unlimited resources and the freedom to chase my curiosities and explore my ideas, always standing by my decisions and guiding me through challenging crossroads. I will always be grateful for the invaluable lessons he has taught me regarding the importance of innovation and creativity in scientific research, as well as the art of presenting one's findings to the broader world. His profound influence on my academic journey has not only shaped my present but promises to be a guiding light in all my future endeavors.

In addition, I would like to thank the members of my committee: Professor John Arnold, Professor Jeffrey A. Reimer, and Professor Kenneth N. Raymond. Their insightful comments and suggestions during my qualifying exam established a robust foundation for the direction of my subsequent PhD work.

Furthermore, I want to thank my undergraduate research advisor Prof. Kyle M. Lancaster from Cornell University, who introduced me to the world of scientific research. My experience in Prof. Lancaster's group ignited my passion for chemistry, where I had the privilege of immersing myself in both wet lab synthesis and computational modeling. The lessons I learned from him and the members of the Lancaster group have been pivotal, teaching me to approach research with creativity, caution, and innovation.

My heartfelt thanks go to Dr. Xiaokun Pei for mentoring me during the initial years of my PhD. Her guidance was instrumental as I ventured into the realm of reticular chemistry. I'm deeply grateful for her patience, wisdom, and trust. I thank her for the patience, guidance, and trust that he has given me. I'm also grateful to Drs. Nikita Hanikel, Ha Lac Nguyen, Tianqiong Ma, Xing Han, and Nakul Rampal from the Yaghi Lab. Their meticulous approach to research reshaped my perspective on addressing challenges in chemistry research. I'd also like to express my gratitude for the camaraderie and consistent support from my colleagues Boyu Qie, Ziyi Wang, and Yang Wu from the College of Chemistry. Our cherished memories of regular gatherings, ordering fried chicken and rice noodles, sipping wine, and watching CCTV-13 together will forever remain etched in my heart.

Moving beyond the confines of chemistry, I acknowledge my high school friends, Jiayi Weng, Xinshu Jiang, Kefan Dong, and his wife Dangling Ma. Celebrating over a decade of friendship since our days at Fuzhou No.1 High School, their insights from diverse fields have been enriching.

I am grateful that their varied professional paths and distinct experiences have consistently provided me with fresh perspectives, pushing me to think beyond conventional boundaries. I'm equally indebted to my college peers, Oufan Zhang and Zeqi Gu, for their influential guidance on computer science. Their enlightening discussions paved the way for my foray into artificial intelligence, a field I wouldn't have considered as an experimental chemist. It not only deepened my research but also introduced a multidisciplinary approach I hadn't initially imagined.

This work would not have been possible without Yifan Deng, whose substantial contributions to my work have been absolutely crucial. From the inception to the completion of my research, Yifan has been a constant source of support and inspiration. Her love, unwavering support, and infectious joy for life have been the bedrock upon which my scholarly and personal journey has been anchored during my graduate life. In moments of triumph and challenge alike, her presence has been a perpetual source of happiness and strength. I am profoundly grateful for her endless patience, especially during the long nights of research and writing, where her gentle spirit and optimistic outlook have invariably guided me through. Her belief in my capabilities, even in moments when I felt uncertain about myself, has been a pivotal force propelling me forward.

Furthermore, I would like to give special thanks to the people for their intellectual contribution and instrumental influence on me throughout this dissertation: Professor Jennifer T. Chayes, Professor Christian Borgs, Professor Laura Gagliardi, Professor Woochul Song, Professor T. Grant Glover, Professor Lars Öhrström, Professor Yue-Biao Zhang, Professor Seth M. Cohen, Dr. David R. Moore, Dr. Cornelius Gropp, Dr. Daria Kurandina, Dr. Nobuya Tsuji, Dr. Magdalena Heiland, Dr. Eugene Kapustin, Dr. Hao Lyu, Dr. Wentao Xu, Dr. Saumil Chheda, Dr. Chuanshuai Li, Zichao Rong, Ali H. Alawadhi, S. Ephraim Neumann, Kelvin Kam-Yun Li, Zihui Zhou, Oscar Iu-Fan Chen, Matthew Burigana, Xinyu Chen, Zhiguo He, Kaiyu Wang, Haozhe Li, Yen-hsu Lin, Abdullah Alghamdi, Kevin Greco, and George Chiang, as well as the rest of the Yaghi group family from the past and present.

Finally, I must also reserve a special place in my heart and this acknowledgment for my parents, Mingxiang Xue and Meizhou Zheng. Their unwavering faith in me, their countless sacrifices, and the endless love they showered upon me have been the bedrock upon which my aspirations were built. I am immensely proud to be their child. At countless crossroads in my life, when faced with uncertainties and dilemmas, it was their wisdom, patience, and guidance that pointed me in the right direction. I cannot overstate how pivotal their role has been in shaping the individual I've become. Without their steadfast support and encouragement, I wouldn't have achieved the milestones that now mark my journey. They've always championed my decisions, encouraging me to pursue my passions and chase after what genuinely ignites my interest. Their teachings, both spoken and unspoken, have been my moral compass, guiding me through the challenges of life and academia. I appreciate the education they gave me and the freedom to pursue the career that I love. I am also deeply grateful to my extended family, including Minghua Xue, Xiurong Zhang, and Huayin Xue. Their support, encouragement, and the countless joyful moments we've shared have been a source of strength and inspiration. To them, I owe a debt of gratitude that words can barely express, for they have been the silent pillars holding up the edifice of my dreams.

To my beloved parents Mingxiang Xue and Meizhou Zheng

Chapter I

Introduction to Water-Harvesting Metal-Organic Frameworks

1.1 Introduction

Water scarcity is an escalating global challenge, with over half the world's population experiencing shortages of this vital resource due to irregularities in its spatial and temporal distribution.[1,2] Many arid regions face heightened scarcity due to inadequate transportation and infrastructure, making their fresh water supplies even more precious.[3,4] As we navigate the complexities of the 21st century, the confluence of climate change and rapid population growth further intensifies the water crisis.[1-5] While better water management might mitigate the situation in certain regions, there remains a compelling need for new means of freshwater generation, especially in arid regions. Notably, while desalination emerges as a potent solution, its practicality is mostly confined to coastal areas.[6] As such, landlocked nations and many developing rural areas face challenges in harnessing desalination due to financial and infrastructural constraints, underscoring the gravity of dwindling freshwater reserves and the limitations of current water generation technologies.[7, 8]

Fortunately, in recent years, atmospheric water harvesting has been proposed as a promising solution to address this issue.[9] This technique involves the extraction of water vapor from the surrounding air and its conversion to liquid form. Water harvesters, the devices developed for this purpose, vary in complexity and are tailored to function in different environmental scenarios. They predominantly employ solid sorbents to attract water molecules at low relative humidity (RH), releasing them with minimal energy expenditure.[10-12] Since this approach is neither spatially nor temporally restricted, the supplement of fresh water by the water harvesters equipped with desirable sorbents can be achieved at any location and at any time of the year.[11] Conceptually, this technique can potentially provide access to an inexhaustible source of water.[13-16] However, the challenge lies in developing materials that can efficiently capture this water, particularly in arid regions where the need is most urgent. Furthermore, the synthesis of these

materials should be scalable, cost-effective, and adaptable to devices tailored for household use, ensuring widespread accessibility. Succinctly, to enhance the efficacy of atmospheric water harvesting, three pivotal areas demand attention: the material's design, its synthesis, and the device's development.

1.2 Metal-organic frameworks for water harvesting from air

Microporous metal-organic frameworks (MOFs) have recently gained attention as sorbents for atmospheric water harvesting due to their high tunability, unprecedented variety, and intrinsic porosity, and have been successfully employed in desert water harvesting.[5,6,10,12-15] In particular, MOFs are formed by linking inorganic and organic molecular building blocks through strong bonds.[17] The inorganic building blocks, known as the secondary building units (SBUs). are metal clusters, and the organic building blocks are either monotopic or polytopic organic ligands that exhibit coordinating groups such as carboxylate, catecholate, imidazolate, and pyrazolate.[18] MOFs possess extremely high surface (1000 to 10,000 m^2/g) and large void spaces (typically accounting for more than 50% of the MOF crystal volume), making them ideal for extracting water from the air and utilizing their porous space (Figure 1.1).

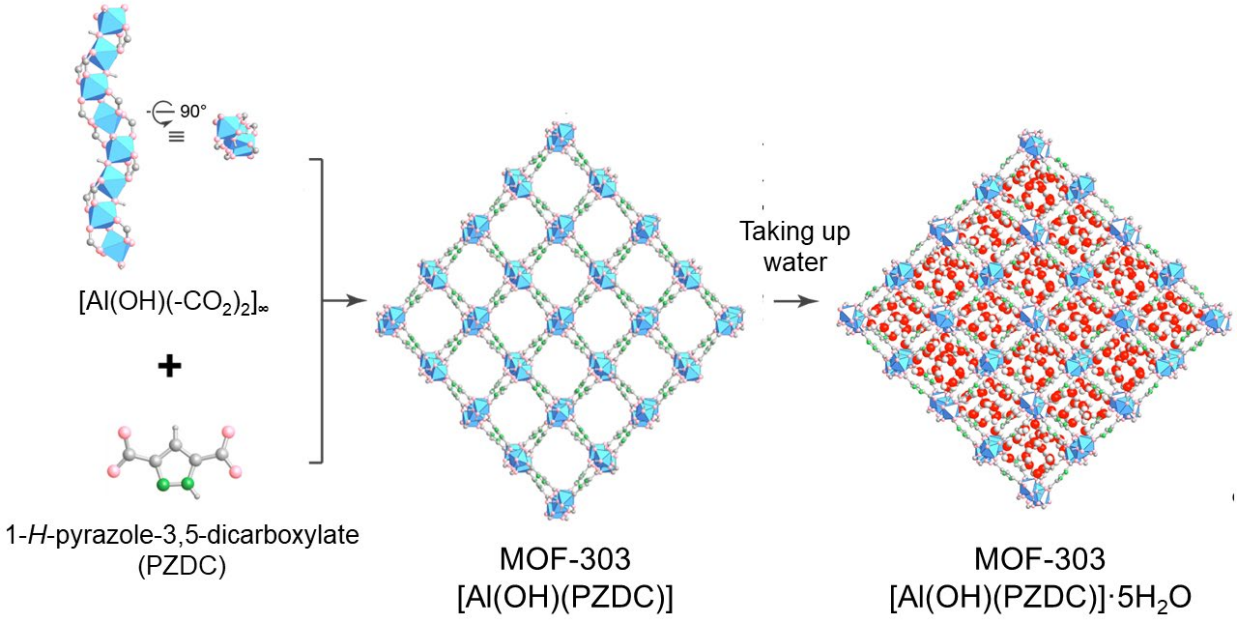

Figure 1.1 An illustration of the porous framework material for water harvesting (center). This particular material, denoted as MOF-303, consists of infinite $[Al(OH)(–CO_2)_2]_n$ rod SBUs connected by PZDC organic linking units. The material captures water vapor from the air under ambient conditions, with the water content in the pores reaching up to about 40% of its weight. This class of material is capable of storing a significant quantity of water molecules in its hydrophilic pore pockets. Color code: Al, blue; O, pink (SBU) or red (water); C, gray; N, green.

When compared to other solid sorbents for water harvesting such as simple inorganic salts, zeolites, and porous silica materials such as mesoporous silicas or carbons, MOFs exhibit faster kinetics of uptake and release cycles.[19] As a result, the water harvesting cycle is shorter. They are also more hydrothermally stable, have a higher water uptake capacity at low relative humidity (RH), and display lower water adsorption energy.[10-12] These advantages arise from the MOFs' diverse chemical functionalities, which can be fine-tuned through the deliberate design of inorganic joints and organic struts. This adaptability allows for the adjustment of water sorption properties, such as uptake, regeneration temperature, and operational RH.

To date, there has been a growing amount of research focused on measuring the water sorption profiles of various MOFs. Different techniques have been employed to understand how these frameworks capture water, and more importantly, how to develop MOF sorbents with tailored capacity and isotherm shape.[16-18] In this chapter, I aim to highlight the significant potential of this class of materials for moisture capture from air by addressing both MOF development and its practical integration into water harvesters.

1.3 Reticular design of MOFs

The successful application of MOFs in water harvesting hinges on the rational synthesis of frameworks with specific structures, compositions, and properties, a core focus in this field of chemistry.[20] Reticular design has emerged as a pivotal strategy for the development of MOFs. This approach involves assembling carefully selected rigid molecular building blocks into predefined networks.[21, 22] The coherent synthesis of the MOF is thus accomplished by understanding the intended network, pinpointing the necessary building blocks, and determining the synthesis conditions that consistently yield these building blocks. In this section, key parameters related to water harvesting properties are highlighted, showcasing how reticular design enables the tailoring of MOFs for atmospheric water harvesting applications.

Thermal and Water Stability

For a specific MOF to be suitable for water harvesting, it must possess both thermal and hydrolytic stability. Thermal stability ensures that the MOF can endure the heating temperatures during water release, while hydrolytic stability ensures that it remains intact and does not degrade, thereby retaining its capacity during operation. Many MOFs are primarily formed through metal-carboxylate coordination bonds, endowing them with thermal stability. However, they might lack long-term water stability due to the hydrolysis of the coordination bond between the SBU and the linker.

In this context, MOFs with rod-like metal-containing SBUs are preferred. Their enhanced chemical stability, especially against water, makes them more attractive candidates compared to MOFs constructed from other types of SBUs (e.g., discrete metal clusters). This superiority is ascribed to the steric shielding of metal ions by the linkers.[12, 23] Additionally, the channels created

within the framework by the rod packings are expansive, facilitating the unhindered and rapid movement of guest molecules.[11] Such compelling attributes render rod MOFs as potent and long-lasting candidates for water harvesting materials (Figure 1.2).

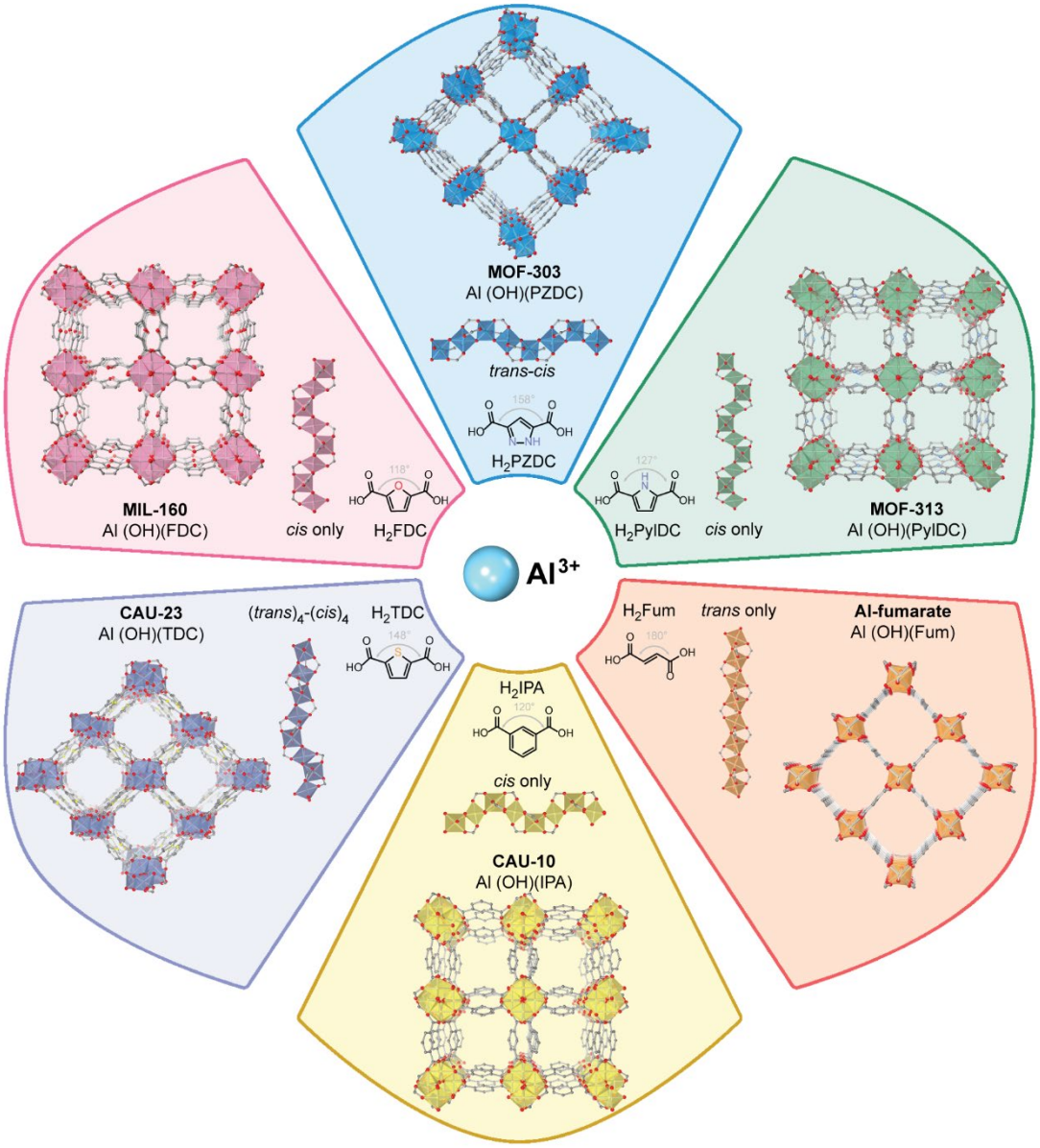

Figure 1.2 Illustration of structural diversity and tunability in rod MOFs for water harvesting. The aluminum-based MOFs are constructed using ditopic carboxylate linkers with opening angles ranging from 118° to 180°. The rod-like SBUs consist of either *cis*-only, *trans*-only, *cis-trans*-alternating, or $(cis)_4$-$(trans)_4$-alternating corner-shared AlO6 octahedra, which are variably colored in different MOFs. Color code: O, red; C, gray; N, purple; S, orange. H atoms are omitted for clarity. Abbreviations: H_2PZDC, 1-*H*-pyrazole-3,5-dicarboxylic acid; H_2PylDC, pyrrole-2,5-dicarboxylic.

In addition to utilizing infinite aluminum-based rod SBUs and altering the organic linker in the reticular design of water-stable MOFs, a similar approach is to produce kinetically water-stable MOFs by incorporating highly connected zirconium-based SBUs.[24] In both cases, hydrolysis is deterred due to the steric shielding of the SBU by the linkers. Remarkably, this objective can also be accomplished by incorporating bulky linkers or modulators.[25, 26] Additionally, inert cations, such as Cr^{3+} in an octahedral coordination geometry, can be integrated into MOFs. This ensures that any potential hydrolysis occurs at an imperceptibly slow rate, rendering the resultant framework hydrolytically metastable and suitable for prolonged use in water harvesters.[27, 28]

It is crucial to note that while hydrolysis can often be anticipated based on fundamental chemical principles and steric effects, predicting architectural stability is more challenging and typically requires empirical determination. The most reliable method to assess a MOF's stability under operational conditions is through a water adsorption-desorption cycling experiment, which evaluates both hydrolytic and architectural stabilities.

Step-shaped isotherm profile

A characteristic that distinguishes MOFs from amorphous sorbents and hygroscopic salts is their tendency to display step-shaped isotherm profiles.[12] A step-shaped water sorption isotherm is favored for water harvesting applications, as it facilitates the release of significant water quantities with slight variations in temperature or pressure—the sharper the profile, the better.[11] Such a profile is essential for the energy-efficient release of water from the sorbent. The emergence of step-shaped water sorption isotherms can be attributed to the formation of structured, hydrogen-bonded water molecule networks within the crystalline MOF during the pore-filling process.

As an example, a previous study on MOF-801 ($Zr_6O_4(OH)_4(fumarate)_6$), which applied both X-ray and neutron diffraction techniques, revealed that at low partial pressures, water molecules initially adsorb at primary adsorption sites situated near the μ_3-OH groups of the Zr-SBU.[24] Introducing small water doses to the crystals and examining their position and geometry within the pores revealed the creation of tetrahedrally and cubically arranged water aggregates, each stabilized by hydrogen bonds. These aggregates are perceived as nucleation sites where additional water molecules can accumulate. This aggregation adheres to a cooperative mechanism, as suggested by the step isotherm behavior. In fact, the step behavior seen in the isotherm might arise due to the intensified water binding, propelled by the creation of these nucleation sites. Importantly, continued examinations of water molecules within the confined micropore settings of MOFs have the potential to guide advanced framework designs. This would enable the manipulation of water behavior at the molecular level, leading to further enhancements in the framework's water harvesting properties.[23]

Humidity cutoff position

Simultaneously, the position of the step fundamentally determines the operation regime of a sorbent, as the uptake at partial vapor pressures below this step is usually small or negligible. To be specific, the humidity cutoff position refers to the specific point or threshold in relative humidity where significant changes or reactions occur in materials or systems. For MOFs, this point is usually the same as the position of the step. In the context of water harvesting, a lower humidity cutoff position is more advantageous, as it denotes the humidity level at which the MOF starts to effectively absorb water from the atmosphere. For example, in desert landscapes, while the absolute amount of atmospheric moisture might be low, MOFs with lower humidity cutoff can efficiently capture and store this moisture. This ensures that even in the most challenging conditions, water harvesting becomes viable, turning otherwise wasted ambient humidity into a valuable resource.

There is a growing drive to use reticular design to modulate the humidity cutoff position by introducing functional side chains into the MOF structure. Specifically, in arid water harvesting scenarios, integrating hydrophilic groups such as hydroxyl groups or amino groups proves promising in relocating the pronounced uptake region to lower humidity cutoff levels.[29, 30] Note that a general challenge exists: while infusing hydrophilic side groups can enhance a framework's operational regime in drier climes, this tactic is encumbered by a decline in free pore volume, consequently reducing total water uptake.[31, 32] An important strategy to enhance hydrophilicity without compromising pore volume entails the integration of heterocycles into the MOF architecture. For instance, by substituting the larger and more hydrophobic H_2IPA linker with the smaller and more hydrophilic alternatives such as H_2FDC or H_2PylDC, MIL-160 and MOF-313 can be synthesized, respectively.[33, 34] Both these MOFs possess a lower humidity cutoff compared to their progenitor, CAU-10 (Figure 1.2). Through this approach, MOFs can achieve a lower humidity cutoff position by utilizing more hydrophilic organic linkers without sacrificing their pore volumes.

Water Uptake

Water uptake, a key parameter in water isotherms, indicates the volume of water that a material can capture and store within its pores. Naturally, higher values are desirable, especially when evaluating the efficiency of a MOF for water harvesting. Typically, this metric is directly linked to the MOF's pore volume: a higher pore volume can, theoretically, accommodate more water molecules.

However, it is a misconception to assume that MOFs with the highest porosity are always the best candidates for water harvesting. A case in point: some of the most porous MOFs reported are constructed using either the octahedral $Zn_4O(\text{-}COO)_6$ or the $Cu_2(\text{-}COO)_4$ paddle wheel SBU, and both types tend to be hydrolytically unstable.[35-37] A notable achievement in this space is the Cr-soc-MOF-1, which exhibits a water uptake of up to 1.95 g g^{-1} and boasts a pore volume of 2.1

$cm^3\ g^{-1}$.[28] These figures hint at the possibility of even higher uptakes with water-stable MOFs, given the correlation between uptake and pore volume. Nevertheless, designing an efficient MOF for water harvesting is not just about maximizing pore volume. One must consider the architectural stability of the MOF, especially during regeneration phases, as the substantial capillary forces of water can strain and potentially compromise the structure. Furthermore, a MOF's hydrophilicity tends to decrease with its pore volume, as the longer linker usually consists of a high portion of less hydrophilic carbon atoms, rendering it less effective in arid environments.

The overarching goal, then, is to harmoniously balance pore volume, hydrophilicity, and architectural stability. This entails the judicious selection and modification of both the SBUs and the organic linkers in the reticular design, ensuring optimal performance across all essential parameters (Table 1.1). While a higher water uptake is favored, maintaining a low humidity cutoff is essential for water harvesting in arid regions.

Table 1.1 Representative MOFs for water harvesting with their metal centers, pore volume, water uptake, and humidity cutoff.

MOF	Metal	Pore volume ($cm^3\ g^{-1}$)	Water uptake at P/P_{sat} = 0.90 ($g\ g^{-1}$)	Humidity cutoff position (% RH)	Ref.
MIL-160	Al^{3+}	0.38	0.36	7	38
MOF-801	Zr^{4+}	0.45	0.35	9	24
MOF-303	Al^{3+}	0.47	0.39	12	38
Co-CUK-1	Co^{2+}	0.26	0.29	12	39
Ni-CUK-1	Ni^{2+}	0.26	0.30	13	39
MOF-313	Al^{3+}	0.41	0.34	13	38
CAU-10	Al^{3+}	0.24	0.32	17	38
MIP-200	Zr^{4+}	0.40	0.42	18	40
MOF-333	Al^{3+}	0.48	0.38	22	23
MOF-841	Zr^{4+}	0.53	0.51	25	24
CAU-23	Al^{3+}	0.46	0.33	26	38
MOF-LA2-1	Al^{3+}	0.67	0.68	26	41
Al-Fum	Al^{3+}	0.41	0.39	27	38
Mg-CUK-1	Mg^{2+}	0.28	0.35	27	39
MIP-211	Al^{3+}	0.60	0.60	30	42
UiO-66	Zr^{4+}	0.49	0.43	37	24
MIL-53-muc	Al^{3+}	0.63	0.60	56	42
Cr-soc-MOF-1	Cr^{3+}	2.10	1.95	68	28
PIZOF-2	Zr^{4+}	0.88	0.68	76	24

1.4 Synthesis of water harvesting MOFs

In addition to having excellent water sorption properties, a desirable sorbent should be scalable, cost-effective, and reproducible in manufacturing in order to be practical for use in various complex real-world conditions.[9-11] Therefore, the choice of synthesis method not only affects the MOF's structure and performance but also its practical feasibility in large-scale water harvesting.

Since the inception of MOFs over 20 years ago,[43] the solvothermal method has remained a cornerstone in MOF synthesis, renowned for yielding high-purity products.[18] However, the extended reaction durations and elevated temperature requirements could pose challenges, particularly concerning scalability and cost. Despite these limitations, its robustness and reproducibility have made it a primary approach in numerous laboratories and industrial settings.[44-46] A quicker alternative to traditional heating is microwave-assisted synthesis. By expediting MOF production, it potentially minimizes time and costs.[47-49] The consistent and swift heating provided by microwaves occasionally assists in procuring MOF structures that are challenging to achieve via conventional methods, making this approach both efficient and adaptable.[48, 50]

Other innovative methods are also emerging. Mechanochemical synthesis is drawing attention as an eco-friendly option, negating solvent requirements. Utilizing ball mills, it represents a scalable and potentially more cost-effective route.[51, 52] Additionally, electrochemical synthesis offers controlled MOF growth by using applied voltage, a technique that holds promise for specialized applications.[53] On the other hand, the conventional solvent evaporation method, employing stirring and heating with reflux, has been increasingly developed and optimized for MOF synthesis.[54, 55] Its simplicity and adaptability make it a prevalent choice for initial explorations and optimizations in the laboratory. As the reaction conditions are typically straightforward and readily tunable, this method is ideal for establishing the preliminary feasibility of a given MOF structure. Though it might not be as rapid as microwave-assisted synthesis or as environmentally friendly as mechanochemical approaches, its widespread accessibility and established protocol history ensure its continued relevance in MOF research.

It is worthwhile mentioning that, besides direct synthesis, post-synthetic modification (PSM) offers opportunities to refine MOFs after their initial synthesis. It serves as a method to introduce functional groups, replace metal centers, or adjust the porosity of the MOFs after their initial fabrication.[56] This capability ensures that MOFs can be meticulously optimized for enhanced water harvesting performance, even after the primary synthesis has been completed.[12] While PSM offers unparalleled precision in functionalizing MOFs, it is crucial to evaluate its implications on the overall production costs, reproducibility, and scalability, especially when envisioning its application in large-scale and real-world scenarios.

1.5 Development of MOF water harvesters

To tap into the potential of water-harvesting MOFs effectively, it is necessary to develop and establish specialized devices known as MOF water harvesters. These devices use MOFs as sorbents to extract water from ambient air. The fundamental operation of all sorbent-assisted water harvesters remains the same: Initially, water vapor is concentrated within the sorbent, after which it is released by lowering the relative vapor pressure surrounding the MOF (Figure 1.3a). This release can be triggered either through a change in temperature or pressure. Once the water vapor has been concentrated, it is condensed to produce liquid water. Depending on design specifics, this water harvesting process can be carried out once (monocyclic) or multiple times (multicyclic) within a day. While some devices rely on external energy sources, such as electrical heating or vapor compression, others operate passively, leveraging ambient sunlight and natural cooling mechanisms.

In 2018, the pioneering MOF-based water harvester was introduced, designed as a box-within-a-box system. The inner compartment, containing MOF powder, is open to allow atmospheric interaction. The outer compartment, with its adjustable lid, is opened during the night to allow water from the air to be adsorbed by the MOF-801 and closed during the daytime, leveraging sunlight. Field tests in the Arizona desert recorded water yields ranging from 200-300 mL per kilogram of MOF daily under specific humidity and temperature conditions, with internal temperatures reaching nearly 80°C.

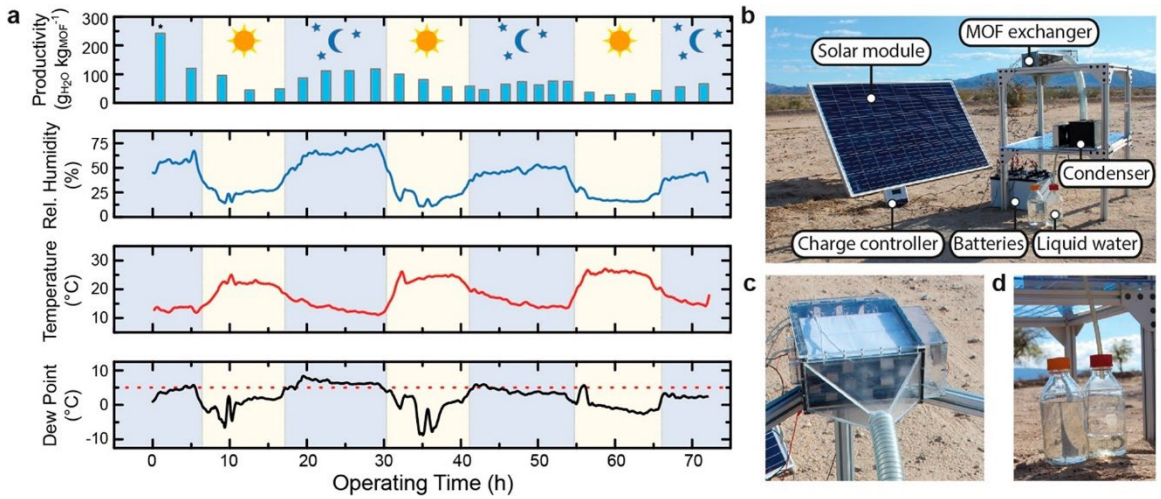

Figure 1.3 Practical atmospheric water harvesting in the Mojave Desert. (a) Diagram displaying the water harvesting productivity after each water harvesting cycle, the ambient relative humidity and temperature, and the corresponding dew point. (b) Photograph of the water harvester with labeled parts. Close-up views of the MOF exchanger (c) and the water collected under continuous operation (d). Adapted with permission from ref. 19. Copyright © 2019 American Chemical Society.

However, insights from these tests highlighted two key areas for optimization: the need for improved sorbents and the importance of efficient airflow and heat/mass transfer within the device. The former aims to produce sorbents that can perform faster adsorption–desorption cycles at reduced temperatures, enabling more operational cycles within a day. The latter focuses on optimizing device efficiency in both capturing and releasing water. Building on these insights, in 2019 a new design featured a scaled-up MOF water harvester built around the more advanced MOF-303. This harvester, powered by solar energy via a photovoltaic module, was designed to operate both day and night. It employed mild heating for the MOF, negating the need for direct sun exposure and, hence, allowing for a more compact design (Figure 1.3b). Quick heat and mass transfers were ensured by placing the MOF in slim trays, organized into cartridges equipped with two sets of channels (Figure 1.3c). While one set facilitated abundant airflow during the adsorption phase, the other guided the release of water vapor during desorption towards the condenser (Figure 1.3d). Field tests in the Mojave Desert, California, demonstrated the device's reliability, consistently producing water throughout a continuous three-day operation.

1.6 Current state-of-the-art and future opportunities

The journey towards the development of water-harvesting MOFs and their associated devices has witnessed impressive strides. MOFs, thanks to their high porosity and crystallinity, outshine many solid sorbents by offering faster kinetics, increased water uptake, and requiring lower energy or pressure for each cycle, establishing them as sought-after sorbents.[10, 16, 57] The reticular design intrinsic to MOFs endows them with remarkable tunability.[18] This enables the rational design of structures by selecting appropriate SBUs and linkers, ensuring optimal water sorption properties. Additionally, numerous MOF-based atmospheric water harvesters have been devised and successfully tested in desert conditions.[19, 58, 59] Initial explorations into device design have unveiled crucial parameters for enhancing water harvesting efficiency. Although many of these strategies have emerged recently, they hold the promise of further optimizing the water sorption properties of MOFs as more in-depth research is undertaken.

However, plenty of avenues remain open for exploration, both in terms of materials and device development. A pivotal step towards the commercial viability of MOF-based atmospheric water harvesters is the cost-effective and scalable production of MOFs, ideally via environmentally friendly means.[51, 60] The establishment of robust synthesis protocols yielding high MOF outputs is essential to curb production costs.[60-62] Green synthesis methods should be prioritized in future MOF production.[38, 60] On the device front, there's room for increasing the productivity of MOFs in monocyclic devices by refining the device's geometry and maximizing sunlight utilization, essentially engineering energy management in the next generation of harvesters.[11] Monitoring and ensuring the productivity and durability of these devices over extended field usage will be pivotal. Incorporating features that guard against environmental contaminants can extend device longevity and ensure they meet health standards.[12] Similar to solar panels, the next wave of harvesters should be scalable—whether by parallel expansion or enlargement—catering to both household use and larger applications. Lastly, a close examination

of production and maintenance costs is essential to make these devices both affordable and efficient, positioning them as potential solutions to the global water shortage challenge.

1.7 Reference

(1) McDonald, R. I.; Green, P.; Balk, D.; Fekete, B. M.; Revenga, C.; Todd, M.; Montgomery, M., Urban growth, climate change, and freshwater availability. *Proc. Natl. Acad. Sci. U.S.A.* **2011,** *108* (15), 6312-6317.

(2) Flörke, M.; Schneider, C.; McDonald, R. I., Water competition between cities and agriculture driven by climate change and urban growth. *Nat Sustain* **2018,** *1* (1), 51-58.

(3) Jaeger, W. K.; Plantinga, A. J.; Chang, H.; Dello, K.; Grant, G.; Hulse, D.; McDonnell, J.; Lancaster, S.; Moradkhani, H.; Morzillo, A., Toward a formal definition of water scarcity in natural-human systems. *Water Resour. Res.* **2013,** *49* (7), 4506-4517.

(4) Malmqvist, B.; Rundle, S., Threats to the running water ecosystems of the world. *Environ. Conserv.* **2002,** *29* (2), 134-153.

(5) Water, U. N. 2018 UN World Water Development Report, Nature-based Solutions for Water. https://www.unwater.org/publications/world-water-development-report-2018/.

(6) Elimelech, M.; Phillip, W. A., The future of seawater desalination: energy, technology, and the environment. *Science* **2011,** *333* (6043), 712-717.

(7) Shannon, M. A.; Bohn, P. W.; Elimelech, M.; Georgiadis, J. G.; Marinas, B. J.; Mayes, A. M., Science and technology for water purification in the coming decades. *Nanosci. Technol.* **2010**, 337-346.

(8) Oelkers, E. H.; Hering, J. G.; Zhu, C., Water: is there a global crisis? *Elements* **2011,** *7* (3), 157-162.

(9) Zhou, X.; Lu, H.; Zhao, F.; Yu, G., Atmospheric water harvesting: a review of material and structural designs. *ACS Mater. Lett.* **2020,** *2* (7), 671-684.

(10) Lin, H.; Yang, Y.; Hsu, Y. C.; Zhang, J.; Welton, C.; Afolabi, I.; Loo, M.; Zhou, H. C., Metal-Organic Frameworks for Water Harvesting and Concurrent Carbon Capture: A Review for Hygroscopic Materials. *Adv. Mater.* **2023**, 2209073.

(11) Xu, W.; Yaghi, O. M., Metal–organic frameworks for water harvesting from air, anywhere, anytime. *ACS Cent. Sci.* **2020,** *6* (8), 1348-1354.

(12) Hanikel, N.; Prévot, M. S.; Yaghi, O. M., MOF water harvesters. *Nat. Nanotechnol.* **2020,** *15* (5), 348-355.

(13) Wahlgren, R. V., Atmospheric water vapour processor designs for potable water production: a review. *Water Res.* **2001,** *35* (1), 1-22.

(14) Lord, J.; Thomas, A.; Treat, N.; Forkin, M.; Bain, R.; Dulac, P.; Behroozi, C. H.; Mamutov, T.; Fongheiser, J.; Kobilansky, N., Global potential for harvesting drinking water from air using solar energy. *Nature* **2021,** *598* (7882), 611-617.

(15) Lu, H.; Shi, W.; Guo, Y.; Guan, W.; Lei, C.; Yu, G., Materials engineering for atmospheric water harvesting: progress and perspectives. *Adv. Mater.* **2022,** *34* (12), 2110079.

(16) Wang, J.; Hua, L.; Li, C.; Wang, R., Atmospheric water harvesting: critical metrics and challenges. *Energy Environ. Sci.* **2022,** *15* (12), 4867-4871.

(17) Yaghi, O. M.; Kalmutzki, M. J.; Diercks, C. S., *Introduction to reticular chemistry: metal-organic frameworks and covalent organic frameworks*. John Wiley & Sons: 2019.

(18) Freund, R.; Canossa, S.; Cohen, S. M.; Yan, W.; Deng, H.; Guillerm, V.; Eddaoudi, M.; Madden, D. G.; Fairen-Jimenez, D.; Lyu, H., 25 years of reticular chemistry. *Angew. Chem. Int. Ed.* **2021,** *60* (45), 23946-23974.
(19) Hanikel, N.; Prévot, M. S.; Fathieh, F.; Kapustin, E. A.; Lyu, H.; Wang, H.; Diercks, N. J.; Glover, T. G.; Yaghi, O. M., Rapid cycling and exceptional yield in a metal-organic framework water harvester. *ACS Cent. Sci.* **2019,** *5* (10), 1699-1706.
(20) Yaghi, O. M., The reticular chemist. *Nano Lett.* **2020,** *20* (12), 8432-8434.
(21) Kalmutzki, M. J.; Hanikel, N.; Yaghi, O. M., Secondary building units as the turning point in the development of the reticular chemistry of MOFs. *Sci. Adv.* **2018,** *4* (10), eaat9180.
(22) Yaghi, O. M.; O'Keeffe, M.; Ockwig, N. W.; Chae, H. K.; Eddaoudi, M.; Kim, J., Reticular synthesis and the design of new materials. *Nature* **2003,** *423* (6941), 705-714.
(23) Hanikel, N.; Pei, X.; Chheda, S.; Lyu, H.; Jeong, W.; Sauer, J.; Gagliardi, L.; Yaghi, O. M., Evolution of water structures in metal-organic frameworks for improved atmospheric water harvesting. *Science* **2021,** *374* (6566), 454-459.
(24) Furukawa, H.; Gandara, F.; Zhang, Y.-B.; Jiang, J.; Queen, W. L.; Hudson, M. R.; Yaghi, O. M., Water adsorption in porous metal–organic frameworks and related materials. *J. Am. Chem. Soc.* **2014,** *136* (11), 4369-4381.
(25) Gong, W.; Xie, H.; Idrees, K. B.; Son, F. A.; Chen, Z.; Sha, F.; Liu, Y.; Cui, Y.; Farha, O. K., Water sorption evolution enabled by reticular construction of zirconium metal–organic frameworks based on a unique [2.2] paracyclophane scaffold. *J. Am. Chem. Soc.* **2022,** *144* (4), 1826-1834.
(26) Jasuja, H.; Walton, K. S., Effect of catenation and basicity of pillared ligands on the water stability of MOFs. *Dalton Trans.* **2013,** *42* (43), 15421-15426.
(27) Chen, Z.; Li, P.; Zhang, X.; Li, P.; Wasson, M. C.; Islamoglu, T.; Stoddart, J. F.; Farha, O. K., Reticular access to highly porous acs-MOFs with rigid trigonal prismatic linkers for water sorption. *J. Am. Chem. Soc.* **2019,** *141* (7), 2900-2905.
(28) Abtab, S. M. T.; Alezi, D.; Bhatt, P. M.; Shkurenko, A.; Belmabkhout, Y.; Aggarwal, H.; Weseliński, Ł. J.; Alsadun, N.; Samin, U.; Hedhili, M. N., Reticular chemistry in action: A hydrolytically stable MOF capturing twice its weight in adsorbed water. *Chem* **2018,** *4* (1), 94-105.
(29) Cmarik, G. E.; Kim, M.; Cohen, S. M.; Walton, K. S., Tuning the adsorption properties of UiO-66 via ligand functionalization. *Langmuir* **2012,** *28* (44), 15606-15613.
(30) Solovyeva, M. V.; Shkatulov, A. I.; Gordeeva, L. G.; Fedorova, E. A.; Krieger, T. A.; Aristov, Y. I., Water vapor adsorption on CAU-10-X: Effect of functional groups on adsorption equilibrium and mechanisms. *Langmuir* **2021,** *37* (2), 693-702.
(31) Akiyama, G.; Matsuda, R.; Sato, H.; Hori, A.; Takata, M.; Kitagawa, S., Effect of functional groups in MIL-101 on water sorption behavior. *Microporous Mesoporous Mater.* **2012,** *157*, 89-93.
(32) Reinsch, H.; van der Veen, M. A.; Gil, B.; Marszalek, B.; Verbiest, T.; De Vos, D.; Stock, N., Structures, sorption characteristics, and nonlinear optical properties of a new series of highly stable aluminum MOFs. *Chem. Mater.* **2013,** *25* (1), 17-26.
(33) Cadiau, A.; Lee, J. S.; Damasceno Borges, D.; Fabry, P.; Devic, T.; Wharmby, M. T.; Martineau, C.; Foucher, D.; Taulelle, F.; Jun, C. H., Design of hydrophilic metal organic framework water adsorbents for heat reallocation. *Adv. Mater.* **2015,** *27* (32), 4775-4780.
(34) Cho, K. H.; Borges, D. D.; Lee, U.-H.; Lee, J. S.; Yoon, J. W.; Cho, S. J.; Park, J.;

Lombardo, W.; Moon, D.; Sapienza, A., Rational design of a robust aluminum metal-organic framework for multi-purpose water-sorption-driven heat allocations. *Nat. Commun.* **2020,** *11* (1), 5112.

(35) Furukawa, H.; Ko, N.; Go, Y. B.; Aratani, N.; Choi, S. B.; Choi, E.; Yazaydin, A. Ö.; Snurr, R. Q.; O'Keeffe, M.; Kim, J., Ultrahigh porosity in metal-organic frameworks. *Science* **2010,** *329* (5990), 424-428.

(36) Farha, O. K.; Eryazici, I.; Jeong, N. C.; Hauser, B. G.; Wilmer, C. E.; Sarjeant, A. A.; Snurr, R. Q.; Nguyen, S. T.; Yazaydın, A. O. z. r.; Hupp, J. T., Metal–organic framework materials with ultrahigh surface areas: is the sky the limit? *J. Am. Chem. Soc.* **2012,** *134* (36), 15016-15021.

(37) Burtch, N. C.; Jasuja, H.; Walton, K. S., Water stability and adsorption in metal–organic frameworks. *Chem. Rev.* **2014,** *114* (20), 10575-10612.

(38) Zheng, Z.; Alawadhi, A. H.; Yaghi, O. M., Green Synthesis and Scale-Up of MOFs for Water Harvesting from Air. *Mol. Front. J.* **2023,** *7* (1), 1-20.

(39) Lee, J. S.; Yoon, J. W.; Mileo, P. G.; Cho, K. H.; Park, J.; Kim, K.; Kim, H.; de Lange, M. F.; Kapteijn, F.; Maurin, G., Porous metal–organic framework CUK-1 for adsorption heat allocation toward green applications of natural refrigerant water. *ACS Appl. Mater. Interfaces* **2019,** *11* (29), 25778-25789.

(40) Wang, S.; Lee, J. S.; Wahiduzzaman, M.; Park, J.; Muschi, M.; Martineau-Corcos, C.; Tissot, A.; Cho, K. H.; Marrot, J.; Shepard, W., A robust large-pore zirconium carboxylate metal–organic framework for energy-efficient water-sorption-driven refrigeration. *Nat. Energy* **2018,** *3* (11), 985-993.

(41) Hanikel, N.; Kurandina, D.; Chheda, S.; Zheng, Z.; Rong, Z.; Neumann, S. E.; Sauer, J.; Siepmann, J. I.; Gagliardi, L.; Yaghi, O. M., MOF Linker Extension Strategy for Enhanced Atmospheric Water Harvesting. *ACS Cent. Sci.* **2023,** *9* (3), 551-557.

(42) Matemb Ma Ntep, T. J.; Wahiduzzaman, M.; Laurenz, E.; Cornu, I.; Mouchaham, G.; Dovgaliuk, I.; Nandi, S.; Knop, K.; Jansen, C.; Nouar, F.; Florian, P.; Füldner, G. F.; Maurin, G.; Janiak, C.; Serre, C., When Polymorphism in Metal–Organic Frameworks Enables Water Sorption Profile Tunability for Enhancing Heat Allocation and Water Harvesting Performance. *Adv. Mater.* **2023**, 2211302.

(43) Li, H.; Eddaoudi, M.; Groy, T. L.; Yaghi, O., Establishing microporosity in open metal-organic frameworks: Gas sorption isotherms for Zn (BDC)(BDC= 1, 4-benzenedicarboxylate)[28]. *J. Am. Chem. Soc.* **1998,** *120* (33), 8571-8572.

(44) Rubio-Martinez, M.; Avci-Camur, C.; Thornton, A. W.; Imaz, I.; Maspoch, D.; Hill, M. R., New synthetic routes towards MOF production at scale. *Chem. Soc. Rev.* **2017,** *46* (11), 3453-3480.

(45) Stock, N.; Biswas, S., Synthesis of metal-organic frameworks (MOFs): routes to various MOF topologies, morphologies, and composites. *Chem. Rev.* **2012,** *112* (2), 933-969.

(46) Furukawa, H.; Cordova, K. E.; O'Keeffe, M.; Yaghi, O. M., The chemistry and applications of metal-organic frameworks. *Science* **2013,** *341* (6149), 1230444.

(47) Zheng, Z.; Nguyen, H. L.; Hanikel, N.; Li, K. K.-Y.; Zhou, Z.; Ma, T.; Yaghi, O. M., High-yield, green and scalable methods for producing MOF-303 for water harvesting from desert air. *Nat. Protoc.* **2023,** *18*, 136–156.

(48) Khan, N. A.; Jhung, S. H., Synthesis of metal-organic frameworks (MOFs) with microwave or ultrasound: Rapid reaction, phase-selectivity, and size reduction. *Coord. Chem. Rev.* **2015,**

285, 11-23.
(49) Wu, X.; Bao, Z.; Yuan, B.; Wang, J.; Sun, Y.; Luo, H.; Deng, S., Microwave synthesis and characterization of MOF-74 (M= Ni, Mg) for gas separation. *Microporous Mesoporous Mater.* **2013,** *180*, 114-122.
(50) Klinowski, J.; Paz, F. A. A.; Silva, P.; Rocha, J., Microwave-assisted synthesis of metal–organic frameworks. *Dalton Trans.* **2011,** *40* (2), 321-330.
(51) Crawford, D.; Casaban, J.; Haydon, R.; Giri, N.; McNally, T.; James, S. L., Synthesis by extrusion: continuous, large-scale preparation of MOFs using little or no solvent. *Chem. Sci.* **2015,** *6* (3), 1645-1649.
(52) Chen, D.; Zhao, J.; Zhang, P.; Dai, S., Mechanochemical synthesis of metal–organic frameworks. *Polyhedron* **2019,** *162*, 59-64.
(53) Varsha, M.; Nageswaran, G., Direct electrochemical synthesis of metal organic frameworks. *J. Electrochem. Soc.* **2020,** *167* (15), 155527.
(54) Li, Y.; Wen, G.; Li, J.; Li, Q.; Zhang, H.; Tao, B.; Zhang, J., Synthesis and shaping of metal–organic frameworks: a review. *Chem. Commun.* **2022,** *58* (82), 11488-11506.
(55) Liang, Y.; Huang, H.; Kou, L.; Li, F.; Lu, J.; Cao, H. L., Synthesis of Metal–Organic Framework Materials by Reflux: A Faster and Greener Pathway to Achieve Super-Hydrophobicity and Photocatalytic Application. *Cryst. Growth Des.* **2018,** *18* (11), 6609-6616.
(56) Mandal, S.; Natarajan, S.; Mani, P.; Pankajakshan, A., Post-synthetic modification of metal–organic frameworks toward applications. *Adv. Funct. Mater.* **2021,** *31* (4), 2006291.
(57) Entezari, A.; Esan, O. C.; Yan, X.; Wang, R.; An, L., Sorption-based Atmospheric Water Harvesting: Materials, Components, Systems, and Applications. *Adv. Mater.* **2023**, 2210957.
(58) Kim, H.; Rao, S. R.; Kapustin, E. A.; Zhao, L.; Yang, S.; Yaghi, O. M.; Wang, E. N., Adsorption-based atmospheric water harvesting device for arid climates. *Nat. Commun.* **2018,** *9* (1), 1191.
(59) Fathieh, F.; Kalmutzki, M. J.; Kapustin, E. A.; Waller, P. J.; Yang, J.; Yaghi, O. M., Practical water production from desert air. *Sci. Adv.* **2018,** *4* (6), eaat3198.
(60) Lenzen, D.; Bendix, P.; Reinsch, H.; Fröhlich, D.; Kummer, H.; Möllers, M.; Hügenell, P. P.; Gläser, R.; Henninger, S.; Stock, N., Scalable green synthesis and full-scale test of the metal–organic framework CAU-10-H for use in adsorption-driven chillers. *Adv. Mater.* **2018,** *30* (6), 1705869.
(61) Kim, S.-N.; Lee, Y.-R.; Hong, S.-H.; Jang, M.-S.; Ahn, W.-S., Pilot-scale synthesis of a zirconium-benzenedicarboxylate UiO-66 for CO2 adsorption and catalysis. *Catal. Today* **2015,** *245*, 54-60.
(62) Zhao, T.; Jeremias, F.; Boldog, I.; Nguyen, B.; Henninger, S. K.; Janiak, C., High-yield, fluoride-free and large-scale synthesis of MIL-101 (Cr). *Dalton Trans.* **2015,** *44* (38), 16791-16801.

Chapter II

Mass Production of MOFs for Atmospheric Water Harvesting

2.1 Introduction

Water scarcity, intensified by the unequal distribution of resources and escalating demands in arid regions, poses a daunting global challenge and the need for innovative solutions becomes paramount.[1, 2] Atmospheric water, with its vast reservoir surpassing even the volume of all freshwater rivers, emerges as a potential lifeline.[3-5] Yet, tapping into this resource directly, especially in low-humidity regions, remains problematic.[3, 6-9]

Sorbent-assisted water harvesting offers a promising solution. This technique leverages porous solid sorbents, specifically metal-organic frameworks (MOFs), to capture and release water molecules efficiently. While a significant body of work has been created in developing MOF sorbents with tailored capacity and isotherm shape, it has largely been limited to small-scale proof of concepts and there are few reports on the large-scale synthesis of water harvesting MOFs for industrial use.[10-12] On the other hand, it was proposed that the concept of green synthesis methods using water as a solvent can address the challenges of high production cost and environmental hazards in the industrial-scale synthesis of MOFs.[13-15] As such, despite MOFs showcasing their potential in laboratory trials, the main challenge—and the central theme of this chapter—is bridging the gap from these laboratory successes to achieving cost-effective, scalable, and eco-friendly mass production of water harvesting MOFs.

Portions of this chapter have been adapted from:
Zheng, Z.; Alawadhi, A. H.; Yaghi, O. M., Green Synthesis and Scale-Up of MOFs for Water Harvesting from Air. *Mol. Front. J.* **2023,** *7* (1), 1-20.
Zheng, Z.; Nguyen, H. L.; Hanikel, N.; Li, K. K.-Y.; Zhou, Z.; Ma, T.; Yaghi, O. M., High-Yield, Green and Scalable Methods for Producing MOF-303 for Water Harvesting from Desert Air. *Nat. Protoc.* **2023,** *18*, 136–156.

MOF-303 stands out as a leading candidate in this endeavor.[3] Beyond its structural uniqueness and efficiency in water harvesting, the true potential of MOF-303 lies in its green and scalable synthesis (Figure 2.1). In this chapter, the development of a green and reliable synthetic approach to prepare this useful MOF at scale is demonstrated. Particularly, I successfully increased the yield of MOF-303 production from 38% to 91% by modification of the reported aqueous-based reflux synthesis procedure for aluminum MOFs.[10, 16-18] In contrast to the traditional solvothermal methods, it reduced the reaction time. With the optimized mole ratio between NaOH and H_2PZDC linker, the synthesized MOF-303 exhibits high reaction yield and crystallinity. It inspired me to move forward to large-scale synthesis of MOF-303 based on the same approach. It was shown that the synthesis can be scaled to 3.5 kg per batch at homogenous particle size with no compromises to its crystallinity and water uptake capacity. Building on the success with MOF-303, I expanded the horizons to adapt this scalable synthesis method to a series of other aluminum-based MOFs (Table 2.1). This includes notables like CAU-23, MIL-160, MOF-313, Al-fumarate, and CAU-10. Crucially, all these MOFs have been demonstrated to be producible at a kilogram scale with high yields.

Herein, this chapter underscores the development of a green, robust, and high-yield synthesis method for the synthesis of a series of water-harvesting MOFs, emphasizing mass production without compromising on efficiency. Using water as the sole solvent, this environmental-friendly process not only negates the use of harmful organic solvents but also proves cost-effective, especially given the commercial availability of the organic linkers. The protocol ensures that MOFs can be produced in substantial quantities, reaching several kilograms per batch, without compromising their crystallinity, porosity, or water uptake capacities.

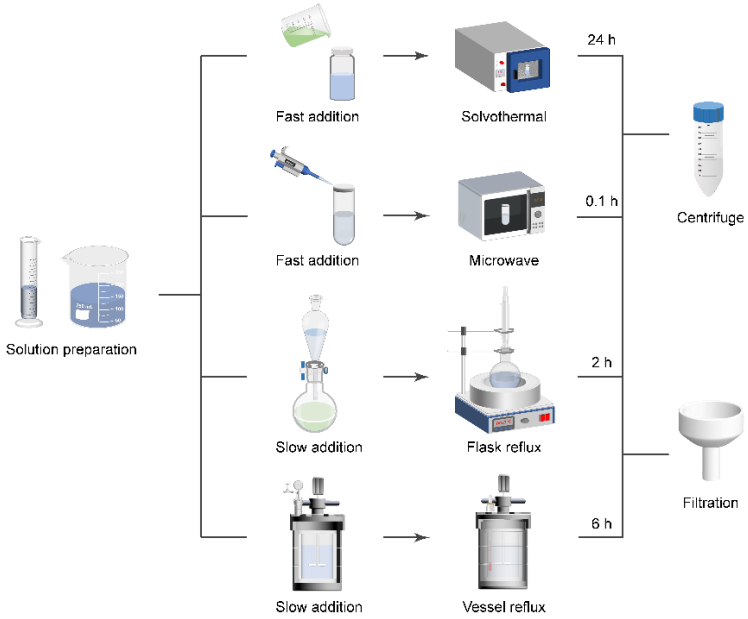

Figure 2.1 Various methods for the synthesis of MOF-303 along with the reaction time of each. This chapter emphasizes the development of the vessel reflux method, which boasts higher yields and has the capability to synthesize MOFs on a kilogram scale, surpassing other methods.

Table 2.1 Comparison of synthesis scale of water-harvesting MOFs.

MOF	Composition[a]	Solvent and volume[b]	Conditions	Dry MOF obtained per batch (g)	Yield[d] (%)	Ref.
Al-Fum	Al(OH)(Fum)	H_2O (50 L)	Reflux, 6 h	2970	94	this work
		H_2O (0.01 L)	60 °C, 2 h	0.4	74	18
CAU-10	Al(OH)(IPA)	H_2O (50 L)	Reflux, 6 h	3810	92	this work
		H_2O (8.19 L), EtOH (0.42 L)	Reflux, 10 h	500[c]	93	10
CAU-23	Al(OH)(TDC)	H_2O (50 L)	Reflux, 6 h	3610	84	this work
		H_2O (0.13 L)	Reflux, 6 h	5	84	17
Co-CUK-1	$Co_3(OH)_2$(2,4-PDC)$_2$	H_2O (0.004 L)	200 °C, 15 h	0.2	67	19
MIL-101-Cr	Cr_3O(OH)(BDC)$_3$	H_2O (2.4 L)	200 °C, 15 h	127	68	20
MIL-125-NH_2	$Ti_8O_8(OH)_4$(BDC-NH_2)$_6$	DMF (0.05 L), MeOH (0.01 L)	110 °C, 5 h	4	94	21
MIL-160	Al(OH)(FDC)	H_2O (50 L)	Reflux, 6 h	3640	92	this work
		H_2O (1 L)	Reflux, 24 h	130[c]	93	22
MIP-200	$Zr_6O_4(OH)_4$(MDIP)$_2$(HCOO)$_4$	Ac_2O (0.035 L), HCOOH (0.025 L)	120 °C, 48 h	1	96	23
MOF-303	Al(OH)(PZDC)	H_2O (50 L)	Reflux, 6 h	3590	91	this work
		H_2O (0.75 L)	100 °C, 24 h	3	35	24
MOF-313	Al(OH)(2,5-PylDC)	H_2O (0.5 L)	Reflux, 6 h	38	96	this work
		H_2O (0.05 L)	Reflux, 12 h	2	93	25
		H_2O (0.005 L)	100 °C, 2 h	0.01	7	26
MOF-801	$Zr_6O_4(OH)_4$(HCOO)$_6$	DMF (0.04 L), HCOOH (0.01 L)	130 °C, 10 h	2	25	24
MOF-841	$Zr_6O_4(OH)_4$(MTB)$_2$(HCOO)$_4$	DMF (0.04 L), HCOOH (0.02 L)	130 °C, 48 h	0.1	55	27
Ni-BTDD	Ni_2Cl_2(BTDD)	DMF (0.2 L), EtOH (0.2 L)	65 °C, 10 d	0.3	87	28
UiO-66	$Zr_6O_4(OH)_4$(BDC)$_6$	DMF (60 L)	115 °C, 24 h	1560[c]	93	11

[a] Formula excluding guests. Abbreviations: Fum = fumarate, IPA = 1,3-benzenedicarboxylate (isophthalate), TDC = thiophene-2,5-dicarboxylate, 2,4-PDC = pyridine-2,4-dicarboxylate, BDC = benzene-1,4-dicarboxylate, BDC-NH_2 = 2-amine-1,4-benzenedicarboxylate, FDC = furan-2,5,-dicarboxylate, MDIP = methylene-diisophthalate, $HCOO^-$ = formate, PZDC = 1*H*-pyrazole-3,5-dicarboxylate, 2,5-PylDC = pyrrole-2,5-dicarboxylate, MTB = 4,4′,4″,4‴-methane-tetrayltetrabenzoate, BTDD = bis(1*H*-1,2,3-triazolo[4,5-b],[4′,5′-i])dibenzo[1,4]dioxin, BDC = 1,4-benzenedicarboxylate. [b] The volume of the modulators, which is much lower than that of other solvents in the reaction, was not listed. EtOH = ethanol, MeOH = methanol, DMF = N, N-Dimethylformamide, and HCOOH = formic acid. [c] The exact weight of dry MOF obtained per batch was not given, and the number was calculated based on the reaction yield. [d] Yield of each MOF based on the amounts of corresponding linkers.

2.2 Experimental section

2.2.1 Starting materials and general procedures

Bulk (40 kg) 1*H*-pyrazole-3,5-dicarboxylic acid ($H_2PZDC \cdot H_2O$, purity ≥ 95%), $AlCl_3 \cdot 6H_2O$ (purity ≥ 99%) and $Al_2(SO_4)_3 \cdot 18H_2O$ (purity ≥ 98%) were purchased from Aaron Chemicals LLC. Bulk (10 kg) 2,5-thiophenedicarboxylic acid (H_2TDC, purity ≥ 98%) was purchased from Ambeed Inc. Bulk (5 kg) 2,5-furandicarboxylic acid (H_2FDC, purity ≥ 98%), isophthalic acid (purity ≥ 98%), and fumaric acid (purity ≥ 98%) were purchased from Arctom Chemicals LLC. Bulk (20 kg) sodium hydroxide pellets (NaOH, purity ≥ 97%) was purchased from Oakwood Products, Inc. Bulk ethanol (EtOH, purity ≥ 99.8%) was purchased from Sigma Aldrich. 1*H*-Pyrrole-2,5-dicarboxylic acid (H_2PylDC, purity ≥ 98%) was purchased from Aaron Chemicals LLC. Deuterated solvents were obtained from Cambridge Isotope Laboratories. Ultrahigh-purity (UHP) grade (99.999%) argon and nitrogen were obtained from Praxair. All starting materials and solvents were used without further purification.

Prior to the analysis and characterization, the MOF samples were washed with H_2O and ethanol, and evacuated at room temperature for 1 h and at 120 °C for an additional 12 h. To analyze the linker composition of the MOF compounds with NMR spectroscopy, the activated sample was fully hydrolyzed using a NaOD solution (10% in D_2O). ^{1}H-NMR spectra were acquired on Bruker NEO-500 MHz spectrometers, and elemental analysis (EA) was performed on a PerkinElmer 2400 Series II CHNS elemental analyzer at the NMR facility and Microanalytical Laboratory of the College of Chemistry, University of California, Berkeley. Thermal gravimetric analysis (TGA) curves were taken using a TA Q500 thermal analysis system with a heating rate of 5 °C/min under N_2 flow. Powder X-ray diffraction (PXRD) patterns were recorded using a Rigaku MiniFlex 6G equipped with a HyPix-400MF Hybrid Pixel Array detector and a normal focus X-ray tube with a Cu-source (λ = 1.54178 Å). Nitrogen sorption experiments were conducted using a Micromeritics Accelerated Surface Area and Porosimetry (ASAP) 2420 System. During the measurement, the sample was cooled to 77 K in a liquid nitrogen bath. Water vapor sorption experiments were carried out on a BEL Japan BELSORP-aqua or a Micromeritics 3Flex Surface Characterization Analyzer. The water vapor source was degassed through five freeze-pump-thaw cycles before the analysis. An isothermal water bath was employed to keep the sample temperature during the measurements.

2.2.2 Preparation of MOF materials

MOF-303, Al(OH)(PZDC). The synthesis of MOF-303 was adopted from our previous reports.[29, 30] In a 200 L glass reaction vessel equipped with a heating jacket, a mixture of $H_2PZDC \cdot H_2O$ (3.48 kg, 20 mol) and NaOH (2.4 kg, 60 mol) were dissolved in 38 L deionized water. The resulting solution was stirred for 60 minutes until all the solids were completely dissolved and the solution cooled down to room temperature. Next, in a 20 L beaker, $AlCl_3 \cdot 6H_2O$ (4.82 kg, 20 mol) was dissolved in 12 L deionized water and transferred to a 15 L glass material-

feeding funnel. The 12 L aluminum chloride solution was slowly added to the 38 L linker solution in the vessel at a rate of 6 L per hour with vigorous stirring. The total addition time lasted 2 hours, and the white precipitate formed during the addition. Afterward, the temperature of the heating jacket was set to 120 °C, thus heating the reaction mixture to 100 °C. After refluxing for 6 hours and letting the reaction mixture cool down to 60 °C, the white solid product was collected in a 20 L filtration funnel. For purification, the white powder was subsequently redispersed by stirring in 15 L aqueous 70% EtOH (v/v) solution, filtered off, and washed again with 30 L anhydrous EtOH at room temperature, followed by filtration and drying under air overnight. The obtained white powder was placed in a 120 °C oven for 48 hours to yield the pure and desolvated product (3.61 kg, 91% based on the linker). Elemental analysis for the activated sample of MOF-303: Calcd. for $AlC_5H_3N_2O_5$ = Al(OH)(PZDC) : C, 30.32; H, 1.53; N, 14.14 wt%; Found: C, 29.77; H, 1.58; N, 13.40 wt%.

CAU-23, Al(OH)(TDC). In a 200 L glass reaction vessel equipped with a heating jacket, a mixture of H_2TDC (3.44 kg, 20 mol) and NaOH (2.4 kg, 60 mol) were dissolved in 38 L deionized water. The resulting solution was stirred for 60 minutes until all the solids were completely dissolved and the solution cooled down to room temperature. Next, in a 20 L beaker, $AlCl_3 \cdot 6H_2O$ (4.82 kg, 20 mol) was dissolved in 12 L deionized water and transferred to a 15 L glass material-feeding funnel. The 12 L aluminum chloride solution was slowly added to the 38 L linker solution in the vessel at a rate of 6 L per hour with vigorous stirring. The total addition time lasted 2 hours, and the white precipitate formed during the addition. Afterward, the temperature of the heating jacket was set to 120 °C, thus heating the reaction mixture to 100 °C. After refluxing for 6 hours and letting the reaction mixture cool down to 60 °C, the white solid product was collected in a 20 L filtration funnel. For purification, the white powder was subsequently redispersed by stirring in 15 L aqueous 70% EtOH (v/v) solution, filtered off, and washed again with 30 L anhydrous EtOH at room temperature, followed by filtration and drying under air overnight. The obtained white powder was placed in a 120 °C oven for 48 hours to yield the pure and desolvated product (3.50 kg, 84% based on the linker). Elemental analysis for the activated sample of CAU-23: Calcd. for $AlC_6H_3SO_5$ = Al(OH)(TDC) : C, 33.66; H, 1.41; N, 37.36; S, 14.97 wt%; Found: C, 33.62; H, 1.48; S, 14.95 wt%.

MIL-160, Al(OH)(FDC). In a 200 L glass reaction vessel equipped with a heating jacket, a mixture of H_2FDC (3.12 kg, 20 mol) and NaOH (2.4 kg, 60 mol) were dissolved in 40 L deionized water. The resulting solution was stirred for 60 minutes until all the solids were completely dissolved and the solution cooled down to room temperature. Next, in a 20 L beaker, $AlCl_3 \cdot 6H_2O$ (4.82 kg, 20 mol) was dissolved in 10 L deionized water and transferred to a 15 L glass material-feeding funnel. The 10 L aluminum chloride solution was slowly added to the 40 L linker solution in the vessel at a rate of 5 L per hour with vigorous stirring. The total addition time lasted 2 hours, and the white precipitate formed during the addition. Afterward, the temperature of the heating jacket was set to 120 °C, thus heating the reaction mixture to 100 °C. After refluxing for 6 hours and letting the reaction mixture cool down to 60 °C, the white solid product was collected in a 20 L filtration funnel. For purification, the white powder was subsequently redispersed by stirring in 15 L aqueous 70% EtOH (v/v) solution, filtered off, and washed again with 30 L anhydrous EtOH at room temperature, followed by filtration and drying under air overnight. The obtained white

powder was placed in a 120 °C oven for 48 hours to yield the pure and desolvated product (3.64 kg, 92% based on the linker). Elemental analysis for the activated sample of MIL-160: Calcd. for $AlC_6H_3O_6$ = Al(OH)(FDC) : C, 36.38; H, 1.53 wt%; Found: C, 36.49; H, 1.48 wt%.

MOF-313, Al(OH)(2,5-PylDC). In a 1 L glass round bottom flask, a mixture of H_2PylDC (31 g, 0.2 mol) and NaOH (24 g, 0.6 mol) were dissolved in 0.4 L deionized water. The resulting solution was stirred for 10 minutes until all the solids were completely dissolved. Next, $AlCl_3 \cdot 6H_2O$ (48.2 g, 0.2 mol) was dissolved in 0.1 L deionized water and added to the round bottom flask dropwise with vigorous stirring. The total addition time lasted 2 hours, and the white precipitate formed during the addition. Afterward, the reaction mixture was heated to 120 °C. After refluxing for 6 hours and letting the reaction mixture cool down to room temperature, the white solid product was collected by centrifugation. For purification, the white powder was washed twice with deionized water and subsequently washed three times with EtOH. The white solid was air-dried overnight. Full activation of the MOF was conducted *in vacuo* at 120 °C for 24 hours, yielding pure and desolvated product (38 g, 96% based on the linker). Elemental analysis for the activated sample of MOF-313: Calcd. for $AlC_6H_4O_5N$ = Al(OH)(2,5-PylDC) : C, 36.57; H, 2.05; N, 7.11 wt%; Found: C, 36.55; H, 2.04; N, 6.26 wt%.

Al-fumarate, Al(OH)(Fum). In a 200 L glass reaction vessel equipped with a heating jacket, a mixture of fumaric acid (2.32 kg, 20 mol) and NaOH (2.4 kg, 60 mol) were dissolved in 26 L deionized water. The resulting solution was stirred for 60 minutes until all the solids were completely dissolved and the solution cooled down to room temperature. Next, $AlCl_3 \cdot 6H_2O$ (4.82 kg, 20 mol) was dissolved in 24 L deionized water and divided into two equal portions. The first portion (12 L) was transferred to a 15 L glass material-feeding funnel and subsequently added to the 26 L linker solution in the vessel slowly at a rate of 12 L per hour with vigorous stirring. The procedure was then repeated for the second portion of the aluminum chloride solution. The total addition time lasted for 2 hours, and the white precipitate formed during the addition. Afterward, the temperature of the heating jacket was set to 110 °C, thus heating the reaction mixture to 100 °C. After refluxing for 6 hours and letting the reaction mixture cool down to room temperature, the white solid product was collected in a 20 L filtration funnel. For purification, the white powder was subsequently redispersed by stirring in 15 L aqueous 70% EtOH (v/v) solution, filtered off, and washed again with 30 L anhydrous EtOH at room temperature, followed by filtration and drying in air overnight. The obtained white powder was placed in a 120 °C oven for 48 hours to yield the pure and desolvated product (2.97 kg, 94% based on the linker). Elemental analysis for the activated sample of Al-fumarate: Calcd. for $AlC_4H_3O_5$ = Al(OH)(Fum): C, 30.40; H, 1.91 wt%; Found: C, 30.28; H, 1.95 wt%.

CAU-10, Al(OH)(IPA). In a 200 L glass reaction vessel equipped with a heating jacket, a mixture of isophthalic acid (3.32 kg, 20 mol) and NaOH (2.4 kg, 60 mol) were dissolved in 26 L deionized water. The resulting solution was stirred for 60 minutes until all the solids were completely dissolved and the solution cooled down to room temperature. Next, $Al_2(SO_4)_3 \cdot 18H_2O$ (6.67 kg, 10 mol) was dissolved in 24 L deionized water and divided into two equal portions. The first portion (12 L) was transferred to a 15 L glass material-feeding funnel and subsequently added

to the 26 L linker solution in the vessel slowly at a rate of 12 L per hour with vigorous stirring. The procedure was then repeated for the second portion of the aluminum sulfate solution. The total addition time lasted 2 hours, and the white precipitate formed during the addition. Afterward, the temperature of the heating jacket was set to 130 °C, thus heating the reaction mixture to 100 °C. After refluxing for 6 hours and letting the reaction mixture cool down to room temperature, the white solid product was collected in a 20 L filtration funnel. For purification, the white powder was subsequently redispersed by stirring in 15 L deionized water, filtered off, and washed again with 3 × 15 L anhydrous EtOH at room temperature, followed by filtration and drying in air overnight. The obtained white powder was placed in a 120 °C oven for 48 hours to yield the pure and desolvated product (3.81 kg, 92% based on the linker). Elemental analysis for the activated sample of CAU-10: Calcd. for $AlC_4H_3O_5$ = Al(OH)(IPA) : C, 46.17; H, 2.42 wt%; Found: C, 45.85; H, 2.35 wt%.

2.2.3 Powder X-ray diffraction analysis

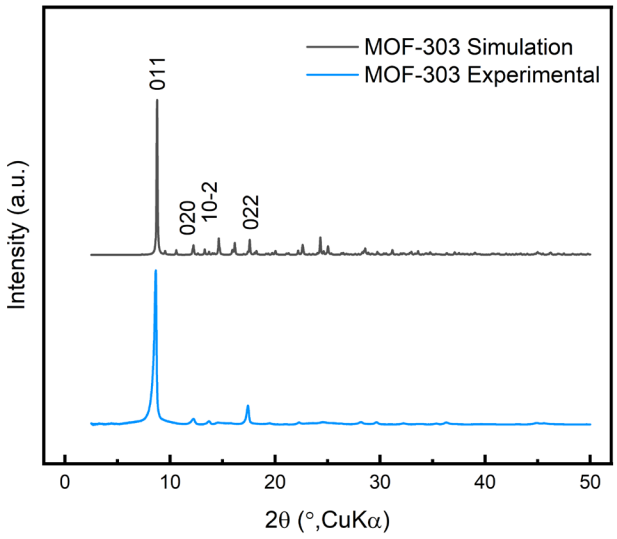

Figure 2.2 Powder x-ray diffraction analysis of MOF-303.

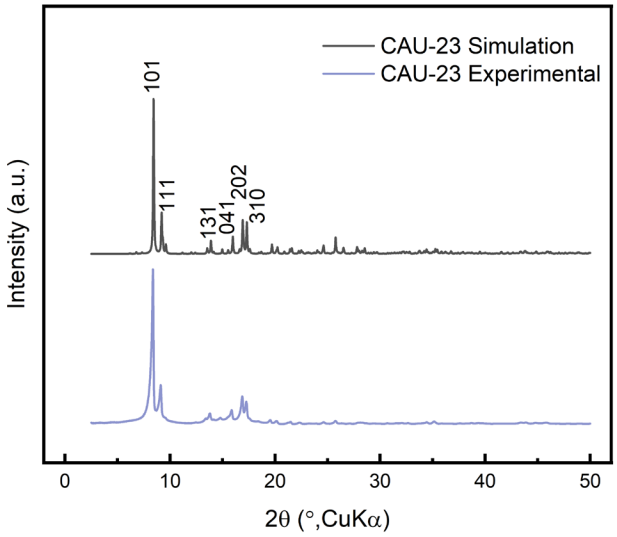

Figure 2.3 Powder x-ray diffraction analysis of CAU-23.

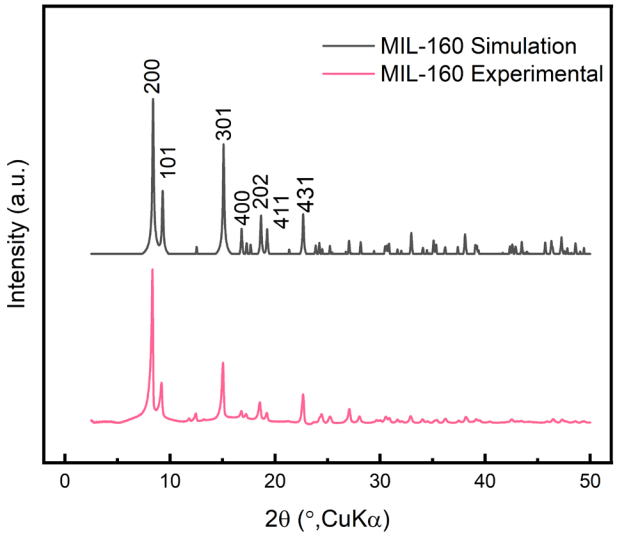

Figure 2.4 Powder x-ray diffraction analysis of MIL-160.

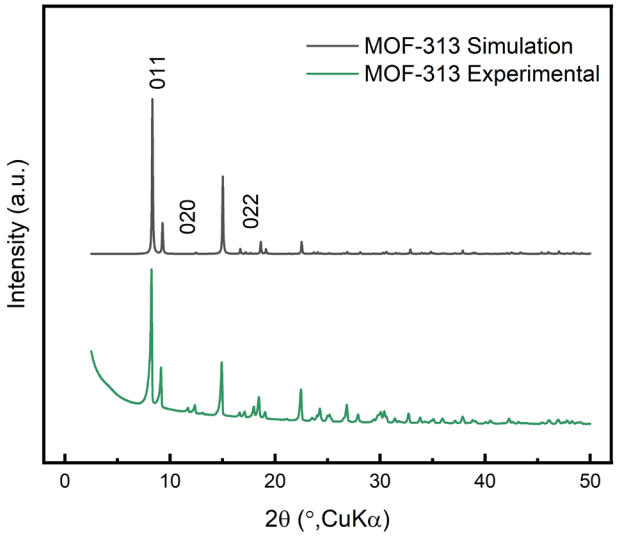

Figure 2.5 Powder x-ray diffraction analysis of MOF-313.

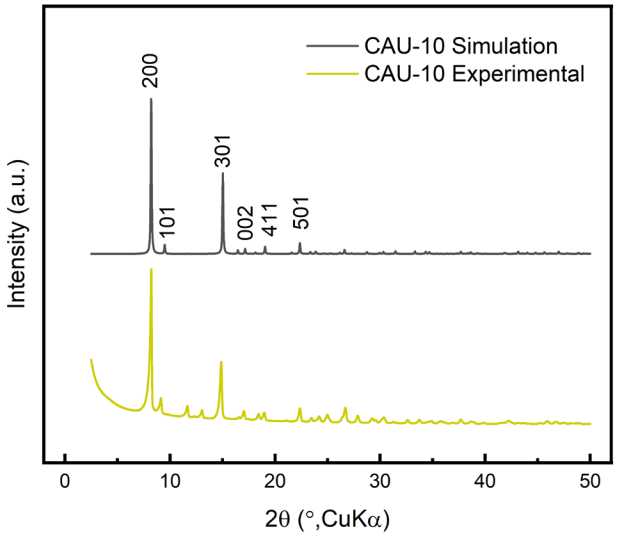

Figure 2.6 Powder x-ray diffraction analysis of CAU-10.

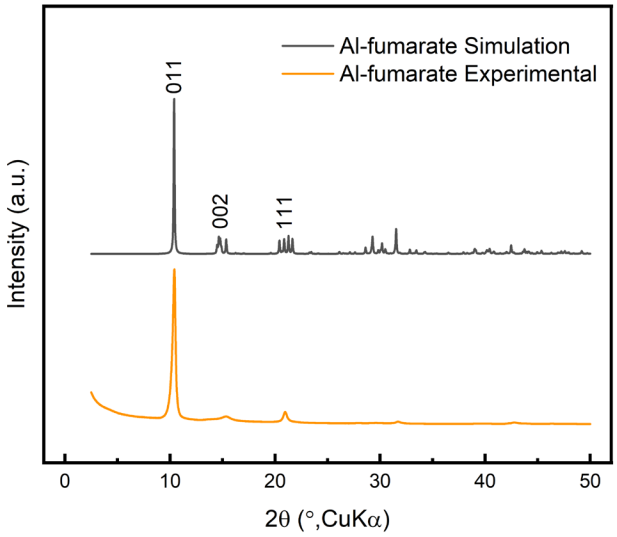

Figure 2.7 Powder x-ray diffraction analysis of Al-fumarate.

2.2.4 Nuclear magnetic resonance spectroscopy

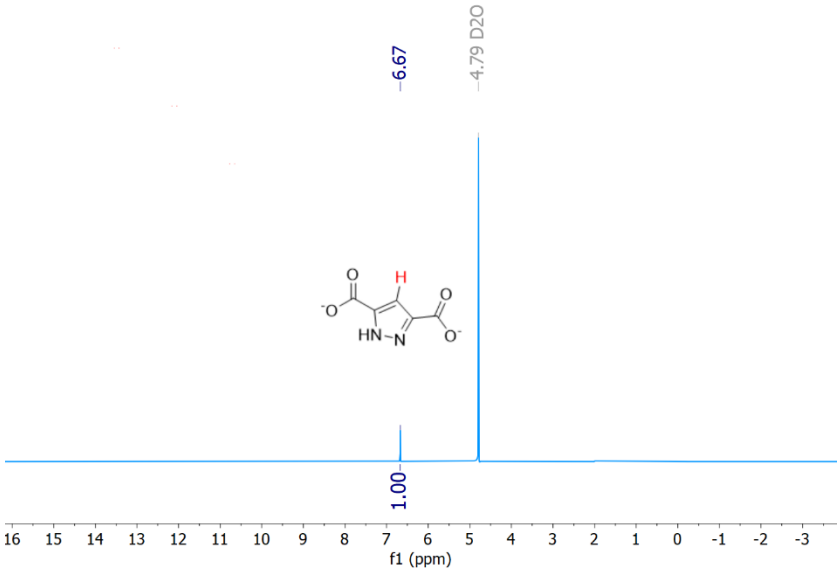

Figure 2.8 ^{1}H-NMR spectrum of MOF-303 after being thoroughly washed with EtOH and digested in 10% NaOD in D_2O.

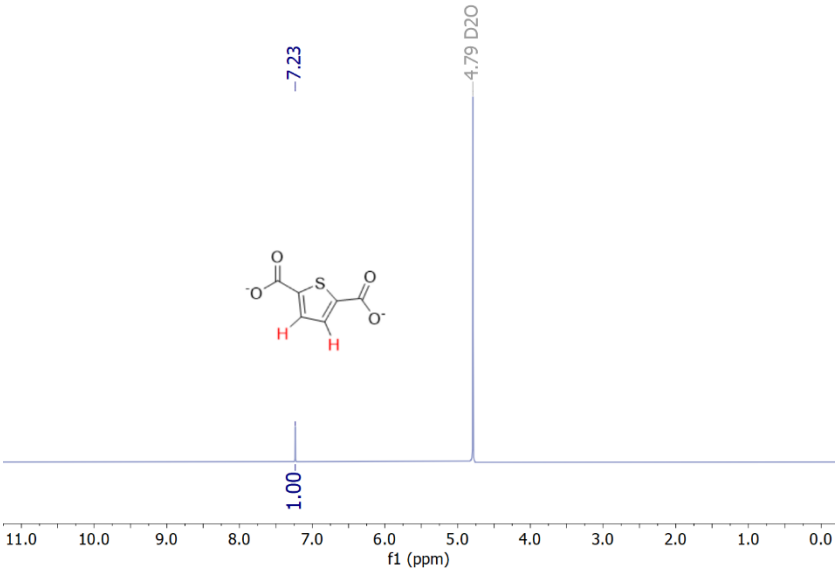

Figure 2.9 ^{1}H-NMR spectrum of CAU-23 after being thoroughly washed with EtOH and digested in 10% NaOD in D_2O.

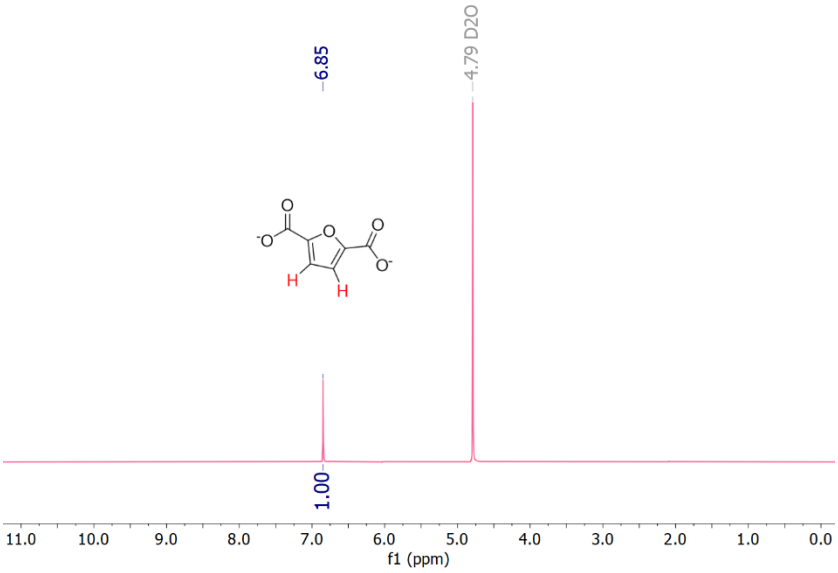

Figure 2.10 ^{1}H-NMR spectrum of MIL-160 after being thoroughly washed with EtOH and digested in 10% NaOD in D_2O.

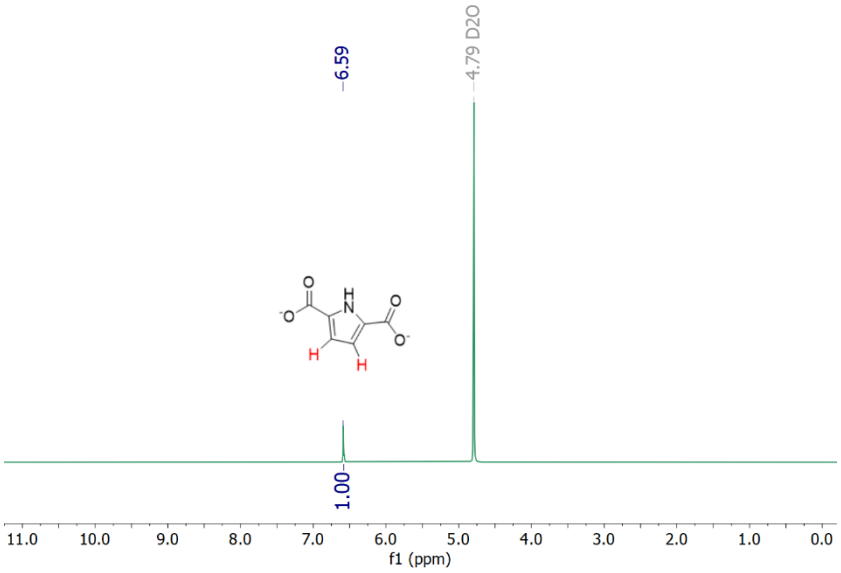

Figure 2.11 [1]H-NMR spectrum of MOF-313 after being thoroughly washed with EtOH and digested in 10% NaOD in D_2O.

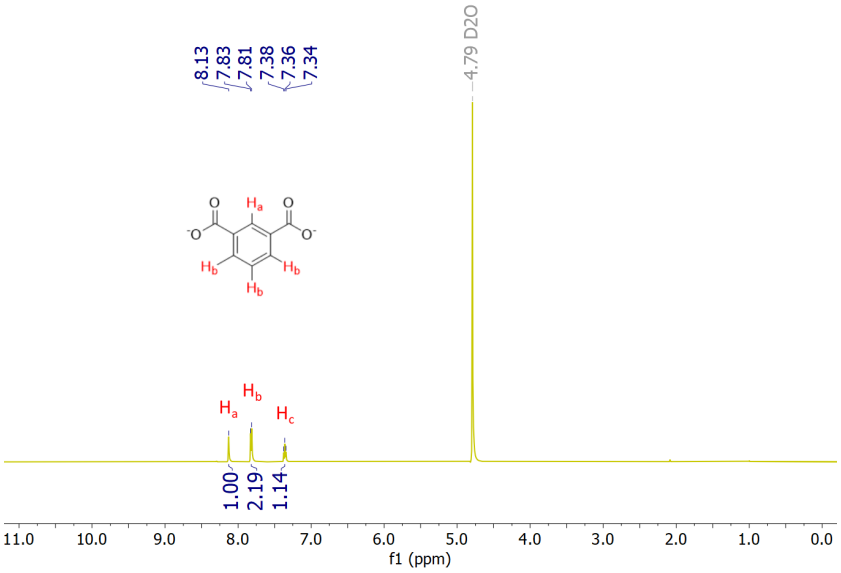

Figure 2.12 [1]H-NMR spectrum of CAU-10 after being thoroughly washed with EtOH and digested in 10% NaOD in D_2O.

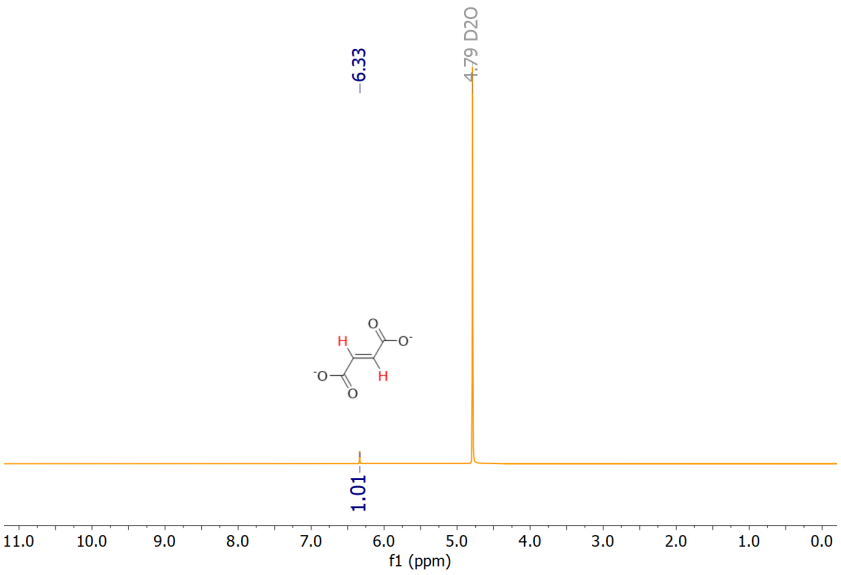

Figure 2.13 ^{1}H-NMR spectrum of Al-fumarate after being thoroughly washed with EtOH and digested in 10% NaOD in D_2O.

2.2.5 Nitrogen sorption analysis

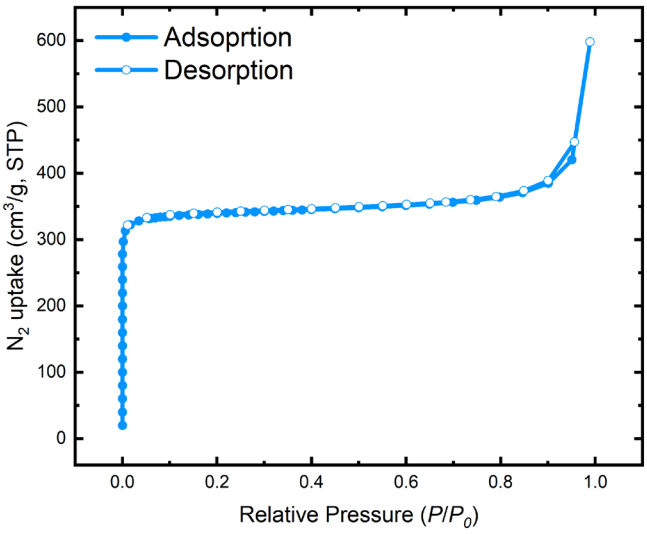

Figure 2.14 Nitrogen sorption analysis of MOF-303 at 77 K (BET surface area 1379 m^2/g; *P*: partial pressure of argon, P_0 = 1 atm, STP: standard temperature and pressure).

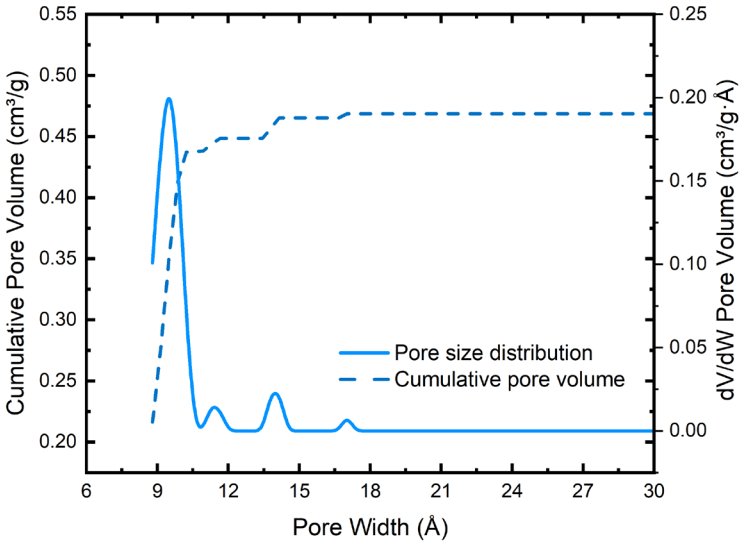

Figure 2.15 Differential and cumulative pore volume of MOF-303 estimated from its nitrogen sorption isotherm at 77 K.

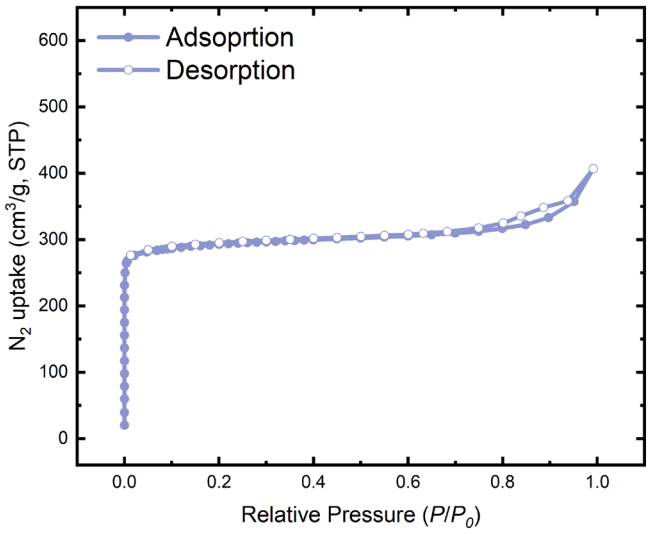

Figure 2.16 Nitrogen sorption analysis of CAU-23 at 77 K (BET surface area 1176 m^2/g; *P*: partial pressure of argon, P_0 = 1 atm, STP: standard temperature and pressure).

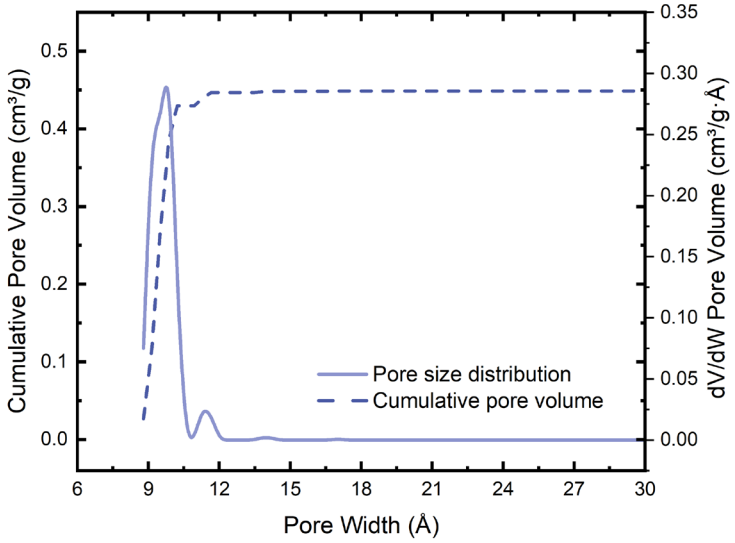

Figure 2.17 Differential and cumulative pore volume of CAU-23 estimated from its nitrogen sorption isotherm at 77 K.

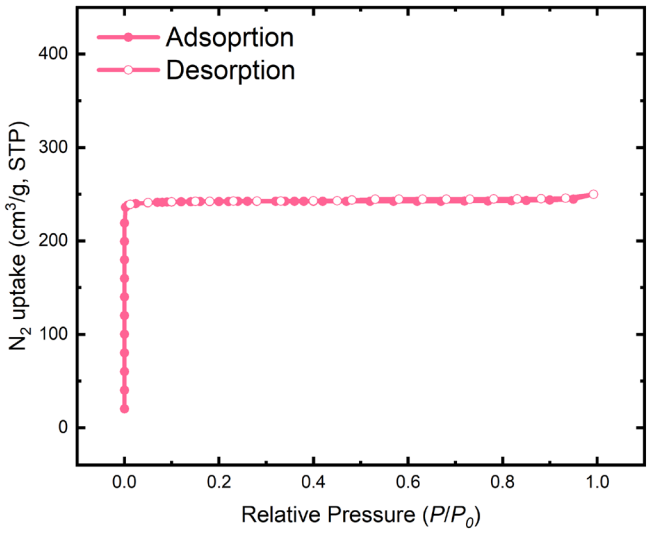

Figure 2.18 Nitrogen sorption analysis of MIL-160 at 77 K (BET surface area 1030 m^2/g; P: partial pressure of argon, P_0 = 1 atm, STP: standard temperature and pressure).

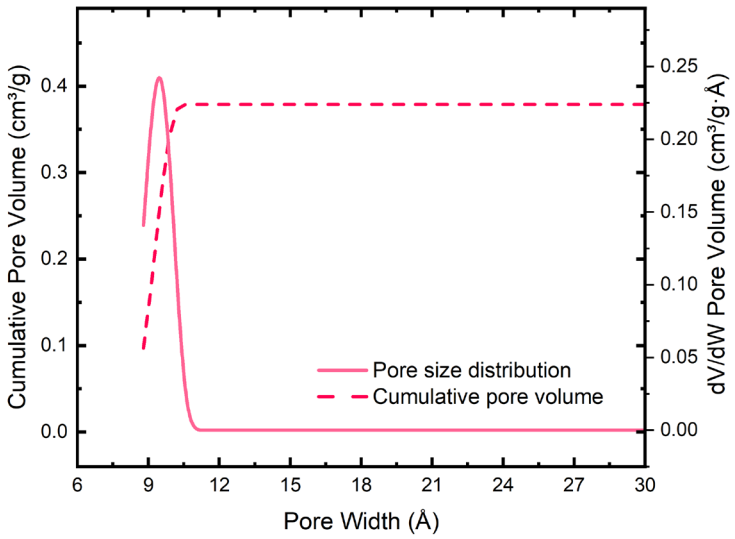

Figure 2.19 Differential and cumulative pore volume of MIL-160 estimated from its nitrogen sorption isotherm at 77 K.

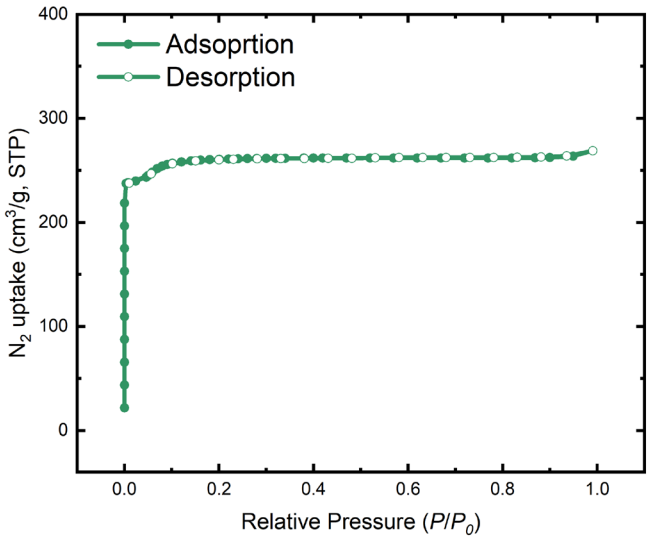

Figure 2.20 Nitrogen sorption analysis of MOF-313 at 77 K (BET surface area 1033 m^2/g; *P*: partial pressure of argon, P_0 = 1 atm, STP: standard temperature and pressure).

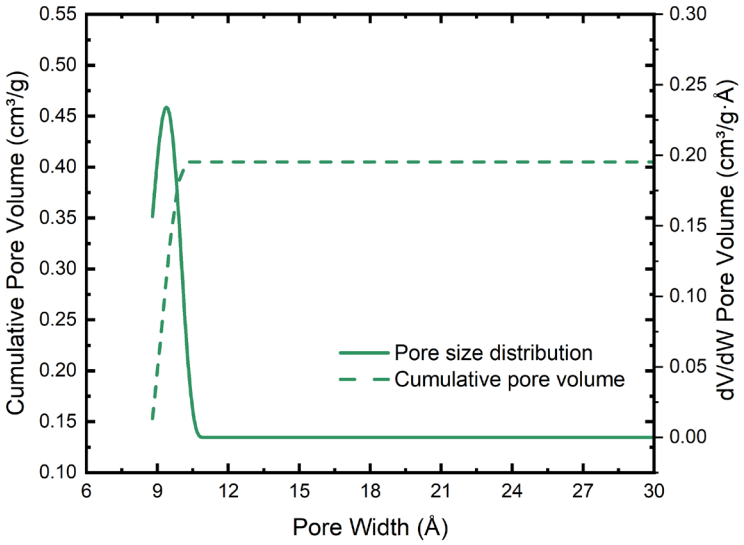

Figure 2.21 Differential and cumulative pore volume of MOF-313 estimated from its nitrogen sorption isotherm at 77 K.

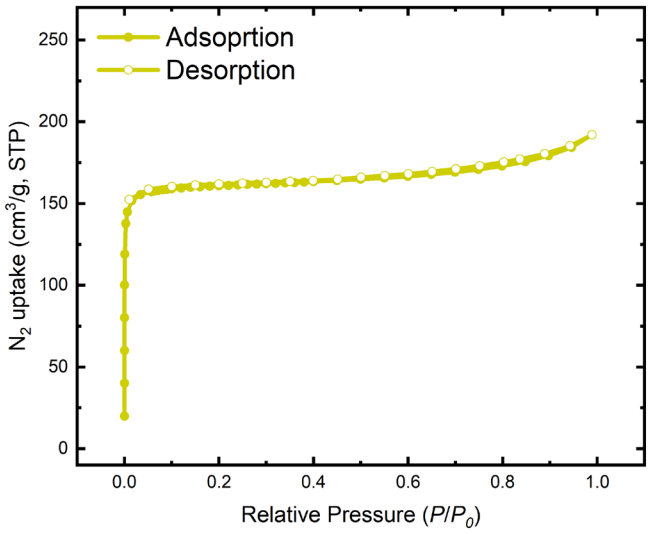

Figure 2.22 Nitrogen sorption analysis of CAU-10 at 77 K (BET surface area 654 m^2/g; *P*: partial pressure of argon, P_0 = 1 atm, STP: standard temperature and pressure).

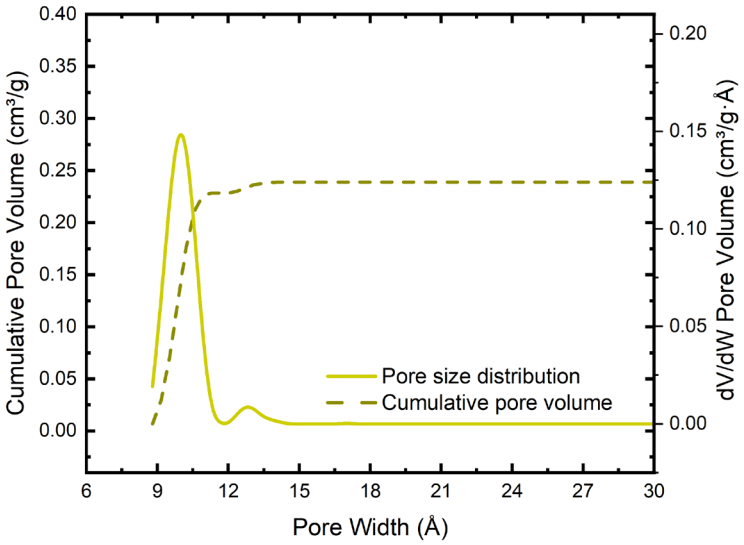

Figure 2.23 Differential and cumulative pore volume of CAU-10 estimated from its nitrogen sorption isotherm at 77 K.

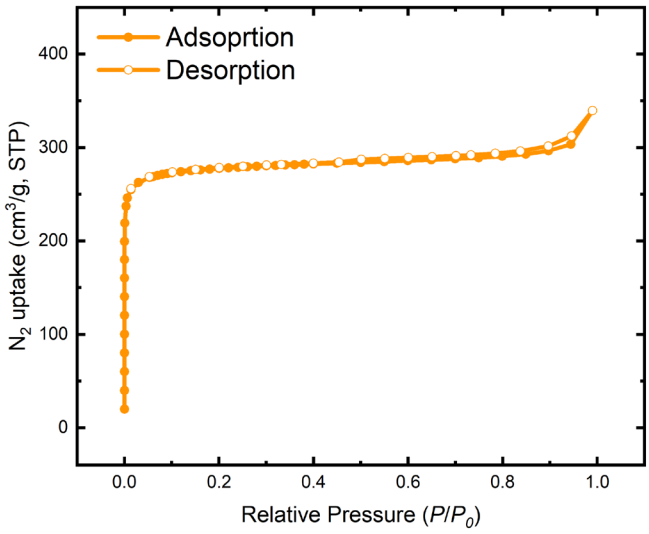

Figure 2.24 Nitrogen sorption analysis of Al-fumarate at 77 K (BET surface area 654 m^2/g; *P*: partial pressure of argon, P_0 = 1 atm, STP: standard temperature and pressure).

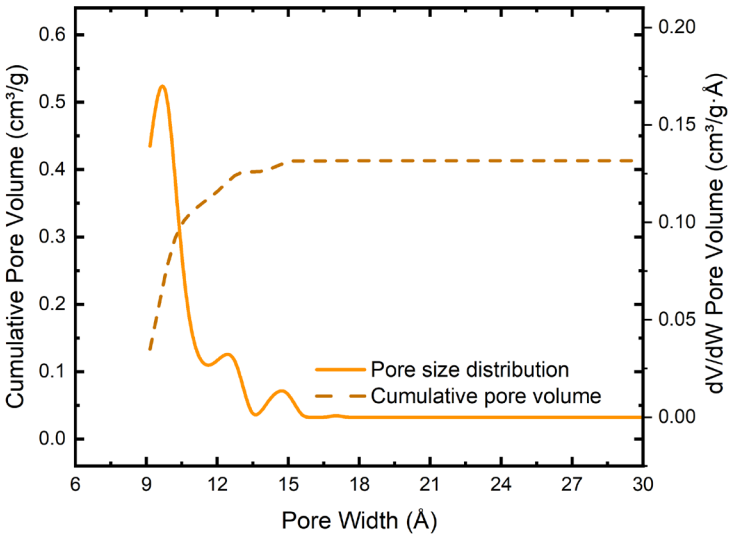

Figure 2.25 Differential and cumulative pore volume of Al-fumarate estimated from its nitrogen sorption isotherm at 77 K.

2.2.6 Water sorption analysis

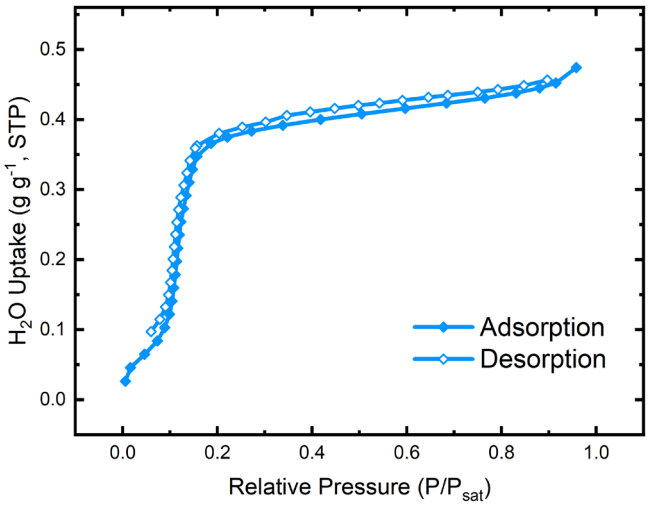

Figure 2.26 Water vapor sorption isotherms of MOF-303 against relative humidity at 25 °C (*P*: partial water vapor pressure, P_{sat}: saturation water vapor pressure at 25 °C, STP: standard temperature and pressure).

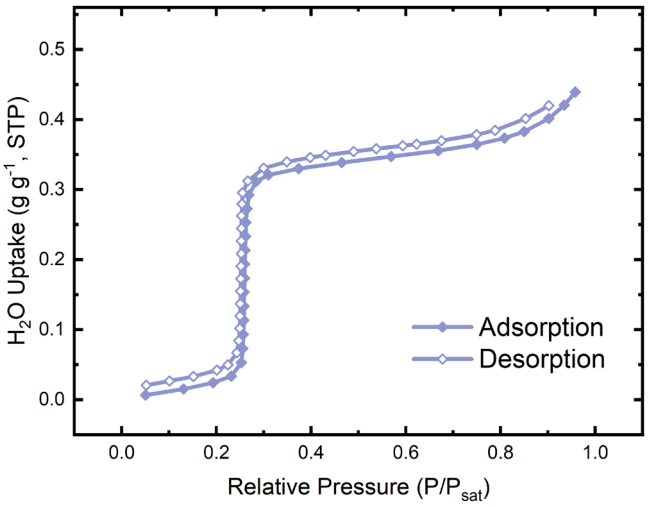

Figure 2.27 Water vapor sorption isotherms of CAU-23 against relative humidity at 25 °C (*P*: partial water vapor pressure, P_{sat}: saturation water vapor pressure at 25 °C, STP: standard temperature and pressure).

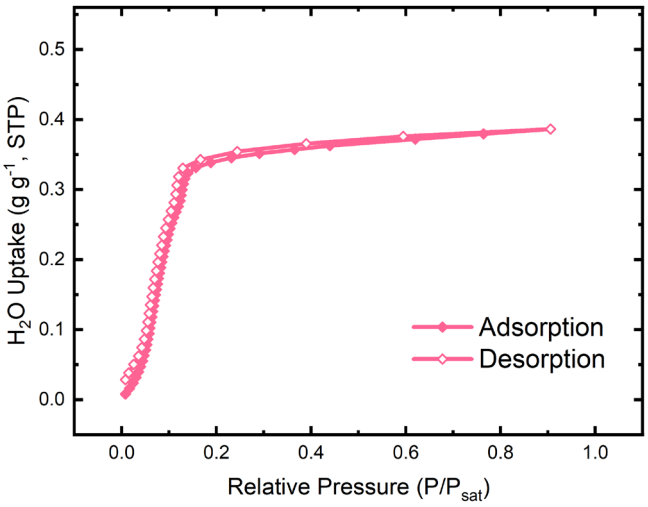

Figure 2.28 Water vapor sorption isotherms of MIL-160 against relative humidity at 25 °C (*P*: partial water vapor pressure, P_{sat}: saturation water vapor pressure at 25 °C, STP: standard temperature and pressure).

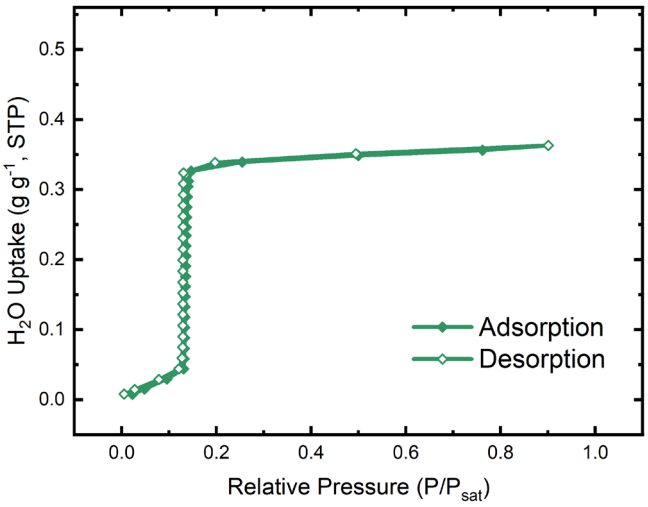

Figure 2.29 Water vapor sorption isotherms of MOF-313 against relative humidity at 25 °C (*P*: partial water vapor pressure, P_{sat}: saturation water vapor pressure at 25 °C, STP: standard temperature and pressure).

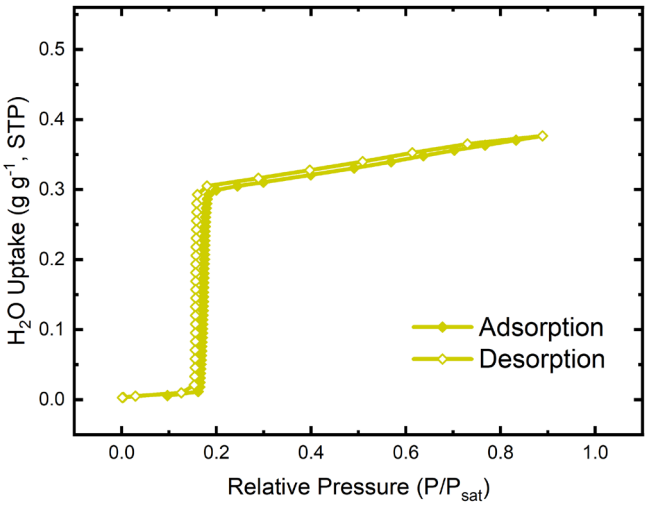

Figure 2.30 Water vapor sorption isotherms of CAU-10 against relative humidity at 25 °C (*P*: partial water vapor pressure, P_{sat}: saturation water vapor pressure at 25 °C, STP: standard temperature and pressure).

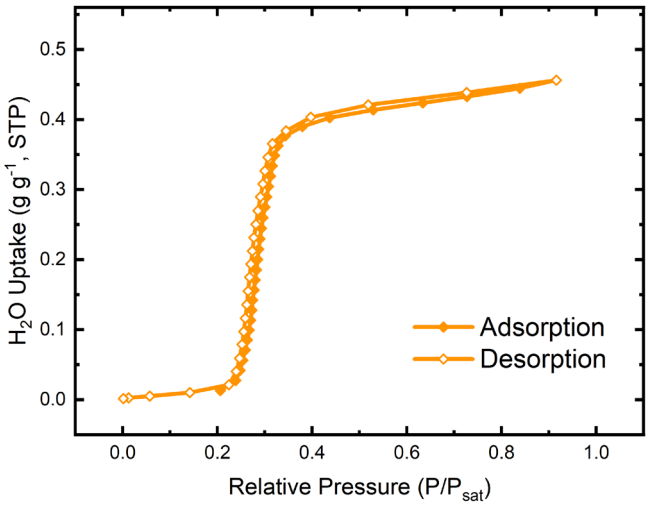

Figure 2.31 Water vapor sorption isotherms of Al-fumarate against relative humidity at 25 °C (*P*: partial water vapor pressure, P_{sat}: saturation water vapor pressure at 25 °C, STP: standard temperature and pressure).

2.3 Optimization of MOF synthesis conditions

In up-scale MOF synthesis, important considerations include linker and metal availability, purity of chemicals, raw material costs, the toxicity of reagents, reaction time, reaction yield, and safety.[14, 31] As highlighted in Section 2.3, all six MOFs were synthesized using commercially available, cost-effective linkers and aluminum salts. It's worth noting that while bulk-purchased linkers typically have a purity ranging from 90 to 95%, if the impurities do not react with Al^{3+} in aqueous solution, the quality of the MOF product will not be affected. On the other hand, minimizing the use of organic solvents, like DMF, becomes crucial when transitioning from lab-scale to industrial-scale syntheses. These solvents are environmentally detrimental and toxic and contribute significantly to production costs.[10, 14, 32] As a solution, water was chosen as the primary solvent and used an adequate base quantity to fully deprotonate the linker, enhancing its solubility.

To overcome the low yield and long incubation time associated with the traditional solvothermal synthesis of MOFs, I developed a reflux-based synthesis technique. Using vigorous stirring, this method ensures swift reaction equilibrium within a mere 6 hours. This method also supports higher concentrations than conventional solvothermal synthesis, leading to a two-fold increase in space-time-yield.[29] More importantly, while solvothermal synthesis has scalability limitations, the reflux approach is adaptable for industrial-scale applications. Initially, I refined the synthesis conditions in a controlled lab setting (100 mL round-bottom-flask with an oil bath),[30] then modified the protocol for large-scale production (200 L reaction vessel with a heated

jacket) to further optimize the process (Figure 2.32a).

During the reaction parameter optimization for synthesizing six aluminum-based MOFs with rod SBUs [Al(L)(OH), where L represents the deprotonated linker such as $PZDC^{2-}$, TDC^{2-}, and FDC^{2-}], it emerged that precisely three equivalents of NaOH were pivotal for maximizing yield. Two of these equivalents deprotonate the dicarboxylic acid linker, while the third aids SBU formation. Interestingly, although a highly crystalline product can form rapidly (within 1 hour), for kilogram-scale synthesis with an extensive solvent volume, maintaining the mixture under reflux for 6 hours is essential. This extended period ensures full porosity, optimal water uptake, and minimizes any undesirable hysteresis in the water isotherm. Leveraging these optimized conditions, I managed to produce around 3 kg of activated MOF per batch (Figure 2.32b). The yield and water uptake were impressive, aligning with gram-scale synthesis results reported in academic literature.[3, 10, 18, 25, 33]

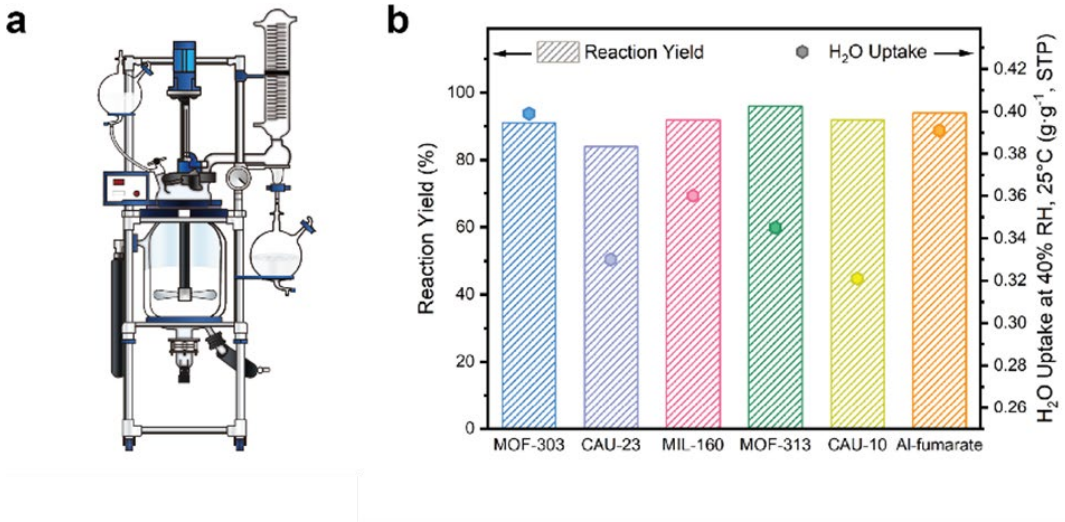

Figure 2.32 Synthesis of water-harvesting MOFs under reflux conditions in a 200 L reaction vessel. (a) Schematic representation of the experimental setup. (b) Comparison of the reaction yields and water uptakes at 40% RH and 25 °C for scaled-up MOF samples.

2.4 Evaluation of crystallinity and compositional characterization

The crystallinity of the scaled-up MOF products was assessed using PXRD measurements (Figure 2.32a). The measured values were in good agreement with the simulation data for each MOF. It should be noted that all materials, after washing, showed high crystallinity, with significant peaks that could be well indexed (Figures 2.2−2.7). This indicates that the scale-up method, provided the refluxing time is appropriate, doesn't compromise the MOF materials' crystallinity.

The composition of the six MOFs was analyzed using NMR spectroscopy and elemental analysis. After activation, five of them show only one singlet peak from the corresponding dicarboxylate linker in the range of 6.3 to 7.2 ppm in their ^{1}H digestion NMR (Figures 2.8–2.13). CAU-10 showed three peaks from its IPA linker in the range of 7.4 to 8.1 ppm in its ^{1}H digestion NMR (Figure 2.12). In all six ^{1}H NMR spectra, there was no evidence of solvent peaks, indicating the successful removal of the washing solvent. This confirms the effective activation of the MOFs and the absence of residual solvent, thereby demonstrating their high purity. Moreover, the close alignment between calculated and obtained elemental compositions for all MOF samples (Section 2.2.2) confirms the complete removal of impurities and the absence of water or EtOH in the activated MOFs.

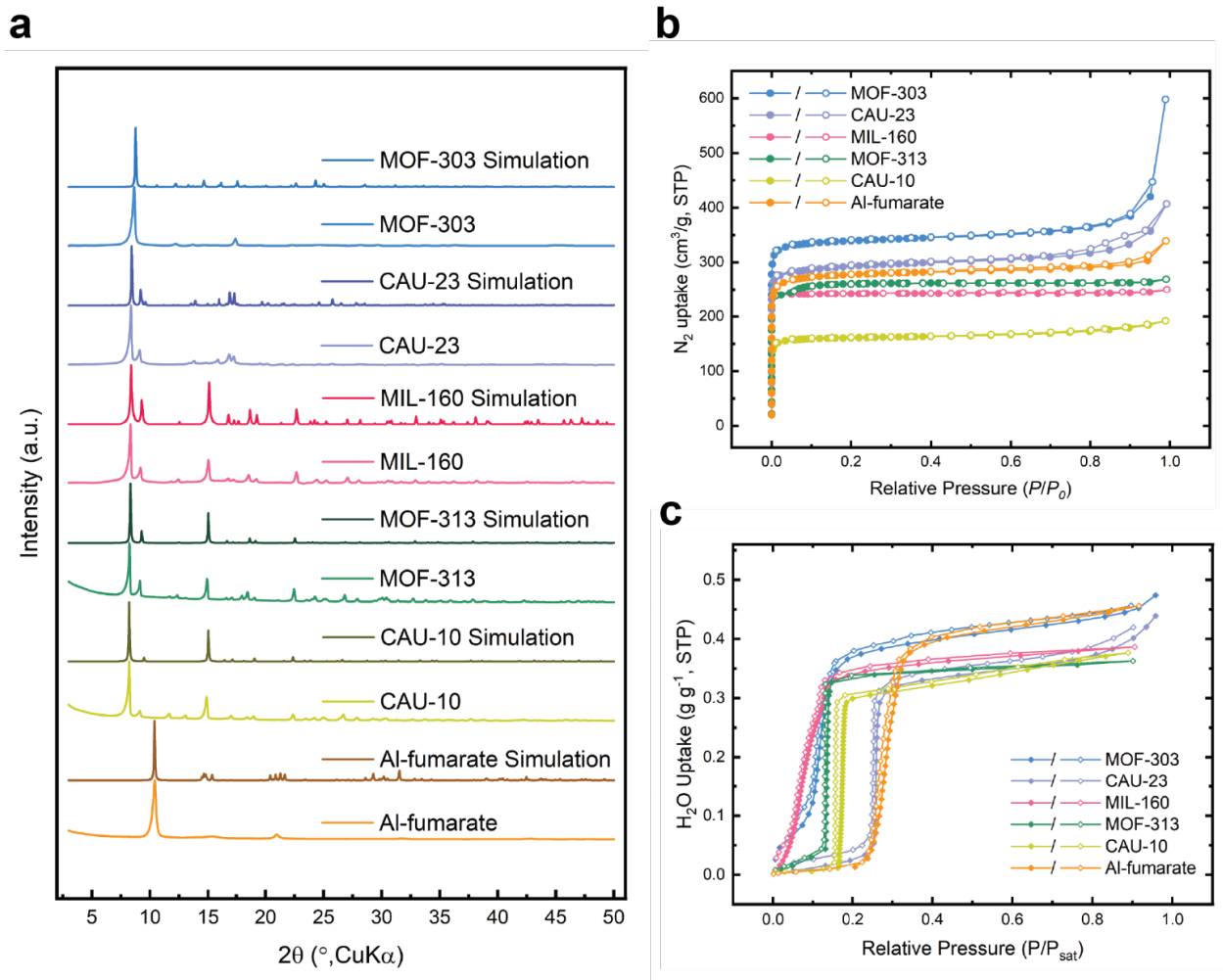

Figure 2.33 Characterization and sorption measurement of MOFs synthesized at scale. (a) PXRD analysis using CuKα radiation. The simulated patterns were calculated using the crystal structures reported in the literature.[9, 25, 34-36] (b) Nitrogen sorption isotherms (T = 77 K). (c) Water sorption isotherms (T = 25 °C). Filled circles depict adsorption; open circles indicate desorption.

2.5 Sorption measurements

Subsequently, the permanent porosity of the aluminum MOF series was investigated using nitrogen sorption analysis (Figure 2.32b). As outlined in Table 2.2, the Brunauer−Emmett−Teller (BET) surface areas and specific pore volumes for the compounds varied between 1379 to 654 m^2/g and 0.47 to 0.23 cm^3/g, respectively. These findings align with literature data,[3, 10, 18, 25, 33] and affirm that all MOFs produced at scale retained optimal BET surface areas, pore sizes, and volumes.

Table 2.2 Summary of nitrogen sorption analysis results for the water-harvesting MOF series.

MOF	BET surface area (m^2/g)	Pore volume calculated by DFT (cm^3/g)	Pore size calculated by DFT (Å)
MOF-303	1379	0.471	9.54
CAU-23	1176	0.450	9.68
MIL-160	1030	0.381	9.54
MOF-313	1033	0.405	9.40
CAU-10	654	0.239	10.01
Al-fumarate	1108	0.410	9.84

Moving forward, the water vapor sorption isotherms of the scaled-up MOF products at 25 °C were measured (Figure 2.14c). All the samples demonstrated consistent S-shaped profiles, albeit with varying water uptake capacities and steps. MOF-303, with an inflection point at 12% RH, boasted the most significant gravimetric water capacity at 39 wt% at 40% RH among the MOFs, likely due to its superior pore volume (Figure 2.26). The hydrophobic nature of the TDC linker resulted in CAU-23 displaying an inflection at 26% RH and a water capacity of 33 wt% at 40% RH (Figure 2.27). MIL-160's hydrophilic pore environment accounted for its lowest inflection point at 7% RH and a gravimetric water capacity of 36 wt% (Figure 2.28). MOF-313, mirroring MOF-303, had an inflection point at 13% RH and a water capacity of 34 wt% (Figure 2.29). The smaller pore volume formed by the bulkier IPA linker in CAU-10 resulted in an inflection point at 17% RH and a water capacity of 32 wt% (Figure 2.30). Al-fumarate recorded an inflection at 27% RH and a water capacity of 39 wt% (Figure 2.31).

Minimal hysteresis was observed between the adsorption and desorption curves for all scaled-up samples. This indicates that optimal conditions—like precise reaction times and temperatures—effectively reduced defects within the crystal lattice. These outcomes suggest that the water isotherm behavior of the six aluminum-based MOFs, synthesized at kilogram scale, matches those documented at gram or milligram scales in academic literature. This further underscores the efficacy of our synthesis method in producing high-quality, scalable water-harvesting MOF materials.

2.6 Conclusions

In this chapter, I demonstrate that a series of important water harvesting MOFs (MOF-303, CAU-23, MIL-160, MOF-313, CAU-10, and Al-fumarate) can be synthesized under industrially suitable, green conditions using inexpensive, commercially available linkers. This facile and robust synthesis method led to the production of MOFs at the kilogram scale without compromising framework crystallinity, porosity, or water-harvesting properties. These results showcase the feasibility of commercializing MOFs as water-harvesting sorbents and will contribute to the widespread adoption of water-harvesting technologies in the future.

2.7 Reference

(1) Oelkers, E. H.; Hering, J. G.; Zhu, C., Water: is there a global crisis? *Elements* **2011,** *7* (3), 157-162.

(2) Shannon, M. A.; Bohn, P. W.; Elimelech, M.; Georgiadis, J. G.; Marinas, B. J.; Mayes, A. M., Science and technology for water purification in the coming decades. *Nanoscience and technology: a collection of reviews from nature Journals* **2010**, 337-346.

(3) Hanikel, N.; Prévot, M. S.; Fathieh, F.; Kapustin, E. A.; Lyu, H.; Wang, H.; Diercks, N. J.; Glover, T. G.; Yaghi, O. M., Rapid cycling and exceptional yield in a metal-organic framework water harvester. *ACS Cent. Sci.* **2019,** *5* (10), 1699-1706.

(4) Kim, H.; Rao, S. R.; Kapustin, E. A.; Zhao, L.; Yang, S.; Yaghi, O. M.; Wang, E. N., Adsorption-based atmospheric water harvesting device for arid climates. *Nat. Commun.* **2018,** *9* (1), 1191.

(5) Kim, H.; Yang, S.; Rao, S. R.; Narayanan, S.; Kapustin, E. A.; Furukawa, H.; Umans, A. S.; Yaghi, O. M.; Wang, E. N., Water harvesting from air with metal-organic frameworks powered by natural sunlight. *Science* **2017,** *356* (6336), 430-434.

(6) Bagi, S.; Wright, A. M.; Oppenheim, J.; Dincă, M.; Román-Leshkov, Y., Accelerated Synthesis of a Ni2Cl2 (BTDD) Metal–Organic Framework in a Continuous Flow Reactor for Atmospheric Water Capture. *ACS Sustain. Chem. Eng.* **2021,** *9* (11), 3996-4003.

(7) Hanikel, N.; Prévot, M. S.; Yaghi, O. M., MOF water harvesters. *Nat. Nanotechnol.* **2020,** *15* (5), 348-355.

(8) Yang, P.; Clark, D. S.; Yaghi, O. M., Envisioning the "Air Economy"—Powered by Reticular Chemistry and Sunlight for Clean Air, Clean Energy, and Clean Water. *Molecular Frontiers Journal* **2021**, 1-8.

(9) Hanikel, N.; Pei, X.; Chheda, S.; Lyu, H.; Jeong, W.; Sauer, J.; Gagliardi, L.; Yaghi, O. M., Evolution of water structures in metal-organic frameworks for improved atmospheric water harvesting. *Science* **2021,** *374* (6566), 454-459.

(10) Lenzen, D.; Bendix, P.; Reinsch, H.; Fröhlich, D.; Kummer, H.; Möllers, M.; Hügenell, P. P.; Gläser, R.; Henninger, S.; Stock, N., Scalable green synthesis and full-scale test of the metal–organic framework CAU-10-H for use in adsorption-driven chillers. *Adv. Mater.* **2018,** *30* (6), 1705869.

(11) Kim, S.-N.; Lee, Y.-R.; Hong, S.-H.; Jang, M.-S.; Ahn, W.-S., Pilot-scale synthesis of a zirconium-benzenedicarboxylate UiO-66 for CO2 adsorption and catalysis. *Catal. Today* **2015,** *245*, 54-60.

(12) Rubio-Martinez, M.; Hadley, T. D.; Batten, M. P.; Constanti-Carey, K.; Barton, T.; Marley, D.; Mönch, A.; Lim, K. S.; Hill, M. R., Scalability of continuous flow production of metal–organic frameworks. *ChemSusChem* **2016,** *9* (9), 938-941.
(13) DeSantis, D.; Mason, J. A.; James, B. D.; Houchins, C.; Long, J. R.; Veenstra, M., Techno-economic analysis of metal–organic frameworks for hydrogen and natural gas storage. *Energy Fuels* **2017,** *31* (2), 2024-2032.
(14) Gaab, M.; Trukhan, N.; Maurer, S.; Gummaraju, R.; Müller, U., The progression of Al-based metal-organic frameworks–From academic research to industrial production and applications. *Microporous Mesoporous Mater.* **2012,** *157*, 131-136.
(15) Khabzina, Y.; Dhainaut, J.; Ahlhelm, M.; Richter, H.-J.; Reinsch, H.; Stock, N.; Farrusseng, D., Synthesis and shaping scale-up study of functionalized UiO-66 MOF for ammonia air purification filters. *Ind. Eng. Chem. Res.* **2018,** *57* (24), 8200-8208.
(16) Cho, K. H.; Borges, D. D.; Lee, U.; Lee, J. S.; Yoon, J. W.; Cho, S. J.; Park, J.; Lombardo, W.; Moon, D.; Sapienza, A., Rational design of a robust aluminum metal-organic framework for multi-purpose water-sorption-driven heat allocations. *Nat. Commun.* **2020,** *11* (1), 5112.
(17) Lenzen, D.; Zhao, J.; Ernst, S.-J.; Wahiduzzaman, M.; Ken Inge, A.; Fröhlich, D.; Xu, H.; Bart, H.-J.; Janiak, C.; Henninger, S., A metal–organic framework for efficient water-based ultra-low-temperature-driven cooling. *Nat. Commun.* **2019,** *10* (1), 3025.
(18) Tannert, N.; Jansen, C.; Nießing, S.; Janiak, C., Robust synthesis routes and porosity of the Al-based metal–organic frameworks Al-fumarate, CAU-10-H and MIL-160. *Dalton Trans.* **2019,** *48* (9), 2967-2976.
(19) Lee, J. S.; Yoon, J. W.; Mileo, P. G.; Cho, K. H.; Park, J.; Kim, K.; Kim, H.; de Lange, M. F.; Kapteijn, F.; Maurin, G., Porous metal–organic framework CUK-1 for adsorption heat allocation toward green applications of natural refrigerant water. *ACS Appl. Mater. Interfaces* **2019,** *11* (29), 25778-25789.
(20) Zhao, T.; Jeremias, F.; Boldog, I.; Nguyen, B.; Henninger, S. K.; Janiak, C., High-yield, fluoride-free and large-scale synthesis of MIL-101 (Cr). *Dalton Trans.* **2015,** *44* (38), 16791-16801.
(21) Sohail, M.; Yun, Y.-N.; Lee, E.; Kim, S. K.; Cho, K.; Kim, J.-N.; Kim, T. W.; Moon, J.-H.; Kim, H., Synthesis of highly crystalline NH2-MIL-125 (Ti) with S-shaped water isotherms for adsorption heat transformation. *Cryst. Growth Des.* **2017,** *17* (3), 1208-1213.
(22) Permyakova, A.; Skrylnyk, O.; Courbon, E.; Affram, M.; Wang, S.; Lee, U. H.; Valekar, A. H.; Nouar, F.; Mouchaham, G.; Devic, T., Synthesis Optimization, Shaping, and Heat Reallocation Evaluation of the Hydrophilic Metal–Organic Framework MIL-160 (Al). *ChemSusChem* **2017,** *10* (7), 1419-1426.
(23) Wang, S.; Lee, J. S.; Wahiduzzaman, M.; Park, J.; Muschi, M.; Martineau-Corcos, C.; Tissot, A.; Cho, K. H.; Marrot, J.; Shepard, W., A robust large-pore zirconium carboxylate metal–organic framework for energy-efficient water-sorption-driven refrigeration. *Nat. Energy* **2018,** *3* (11), 985-993.
(24) Fathieh, F.; Kalmutzki, M. J.; Kapustin, E. A.; Waller, P. J.; Yang, J.; Yaghi, O. M., Practical water production from desert air. *Sci. Adv.* **2018,** *4* (6), eaat3198.
(25) Cho, K. H.; Borges, D. D.; Lee, U.; Lee, J. S.; Yoon, J. W.; Cho, S. J.; Park, J.; Lombardo, W.; Moon, D.; Sapienza, A., Rational design of a robust aluminum metal-organic framework for multi-purpose water-sorption-driven heat allocations. *Nat. Commun.* **2020,** *11* (1), 1-8.
(26) Yaghi, O. M.; Hanikel, N.; Hao, L. Multivariate and other metal-organic frameworks, and

uses thereof. U.S. Patent No. 62/771,537, University of California, 2020.
(27) Furukawa, H.; Gandara, F.; Zhang, Y.-B.; Jiang, J.; Queen, W. L.; Hudson, M. R.; Yaghi, O. M., Water adsorption in porous metal–organic frameworks and related materials. *J. Am. Chem. Soc.* **2014,** *136* (11), 4369-4381.
(28) Rieth, A. J.; Yang, S.; Wang, E. N.; Dincă, M., Record atmospheric fresh water capture and heat transfer with a material operating at the water uptake reversibility limit. *ACS Cent. Sci.* **2017,** *3* (6), 668-672.
(29) Zheng, Z.; Nguyen, H. L.; Hanikel, N.; Li, K. K.-Y.; Zhou, Z.; Ma, T.; Yaghi, O. M., High-yield, green and scalable methods for producing MOF-303 for water harvesting from desert air. *Nat. Protoc.* **2022**, 1-21.
(30) Zheng, Z.; Hanikel, N.; Lyu, H.; Yaghi, O. M., Broadly Tunable Atmospheric Water Harvesting in Multivariate Metal–Organic Frameworks. *J. Am. Chem. Soc.* **2022,** *144* (49), 22669-22675.
(31) Czaja, A.; Leung, E.; Trukhan, N.; Müller, U., Industrial MOF synthesis. *Metal-Organic Frameworks: Applications from Catalysis to Gas Storage* **2011**, 337-352.
(32) Reinsch, H., M. a. van der Veen, B. Gil, B. Marszalek, T. Verbiest, D. de Vos and N. Stock. *Chem. Mater* **2013,** *25*, 17-26.
(33) Kim, H.; Rao, S. R.; Kapustin, E. A.; Zhao, L.; Yang, S.; Yaghi, O. M.; Wang, E. N., Adsorption-based atmospheric water harvesting device for arid climates. *Nat. Commun.* **2018,** *9* (1), 1-8.
(34) Alvarez, E.; Guillou, N.; Martineau, C.; Bueken, B.; Van de Voorde, B.; Le Guillouzer, C.; Fabry, P.; Nouar, F.; Taulelle, F.; De Vos, D., The structure of the aluminum fumarate metal–organic framework A520. *Angew. Chem.* **2015,** *127* (12), 3735-3739.
(35) Fröhlich, D.; Pantatosaki, E.; Kolokathis, P. D.; Markey, K.; Reinsch, H.; Baumgartner, M.; van der Veen, M. A.; De Vos, D. E.; Stock, N.; Papadopoulos, G. K., Water adsorption behaviour of CAU-10-H: a thorough investigation of its structure–property relationships. *J. Mater. Chem. A* **2016,** *4* (30), 11859-11869.
(36) Lenzen, D.; Zhao, J.; Ernst, S.-J.; Wahiduzzaman, M.; Ken Inge, A.; Fröhlich, D.; Xu, H.; Bart, H.-J.; Janiak, C.; Henninger, S., A metal–organic framework for efficient water-based ultra-low-temperature-driven cooling. *Nat. Commun.* **2019,** *10* (1), 1-9.

Chapter III

Passive Device for Producing Fresh Water via Ambient Sunlight

3.1 Introduction

The ongoing global water crisis has necessitated the pursuit of innovative solutions to meet the burgeoning demand for fresh water.[1, 2] While traditional methods like desalination and wastewater treatment have their merits, they often involve high energy costs and infrastructure demands. More importantly, off-grid water supply technology should be developed to close the gap between the regions that cannot receive the benefits from the centralized water supply infrastructures.[3-5] In the quest to address this challenge, nature offers insights. The hydrological cycle, with its processes of evaporation and condensation, has sustained life on Earth for eons. Drawing from this, there is a burgeoning interest in exploring the potential of harnessing ambient sunlight—a readily available and renewable energy source—to drive water production devices.

In the past few years, researchers have developed atmospheric water harvesting (AWH) devices based on metal-organic frameworks (MOFs),[6-8] porous polymers,[9] zeolites,[10] and other porous or hygroscopic materials.[11-14] While many of these harvester prototypes have undergone rigorous testing in laboratories,[8, 14] or in the field, most are dependent on external power sources and are thus categorized as active device.[6, 7, 9-13] Only one system using ambient sunlight with no other source of energy or power, in other words, a passive device, has been tested in the desert.[15] Building on these pioneering efforts and with a vision to advance the field, this chapter delves into the design and construction of a device into which a MOF material has been integrated into a form to maximally expose it to air and allow the extraction of water at night and its collection during the day when exposed to ambient sunlight.

Portions of this chapter have been adapted from:
Song, W.; Zheng, Z.; Alawadhi, A. H.; Yaghi, O. M., MOF Water Harvester Produces Water from Death Valley Desert Air in Ambient Sunlight. *Nat. Water* **2023,** *1* (7), 626–634.

Remarkably, the MOF water harvester discussed in this chapter has demonstrated the ability to collect double the amount of water per kilogram of MOF ($g \cdot H_2O/kg \cdot MOF$) under even more extreme conditions in Death Valley compared to the previously reported passive device.[15] Specifically, as depicted in Figure 3.1a, the device was loaded with MOF-303 [Al(OH)(PZDC); PZDC, 1*H*-pyrazole-3,5-dicarboxylate].[6, 15-17]

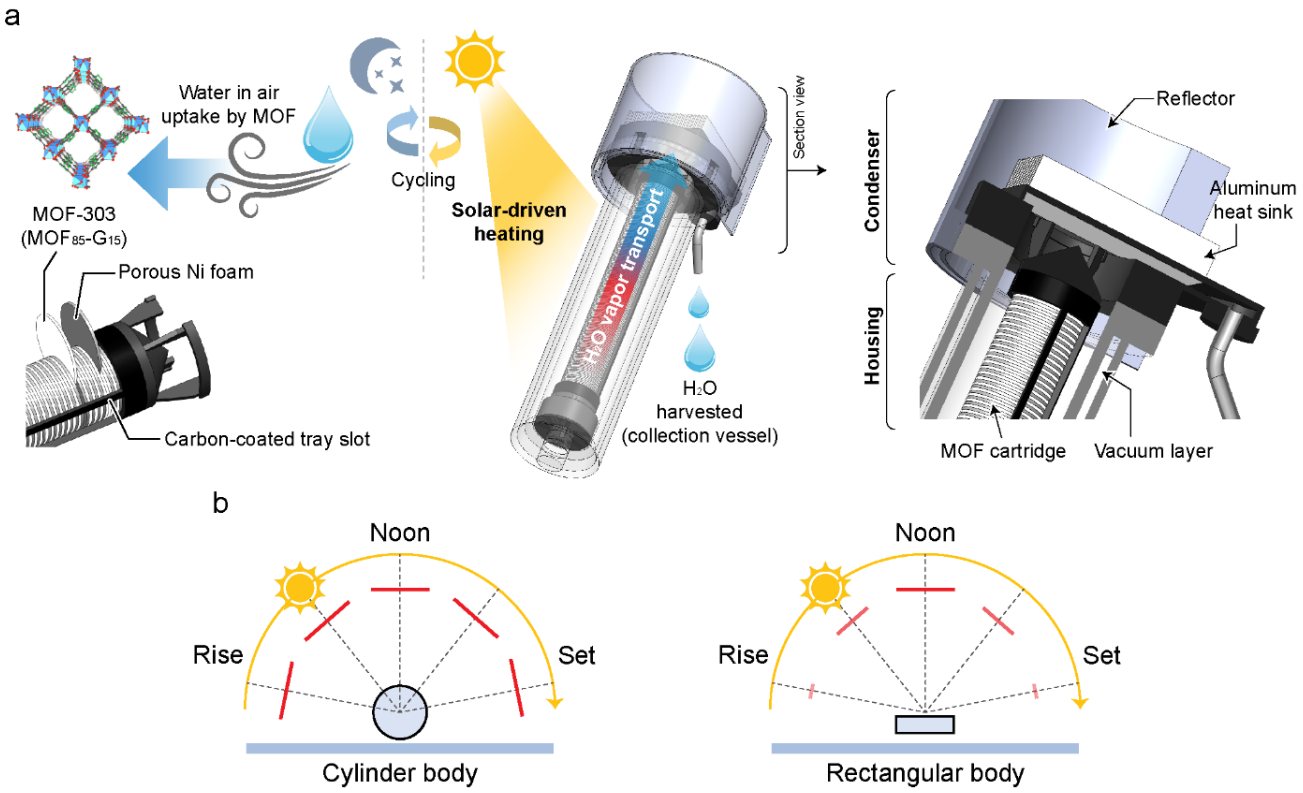

Figure 3.1 New generation of passive MOF water harvester. (a) General configuration of the MOF water harvester. At night, the MOF cartridge is exposed to air to capture atmospheric water. During the day, the MOF cartridge is assembled into the vacuum-insulated device housing and condenser. With the onset of solar irradiance, water is released from the MOF due to solar-driven heating and transported to the condenser. Direct solar irradiance to the condenser is shielded by a reflector, and water condenses at the surface of aluminum heat sinks. The condensed water is collected in a vessel connected to the condenser by a tube. (b) Schematic illustration showing the projected area differences (red lines) between cylindrical and rectangular-shaped bodies from sunrise to sunset.

The new generation of MOF water harvesters presented here was developed with a focus on the following criteria: (1) increasing the volume-to-surface area ratio (VS-r) of the MOF bed, (2) designing the MOF bed assembly, which is essentially MOF cartridge, to efficiently distribute heat under solar irradiance, and (3) optimizing the condenser to enhance condensation rates. Each step plays a pivotal role in effective water sorption, desorption, and condensation, aspects critical for efficient and practical AWH that have not been systematically investigated in this field.

Furthermore, the MOF cartridge was designed to maintain a constant VS-r regardless of the amount of MOF used in the device, a feature that bolsters its scalability. As a result of this comprehensive investigation, the current harvester achieved wholly passive AWH, even under the extremely dry and hot conditions of Death Valley, where the highest ambient temperature near the ground reached 60 °C and the lowest average relative humidity (RH_{avg}) during the nights was 14% in our field tests.

3.2 Construction of the passive MOF water harvester

The device was engineered with two primary compartments: the housing for the MOF cartridge and the condenser (Figure 3.1a and Figure 3.2). The housing, designed as a transparent cylindrical structure, features a vacuum-insulated double wall to minimize conductive heat loss when subjected to solar irradiation. In contrast to the rectangular designs employed by other devices,[10, 15, 18] the cylindrical shape optimizes solar energy absorption from sunrise to sunset due to its consistent projected area towards the sun throughout its trajectory (Figure 3.1b).

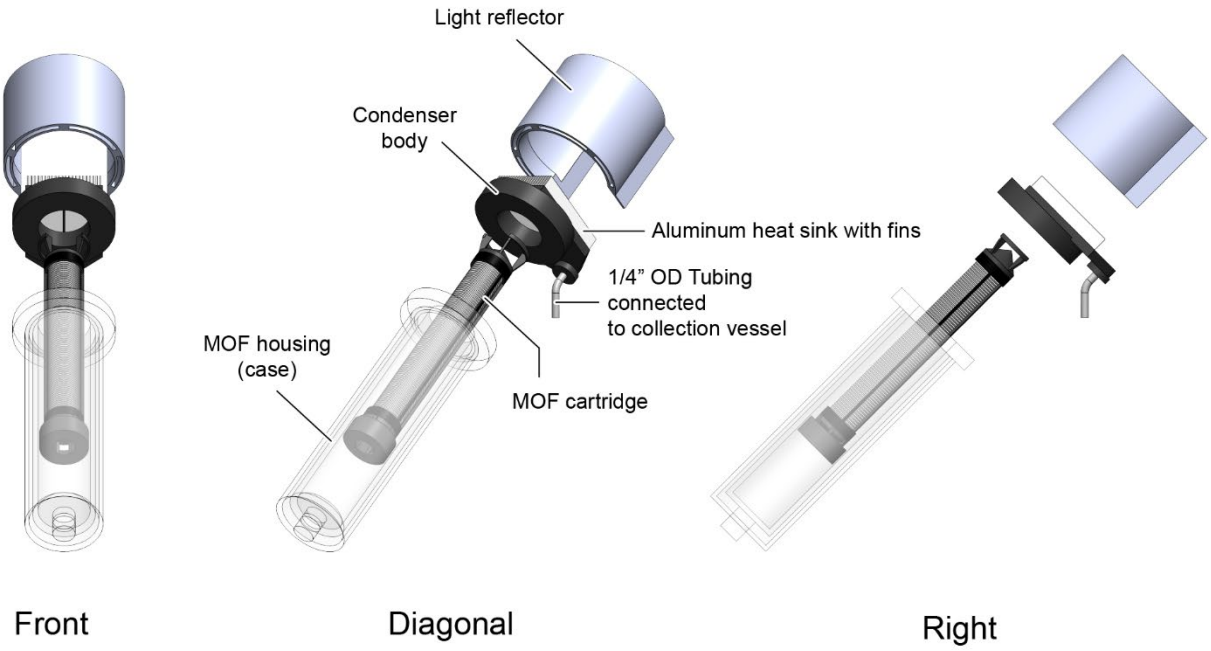

Figure 3.2 3D Drawings of the expanded device structures to show the assembly (and disassembly) of the MOF cartridge with the MOF housing and condenser components between the night and day AWH cycles.

Located atop the housing, the condenser components leverage the internal air density and temperature gradients within the device. This gradient acts as a driving force for the convective vapor transport from the MOFs to the condenser. Ideally, during the day, the MOF cartridge and

condenser should operate under differing thermal conditions to enhance AWH: the cartridge should be heated to facilitate water desorption, while the condenser should be cooled to enable condensation. By strategically positioning the condenser above and separating it from the cartridge compartment, these divergent thermal requirements can be balanced and optimized, drawing parallels to the operational principles of rotary evaporators frequently utilized in chemistry labs. Furthermore, with the condenser exposed to the clear sky, there exists potential in the device design to employ radiative energy dissipation, further enhancing water condensation rates.[19, 20]

3.3 MOF cartridge design and assembly

For effective atmospheric water harvesting, maximizing the exposure of MOFs to external air during both the adsorption and desorption stages is crucial. In a previous study using MOF-801,[15] as the Volume-to-Surface area ratio (VS-r) of MOF beds decreased from 1 to 0.5, the water uptake capacity declined from 230 to 210 g·H_2O/kg·MOF-801. This reduction was attributed to the decreased accessibility of MOFs to air, leading to a diminished AWH capacity from 130 to 56 ·H_2O/kg·MOF-801/day.[15] Consequently, in this study, MOF powders were transformed into thin disc-shaped pellets (with a diameter of 38 mm and a height of approximately 0.8 mm). These pellets were stacked alongside porous nickel (Ni) foam discs (38 mm in diameter and 1.5 mm in height) to maintain a VS-r of 2.6 (Figure 3.1a).

With the Ni foam's porosity exceeding 97%, external air can readily flow and diffuse through it. Sorbent pellets were crafted by blending activated MOF-303 powders with graphite in various weight ratios, then subjecting the mixture to a uniaxial pressure of 78 MPa for two minutes (Figure 3.3). Graphite was introduced as a binder to enhance both the mechanical and thermal conductivity of the pressed bodies. Specifically, the pellets produced using an 85 wt% MOF-303 and 15 wt% graphite mixture (MOF_{85}-G_{15}) were selected for device fabrication.

The BET surface area of MOF_{85}-G_{15} stands at 955 m^2/g·MOF_{85}-G_{15}, which corresponds to 1,120 m^2/g·MOF-303. This indicates that over 85% of the MOF-303 surface area (1370 m^2/g) was retained throughout the pressing process (Figure 3.4). Also, MOF_{85}-G_{15} pellets exhibited the characteristic water isotherm profile of MOF-303, with an inflection point at approximately 12% RH and a water uptake capacity of 29 wt% by MOF_{85}-G_{15} (35 wt% by MOF-303) at 20% RH, which also corresponds to the 85 % capacity of MOF-303 (Figure 3.5). Notably, the hydrophobic graphite binder also played a pivotal role in bolstering the water resistance of the pressed pellets. In experiments, pellets with hydrophilic cellulose binders disintegrated instantly upon water exposure. In contrast, MOF_{85}-G_{15} pellets retained their form for over 24 hours, underscoring their enhanced water resistance.

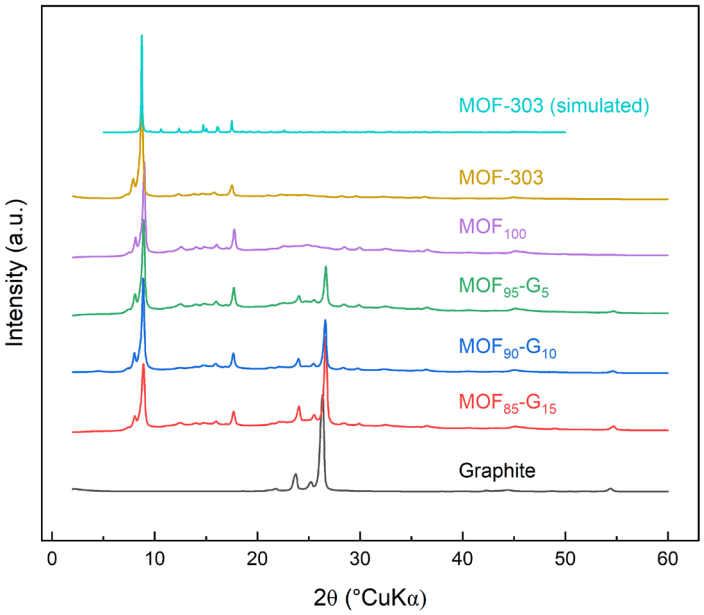

Figure 3.3 PXRD spectra of MOF-303 simulated, activated MOF-303 and graphite powder, sorbent pellets prepared using MOF-303 without graphite (MOF_{100}), 95 wt% MOF-303 and 5 wt% graphite (MOF_{95}-G_5), 90 wt% MOF-303 and 10 wt% graphite (MOF_{90}-G_{10}), and 85 wt% MOF-303 and 15 wt% graphite (MOF_{85}-G_{15}), respectively.

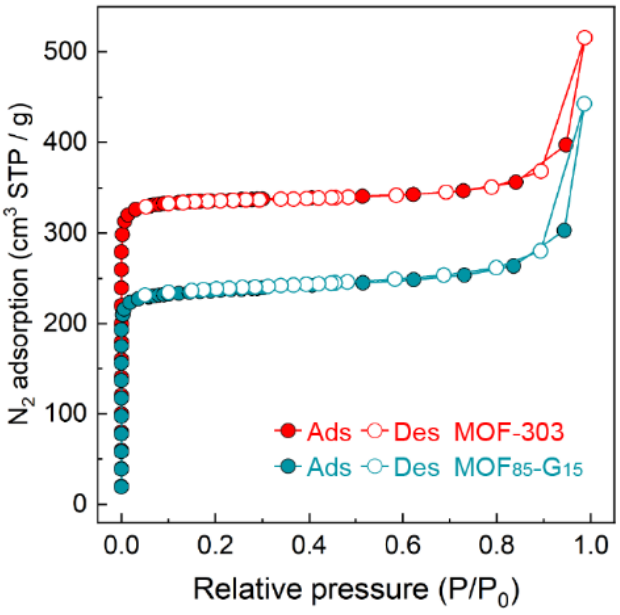

Figure 3.4 Nitrogen sorption analysis of MOF-303 without graphite binders and MOF_{85}-G_{15} pellet at 77 K (*P*: partial pressure of argon, P_0 = 1 atm, STP: standard temperature and pressure).

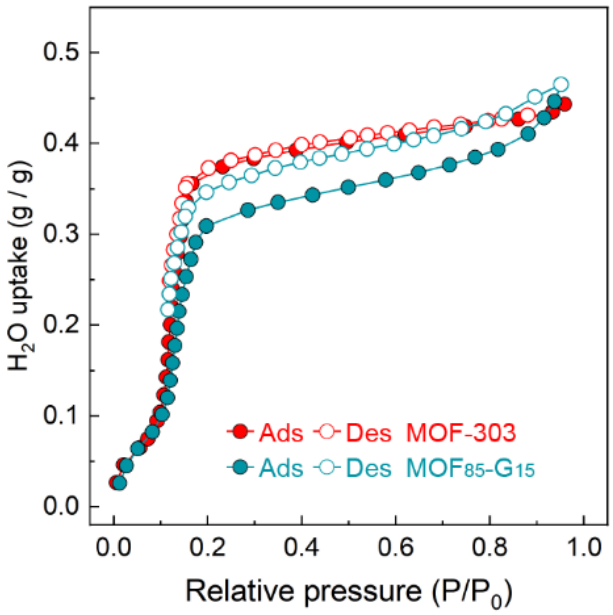

Figure 3.5 Water isotherm of MOF-303 without graphite binders and MOF_{85}-G_{15} pellet at 25 °C.

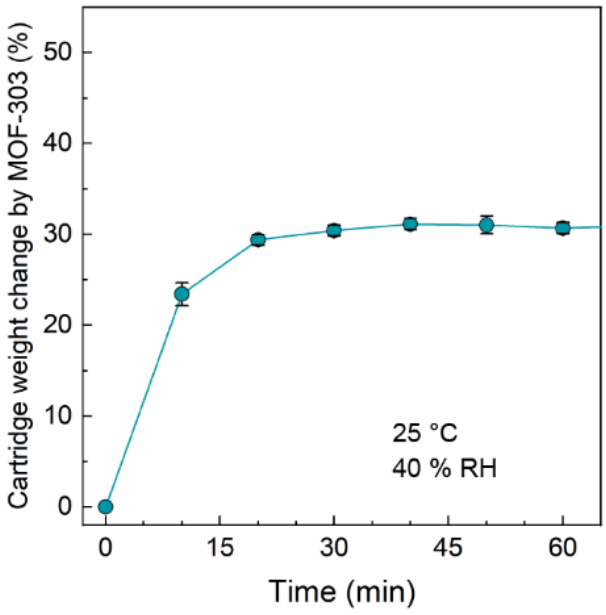

Figure 3.6 Weight change of the MOF cartridge at 25 °C and 40% RH. The weight change is presented normalized to the MOF-303 weight (35 g). Error bars are the standard deviation of three independent measurements.

Water uptake properties of the complete MOF cartridge assembly underwent scrutiny. The cartridge was activated at 140 °C for 24 hours, and the net weight change was assessed at 25°C and 40% RH inside an environmental chamber. Using 35g of MOF-303, which is equivalent to 42 g of MOF_{85}-G_{15}, a weight increase of approximately 32 wt% was noted within two hours. This indicates that over 90% of the MOF-303 in MOF_{85}-G_{15} was accessible (Figure 3.6). Comparable uptake efficiencies were also observed with 25 g and 45 g of MOF-303. This suggests that atmospheric air accessibility remains consistent regardless of the MOF amount used, a feat achieved due to the constant VS-r stemming from the stacked arrangement of MOF_{85}-G_{15} pellets and porous Ni foam discs. Consequently, even on a kilogram scale, water uptake efficiency remains unaffected, highlighting its immense potential for scalability (Figure 3.7).

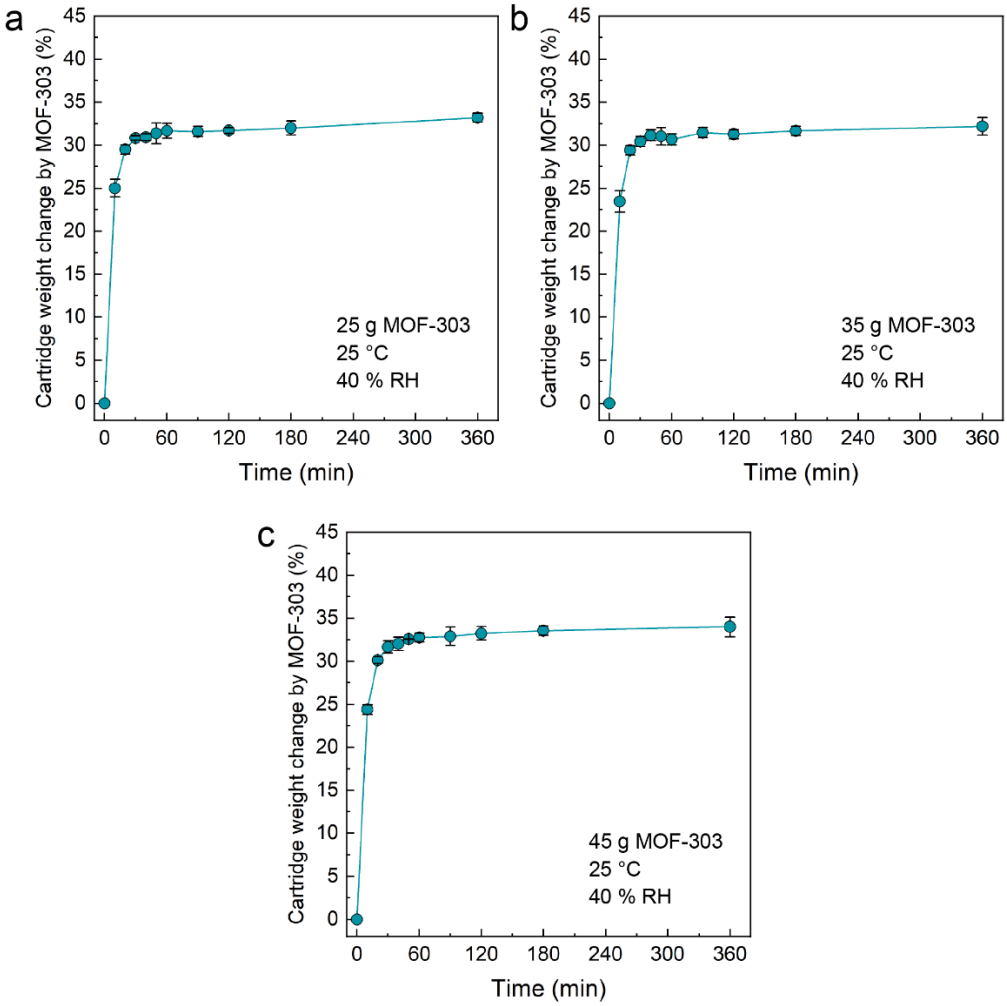

Figure 3.7 Water uptake of MOF cartridge. Time-dependent weight change of the MOF cartridge at 25 °C and 40 % RH with the MOF-303 amounts of (a) 25 g, (b) 35 g, and (c) 45 g, respectively. Error bars are the standard deviation of three independent measurements.

3.4 Heat and energy transfer simulations

Before proceeding with the device's fabrication, the heat and energy transfer were examined under solar irradiation through computational simulations. In particular, a COMSOL simulation, which incorporated equations for radiative, convective, and conductive heat and energy transfers, was conducted. It is worth noting that in this computational exploration, the heat of water desorption from MOF_{85}-G_{15} and the latent heat released by water condensation were excluded. In the simulation, the device's geometry, imported from Solidworks via the Parasolid file format, was analyzed using the Surface-to-Surface Radiation (rad), Heat Transfer in Solids and Fluids 2 (ht2), and Laminar Flow (spf) modules, coupled through Multiphysics. The simulation parameters and boundary conditions included an external radiation source (5000 K, 1000 W/m²), internal weakly compressible air (with gravity), ambient temperature of 25 °C, and convective heat flux to ambient with h = 15 W/(m^2·K). The MOF housing was transparent for solar spectral bands and opaque for ambient spectral bands.

According to the results, when subjected to solar irradiance of 1000 W/m^2 for a duration of 7 hours, the MOF bed temperature increased up to 70 °C (Figure 3.8 and Figure 3.9a) Impressively, temperature variances across the MOF pellet stacks were minimal, not exceeding 2°C, which underscores the cartridge design's efficacy in heat distribution. Moreover, a temperature difference of 10°C in the MOF was discerned when contrasting non-insulated single-wall and vacuum-insulated double-wall MOF housing structures. Crucially, after 7 hours, a temperature disparity exceeding 35°C between the cartridge and the condenser was consistently maintained (Figure 3.9a), showing the successful heat dissipation to environments through heat sinks and therefore the potential for water condensation.

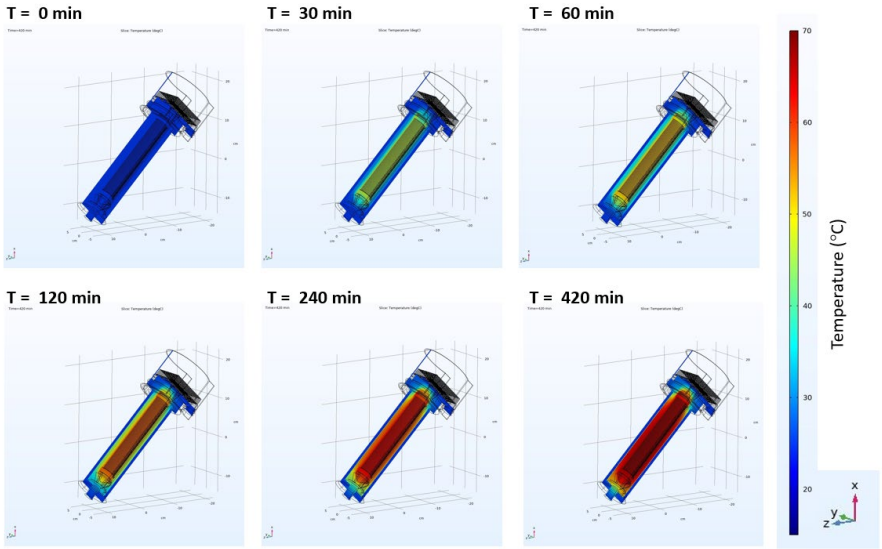

Figure 3.8 Energy and heat transfer simulation of the device under solar irradiance. (a) Simulated time-dependent temperature profiles of the device over a span of 7 hours (420 minutes). The direction of external irradiation was set to (-1, 0, -1) throughout the simulation period.

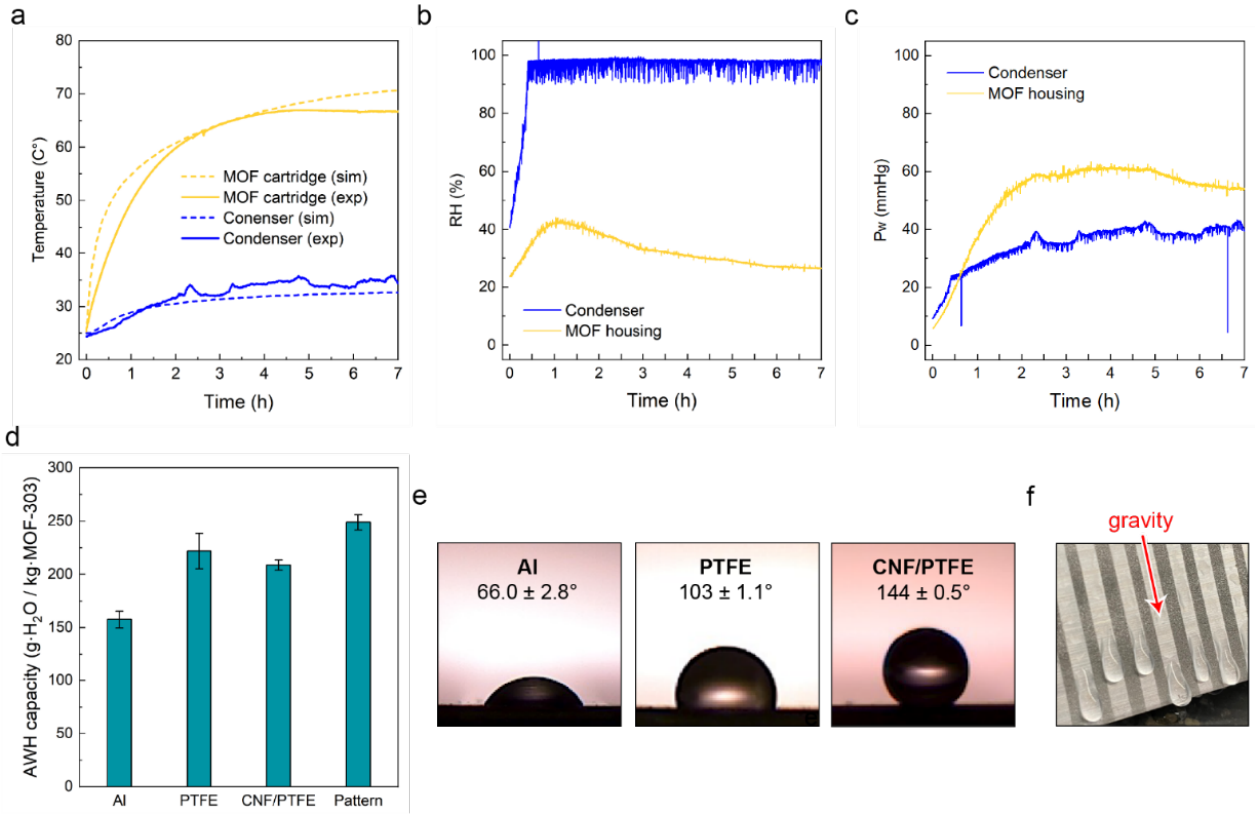

Figure 3.9 Laboratory test of the passive AWH device. (a) Comparison of simulated and experimental temperature variations in the MOF cartridge and condenser under light exposure. (b,c) Experimental RH (b) and P_w (c) change of the MOF housing and condenser during the laboratory test. (d) Assessment of the device's AWH capacity when tested with condensers of varying surface conditions: bare aluminum (Al, non-treated), PTFE coated, CNF/PTFE coated, and a patterned coating with CNF/PTFE. (e) Analysis of the water-air interface contact angles on bare (Al), PTFE-, and CNF/PTFE-coated condensers. (f) Photograph of the condenser surface with linear patterned CNF/PTFE coating (black strips) alongside the direction of gravity.

3.5 Laboratory test of the passive water harvester

Drawing on insights from the MOF cartridge water uptake experiments and energy transfer simulations, the complete device was assembled and subjected to laboratory tests. Initially, an activated cartridge containing 35 g of MOF-303 (equivalent to 42 g of MOF_{85}-G_{15}) was exposed to an environment maintained at 20 °C and 35% RH for a duration of 8 hours within an environmental chamber. Following this moisture absorption phase, the cartridge was integrated with the device, which was then subjected to 4000 K illumination, which is equivalent to 950 W/m^2, for a span of 7 hours. Throughout this duration, temperature and RH variations at different sections of the device were closely monitored (Figure 3.9a and b).

When exposed to the light, the temperature of the MOF_{85}-G_{15} cartridge began an immediate ascent, peaking at 67°C. A juxtaposition of the experimental and simulated temperature profiles revealed a close match (Figure 3.9a). Nonetheless, the experimental temperature of the MOF ascended at a slower pace initially compared to the simulation, and the condenser's temperature was marginally elevated. These discrepancies are potentially due to the exclusion of the heat effects of water desorption and condensation processes in the simulations.

Spatial changes in RH within the device distinctly showcased the vapor's journey from the MOF cartridge to the condenser. After the device's exposure to light, the RH at the condenser consistently rose, achieving 100% within the first hour (Figure 3.9b). Conversely, the RH near the cartridge initially increased, but later decreased as the water condensed and was gathered, elucidating the water's movement path—from the MOF_{85}-G_{15}, through the housing's inner space, and finally to the condenser and collection vessel. The culmination of this process resulted in the harvesting of 5.5(±0.27) g of water, translating to an AWH efficiency of 157(±7.8) g·H_2O/kg·MOF-303 (Figure 3.9c).

Since water condensation is a key step, this effect was further investigated to improve the AWH capacity. A widely-adopted strategy to boost condensation rates involves surface hydrophobization for facilitating dropwise condensations.[21] The polytetrafluoroethylene (PTFE) and carbon nanofiber-PTFE composites (CNF/PTFE) materials were selected for hydrophobic surface treatments, using a reported spray-coating method.[22] The hydrophobicity increased in the order of bare aluminum (Al, non-treated condenser surface) to PTFE- to CNF/PTFE-coated surfaces as confirmed by the water-air interface contact angles that are 66(±2.8)°, 103(±1.1)°, and 144(±0.5)°, respectively (Figure 3.9d). The AWH capacity increased from 157(±7.8) (Al) to 220(±16) (PTFE coating) and 210(±4.7) g·H_2O/kg·MOF-303 (CNF/PTFE coating) (Figure 3.9c).

Despite the enhancements achieved through surface modification, the performance of PTFE- and CNF/PTFE-coated condensers was closely matched. It was hypothesized that as the condensation surface grows increasingly hydrophobic, the nucleation stage assumes greater importance in dictating the condensation rates, especially in passive AWH scenarios. Conventionally, condensation unfolds in a sequential manner, encompassing nucleation, growth, droplet coalescence, and the gravitational removal of water.[21] In most applications, dropwise condensation by hydrophobic surfaces is preferred since it removes the coalesced droplets quickly by gravity to minimize surface wetting which functions as additional resistance for continued condensation. This implies that the nucleation step is less critical in determining the rates, which prefers hydrophilic surfaces with high surface energy.[22] However, in the context of passive AWH, it was postulated that the nucleation phase could be the critical determinant. Given the gentler conditions under which vapor is directed to the condenser compared to other applications such as steam power plants,[23] the gradients pushing for unidirectional vapor-to-liquid phase transitions, initiated by nucleation, might be diminished.[24] Therefore, recognizing the significance of the nucleation phase, strip-patterned CNF/PTFE coatings on the surface were introduced, aligned with the direction of gravity (Figure 3.9e). This design fosters the initiation of water nucleation and promotes the growth of coalesced water droplets within hydrophilic channels. Subsequently, the merged water is removed by gravity, preventing water from adhering across the entire metal surface due to its inherent high surface energy (Figure 3.9e). As a result, when the

hydrophobic strip-pattern was introduced to the condenser surface, the first droplet of the harvested water in the collection vessel was observed within 1.5 hours which is 45 minutes faster than the other conditions. This observation supports the hypothesis that patterned coatings can expedite condensation rates. Consequently, the AWH capacity witnessed an increase from 210(±4.7) to 248(±7.2) g·H_2O/kg·MOF-303 (Figure 3.9c).

3.6 Field test of the passive water harvester in Death Valley

The device was tested in the Death Valley areas during mid-summer in August 2022 to evaluate its AWH capabilities under extremely arid and hot conditions. Three full night-and-day cycles were completed; two cycles took place near the eastern boundary of the Death Valley National Park from August 19 to 21, 2022, and another at Furnace Creek from August 22 to 23, 2022 (Figure 3.10). The latter, due to its location below sea level at the heart of the valley, is notably the driest part of Death Valley (Figure 3.11 and Figure 3.12).

Throughout these tests, the lowest daytime peak temperature near the ground was recorded at 56 °C (August 21) and the highest night-time RH_{avg} was 26% (Figure 3.13). Particularly at the Furnace Creek location, the RH_{avg} during the night was just 14% with the peak of 21% at around 4:30 AM (Figure 3.10b). Despite these challenging conditions, with the condenser temperature reaching up to 65°C, the device successfully harvested water from the air, achieving an AWH capacity of 114 g·H_2O/kg·MOF-303/day. Considering all these tests, the highest productivity of the device was 210 g·H_2O/kg·MOF-303/day in the Death Valley area. For comparison, the AWH capacities are summarized in Figure 3.10c and d as a function of RH_{avg} and T_{avg} during the night and day cycles, respectively. Strong relationships are evident between these two factors and AWH capacity. These figures highlight the profound influence of humidity and temperature on the efficiency of passive MOF water harvesting. Furthermore, the data underscores the vital role of the condensation process in enhancing passive water harvesting capabilities. Such factors have often been overshadowed by other considerations including the intrinsic water uptake properties of sorbents or the structure of the sorbent bed.

For a thorough thermodynamic evaluation of this passive system, the maximum specific yield of water ($SY_{water,max}$) and the device efficiency (η) are calculated for each field test results (Table 3.1). $SY_{water,max}$ (L kWh^{-1} h^{-1}) is maximum amount of water that can be extracted from air at given test conditions, while η (%) shows the actual performance efficiency of the device compared to $SY_{water,max}$. When juxtaposed with other reported systems that typically exhibit efficiencies between 10% and 35%, this device demonstrated efficiencies ranging from 41% to 66%, even under the harshest weather conditions (Table 3.1). While direct comparisons among different passive AWH systems might not be entirely appropriate due to varying key parameters such as desorption temperature, ambient conditions, and isosteric heat of sorption, the results undeniably point to the considerable potential of this design for practical passive AWH applications.

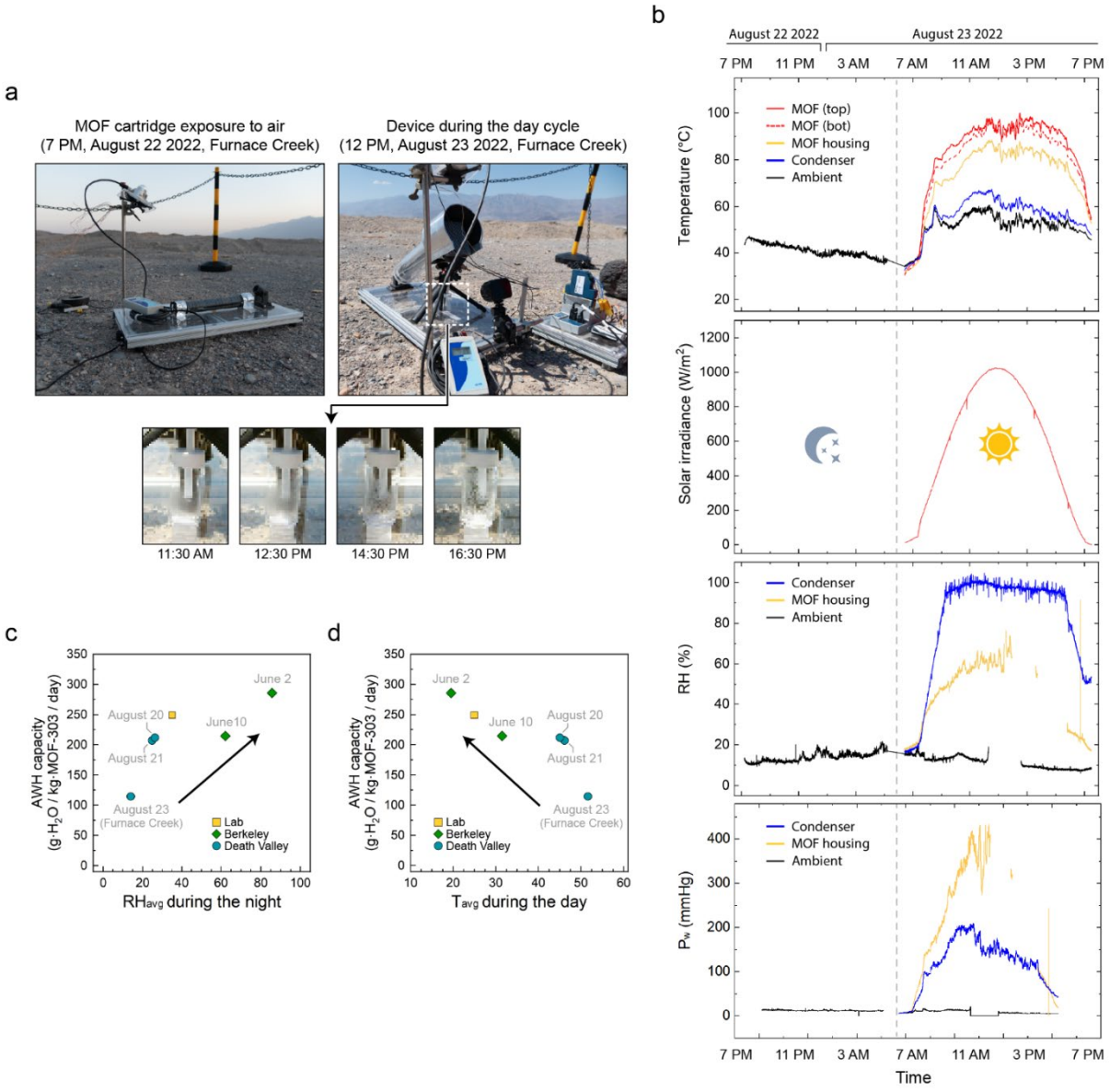

Figure 3.10 AWH in the Death Valley. (a) Photographs of the AWH at Furnace Creek, showing the MOF cartridge exposed to air for water uptake (upper left), the device during the day cycle (upper right), and water collected at different time (bottom). (b) Temperature (°C), solar irradiance (W/m^2), RH (%), and P_w (mmHg) changes of the device and ambient air conditions during the Aug-23 test. Time axes are synced with each other. (c and d) AWH capacity as a function of RH_{avg} (c) and T_{avg} (d) during the night and day cycles, respectively.

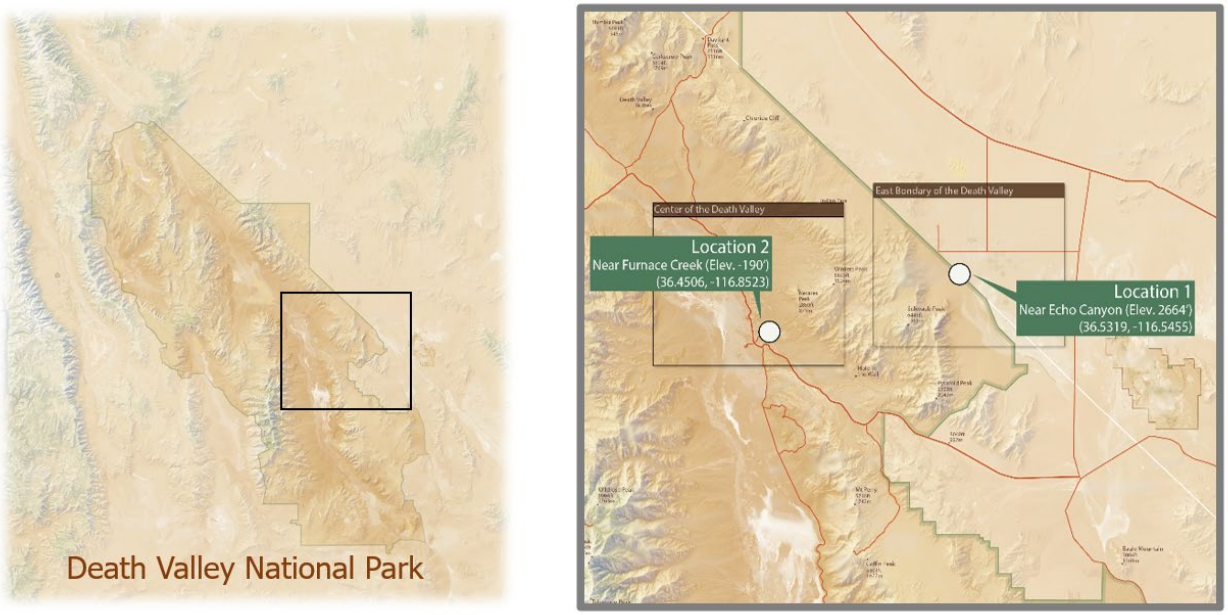

Figure 3.11 Locations of AWH in the Death Valley area. The tests were performed on the Location 1 (East boundary of the Death Valley, 36.5319° N, -116.5455° W) from August 19, 2022 to August 21 2022, and on the Location 2 (Furnace Creek, 36.4506 ° N, -116.8523° W) from August 22 2022 to August 23 2022.

Figure 3.12 Photographs of the MOF cartridge during the (a) night cycle and (b) day cycle (after sunset). The red cargo box was used to protect the electrical devices from direct exposure to sunlight.

Figure 3.13 Illustration of the device set-up and working environment. (a) Device, data acquisition system (DAQ), and laptop without cable connection. (b) Photograph taken during the day cycle of the August 20 test with cable connections. Parasol was used to protect the electrical devices from the direct exposure to sunlight. (c) MOF cartridge during the night cycle. (d) Device after the day cycle test is completed.

Table 3.1 $SY_{water,max}$, η, and the other parameters required for the calculation in the 2022 Death Valley field test.

Date	T_{des}[a] (°C)	T_{amb}[a] (°C)	RH_{avg} (%)	P_{total}[b] (Wh)	L_{max}[b] (mL h^{-1})	$SY_{water,max}$ (L kW^{-1} h^{-1})	η (%)
August 19	64.6	46.5	24.8	0.78	0.95	1.21	60.0%
August 20	70.9	45.0	26.2	0.77	0.92	1.20	60.2%
August 22	79.8	51.6	14	0.61	0.73	1.20	41.9%

[a] Average desorption (des) and ambient (amb) temperatures during the day cycle. [b] L_{max} and P_{total} are maximum water production rate during the day cycle and total energy required to desorb all water molecules from adsorbents, respectively.

3.7 Conclusions

A passive water harvester leveraging MOF-303 was designed and realized, marking a significant leap in efficiency among passive systems. The device showcased a water harvesting capacity of 285 g·H_2O/kg·MOF-303/day, relying solely on ambient sunlight without any additional energy input. The innovative MOF cartridge design combined with a specialized condenser surface treatment was instrumental in achieving these impressive results, especially during field tests in the Death Valley National Park. Additionally, the water harvesting capacity per unit area is a pivotal metric for passive operations to minimize environmental impact. Thanks to the device's compact and modular design, a productivity rate of 200 g·H_2O/m^2/day was achieved, which is three-fold higher than the previously reported passive device design (65 g·H_2O/m^2/day).[15]

Despite the evident potential of passive AWH systems in sourcing water from desert air with minimal environmental impact, certain challenges must be addressed to fully harness this technology for global communities. While passive systems can deliver water with no ongoing costs or emissions post-installation, there is a need for comprehensive economic and environmental assessments covering device fabrication and MOF synthesis processes.[25] Though scalable methods for MOF-303 synthesis have been recently proposed,[26] a thorough evaluation considering costs and environmental impacts related to the preparation of MOF building blocks and activation solvents is still pending. A comprehensive cost-benefit analysis should incorporate these factors, coupled with the long-term performance of the device and potential scalability. In essence, while passive AWH systems are still nascent in their development, there is ample opportunity for further research and refinement in both material development and device design to truly realize their global potential in mitigating water scarcity.

3.8 Reference

(1) Famiglietti, J. S., The global groundwater crisis. *Nat. Clim. Change* **2014,** *4* (11), 945-948.

(2) Hoekstra, A. Y.; Mekonnen, M. M., The water footprint of humanity. *Proc. Natl. Acad. Sci. U.S.A.* **2012,** *109* (9), 3232-3237.

(3) Lord, J.; Thomas, A.; Treat, N.; Forkin, M.; Bain, R.; Dulac, P.; Behroozi, C. H.; Mamutov, T.; Fongheiser, J.; Kobilansky, N., Global potential for harvesting drinking water from air using solar energy. *Nature* **2021,** *598* (7882), 611-617.

(4) Peeters, R.; Vanderschaeghe, H.; Rongé, J.; Martens, J. A., Energy performance and climate dependency of technologies for fresh water production from atmospheric water vapour. *Environ. Sci. Water Res. Technol.* **2020,** *6* (8), 2016-2034.

(5) Lu, H.; Shi, W.; Guo, Y.; Guan, W.; Lei, C.; Yu, G., Materials engineering for atmospheric water harvesting: progress and perspectives. *Adv. Mater.* **2022,** *34* (12), 2110079.

(6) Hanikel, N.; Prévot, M. S.; Fathieh, F.; Kapustin, E. A.; Lyu, H.; Wang, H.; Diercks, N. J.; Glover, T. G.; Yaghi, O. M., Rapid cycling and exceptional yield in a metal-organic framework water harvester. *ACS Cent. Sci.* **2019,** *5* (10), 1699-1706.

(7) Almassad, H. A.; Abaza, R. I.; Siwwan, L.; Al-Maythalony, B.; Cordova, K. E.,

Environmentally adaptive MOF-based device enables continuous self-optimizing atmospheric water harvesting. *Nat. Commun.* **2022,** *13* (1), 4873.
(8) Kim, H.; Yang, S.; Rao, S. R.; Narayanan, S.; Kapustin, E. A.; Furukawa, H.; Umans, A. S.; Yaghi, O. M.; Wang, E. N., Water harvesting from air with metal-organic frameworks powered by natural sunlight. *Science* **2017,** *356* (6336), 430-434.
(9) Deng, F.; Chen, Z.; Wang, C.; Xiang, C.; Poredoš, P.; Wang, R., Hygroscopic Porous Polymer for Sorption-Based Atmospheric Water Harvesting. *Adv. Sci.* **2022,** *9* (33), 2204724.
(10) LaPotin, A.; Zhong, Y.; Zhang, L.; Zhao, L.; Leroy, A.; Kim, H.; Rao, S. R.; Wang, E. N., Dual-stage atmospheric water harvesting device for scalable solar-driven water production. *Joule* **2021,** *5* (1), 166-182.
(11) Shan, H.; Li, C.; Chen, Z.; Ying, W.; Poredoš, P.; Ye, Z.; Pan, Q.; Wang, J.; Wang, R., Exceptional water production yield enabled by batch-processed portable water harvester in semi-arid climate. *Nat. Commun.* **2022,** *13* (1), 5406.
(12) Song, Y.; Xu, N.; Liu, G.; Qi, H.; Zhao, W.; Zhu, B.; Zhou, L.; Zhu, J., High-yield solar-driven atmospheric water harvesting of metal–organic-framework-derived nanoporous carbon with fast-diffusion water channels. *Nat. Nanotechnol.* **2022,** *17* (8), 857-863.
(13) Wang, J.; Dang, Y.; Meguerdichian, A. G.; Dissanayake, S.; Kankanam-Kapuge, T.; Bamonte, S.; Tobin, Z. M.; Achola, L. A.; Suib, S. L., Water harvesting from the atmosphere in arid areas with manganese dioxide. *Environmental science & technology letters* **2019,** *7* (1), 48-53.
(14) Guo, Y.; Guan, W.; Lei, C.; Lu, H.; Shi, W.; Yu, G., Scalable super hygroscopic polymer films for sustainable moisture harvesting in arid environments. *Nat. Commun.* **2022,** *13* (1), 2761.
(15) Fathieh, F.; Kalmutzki, M. J.; Kapustin, E. A.; Waller, P. J.; Yang, J.; Yaghi, O. M., Practical water production from desert air. *Sci. Adv.* **2018,** *4* (6), eaat3198.
(16) Zheng, Z.; Hanikel, N.; Lyu, H.; Yaghi, O. M., Broadly Tunable Atmospheric Water Harvesting in Multivariate Metal–Organic Frameworks. *J. Am. Chem. Soc.* **2022,** *144* (49), 22669-22675.
(17) Hanikel, N.; Pei, X.; Chheda, S.; Lyu, H.; Jeong, W.; Sauer, J.; Gagliardi, L.; Yaghi, O. M., Evolution of water structures in metal-organic frameworks for improved atmospheric water harvesting. *Science* **2021,** *374* (6566), 454-459.
(18) Kim, H.; Rao, S. R.; Kapustin, E. A.; Zhao, L.; Yang, S.; Yaghi, O. M.; Wang, E. N., Adsorption-based atmospheric water harvesting device for arid climates. *Nat. Commun.* **2018,** *9* (1), 1-8.
(19) Catalanotti, S.; Cuomo, V.; Piro, G.; Ruggi, D.; Silvestrini, V.; Troise, G., The radiative cooling of selective surfaces. *Sol Energy* **1975,** *17* (2), 83-89.
(20) Raman, A. P.; Anoma, M. A.; Zhu, L.; Rephaeli, E.; Fan, S., Passive radiative cooling below ambient air temperature under direct sunlight. *Nature* **2014,** *515* (7528), 540-544.
(21) Goswami, A.; Pillai, S. C.; McGranaghan, G., Surface modifications to enhance dropwise condensation. *Surf. Interfaces* **2021,** *25*, 101143.
(22) Donati, M.; Lam, C. W. E.; Milionis, A.; Sharma, C. S.; Tripathy, A.; Zendeli, A.; Poulikakos, D., Dropwise Condensation: Sprayable Thin and Robust Carbon Nanofiber Composite Coating for Extreme Jumping Dropwise Condensation Performance. *Adv. Mater. Interfaces* **2021,** *8* (1), 2170002.
(23) Cha, H.; Vahabi, H.; Wu, A.; Chavan, S.; Kim, M.-K.; Sett, S.; Bosch, S. A.; Wang, W.;

Kota, A. K.; Miljkovic, N., Dropwise condensation on solid hydrophilic surfaces. *Sci. Adv.* **2020,** *6* (2), eaax0746.
(24) Tanner, D.; Potter, C.; Pope, D.; West, D., Heat transfer in dropwise condensation—Part I The effects of heat flux, steam velocity and non-condensable gas concentration. *Int. J. Heat Mass Transfer* **1965,** *8* (3), 419-426.
(25) Hanikel, N.; Prévot, M. S.; Yaghi, O. M., MOF water harvesters. *Nat. Nanotechnol.* **2020,** *15* (5), 348-355.
(26) Zheng, Z.; Nguyen, H. L.; Hanikel, N.; Li, K. K.-Y.; Zhou, Z.; Ma, T.; Yaghi, O. M., High-yield, green and scalable methods for producing MOF-303 for water harvesting from desert air. *Nat. Protoc.* **2023,** *18*, 136–156.

Chapter IV

Multivariate Strategy for Broadly Tunable Water Sorption Profiles

4.1 Introduction

Water is an invaluable resource with unequal distribution worldwide and escalating demand.[1] Many regions suffer from its scarcity, affecting the quality of life for countless individuals.[2] The development of materials that can harvest water from the air presents a potential solution to this challenge, particularly in arid regions.[3, 4] Recently, metal–organic frameworks (MOFs) were successfully deployed for harvesting moisture from air.[5-19] To further advance this emerging field of research, it is imperative to establish strategies for generation of on-demand water-harvesting systems, which can be easily tailored to a variety of environmental conditions for efficient atmospheric water harvesting any time of the year and anywhere in the world.[20]

This chapter underscores the multivariate approach in making MOFs[21-23] as a means to regulate the hydrophilic attributes of the pores. This, in turn, affects the regeneration temperature, heat, and the specific humidity threshold at which the MOF becomes operational. The primary objective is to explore strategies for engineering enhanced MOF sorbents. As such, MOF-303 (Al(OH)(PZDC)), where $PZDC^{2-}$ is 1*H*-pyrazole-3,5-dicarboxylate, serves as the foundational subject of this study due to its proven efficacy in water-harvesting field tests in deserts.[24] The overarching aim is to refine the properties of MOF-303 to yield more effective MOF sorbents.

Prior study demonstrated that the nitrogen atoms in the $PZDC^{2-}$ linker serve as the main adsorptive sites for water molecules, with the strength of this interaction playing a pivotal role in the formation of water structures within the pores.[6] I sought to tune the hydrophilicity of these

---

Portions of this chapter have been adapted from:
Zheng, Z.; Hanikel, N.; Lyu, H.; Yaghi, O. M., Broadly Tunable Atmospheric Water Harvesting in Multivariate Metal–Organic Frameworks. *J. Am. Chem. Soc.* **2022,** *144* (49), 22669-22675.

sites by introduction of thiophene-2,5-dicarboxylate (TDC^{2-}) along with $PZDC^{2-}$ in the MOF backbone. Leveraging these two linkers, nine multivariate PT-MOFs, denoted as $[Al(OH)(PZDC)_{1-x}(TDC)_x]$ and spanning a complete linker mixing spectrum (x = 0, 0.125, 0.25, 0.375, 0.5, 0.625, 0.75, 0.875, 1; Figure 4.1), were produced. These compounds have been made under both solvothermal and reflux-based conditions, and their structure, composition, and porosity were fully characterized. These compounds were developed under both solvothermal and reflux conditions, with thorough analyses conducted on their structures, compositions, and porosities. The efficacy of the multivariate approach becomes evident in the water sorption capabilities of the PT-MOF series, which allow for (i) adaptability and engagement with a wider range of relative humidity levels and (ii) a more energy-efficient water-harvesting process, marked by reduced regeneration temperatures and heats. These advancements significantly surpass previous findings and prove beneficial for water harvesting in arid environments.[16,17] Moreover, the production of these multivariate compounds can be scaled up to kilogram quantities, achieving impressive space-time yields using easily sourced raw materials.

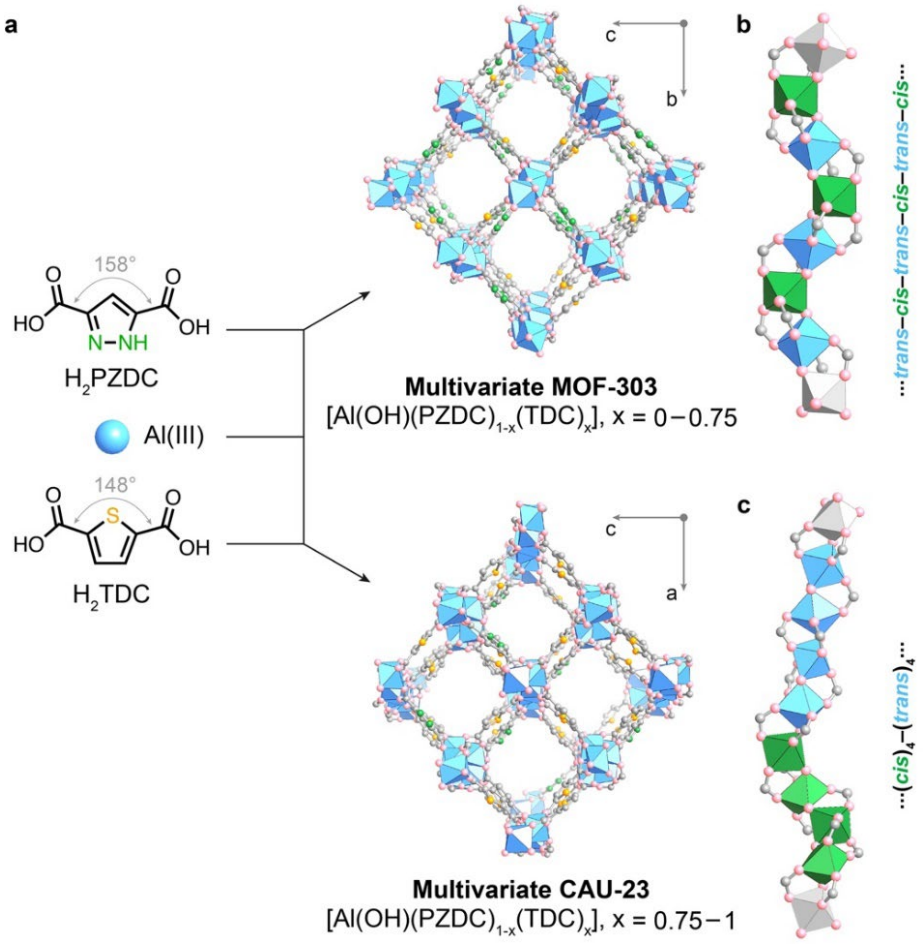

Figure 4.1 Illustration of the crystal structures of multivariate MOF-303 and CAU-23. (a) The organic linkers. (b) Rod-like SBU featuring *cis–trans*-alternating corner-shared AlO_6 octahedra (c) Rod-like SBU with $(cis)_4$–$(trans)_4$-alternating corner-shared AlO_6 octahedra patterns. The term "PTnm" denotes the molar input ratio of H_2PZDC to H_2TDC (n to m).

4.2 Experimental section

4.2.1 Starting materials and general procedures

1*H*-pyrazole-3,5-dicarboxylic acid monohydrate ($H_2PZDC \cdot H_2O$, purity ≥ 98%), thiophene-2,5-dicarboxylic acid (H_2TDC, purity ≥ 98%), aluminum chloride hexahydrate ($AlCl_3 \cdot 6\ H_2O$, purity ≥ 99%), sodium hydroxide (NaOH, purity ≥ 97%) were purchased from AK Scientific Inc. Bulk (40 kg) $H_2PZDC \cdot H_2O$ (purity ≥ 95%) and $AlCl_3 \cdot 6\ H_2O$ (purity ≥ 99%) were purchased from Aaron Chemicals LLC. Bulk (10 kg) H_2TDC (purity ≥ 98%) was purchased from Ambeed Inc. Bulk (20 kg) sodium hydroxide pellets (NaOH, purity ≥ 97%) were purchased from Oakwood Products, Inc. Ethanol (EtOH, purity ≥ 99.8%) was purchased from Sigma Aldrich. Deuterated solvents were obtained from Cambridge Isotope Laboratories. Ultrahigh-purity (UHP) grade (99.999%) argon, nitrogen and helium, as well as ultra-zero grade air were obtained from Praxair. All chemicals were used without further purification.

PXRD analyses were conducted on a Bruker D8 Advance X-ray diffractometer equipped with a Cu anode and a Ni filter (CuKa radiation) in Bragg-Brentano geometry. For PXRD measurements, the crystalline, powderous samples were mounted on zero-background holders and leveled with a spatula. The PXRD patterns were recorded between 3 and 50° with 2303 steps (~0.02° per step) with an acquisition time of 0.5–10 seconds per step, thus resulting in ~20 minutes to ~6.5 hours analysis time per measurement. ^{1}H-NMR spectra were acquired on Bruker AVB-400 and NEO-500 MHz spectrometers at the NMR facility of the College of Chemistry, University of California, Berkeley. To analyze the linker composition of the MOF compounds with NMR spectroscopy, prior to the measurement, the frameworks were thoroughly washed with H_2O and methanol, and then fully hydrolyzed using a NaOD solution (10% in D_2O).

EA measurements were performed using a Perkin Elmer 2400 Series II CHNS elemental analyzer at the Microanalytical Laboratory of the College of Chemistry, University of California, Berkeley. Prior to EA of the MOF compounds, each sample was thoroughly washed with H_2O and methanol. Then, it was fully activated under dynamic vacuum (~10^{-3} mbar) through ramping the temperature to 120 °C over a period of 6 hours. After activation and until the measurement, the compounds were kept under inert atmosphere to avoid water adsorption.

SEM images were obtained on a FEI Quanta 3D FEG scanning electron microscope using an accelerating voltage of 10 kV and a working distance of 10.0 mm. EDS data were acquired with an Oxford X-Max EDS system using an accelerating voltage of 10 kV. Prior to conducting SEM-EDS experiments, each sample was thoroughly washed with H_2O and methanol. Afterwards, the crystalline powder was dispersed in ethanol. The resulting suspension was sonicated for 60 seconds to break up larger agglomerates and a droplet of it was applied to a silicon wafer. After the ethanol evaporated, the deposited sample was dried overnight under dynamic vacuum (~10^{-3} mbar).

The TGA curves were recorded on a Netzsch Jupiter, STA449 F5 apparatus. Prior to the measurement, the samples were dried by heating to 150 °C at a rate of 1 °C min^{-1}. The measurement was then initiated after the temperature in the TGA oven decreased to 40 °C. For the TGA measurement, the temperature was ramped from 40° to 800 °C at a heating rate of 1 °C min^{-1}. During the experiment, UHP grade Ar at a flow rate of 60 mL min^{-1} was used for the balance purge flow; and UHP grade Ar (inert conditions) or ultra-zero grade air (oxidative conditions) at a flow rate of 60 mL min^{-1} was used for the sample purge flow.

Nitrogen sorption experiments were conducted using a Micromeritics 3Flex Surface Characterization Analyzer or a Micromeritics Accelerated Surface Area and Porosimetry (ASAP) 2420 System. UHP grade N_2 and He were utilized as adsorbate and for free space corrections, respectively. During the measurement, the sample was cooled to 77 K by using a liquid nitrogen bath. The data analyses were carried out using the Micromeritics MicroActive software.[25]

Water vapor sorption experiments were carried out on a BEL Japan BELSORP-aqua^3. The water vapor source was degassed through five freeze-pump-thaw cycles before the analysis. UHP grade He was used for free space corrections and an isothermal bath was employed to adjust the sample temperature during the measurements. The isobar measurements were conducted with a TA Instruments DSC SDT Q600 Thermogravimetric Analyzer & Differential Scanning Calorimeter. The temperature and relative humidity (RH) were monitored using high-accuracy thermocouples and humidity sensors downstream of the TGA chamber. To adjust the RH in the TGA, a dry and a humidified N_2 feed were connected to the primary and secondary TGA inlet, respectively, and their flow rate ratio was varied according to a pre-recorded calibration curve, while maintaining the overall sum of both flow rates constant at 200 mL min^{-1}. UHP grade N_2 was utilized as the dry N_2 feed. To generate the humidified N_2 feed, UHP grade N_2, regulated by the Sierra SmartTrak® 100 mass flow controller, was passed through a H_2O-filled 2 L gas washing bottle, which was refilled frequently to ensure steady humidification.

4.2.2 Synthesis of metal–organic frameworks

Solvothermal synthesis. In a 20 mL vial, a mixture (0.5 mmol) of H_2PZDC and H_2TDC was fully dissolved in aqueous NaOH solution (0.079 m, 9.5 mL, 1.5 eq.). The mole ratio of H_2PZDC to H_2TDC (n to m) was adjusted to prepare multivariate MOFs, and the materials prepared from the linker mixtures are denoted as PTnm (P, H_2PZDC; T, H_2TDC; n, mole ratio of H_2PZDC; m, mole ratio of H_2TDC). Afterwards, aqueous $AlCl_3$ solution (1 m, 0.5 mL) was added and the resulting clear mixture was incubated for 2–4 days in a pre-heated oven at 100 °C. The obtained white solid was washed with deionized water (3 × 15 mL) and methanol (3 × 15 mL) over a period of one day each. Next, the MOF was dried under dynamic vacuum (~10^{-3} mbar) and heated to 120 °C over a period of 6 hours to yield the pure, activated product (47–53 mg, 47–50%).

The synthesis of PT26 had to be modified by increasing the base stoichiometry to obtain a single-phase product: In a 20 mL vial, a mixture of H_2PZDC · H_2O (21.8 mg, 0.125 mmol) and

H_2TDC (64.5 mg, 0.375 mmol) was fully dissolved in aqueous NaOH solution (0.132 m, 9.5 mL, 2.5 eq.). Afterwards, aqueous $AlCl_3$ solution (1 m, 0.5 mL) was added, resulting in the formation of a white precipitate. The reaction mixture was then incubated for 4 days in a pre-heated oven at 100 °C. The obtained white solid was washed with deionized water (3 × 15 mL) and methanol (3 × 15 mL) over a period of one day each. Next, the MOF was dried under dynamic vacuum (~10^{-3} mbar) and heated to 120 °C over a period of 6 hours to yield the pure, activated product (82 mg, 78%).

Reflux synthesis. In a 250 mL round-bottom flask, a mixture (10 mmol) of H_2PZDC and H_2TDC was fully dissolved in aqueous NaOH solution (0.6 m, 50 mL). The mole ratio of H_2PZDC to H_2TDC (n to m) was adjusted to prepare multivariate MOFs, and the materials prepared from the linker mixtures are denoted as PTnm-HY (P, H_2PZDC; T, H_2TDC; n, mole ratio of H_2PZDC; m, mole ratio of H_2TDC; HY, high yield). $AlCl_3 \cdot 6\ H_2O$ (2.41g, 10 mmol) was dissolved in 50 mL deionized water and added dropwise to the linker solution in the round-bottom flask at room temperature under vigorous stirring. The total addition time was 2 hours, resulting in the formation of a white precipitate. The reaction mixture was then heated to 120 °C and refluxed for 3 hours at all linker mixing ratios. For PT26-HY, the refluxing time was varied between 3 and 40 hours, and the respective samples are labeled PT26-HY-xh (P, H_2PZDC; T, H_2TDC; HY, high yield; x, refluxing time in hours). After the solution cooled down to room temperature, the resulting white powder was collected by centrifugation and washed twice with deionized water. The white solid was subsequently washed three times with EtOH and dried under air overnight. Full activation of the MOF was conducted under dynamic vacuum (~10^{-3} mbar) at 120 °C for 24 hours, yielding pure and desolvated product (1.86–2.01 g, 90–96%).

Large-scale reflux synthesis. In a 200 L glass reaction vessel, a mixture of H_2PZDC and H_2TDC (20 mol), as well as NaOH (2.4 kg, 60 mol) were dissolved in 38 L deionized water. The mole ratio of H_2PZDC to H_2TDC (n to m) was adjusted to prepare multivariate MOFs. The materials synthesized from these linker mixtures are denoted as PTnm-HYS (P, H_2PZDC; T, H_2TDC; n, mole ratio of H_2PZDC; m, mole ratio of H_2TDC; HYS, high yield and scale). The resulting suspension was stirred for 60 minutes until all the solids dissolved completely and the solution cooled down to room temperature. Afterwards, $AlCl_3 \cdot 6\ H_2O$ (4.82 kg, 20 mol) was dissolved in 12 L deionized water and transferred to a 15 L glass material-feeding funnel. The aluminum chloride solution was added at a rate of 6 L per hour to the reaction vessel with the spinner rotating at 100 rpm. The total addition time lasted for 2 hours, resulting in the formation of a white precipitate. Next, the temperature of the heating jacket was set to 120 °C, thus heating the reaction mixture to 100 °C. After refluxing for 6 hours and letting the reaction mixture cool down to 60 °C, the solid product was collected in a 20 L filtration funnel and washed with 15 a L aqueous 70% EtOH (v/v) solution. For further purification, the white powder was subsequently redispersed by stirring in 30 L anhydrous EtOH at room temperature, followed by filtration and drying under air overnight. The obtained white powder was placed in a 120 °C oven for 48 hours to yield pure and desolvated product (3.50–3.61 kg, 84–91%).

Table 4.1 Comparison of the yields (in g and %) achieved for the multivariate PT-MOF series by employing different synthesis methods.

MOF	Yield (g)		
	Solvothermal	**Reflux in flask**	**Reflux in reaction vessel**
PT80	0.049 (49%)	1.87 (94%)	3590 (91%)
PT71	0.047 (47%)	1.92 (91%)	N/A
PT62	0.048 (48%)	1.86 (92%)	3540 (88%)
PT53	0.049 (48%)	1.96 (96%)	N/A
PT44	0.049 (48%)	1.91 (93%)	3500 (85%)
PT35	0.049 (47%)	1.88 (90%)	N/A
PT26-3h	0.082 (78%)	1.91 (91%)	3610 (86%)
PT26-4h		2.01 (96%)	
PT26-8h		1.98 (94%)	
PT26-16h		1.97 (94%)	
PT26-20h		1.99 (95%)	
PT26-28h		1.90 (90%)	
PT26-40h		1.99 (95%)	
PT17	0.052 (49%)	1.89 (90%)	N/A
PT08	0.053 (50%)	1.93 (90%)	3610 (84%)

Table 4.2 Comparison of the space-time yields achieved for the multivariate PT-MOF series by employing different synthesis methods.

MOF	Space-time yield (kg m^{-3} day^{-1})		
	Solvothermal	**Reflux in flask**	**Reflux in reaction vessel**
PT80	1.6	89.8	215
PT71	1.6	92.2	N/A
PT62	1.6	89.3	212
PT53	1.6	94.1	N/A
PT44	1.6	91.7	210
PT35	1.6	90.2	N/A
PT26-3h	2.7	91.7	217
PT26-4h		80.4	
PT26-8h		47.5	
PT26-16h		26.3	
PT26-20h		21.7	
PT26-28h		15.2	
PT26-40h		11.4	
PT17	1.7	90.7	N/A
PT08	1.8	92.6	217

4.2.3 Powder x-ray diffraction analysis

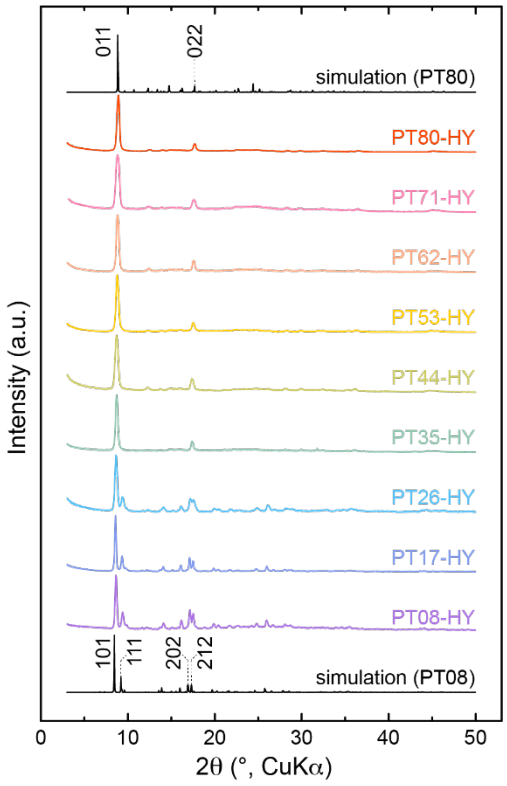

Figure 4.2 Powder X-ray diffraction analysis of multivariate PT-HY-MOF compounds synthesized under reflux for 3 hours in a flask. The simulated patterns at the top and bottom were generated using the fully water-loaded crystal structures of MOF-303 (PT80) and CAU-23 (PT08),[6, 9] respectively.

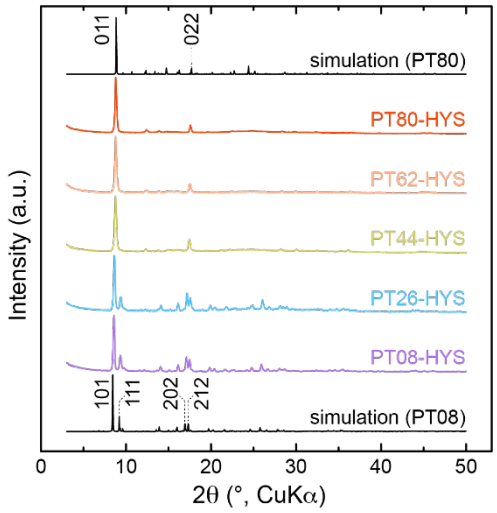

Figure 4.3 Powder X-ray diffraction analysis of multivariate PT-HYS-MOF compounds synthesized under reflux in a reaction vessel. The simulated patterns at the top and bottom were generated using the fully water-loaded crystal structures of MOF-303 (PT80) and CAU-23 (PT08),[6, 9] respectively.

4.2.4 Proton nuclear magnetic resonance spectroscopy and elemental analysis

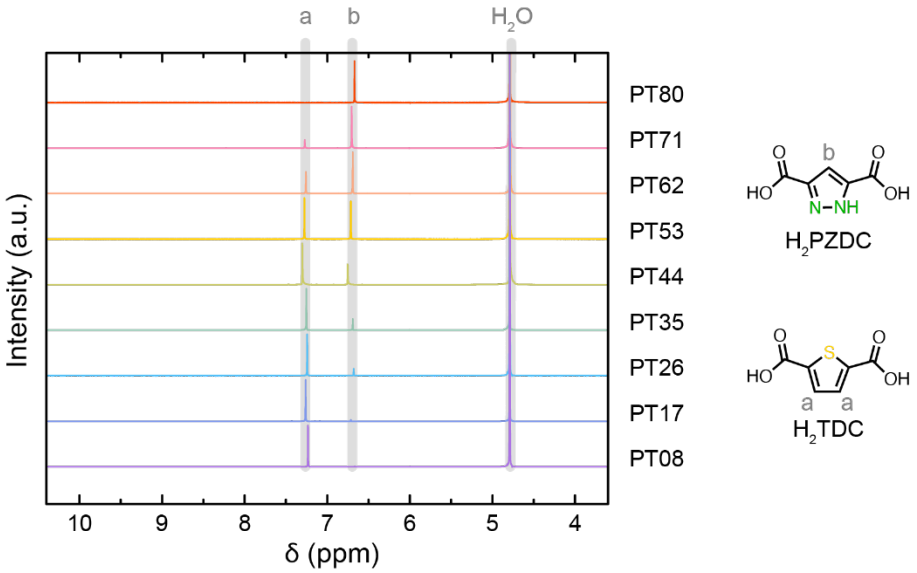

Figure 4.4 ^{1}H-NMR spectra in NaOD solution (10% in D_2O) of thoroughly washed and then fully base-hydrolyzed multivariate PT-MOF compounds synthesized under solvothermal conditions. Gray letters indicate signal assignment to the respective ^{1}H in the molecular structures. The carboxylic acid groups are deprotonated at these conditions.

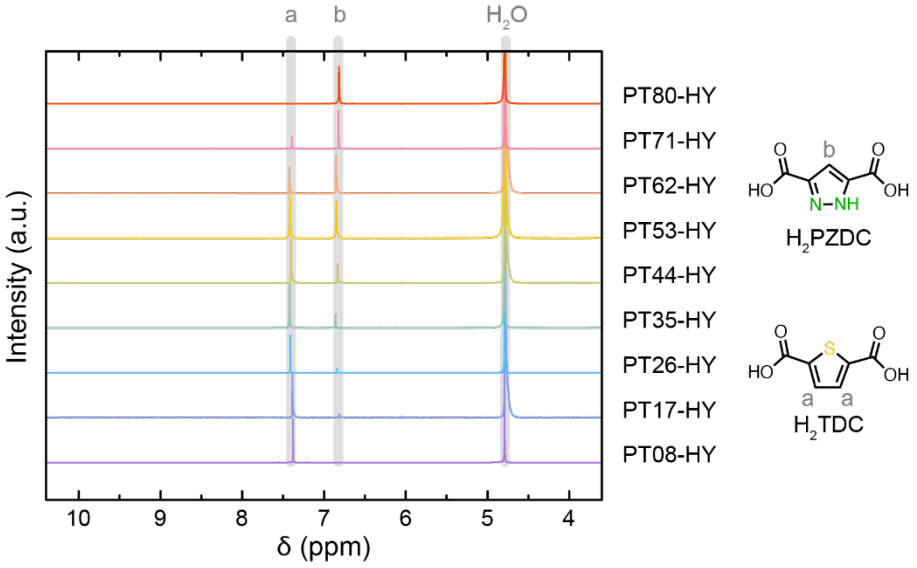

Figure 4.5 ^{1}H-NMR spectra in NaOD solution (10% in D_2O) of thoroughly washed and then fully base-hydrolyzed multivariate PT-HY-MOF compounds synthesized under reflux for 3 hours in a flask. Gray letters indicate signal assignment to the respective ^{1}H in the molecular structures. The carboxylic acid groups are deprotonated at these conditions.

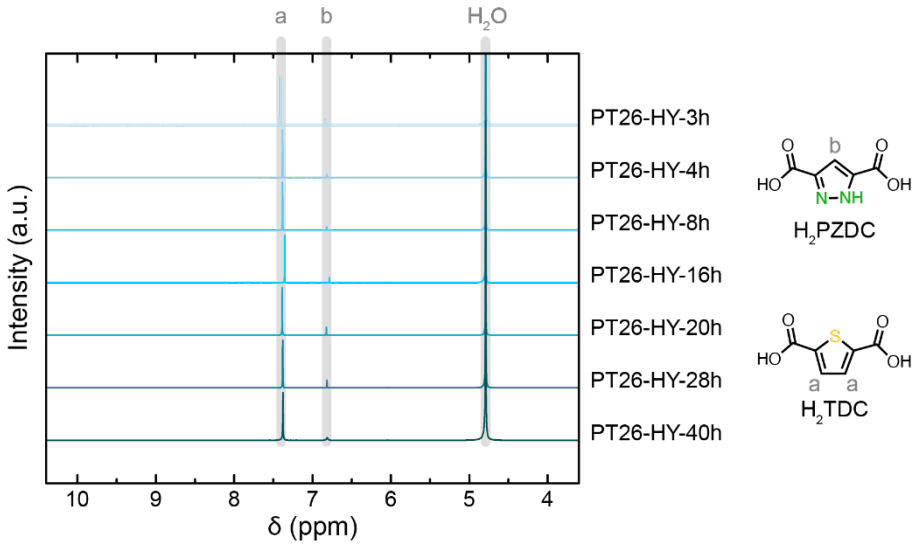

Figure 4.6 ^{1}H-NMR spectra in NaOD solution (10% in D_2O) of thoroughly washed and then fully base-hydrolyzed multivariate PT-HY-xh-MOF compounds synthesized under reflux for 3–40 hours in a flask. Gray letters indicate signal assignment to the respective ^{1}H in the molecular structures. The carboxylic acid groups are deprotonated at these conditions.

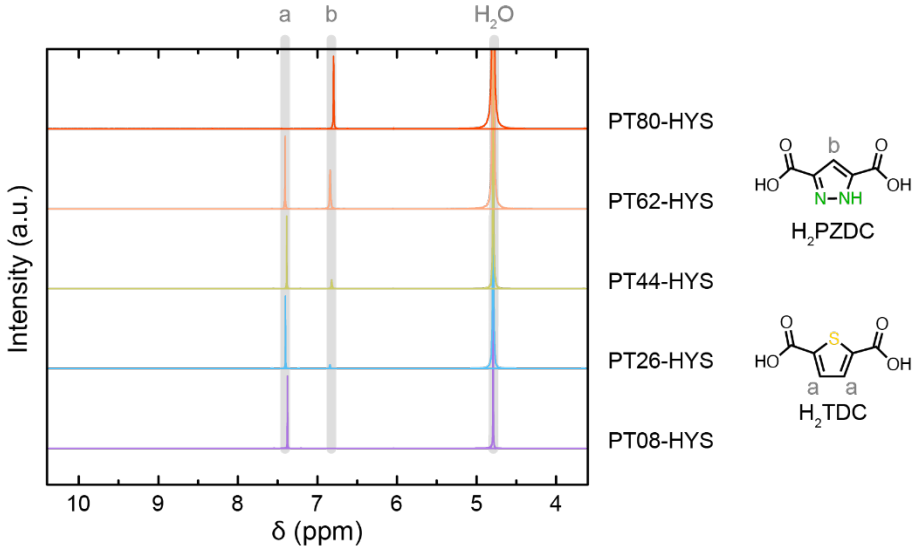

Figure 4.7 ^{1}H-NMR spectra in NaOD solution (10% in D_2O) of thoroughly washed and then fully base-hydrolyzed multivariate PT-HYS-MOF compounds synthesized under reflux conditions in a reaction vessel. Gray letters indicate signal assignment to the respective ^{1}H in the molecular structures. The carboxylic acid groups are deprotonated at these conditions.

Table 4.3 Summary of the composition assessment of the multivariate PT-MOF series (synthesized by employing different procedures and reaction times) with help of ^{1}H-nuclear magnetic resonance (NMR) spectroscopy based on the peak integration.

MOF	Input H_2PZDC ratio (%)	Observed H_2PZDC ratio (%) by NMR		
		Solvothermal	Reflux in flask	Reflux in reaction vessel
PT80	100	100	100	100
PT71	87.5	91.3	87.3	N/A
PT62	75	79.4	75.8	73.2
PT53	62.5	64.7	63.1	N/A
PT44	50	49.4	49.6	46.9
PT35	37.5	34.8	37.5	N/A
PT26-3h	25	24.2	24.9	21.9
PT26-4h			24.8	
PT26-8h			24.7	
PT26-16h			25.1	
PT26-20h			25.3	
PT26-28h			25.0	
PT26-40h			25.0	
PT17	12.5	6.1	12.4	N/A
PT08	0	0	0	0

Table 4.4 Summary of the composition assessment of the multivariate PT-MOF series (synthesized by employing different procedures and reaction times) with help of elemental analysis (EA). The observed H_2PZDC ratio was determined from EA under consideration of the obtained nitrogen to sulfur ratio.

MOF	Input H_2PZDC ratio (%)	Observed H_2PZDC ratio (%) by NMR		
		Solvothermal	Reflux in flask	Reflux in reaction vessel
PT80	100	100	100	100
PT71	87.5	86.6	84.5	N/A
PT62	75	72.8	72.2	69.6
PT53	62.5	61.1	59.1	N/A
PT44	50	46.3	48.1	44.4
PT35	37.5	33.3	36.1	N/A
PT26-3h	25	24.9	25.8	21.0
PT26-4h			25.0	
PT26-8h			24.0	
PT26-16h			25.6	
PT26-20h			26.0	
PT26-28h			25.9	
PT26-40h			27.3	
PT17	12.5	5.8	12.9	N/A
PT08	0	0	0	0

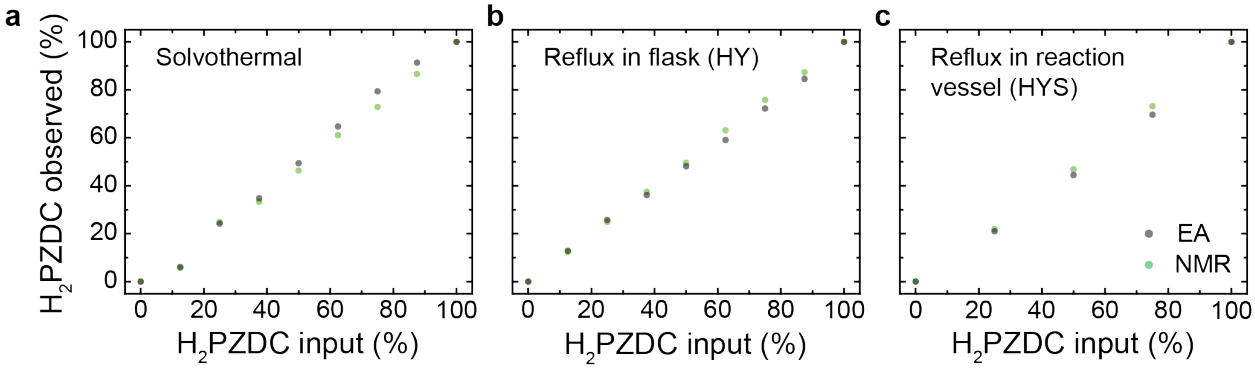

Figure 4.8 Molar H_2PZDC linker ratios of PT samples, prepared under (a) solvothermal conditions, (b) reflux in flask, and (c) reflux in reaction vessel, as determined by NMR of thoroughly washed and fully hydrolyzed MOF samples, as well as N/S elemental analysis (EA) of activated frameworks, are plotted against the respective input linker ratio.

4.2.5 Scanning electron microscopy with energy dispersive X-ray spectroscopy

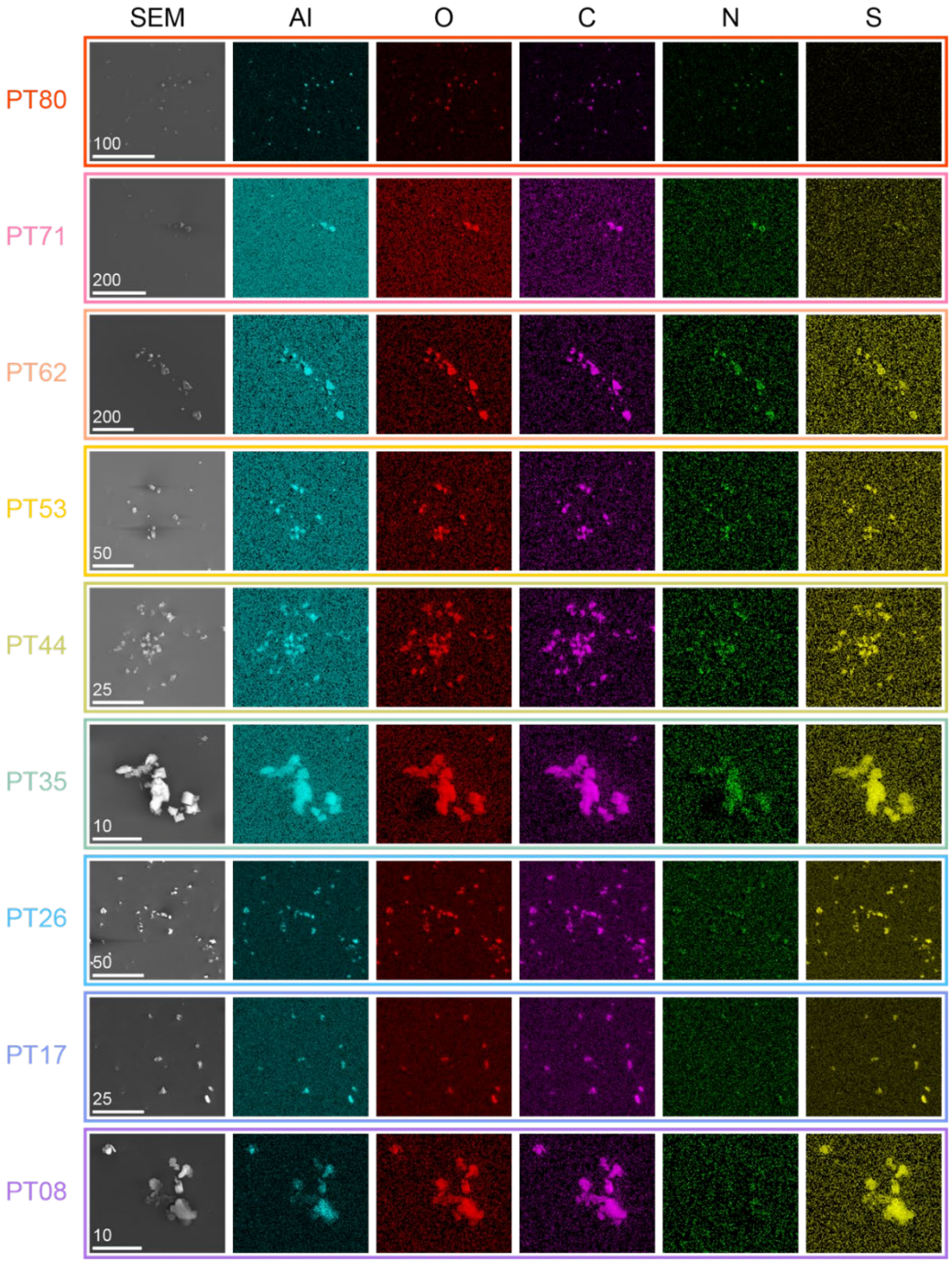

Figure 4.9 Scanning electron microscopy with energy dispersive X-ray spectroscopy capturing the bulk material of the multivariate PT-MOF series. Prior to imaging, the crystals were washed with water and methanol, and dried under reduced pressure. Scale bars are given in µm.

4.2.6 Thermogravimetric analysis

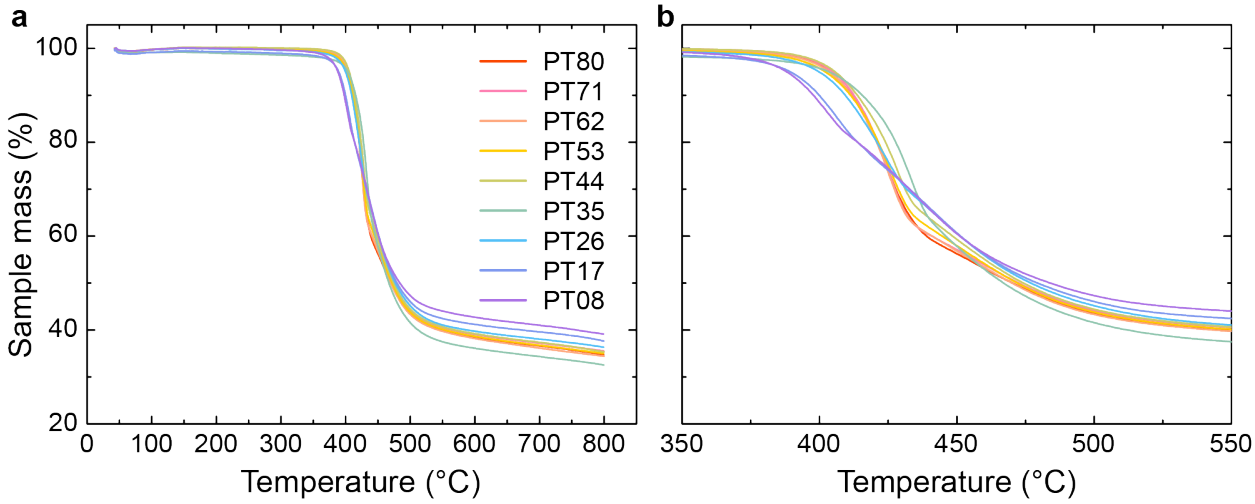

Figure 4.10 (a) Full-range and (b) decomposition-temperature region of the thermogravimetric analysis on the multivariate PT-MOF series under argon atmosphere.

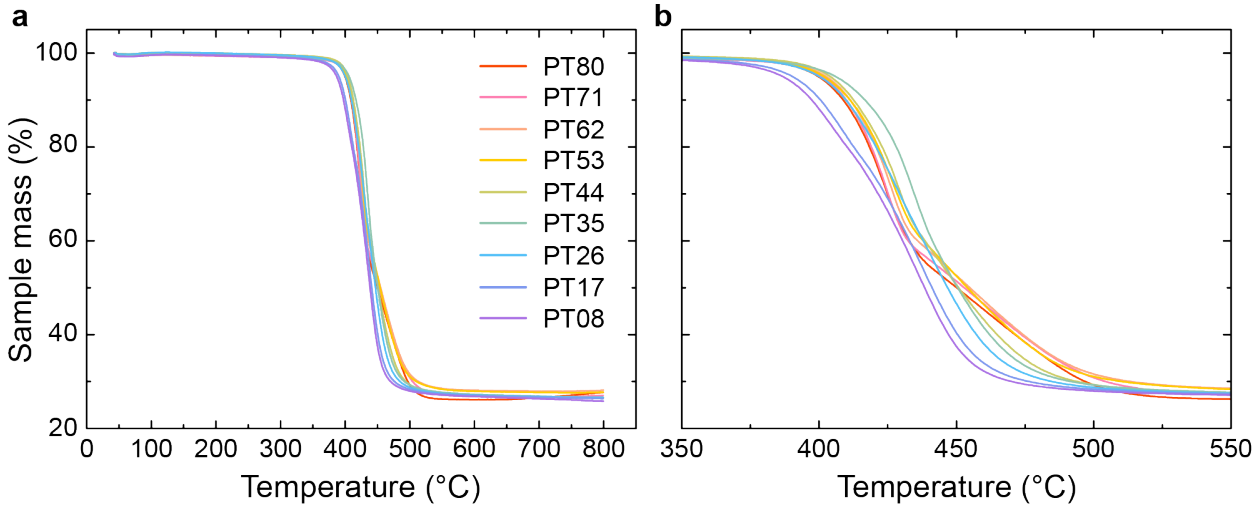

Figure 4.11 (a) Full-range and (b) decomposition-temperature region of the thermogravimetric analysis on the multivariate PT-MOF series under air atmosphere.

4.2.6 Estimation of adsorption enthalpy

The differential enthalpy of adsorption, Δh_{ads}, for each loading increment was ascertained following a method analogous to previously described techniques.[6] Initially, water adsorption curves at varying temperatures, T, were subjected to linear interpolation. Subsequently, for each specific loading, m, the corresponding pressures P_m at different temperatures were identified. Fom this, the ratio $\ln(P_m/P_0)$ was plotted against $1/T$, where with $P_0 = 1$ bar. The Clausius-Clapeyron equation (Eq. 1) was then applied, using the slope to deduce Δh_{ads}.

$$\ln(P_m/P_0) = \frac{\Delta h_{ads,m}}{R} \cdot \frac{1}{T} - \frac{\Delta s_{ads,m}}{R} \qquad \text{(Eq. 1)}$$

Within this context, it is important to acknowlege that the Clausius-Clapeyron relation may yield imprecise results for highly hydrophilic compounds at minimal vapor pressures. This imprecision is attributed to the marginal isotherm separation at reduced pressures during measurements at different temperatures (extending to roughly one water molecule per asymmetric unit for the multivariate MOF series).[26] However, for the MOF compounds under study, this approach should provide a reasonably accurate estimate at elevated loadings.

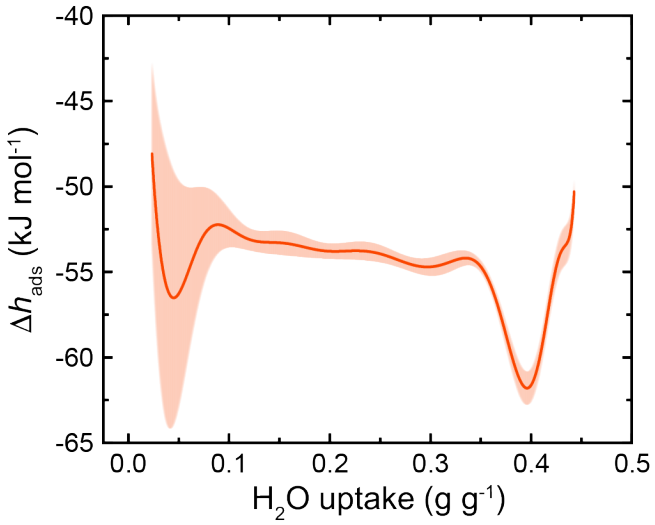

Figure 4.12 Differential heat of adsorption Δh_{ads} of PT80 in dependence of water loading. The shaded region represents the standard error of the linear regression at each loading increment.

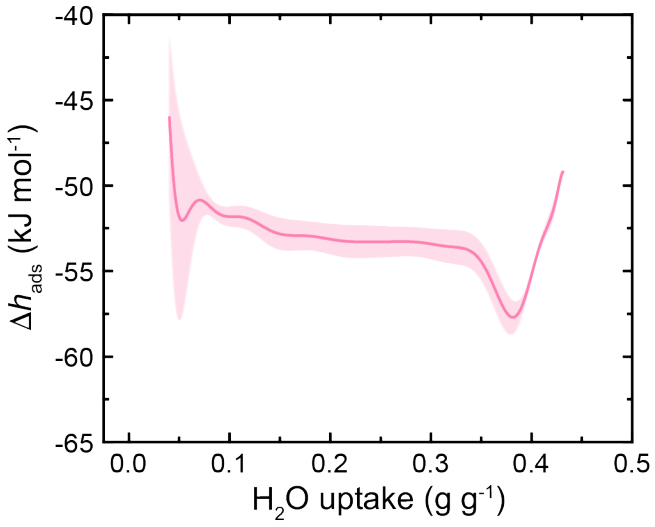

Figure 4.13 Differential heat of adsorption Δh_{ads} of PT71 in dependence of water loading. The shaded region represents the standard error of the linear regression at each loading increment.

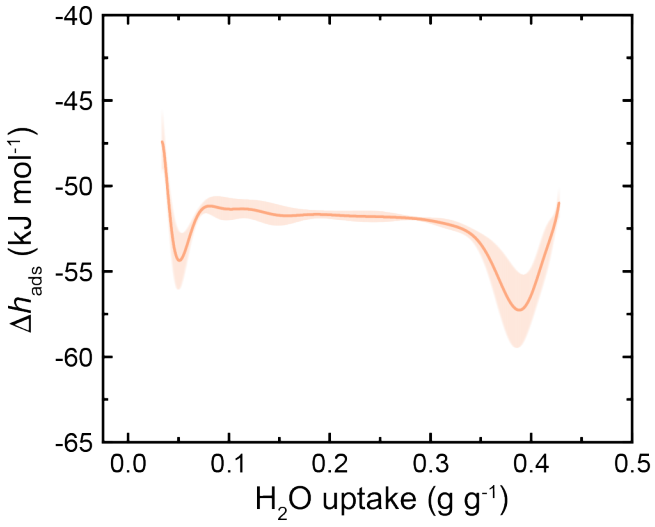

Figure 4.14 Differential heat of adsorption Δh_{ads} of PT62 in dependence of water loading. The shaded region represents the standard error of the linear regression at each loading increment.

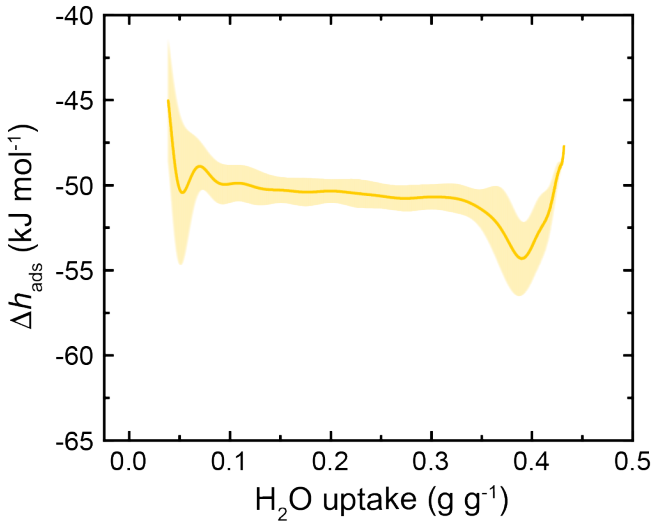

Figure 4.15 Differential heat of adsorption Δh_{ads} of PT53 in dependence of water loading. The shaded region represents the standard error of the linear regression at each loading increment.

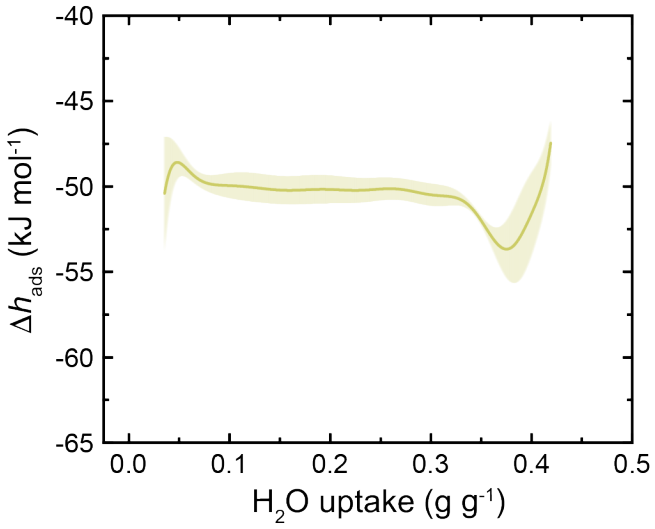

Figure 4.16 Differential heat of adsorption Δh_{ads} of PT44 in dependence of water loading. The shaded region represents the standard error of the linear regression at each loading increment.

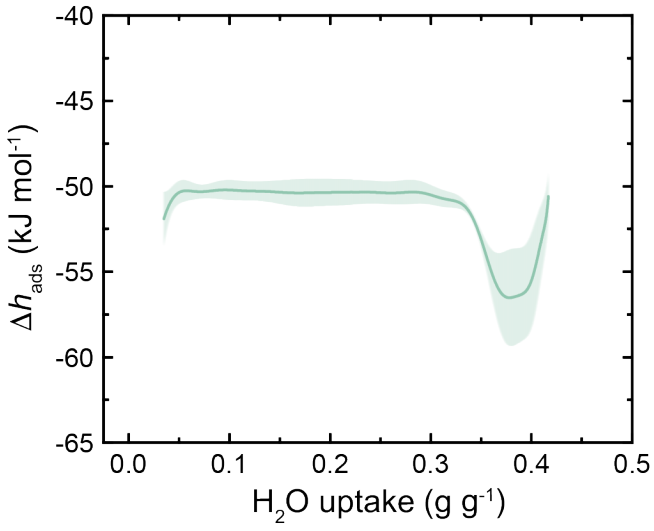

Figure 4.17 Differential heat of adsorption Δh_{ads} of PT53 in dependence of water loading. The shaded region represents the standard error of the linear regression at each loading increment.

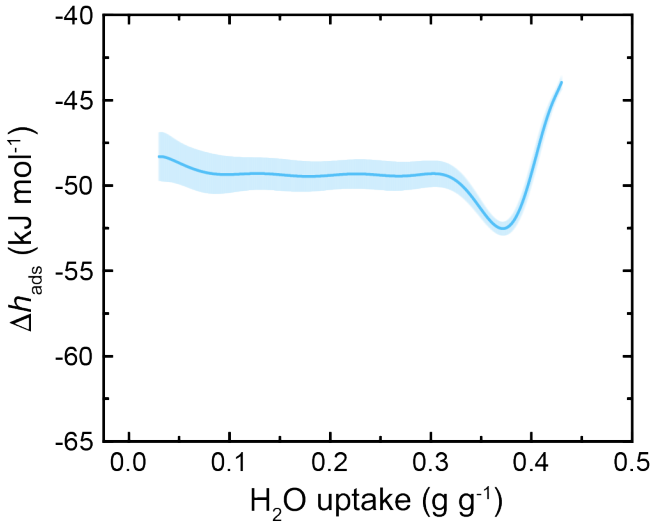

Figure 4.18 Differential heat of adsorption Δh_{ads} of PT62 in dependence of water loading. The shaded region represents the standard error of the linear regression at each loading increment.

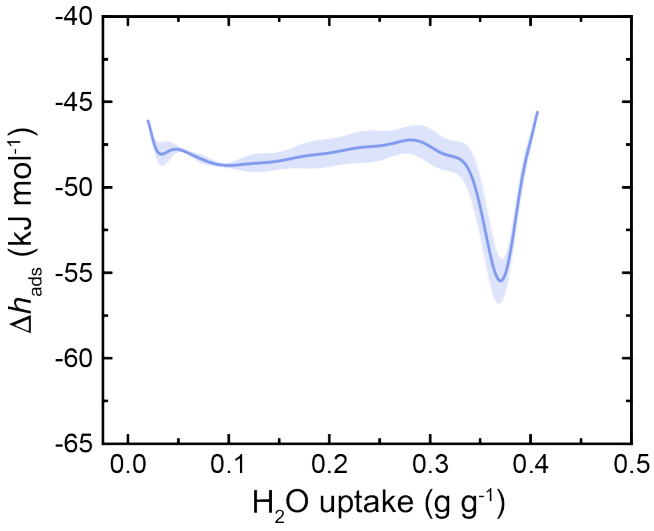

Figure 4.19 Differential heat of adsorption Δh_{ads} of PT71 in dependence of water loading. The shaded region represents the standard error of the linear regression at each loading increment.

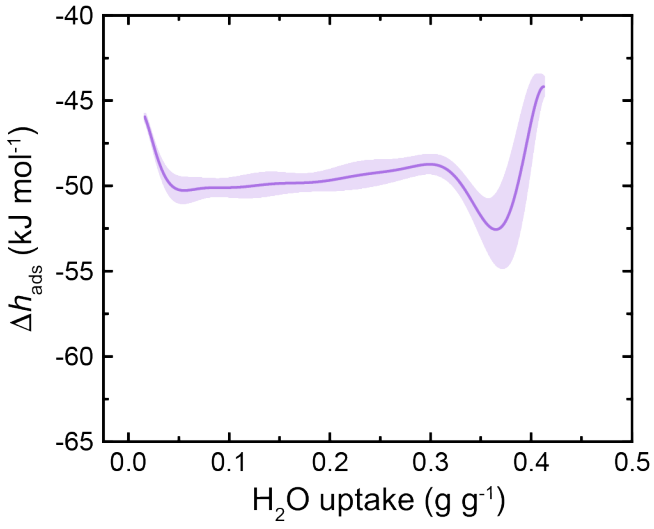

Figure 4.20 Differential heat of adsorption Δh_{ads} of PT80 in dependence of water loading. The shaded region represents the standard error of the linear regression at each loading increment.

4.3 Reticular design and characterization of MTV-MOFs

In determining the second linker for the MOF-303-based multivariate framework series, both its availability and hydrophobicity stand as critical considerations. Moreover, the angle between the carboxylic acid groups must align closely to facilitate the crystallization of both linkers within the same crystal lattice, ensuring the prevention of forming a blend of single-linker MOFs (Figure 4.1).[27] According to a survey in the Cambridge Chemical Database via the Mogul software,[28, 29] the angle between the carboxylic acid groups of protonated, uncoordinated H_2TDC is 147.7(17)°, thus exhibiting a deviation of 10° in comparison to H_2PZDC. This difference seems to be significant enough to result in single-linker MOFs of different topology, space group, and with secondary building units (SBUs) of different stereochemistry.[9, 30]

Depending on the linker ratio employed in synthesis, the formation of two distinct phases was identified through powder X-ray diffraction (PXRD) analysis of the synthesized multivariate PT MOF series. Notably, for the majority of the input ratios of H_2PZDC (PT80 to PT26), phases isostructural to MOF-303 were evident. However, compounds formulated with lower input ratios of H_2PZDC (PT17 and PT08) revealed CAU-23-like structures (Figure 4.21a).

The composition of the multivariate PT-MOFs underwent evaluation through charaterzation techniques including NMR spectroscopy, elemental analysis (EA), and scanning electron microscopy (SEM) paired with energy dispersive X-ray spectroscopy (EDS). Before the NMR spectroscopic analysis, MOFs underwent comprehensive washing and were subsequently base-hydrolyzed using a concentrated NaOD solution (Section 4.2.4). The H_2PZDC content was deduced from EA of activated MOF samples by referencing the N to S ratio. Both the NMR and EA data reflected formulaic patterns of the bulk PT-MOF samples, demonstrating that the observed output ratio of H_2PZDC correlated with the input ratio of the respective linker (Figure 4.21b). The presence of both linkers in the same crystallites was confirmed using SEM-EDS measurements on separated crystals of all members of the multivariate PT-MOF series (Figure 4.21c) as well as larger portions of the sample materials (Figure 4.9). EDS signals associated with Al, O, and C were observed in all crystallites, while the N signal diminished and the S signal increased with higher incorporation ratios of the TDC^{2-} linker. If present, both the N and S signals uniformly resembled the crystal outlines, thus indicating homogenous distribution of both linkers within the multivariate PT-MOFs. Interestingly, some distinct crystal morphologies became apparent when comparing SEM images of the MOF 303-like phase to the CAU-23-like phase (Figure 4.21c).

Subsequently, thermogravimetric analysis (TGA) and nitrogen sorption analysis were employed to assess the thermal stability and porosity of the multivariate compounds. Notably, all multivariate compounds isostructural to MOF-303 (PT80 to PT26) displayed no weight reduction up to approximately 400 °C in both argon and air atmospheres. However, PT17 and PT08 began decomposing slightly earlier under both conditions (~375 °C; Figure 4.10 and Figure 4.11). The BET surface areas and specific pore volumes decreased continuously from 1370 to 1220 $m^2\ g^{-1}$ and from 0.50 to 0.45 $cm^3\ g^{-1}$, respectively, with increasing incorporation of TDC^{2-} into the MOF

structure, as one would expect considering the molecular weight difference between $PZDC^{2-}$ and TDC^{2-} (Table 4.5). The pore sizes were approximated to lie in the same range for all nine compounds (9.4–9.6 Å), as anticipated for frameworks constructed from linker molecules of similar length and in absence of dangling side chains restricting the pore diameters.

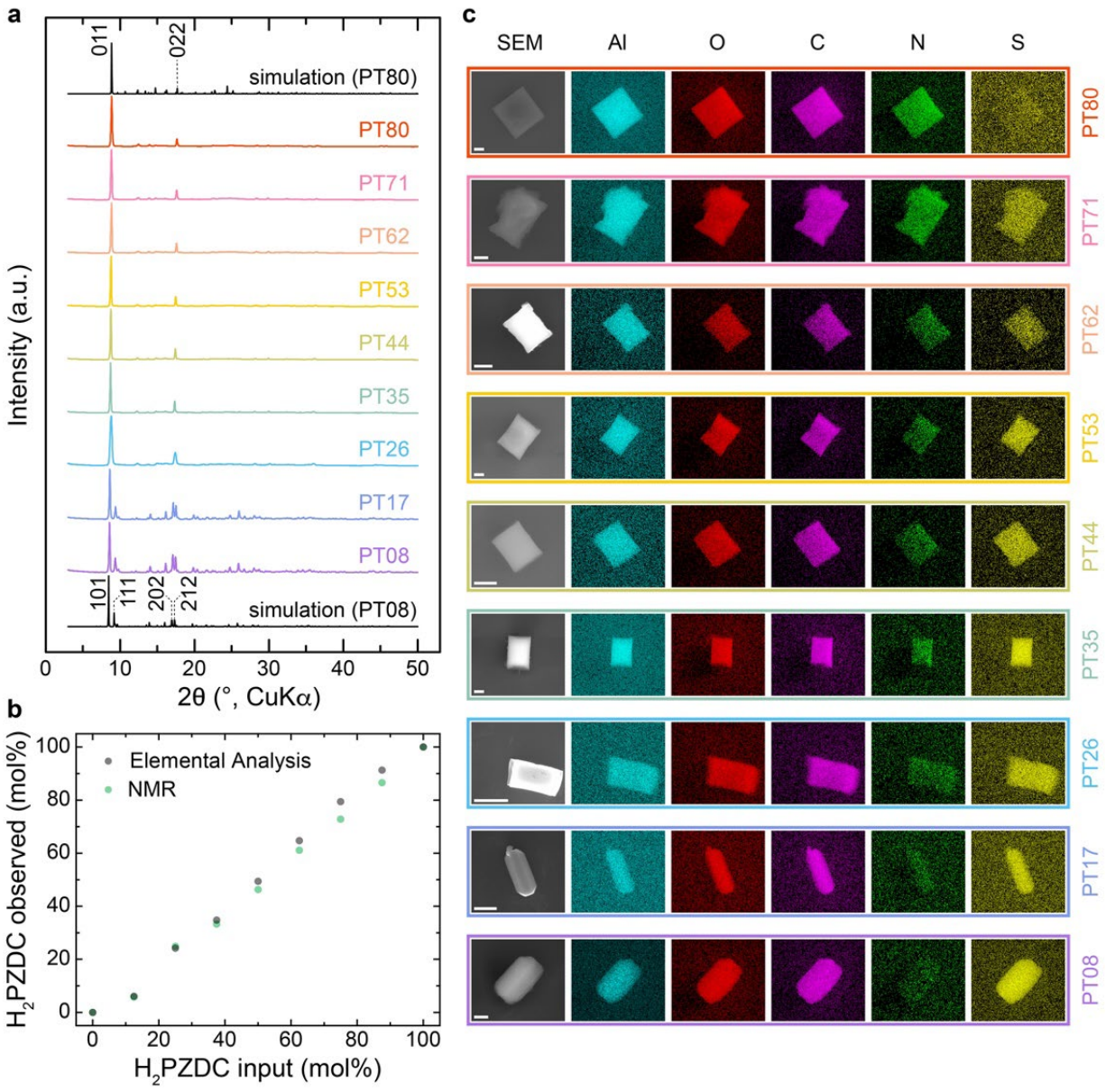

Figure 4.21 Structural and compositional characterization of the PT-MOF series synthesized under solvothermal conditions. (a) Powder X-ray diffraction analysis using CuKa radiation. (**b**) Molar H_2PZDC linker ratios, as determined by NMR of thoroughly washed and fully hydrolyzed MOF samples, as well as N/S elemental analysis of activated frameworks, are plotted against the respective input linker ratio. (**c**) Scanning electron microscopy (SEM) with energy dispersive X-ray spectroscopy

of separated crystals of all members of the multivariate PT-MOF series.

Table 4.5 Pore volume and size estimations from the nitrogen sorption analysis of the multivariate PT-MOF series.

MOF	Pore volume (P/P_0 = 0.95) ($cm^3\ g^{-1}$)	Pore volume (DFT) ($cm^3\ g^{-1}$)	Pore size (DFT) (Å)
PT80	0.519	0.498	9.4
PT71	0.524	0.503	9.4
PT62	0.527	0.503	9.4
PT53	0.535	0.498	9.6
PT44	0.509	0.479	9.5
PT35	0.519	0.473	9.4
PT26	0.515	0.470	9.4
PT17	0.511	0.457	9.5
PT08	0.498	0.453	9.6

4.4 Tuning of water sorption properties

The water sorption isotherms of the multivariate PT-MOFs shifted from 12% RH for PT80 (MOF-303) to 27% RH for PT08 (CAU-23; Figure 4.22a). Consequently, by combining these two linkers, the tuning range expanded by 50% compared to the previously reported multivariate MOF system.[6] The gravimetric water uptake capacity diminished from 0.45 to 0.42 g g^{-1}. This decrease can be attributed, analogous to the BET surface areas and specific pore volumes, to the molecular weight disparity between the two linkers. These MOFs displayed only a minimal hysteresis (Figure 4.22b), which is an important prerequisite for energy efficient atmospheric water harvesting. Interestingly, the structural type of the framework impacted the water sorption isotherm profile: While the CAU-23-type frameworks exhibited steep isotherm profiles, the compounds isostructural to MOF-303 displayed more gradual and shallow uptakes (Figure 4.22b), leading to the step position of PT26 at 28% being shifted to more hydrophobic values than PT08.

In order to estimate the differential enthalpies of adsorption using the Clausius-Clapeyron equation (Section 4.2.6), additional water sorption data was collected on all compounds at 15 and 35 °C. The respective average values $\overline{\Delta h_{ads}}$ exhibited an impressive increase from –54 to –49 kJ mol^{-1} across the multivariate MOF series (Figure 4.22c). Considering that the heat of condensation of water at 25 °C is –44 kJ mol^{-1}, this corresponds to a decrease of the heat of adsorption penalty by a substantial 50%. Furthermore, the multivariate approach allowed for a significant lowering of the desorption temperatures, as was estimated using water vapor desorption isobar measurements. At a water vapor pressure of 1.70 kPa, the desorption temperature experienced a shift of over 14 °C using the multivariate approach (Figure 4.22d). The

distinctions in steepness and step positions between the water sorption isotherm profiles of the MOF-303-type and the CAU-23-type structures were also mirrored in their isobaric curves. As a result, the isobaric curve of PT26 showed its desorption step at reduced temperatures relative to PT08 but simultaneously demanded higher temperatures for full desorption (Figure 4.22d).

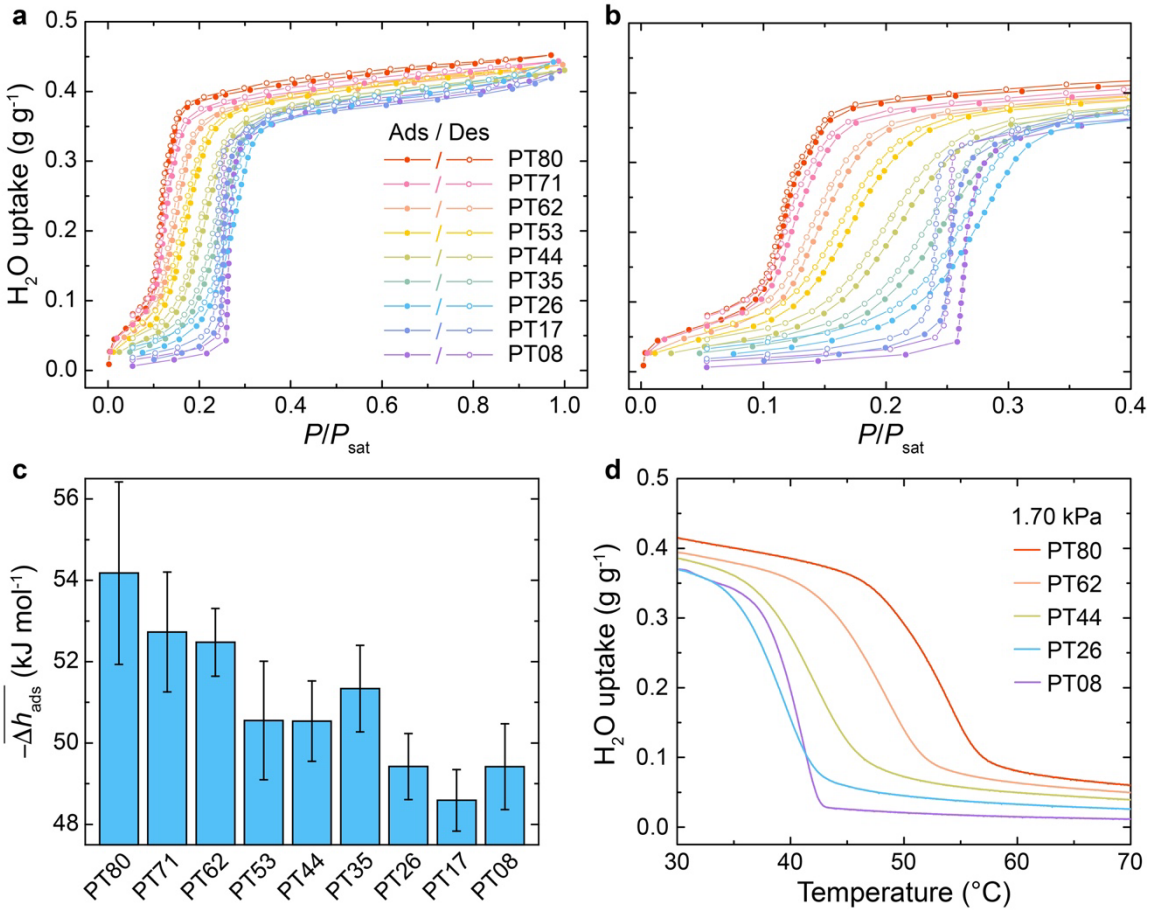

Figure 4.22 Water sorption properties of the multivariate PT-MOF series. (a) Full-range and (b) low-pressure region of the water sorption analyses at 25 °C, where P is water vapor pressure and P_{sat} is the saturation water vapor pressure. (c) Average negative differential adsorption enthalpy values $-\overline{\Delta h_{ads}}$ of the multivariate PT-MOF series. (d) Water vapor desorption isobar measurements of PT80, PT62, PT44, PT26, and PT08 at 1.70 kPa.

4.5 Efficient synthesis and scalability of multivariate MOFs

Traditionally, MOF-303 synthesis was conducted using 1.5 base equivalents, involving an overnight incubation in an isothermal oven.[31] When these conditions were applied to the synthesis of multivariate MOFs, some linker mixing ratios led to compounds exhibiting significant hysteresis in their water sorption isotherms, necessitating extended incubation times (2–4 days).

Moreover, the yields consistently fell below 50%, directly tied to the base stoichiometry used during synthesis (Table 4.1). Ideally, to obtain quantitative yields, three base equivalents would be required: two for the full deprotonation of the dicarboxylic acid linker and one for the formation of the SBU. However, using this base stoichiometry under solvothermal conditions resulted in defect-rich MOFs. This solvothermal procedure also proved unscalable, limiting its industrial application.

To address these challenges, a reflux-based synthesis method was established, incorporating stirring and using three base equivalents (Figure 4.23a and Section 4.2.2). This method reduced reaction times to just 5 hours, and improved yields to over 90% (Table 4.1). This approach significantly boosted the space-time yields for all multivariate PT-MOFs (Figure 4.23b and Table 4.2). The resulting products, designated as PTnm-HY (HY, high yield), displayed high crystallinity (Figure 4.2), and the observed output ratio of H2PZDC was consistent with the input ratio (Figure 4.8). Additionally, BET surface areas, determined through nitrogen sorption analysis, were comparable to those of frameworks synthesized under solvothermal conditions.

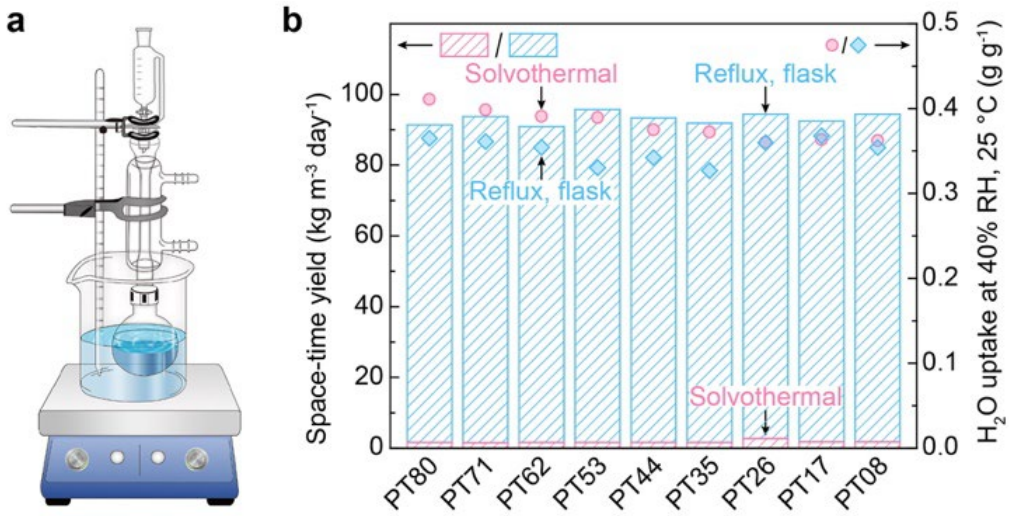

Figure 4.23 Synthesis of multivariate PT-HY-MOFs under reflux conditions in a flask. (a) Schematic representation of the experimental setup. (b) Comparison of the space-time yields and water uptakes at 40% RH and 25 °C for the multivariate PT-MOF series synthesized under solvothermal and reflux conditions in a flask.

It is worthwhile mentioning that the products obtained at a linker input ratio of 2 to 6 (H_2PZDC to H_2TDC) varied with the reaction time. Although solvothermally-prepared PT26 was isostructural to MOF-303 (Figure 4.22a), the PXRD pattern of PT26-HY resembled a CAU-23-type structure (Figure 4.2). Compounds named PT26-HY-xh (where x represents refluxing time in hours) were prepared over varied reaction times. As the refluxing time increased, the formation of a MOF-303-type product became dominant (Figure 4.24a). This variation was further evident in their respective water sorption isotherm profiles (Figure 4.24b).

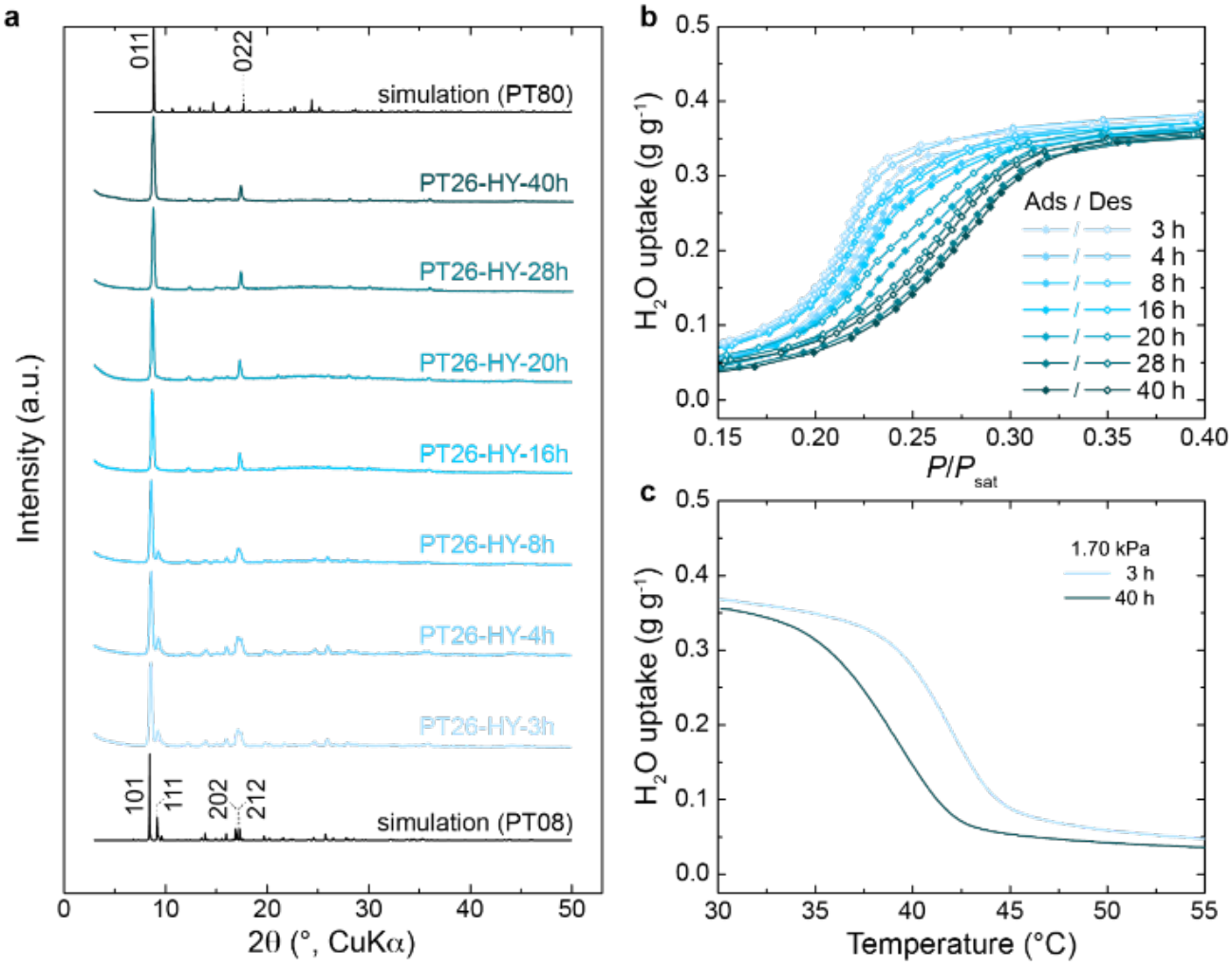

Figure 4.24 Structural characterization and water sorption properties of the multivariate PT26-HY-xh compounds synthesized under reflux for 3–40 hours in a flask. (a) Powder X-ray diffraction analysis using CuKa radiation. The simulated patterns at the top and bottom were generated using the fully water-loaded crystal structures of MOF-303 (PT80) and CAU-23 (PT08), respectively. (b) Low-pressure region of the water sorption isotherms at 25 °C, where P is water vapor pressure and P_{sat} is the saturation water vapor pressure. (c) Water vapor desorption isobar measurements of PT26-HY-3h and PT26-HY-40h at 1.70 kPa.

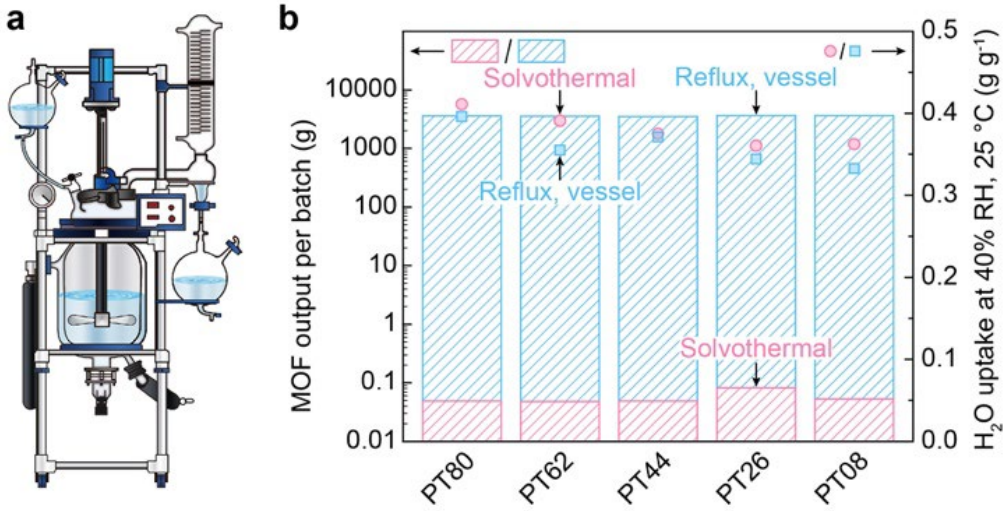

Figure 4.25 Synthesis of multivariate PT-MOFs under reflux conditions in a reaction vessel. (a) Schematic representation of the experimental setup. (b) Comparison of the MOF outputs per batch and water uptakes at 40% RH and 25 °C for the multivariate PT-MOF series synthesized under solvothermal conditions and reflux conditions in a reaction vessel.

Inspired by the successful results from the reflux-based synthesis in a flask, the methodology was scaled up to a 200 L-reaction vessel (Figure 4.25a and Section 4.2.2). This adaptation yielded approximately 3.5 kg of activated MOF per batch in just 8 hours (Figure 4.25b). Consequently, it resulted in a doubling of the space-time yields compared to the flask-based synthesis (Table 4.2). The produced MOFs exhibited high crystallinity (Figure 4.3), formulaic behavior concerning the linker output ratios (Figure 4.8), and high BET surface areas. Their water sorption analysis further highlighted their high tunability and water uptake capacities (Figure 4.24b).

4.5 Conclusions

In this chapter, a multivariate MOF system was successfully developed using accessible starting materials. The synthesized frameworks showcased an enhanced degree of tunability across various parameters: humidity range for atmospheric moisture uptake, regeneration temperature, and adsorption enthalpies. Collectively, these enhancements pave the way for a more energy-efficient and adaptable water-harvesting mechanism, especially in arid environments. A notable achievement was the establishment of a synthesis method that facilitates the production of these MOFs at a kilogram scale using water as a solvent. This method ensures high space-time yields without sacrificing the MOFs' water-harvesting capabilities. These promising results underscore the potential for commercial application of water-harvesting technology and the incorporation of these materials in expansive atmospheric moisture extraction systems, ensuring reliable water production in diverse conditions.

4.6 Reference

(1) Water, U. N. 2018 UN World Water Development Report, Nature-based Solutions for Water. https://www.unwater.org/publications/world-water-development-report-2018/.

(2) Mekonnen, M. M.; Hoekstra, A. Y., Four billion people facing severe water scarcity. *Sci. Adv.* **2016,** *2* (2), e1500323.

(3) Hanikel, N.; Prévot, M. S.; Yaghi, O. M., MOF water harvesters. *Nat. Nanotechnol.* **2020,** *15* (5), 348-355.

(4) Elmer, T. H.; Hyde, J. F., Recovery of water from atmospheric air in arid climates. *Sep. Sci. Technol.* **1986,** *21* (3), 251-266.

(5) Sohail, M.; Yun, Y.-N.; Lee, E.; Kim, S. K.; Cho, K.; Kim, J.-N.; Kim, T. W.; Moon, J.-H.; Kim, H., Synthesis of highly crystalline NH2-MIL-125 (Ti) with S-shaped water isotherms for adsorption heat transformation. *Cryst. Growth Des.* **2017,** *17* (3), 1208-1213.

(6) Hanikel, N.; Pei, X.; Chheda, S.; Lyu, H.; Jeong, W.; Sauer, J.; Gagliardi, L.; Yaghi, O. M., Evolution of water structures in metal-organic frameworks for improved atmospheric water harvesting. *Science* **2021,** *374* (6566), 454-459.

(7) Zheng, Z.; Nguyen, H. L.; Hanikel, N.; Li, K. K.-Y.; Zhou, Z.; Ma, T.; Yaghi, O. M., High-yield, green and scalable methods for producing MOF-303 for water harvesting from desert air. *Nat. Protoc.* **2023,** *18*, 136–156.

(8) Wang, S.; Lee, J. S.; Wahiduzzaman, M.; Park, J.; Muschi, M.; Martineau-Corcos, C.; Tissot, A.; Cho, K. H.; Marrot, J.; Shepard, W., A robust large-pore zirconium carboxylate metal–organic framework for energy-efficient water-sorption-driven refrigeration. *Nat. Energy* **2018,** *3* (11), 985-993.

(9) Lenzen, D.; Zhao, J.; Ernst, S.-J.; Wahiduzzaman, M.; Ken Inge, A.; Fröhlich, D.; Xu, H.; Bart, H.-J.; Janiak, C.; Henninger, S., A metal–organic framework for efficient water-based ultra-low-temperature-driven cooling. *Nat. Commun.* **2019,** *10* (1), 1-9.

(10) Cho, K. H.; Borges, D. D.; Lee, U.-H.; Lee, J. S.; Yoon, J. W.; Cho, S. J.; Park, J.; Lombardo, W.; Moon, D.; Sapienza, A., Rational design of a robust aluminum metal-organic framework for multi-purpose water-sorption-driven heat allocations. *Nat. Commun.* **2020,** *11* (1), 5112.

(11) Zheng, Z.; Alawadhi, A. H.; Yaghi, O. M., Green Synthesis and Scale-Up of MOFs for Water Harvesting from Air. *Mol. Front. J.* **2023,** *7* (1), 1-20.

(12) Akiyama, G.; Matsuda, R.; Sato, H.; Hori, A.; Takata, M.; Kitagawa, S., Effect of functional groups in MIL-101 on water sorption behavior. *Microporous Mesoporous Mater.* **2012,** *157*, 89-93.

(13) Solovyeva, M. V.; Shkatulov, A. I.; Gordeeva, L. G.; Fedorova, E. A.; Krieger, T. A.; Aristov, Y. I., Water vapor adsorption on CAU-10-X: Effect of functional groups on adsorption equilibrium and mechanisms. *Langmuir* **2021,** *37* (2), 693-702.

(14) Rieth, A. J.; Wright, A. M.; Skorupskii, G.; Mancuso, J. L.; Hendon, C. H.; Dincă, M., Record-setting sorbents for reversible water uptake by systematic anion exchanges in metal–organic frameworks. *J. Am. Chem. Soc.* **2019,** *141* (35), 13858-13866.

(15) Furukawa, H.; Gandara, F.; Zhang, Y.-B.; Jiang, J.; Queen, W. L.; Hudson, M. R.; Yaghi, O. M., Water adsorption in porous metal–organic frameworks and related materials. *J. Am. Chem. Soc.* **2014,** *136* (11), 4369-4381.

(16) Lin, H.; Yang, Y.; Hsu, Y. C.; Zhang, J.; Welton, C.; Afolabi, I.; Loo, M.; Zhou, H. C., Metal-Organic Frameworks for Water Harvesting and Concurrent Carbon Capture: A Review for Hygroscopic Materials. *Adv. Mater.* **2023**, 2209073.
(17) Cadiau, A.; Lee, J. S.; Damasceno Borges, D.; Fabry, P.; Devic, T.; Wharmby, M. T.; Martineau, C.; Foucher, D.; Taulelle, F.; Jun, C. H., Design of hydrophilic metal organic framework water adsorbents for heat reallocation. *Adv. Mater.* **2015,** *27* (32), 4775-4780.
(18) Silva, M.; Ribeiro, A.; Silva, C.; Nogueira, I.; Cho, K.-H.; Lee, U.; Faria, J.; Loureiro, J.; Chang, J.-S.; Rodrigues, A., MIL-160 (Al) MOF's potential in adsorptive water harvesting. *Adsorption* **2021,** *27* (2), 213-226.
(19) Zhou, X.; Lu, H.; Zhao, F.; Yu, G., Atmospheric water harvesting: a review of material and structural designs. *ACS Mater. Lett.* **2020,** *2* (7), 671-684.
(20) Xu, W.; Yaghi, O. M., Metal–organic frameworks for water harvesting from air, anywhere, anytime. *ACS Cent. Sci.* **2020,** *6* (8), 1348-1354.
(21) Deng, H.; Doonan, C. J.; Furukawa, H.; Ferreira, R. B.; Towne, J.; Knobler, C. B.; Wang, B.; Yaghi, O. M., Multiple functional groups of varying ratios in metal-organic frameworks. *Science* **2010,** *327* (5967), 846-850.
(22) Viciano-Chumillas, M.; Liu, X.; Leyva-Perez, A.; Armentano, D.; Ferrando-Soria, J.; Pardo, E., Mixed component metal-organic frameworks: Heterogeneity and complexity at the service of application performances. *Coord. Chem. Rev.* **2022,** *451*, 214273.
(23) Furukawa, H.; Müller, U.; Yaghi, O. M., "Heterogeneity within order" in metal–organic frameworks. *Angew. Chem. Int. Ed.* **2015,** *54* (11), 3417-3430.
(24) Hanikel, N.; Prévot, M. S.; Fathieh, F.; Kapustin, E. A.; Lyu, H.; Wang, H.; Diercks, N. J.; Glover, T. G.; Yaghi, O. M., Rapid cycling and exceptional yield in a metal-organic framework water harvester. *ACS Cent. Sci.* **2019,** *5* (10), 1699-1706.
(25) Micromeritics Instruments Corporation. Norcross, GA, USA. MicroActive: 2018.
(26) Kim, H.; Cho, H. J.; Narayanan, S.; Yang, S.; Furukawa, H.; Schiffres, S.; Li, X.; Zhang, Y.-B.; Jiang, J.; Yaghi, O. M., Characterization of adsorption enthalpy of novel water-stable zeolites and metal-organic frameworks. *Sci. Rep.* **2016,** *6* (1), 19097.
(27) Schlüsener, C.; Jordan, D. N.; Xhinovci, M.; Ntep, T. J. M. M.; Schmitz, A.; Giesen, B.; Janiak, C., Probing the limits of linker substitution in aluminum MOFs through water vapor sorption studies: mixed-MOFs instead of mixed-linker CAU-23 and MIL-160 materials. *Dalton Trans.* **2020,** *49* (22), 7373-7383.
(28) Groom, C. R.; Bruno, I. J.; Lightfoot, M. P.; Ward, S. C., The Cambridge structural database. *Acta. Crystallogr. B.* **2016,** *72* (2), 171-179.
(29) Bruno, I. J.; Cole, J. C.; Kessler, M.; Luo, J.; Motherwell, W. S.; Purkis, L. H.; Smith, B. R.; Taylor, R.; Cooper, R. I.; Harris, S. E., Retrieval of crystallographically-derived molecular geometry information. *J. Chem. Inf. Comput. Sci.* **2004,** *44* (6), 2133-2144.
(30) Tschense, C. B.; Reimer, N.; Hsu, C. W.; Reinsch, H.; Siegel, R.; Chen, W. J.; Lin, C. H.; Cadiau, A.; Serre, C.; Senker, J., New Group 13 MIL-53 Derivates based on 2, 5-Thiophenedicarboxylic Acid. *Z. Anorg. Allg. Chem.* **2017,** *643* (21), 1600-1608.
(31) Fathieh, F.; Kalmutzki, M. J.; Kapustin, E. A.; Waller, P. J.; Yang, J.; Yaghi, O. M., Practical water production from desert air. *Sci. Adv.* **2018,** *4* (6), eaat3198.

Chapter V

Linker Extension Strategy for Enhanced Water Capacity

5.1 Introduction

Water scarcity is a pressing global issue, affecting almost half the world's population.[1, 2] As the atmosphere offers a reservoir of clean water, there has been a surge in research to find and optimize materials capable of drawing this moisture from the air.[3] Ideal water-harvesting materials should efficiently absorb water, even from arid conditions, possess a step-like water isotherm, release water easily, demonstrate hydrothermal stability, and be eco-friendly.

Metal–organic frameworks (MOFs) stand out in this pursuit as they can be designed and modified to achieve desired properties.[4-6] A notable development was MOF-303,[7] which, thanks to its rod-like aluminum secondary building units (SBUs) and specific linkers, boasts a unique structure favorable for water molecule binding.[8, 9] However, enhancing water absorption without compromising favorable water-uptake attributes is challenging. Traditional methods to enhance pore volume in such MOFs often results in hydrophobic structures with less ideal properties.[10-12]

Paving a new path forward, this chapter introduces an innovative strategy centered on the reticular design of MOFs via linker expansion. The technique involves the addition of a single vinyl group to $PZDC^{2-}$ (Figure 5.1). This results in the discovery of MOF-LA2-1 (Al(OH)(PZVDC)), where $PZVDC^{2-}$ denotes (*E*)-5-(2-carboxylatovinyl)-1*H*-pyrazole-3-

Portions of this chapter have been adapted from:
Hanikel, N.; Kurandina, D.; Chheda, S.; Zheng, Z.; Rong, Z.; Neumann, S. E.; Sauer, J.; Siepmann, J. I.; Gagliardi, L.; Yaghi, O. M., MOF Linker Extension Strategy for Enhanced Atmospheric Water Harvesting. *ACS Cent. Sci.* **2023,** *9* (3), 551-557.
Zheng, Z.; Zhang, O.; Nguyen, H. L.; Rampal, N.; Alawadhi, A.; Rong, Z.; Head-Gordon, T.; Borgs, C.; Chayes, J. T.; Yaghi, O. M., ChatGPT Research Group for Optimizing Crystallinity of MOFs and COFs. *ACS Cent. Sci.* **2023,** *9* (11), 2161–2170.

carboxylate. Impressively, while maintaining structural congruence with MOF-303, MOF-LA2-1 boasts a 50% expansion in pore volume, reflecting in its heightened water uptake. Additionally, MOF-LA2-1 demands a reduced regeneration temperature and energy and showcases robust stability during water adsorption and desorption cycles.

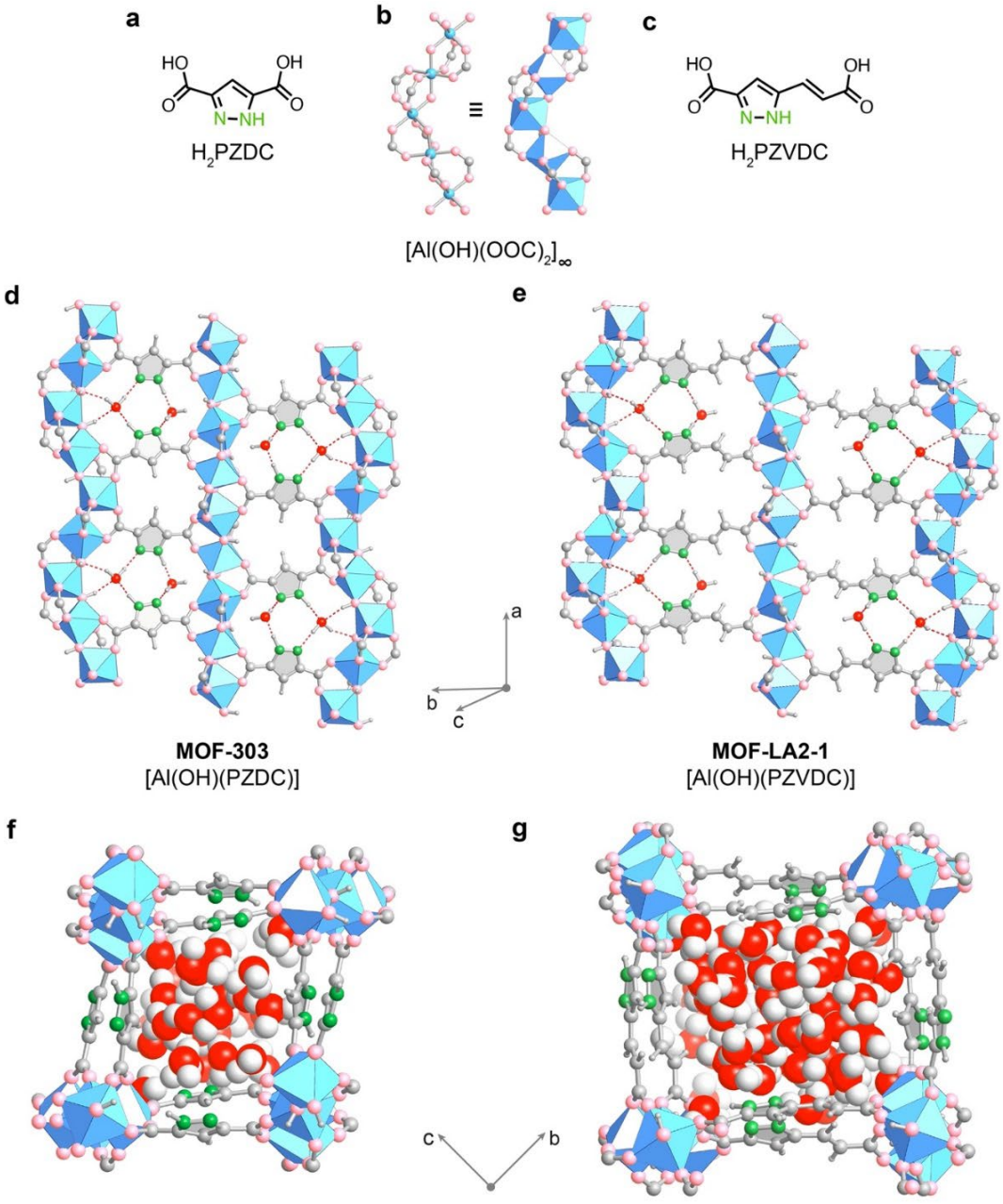

Figure 5.1 Comparison of the framework structures and water arrangement in MOF-303 (left) and MOF-LA2-1 (right). (a) The linker of MOF-303. (b) The SBUs of both MOFs. (c) The linker of MOF-LA2-1 (d,e) A cut-away view of the pores displaying the alignment of the linkers. (f,g) Snapshots of the water structures from Monte Carlo simulations at full water loading. Color code: Al, blue octahedron; C and H, gray; N, green; O in framework, pink; O in H_2O, red.

5.2 Experimental section

5.2.1 Starting materials and general procedures

All chemicals were purchased from commercial sources and used without prior purification. Ethyl 5-formyl-1*H*-pyrazole-3-carboxylate (**1**) was purchased from Enamine. *N*,*N*-dimethylformamide (DMF), methanol, acetone, hexane, tetrahydrofuran (THF) and methyl (triphenylphosphoranylidene)acetate (**2**) were purchased from Sigma-Aldrich. Ultrahigh-purity-grade (UHP-grade) N_2, He, and Ar (purity 99.999%), as well as ultra-zero-grade air were purchased from Praxair.

Liquid-state ^{1}H and ^{13}C NMR spectra were acquired on a Bruker NEO-500 (500 MHz). ^{1}H signals are referenced to residual $CHCl_3$ at 7.26 ppm or DMSO at 2.50 ppm. ^{13}C signals are referenced to $CDCl_3$ at 77.16 ppm or DMSO-d_6 at 39.52 ppm. Elemental analysis measurements were performed using a Perkin Elmer 2400 Series II CHNS elemental analyzer. PXRD analysis was conducted on a Bruker D8 Advance x-ray diffractometer equipped with a Cu anode and a Ni filter (CuKa radiation) in Bragg-Brentano geometry. A sample was mounted on zero-background holders and leveled with a spatula. The PXRD patterns were recorded between 3 and 50° with 2303 steps (~0.02° per step) with an acquisition time of 10 seconds per step, thus resulting in ~6.5 hours analysis time. The MOF-LA2-1 obtained via green synthesis was measured by Rigaku MiniFlex 6G equipped with a HyPix-400MF Hybrid Pixel Array detector and a normal focus X-ray tube with a Cu-source (λ = 1.54178 Å). The zero-background holder is made of single crystal Si cut on a 310 axis. The PXRD patterns were recorded between 2 and 50° with 4801 steps (~0.01° per step) with scan speed of 0.5° per minute, thus resulting in~1.5 hours analysis time per measurement.

Single-crystal X-ray diffraction (SCXRD) measurements were conducted at the beamline 12.2.1 at the Advanced Light Source (Lawrence Berkeley National Laboratory, USA) using a radiation wavelength of λ = 0.7288 Å. The beamline was equipped with a PHOTON-II CMOS detector operating in shutterless mode and a Si(111) monochromator. For the measurement, the crystal was mounted on a Kapton® MiTeGen MicroMount™ in a minimal amount of Paratone® N oil and submerged in a cold gas stream generated by an Oxford Cryosystems 800 Series Cryostream. Raw data processing was carried out with the APEX software package.[13] The data were integrated by using SAINT[14] and corrected for absorption with SADABS[15]. The structural solutions were determined by using intrinsic phasing (SHELXT)[16] and refined by the principle of least squares (SHELXL)[17]. Both solution and refinement were conducted by using the Olex2 software package.[6]

Scanning electron microscopy (SEM) images were obtained on a Hitachi S-5000 high resolution, cold field emission SEM with accelerating voltages of 5.0 to 10.0 kV. The samples were dispersed on conductive carbon tape, mounted on stubs, and sputter coated (Pd/Au) with a Tousimis sputter coater on top of a Bio-Rad E5400 controller.

The TGA curves were recorded on a Netzsch Jupiter, STA 449 F5 apparatus. Prior to the measurement, the samples were dried by heating to 150 °C at a rate of 1 °C min^{-1}. The measurement was then initiated after the temperature in the TGA oven decreased to 40 °C. For the TGA measurement, the temperature was ramped from 40 to 800 °C at a heating rate of 1 °C min^{-1}. During the experiment, UHP-grade Ar at a flow rate of 60 mL min^{-1} was used for the balance purge flow; and UHP-grade Ar (inert conditions) or ultra-zero-grade air (oxidative conditions) at a flow rate of 60 mL min^{-1} was used for the sample purge flow. Low-pressure nitrogen sorption measurements were carried out on a Micromeritics ASAP 2420 surface area analyzer. The N_2 isotherms were measured using a liquid nitrogen bath (77 K). UHP-grade He was used for free space corrections.

Water vapor sorption experiments were carried out on a BEL Japan BELSORP-aqua[3]. Prior to the measurements, the vapor source was degassed through five cycles freeze-pump-thaw. The measurement temperature was maintained in a water bath equipped with a thermostatic circulator. UHP-grade He was used for free space corrections. The isobar measurements as well as the uptake and release cycling experiments were conducted with a TA Instruments DSC SDT Q600 Thermogravimetric Analyzer & Differential Scanning Calorimeter. The temperature and relative humidity (RH) were monitored using high-accuracy thermocouples and humidity sensors downstream of the TGA chamber. To adjust the RH in the TGA, a dry and a humidified N_2 feed were connected to the primary and secondary TGA inlet, respectively, and their flow rate ratio was varied according to a pre-recorded calibration curve, while maintaining the overall sum of both flow rates constant at 200 mL min^{-1}. UHP-grade N_2 was utilized as the dry N_2 feed. To generate the humidified N_2 feed, UHP-grade N_2, regulated by the Sierra SmartTrak® 100 mass flow controller, was passed through a H_2O-filled 2-L gas washing bottle, which was refilled frequently to ensure steady humidification.

5.2.2 Synthesis of MOF linker

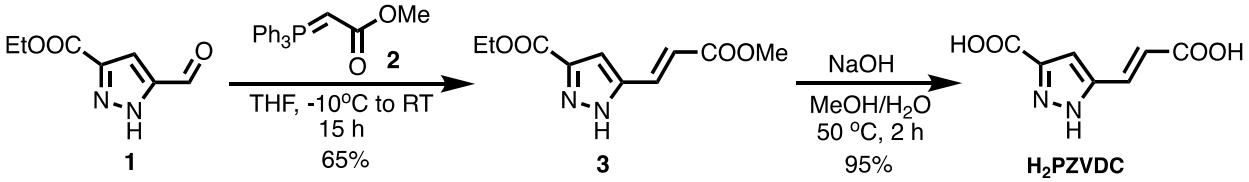

Step 1: A 100-mL round-bottom flask equipped with a stirring bar was charged with **1** (1.5 g, 8.9 mmol, 1 equiv.) and dry THF (50 mL) under argon atmosphere. The mixture was cooled down to –10 °C using acetone/ice bath, and **2** (3.5 g, 10.5 mmol, 1.2 equiv.) was added portion-wise. The reaction was allowed to warm up to room temperature overnight. After concentrating the resulting solution under reduced pressure, a mixture containing *E* and *Z*-isomers was identified via ^{1}H NMR analysis. The desired *E*-isomer **3** was isolated via column chromatography using acetone/hexane (5/1) as eluent (R_f = 0.1). Yield: 1.3 g, 65%. ^{1}H NMR (400 MHz, $CDCl_3$) δ 10.93 (s, 1H), 7.67 (d, J = 16.0 Hz, 1H), 7.04 (s, 1H), 6.48 (d, J = 16.0 Hz, 1H), 4.41 (q, J = 7.1 Hz, 2H), 3.81 (s, 3H), 1.41 (t, J = 7.1 Hz, 3H) ppm.

Step 2: A 100-mL round-bottom flask equipped with a stirring bar was charged with **3** (1.3 g, 5.8 mmol, 1 equiv.), MeOH (50 mL) and aqueous NaOH solution (20 mL, 1.5 M, 5 equiv.). The reaction was heated at 50 °C (oil bath temperature) until the starting material was consumed, as monitored by TLC (2 h). The solution was concentrated under reduced pressure and 5 M HCl was added dropwise until pH = 2-3. The resulting precipitate was filtered off and thoroughly washed with H_2O (4 × 10 mL) and MeOH (1 × 5 mL). After drying at 50 °C in vacuo, the linker H_2PZVDC was obtained as white powder. Yield: 1.0 g, 95%. ^{1}H NMR (500 MHz, DMSO-d_6) δ 13.80–13.10 (br. s, 3H), 7.46 (d, J = 16.2 Hz, 1H), 7.17 (s, 1H), 6.53 (d, J = 16.1 Hz, 1H). ^{13}C NMR (126 MHz, DMSO-d_6) ppm. δ 167.4, 161.4, 120.6, 108.4 ppm. HRMS (m/z): $[M-H]^-$ calcd. for $C_7H_5N_2O_4$, 181.0255; found, 181.0255.

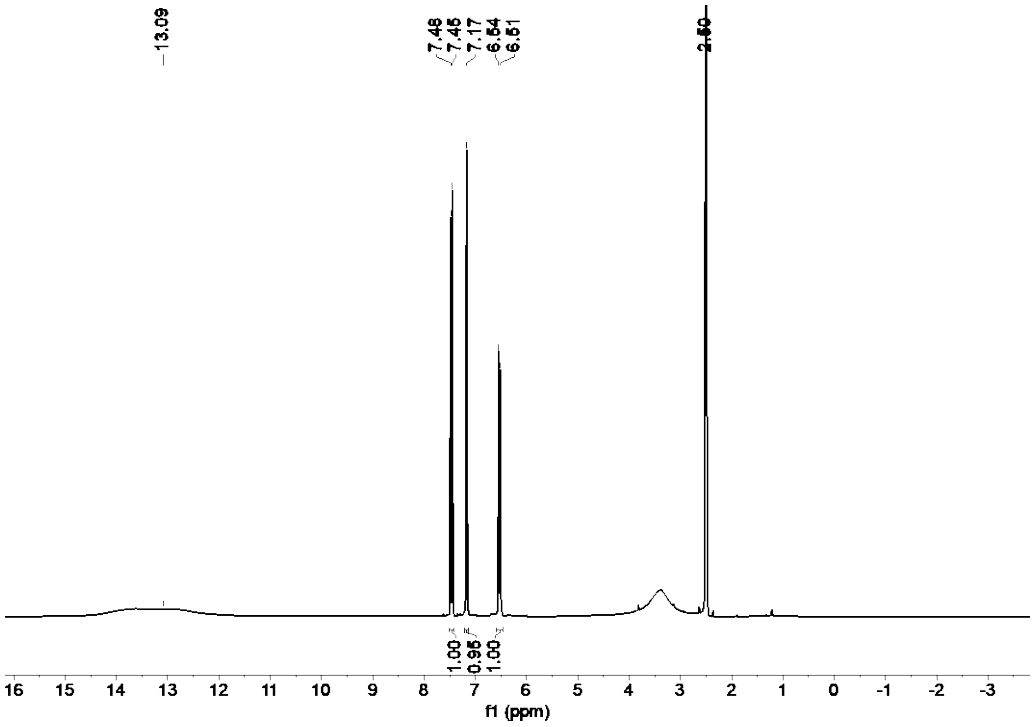

Figure 5.2 ^{1}H NMR spectrum of H_2PZVDC (500 MHz, DMSO-d_6).

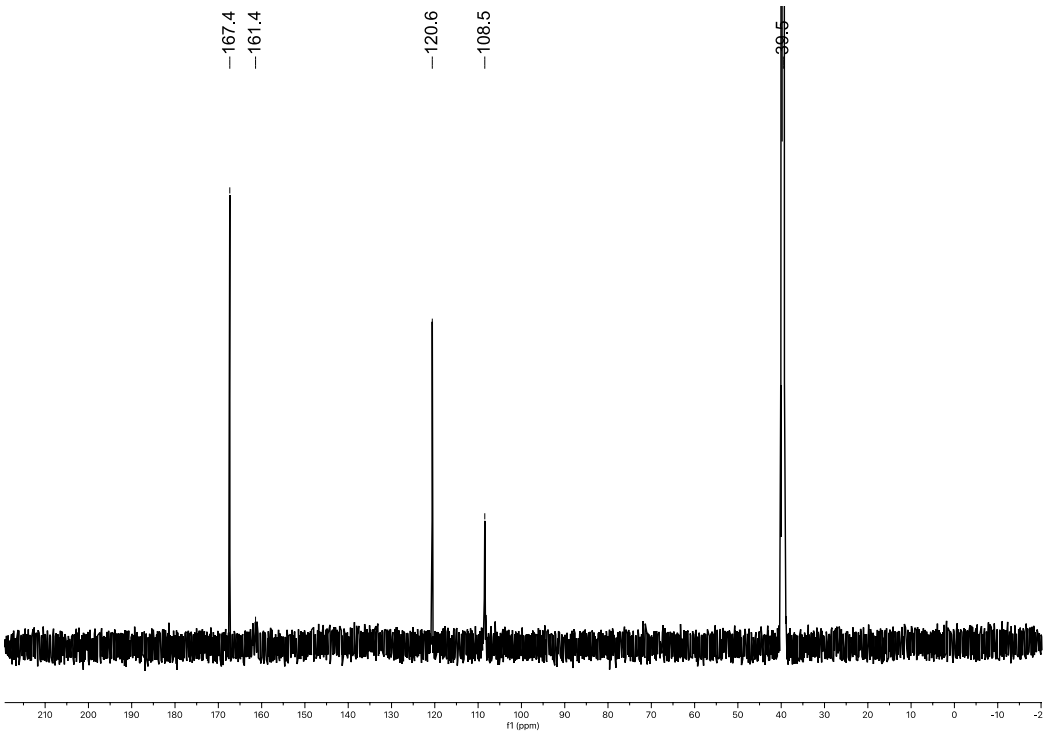

Figure 5.3 ^{13}C NMR spectrum of H_2PZVDC (126 MHz, DMSO-d_6).

5.2.3 Synthesis of MOF-LA2-1

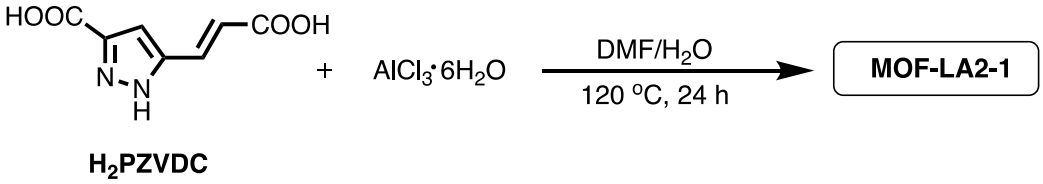

H_2PZVDC

Solvothermal synthesis. In a 4-mL scintillation vial, linker H_2PZVDC (91.0 mg, 0.5 mmol, 1 equiv.) was dissolved in *N*,*N*-dimethylformamide (DMF) (0.6 mL) upon sonication. An aqueous solution of $AlCl_3 \cdot 6H_2O$ (2.4 mL, 0.2 M, 1 equiv.) was added dropwise, and the resulting mixture was heated in a 120 °C oven for 24 h. After cooling down to room temperature, the white precipitate was collected by centrifuging and washed with H_2O (3 × 30 mL) and MeOH (3 × 30 mL). MOF-LA2-1 was activated under dynamic vacuum (~10^{-3} mbar) for 12 h at room temperature, followed by gradual heating to 120 °C for 6.5 hours. Yield: 65.0 mg, 58%. Elem. Anal. of MOF-LA2-1: Calcd. for $C_{56}H_{40}N_{16}O_{40}Al_8$: C, 37.52; H, 2.25; N, 12.50%. Found: C, 36.78; H, 2.38; N, 11.95%.

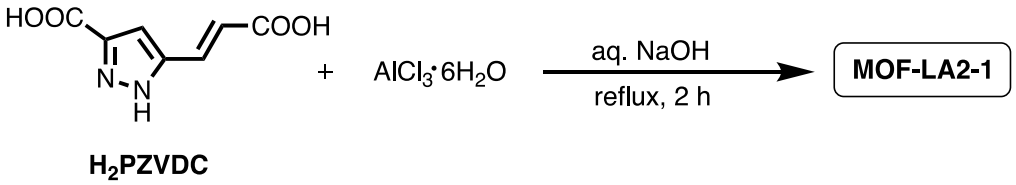

H_2PZVDC

Green synthesis. In a 50-mL round-bottom flask, linker H_2PZVDC (364 mg, 2 mmol, 1 equiv.) and NaOH (160 mg, 4 mmol, 2 equiv.) were dissolved in deionized water (10 mL) upon sonication. An aqueous solution of $AlCl_3 \cdot 6H_2O$ (6 mL, 0.33 M, 1 equiv.) was added dropwise for 10 minutes, and the reaction mixture was heated to 120 °C and refluxed for 2 hours. After cooling down to room temperature, the white powder was collected by centrifuging and washed with deionized water (2 × 10 mL) and EtOH (3 × 10 mL). The white powder was dried under air overnight, followed by activation under dynamic vacuum (~10^{-3} mbar) for 12 hours at 120 °C. Yield: 301 mg, 66%. Elem. Anal. of MOF-LA2-1: Calcd. for $C_{56}H_{40}N_{16}O_{40}Al_8$: C, 37.52; H, 2.25; N, 12.50%. Found: C, 37.29; H, 2.43; N, 12.10%.

5.2.4 Scanning electron microscopy

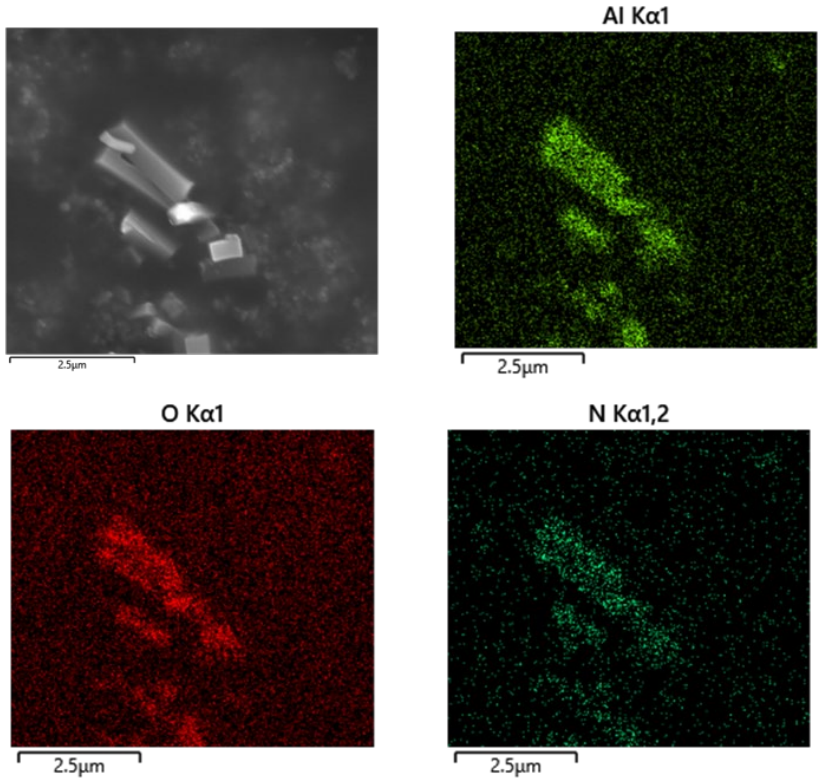

Figure 5.4 Scanning electron microscopy coupled with energy dispersive X-ray spectroscopy capturing a representative fraction of the bulk material of MOF-LA2-1.

5.2.5 Single-crystal x-ray diffraction analysis

Single crystals of MOF-LA2-1 were synthesized in a 4-mL scintillation vial. Initially, the linker H_2PZVDC (13.7 mg, 0.075 mmol, 1 equiv.) was dissolved in a solution containing 1.500 mL of ethanol and 1.388 mL of $_H$2O. Subsequent to this, aqueous solutions of $Al_2(SO_4)_3$ (75 µL, 0.5 M, 1 equiv.) and urea (37.5 µL, 2 M, 1 equiv.) were added drop by drop. The transparent mixture thus formed was then heated at 85°C for 7 days, producing single crystals measuring around 10 × 10 × 30 μm^3 (Figure 5.5a).

These crystals were subjected to synchrotron single-crystal X-ray diffraction (SCXRD) analysis (see Section 5.2.1 for more details). he SCXRD data provided information on the unit cell parameters, where a = 12.030(12) Å, b = 17.398(17) Å, c = 17.706(17) Å, and β = 99.33(2)°, as well as insights into the SBU stereochemistry (Figure 5.5b). It is hypothesized that the significant intrinsic positional disorder of the asymmetric linker within the crystal structure led to a relatively low crystallinity in these crystals. This limitation impacted the SCXRD data quality and hindered the determination of the precise linker configuration in MOF-LA2-1.

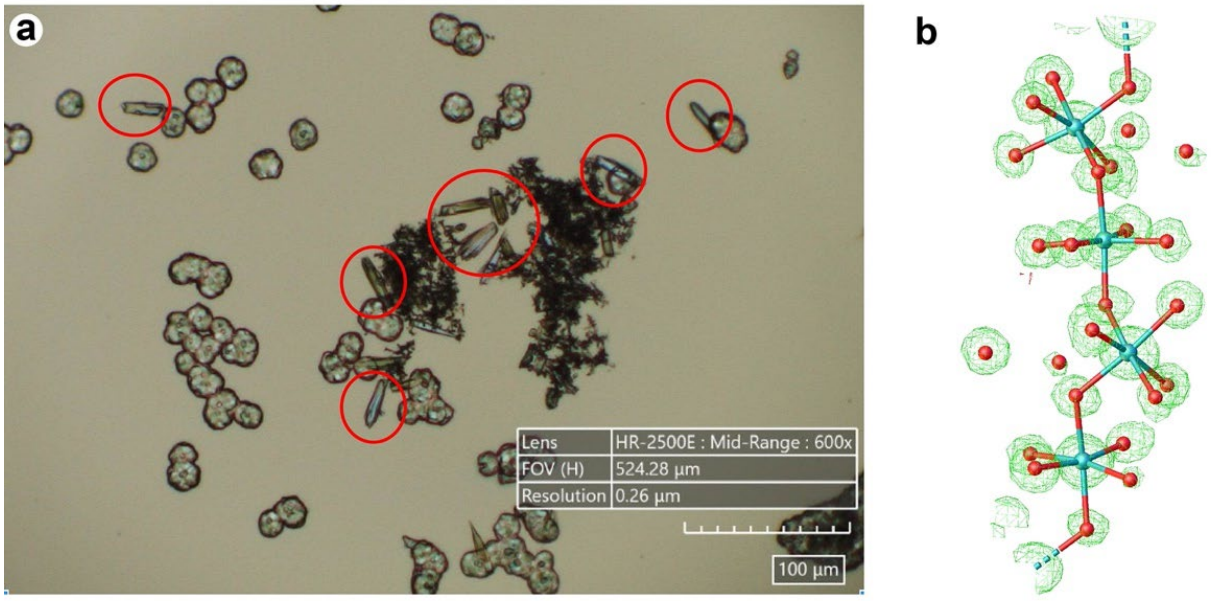

Figure 5.5 Single-crystal X-ray diffraction (SCXRD) analysis of MOF-LA2-1. (a) Microscope image of the sample that was subjected to SCXRD analysis. MOF-LA2-1 single crystals are circled in red. (b) Electron density map obtained from SCXRD analysis and the associated atom assignment. This showcases an SBU featuring alternating *cis–trans*-corner-shared AlO_6 octahedra and H_2O molecules H-bonded to it. Al, blue; O, red.

5.2.6 Powder x-ray diffraction analysis

MOF-LA2-1 was modeled in the space group $P2_1/c$ (No. 14). Utilizing the BIOVIA Materials Studio 2020 software, a Pawley refinement was performed on the experimental powder X-ray diffraction (PXRD) data for MOF-LA2-1. This yielded the unit cell parameters as follows: a = 12.1 Å, b = 17.3 Å, c = 17.8 Å, and b = 98.6°. he refinement achieved commendable agreement factors, with R_p = 6.01%, and R_{wp} = 3.47%.

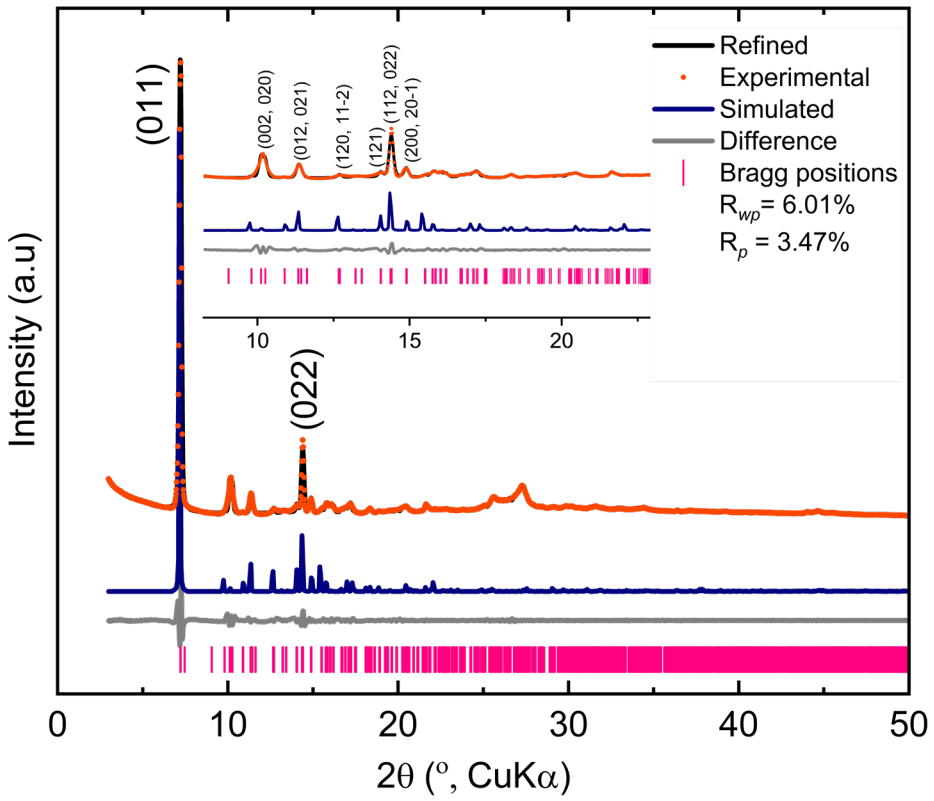

Figure 5.6 Pawley refinement of MOF-LA2-1 against the experimental PXRD pattern obtained from the sample prepared by solvothermal synthesis. Major peaks are indexed.

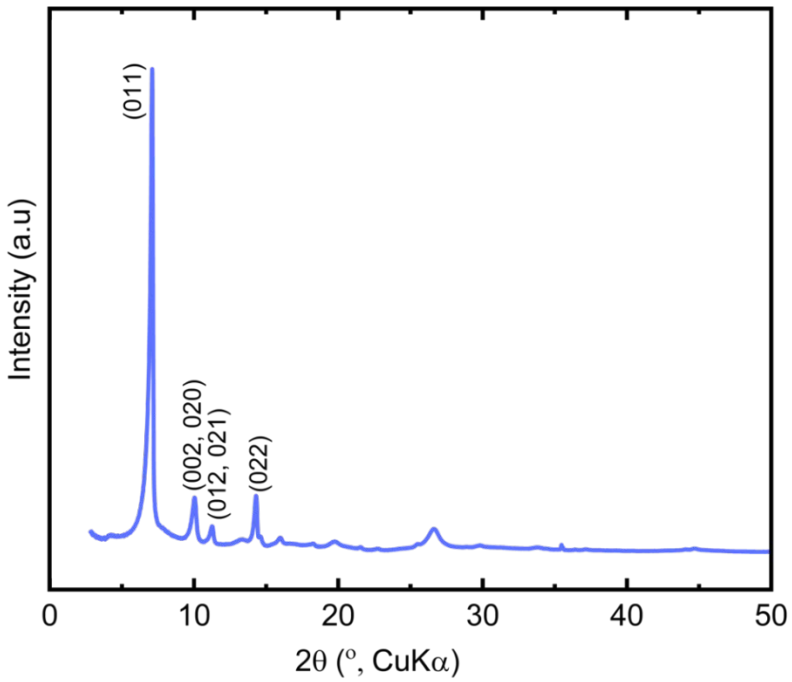

Figure 5.7 Powder X-ray diffraction pattern of MOF-LA2-1 prepared via green synthesis.

5.2.7 Thermogravimetric analysis

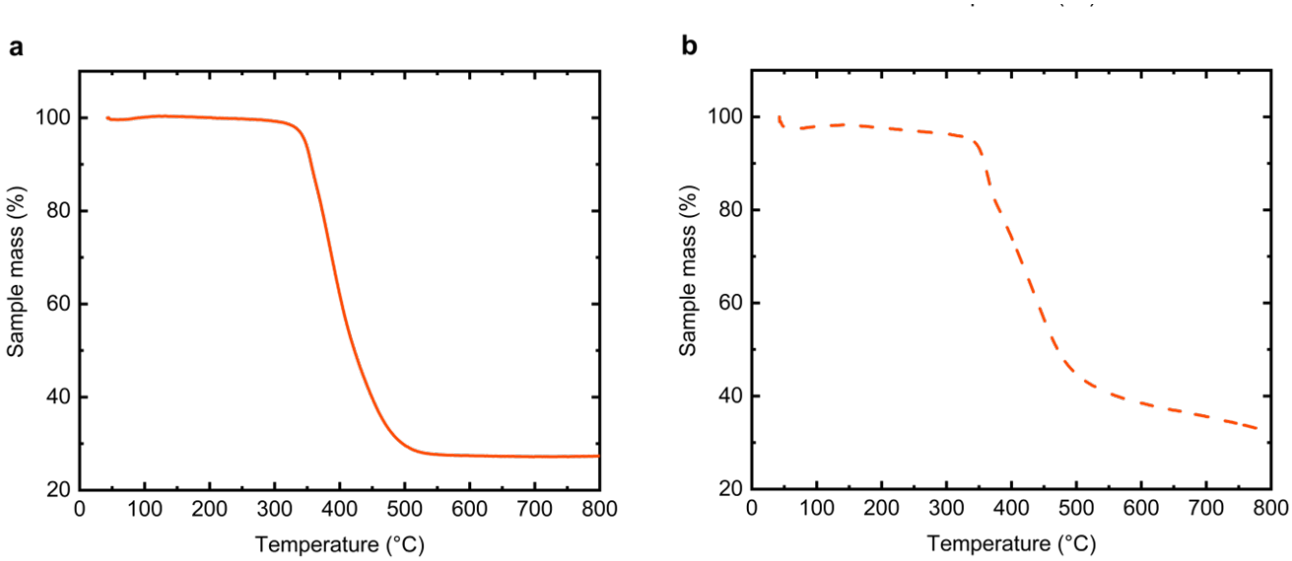

Figure 5.8 TGA curves of MOF-LA2-1 conducted under (a) air and (b) argon atmosphere.

5.2.8 Nitrogen sorption analysis

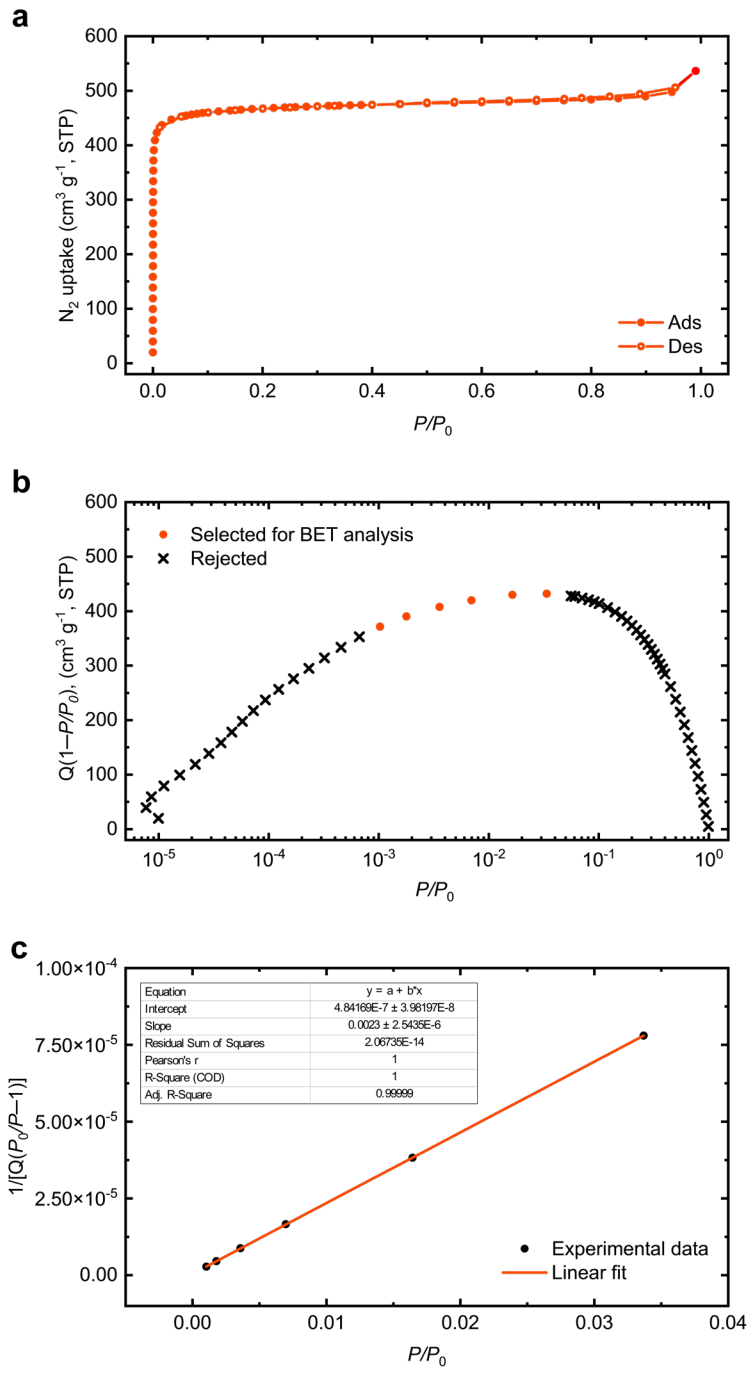

Figure 5.9 Nitrogen sorption analysis of MOF-LA2-1 prepared via solvothermal synthesis: (a) N_2 sorption isotherm at 77 K. (b) Rouquerol plot for determination of the appropriate pressure range for BET analysis. (c) BET plot yielding a BET surface area of 1892±2 m^2 g^{-1}. *P*, nitrogen pressure; P_0 = 1 atm; STP, standard temperature and pressure.

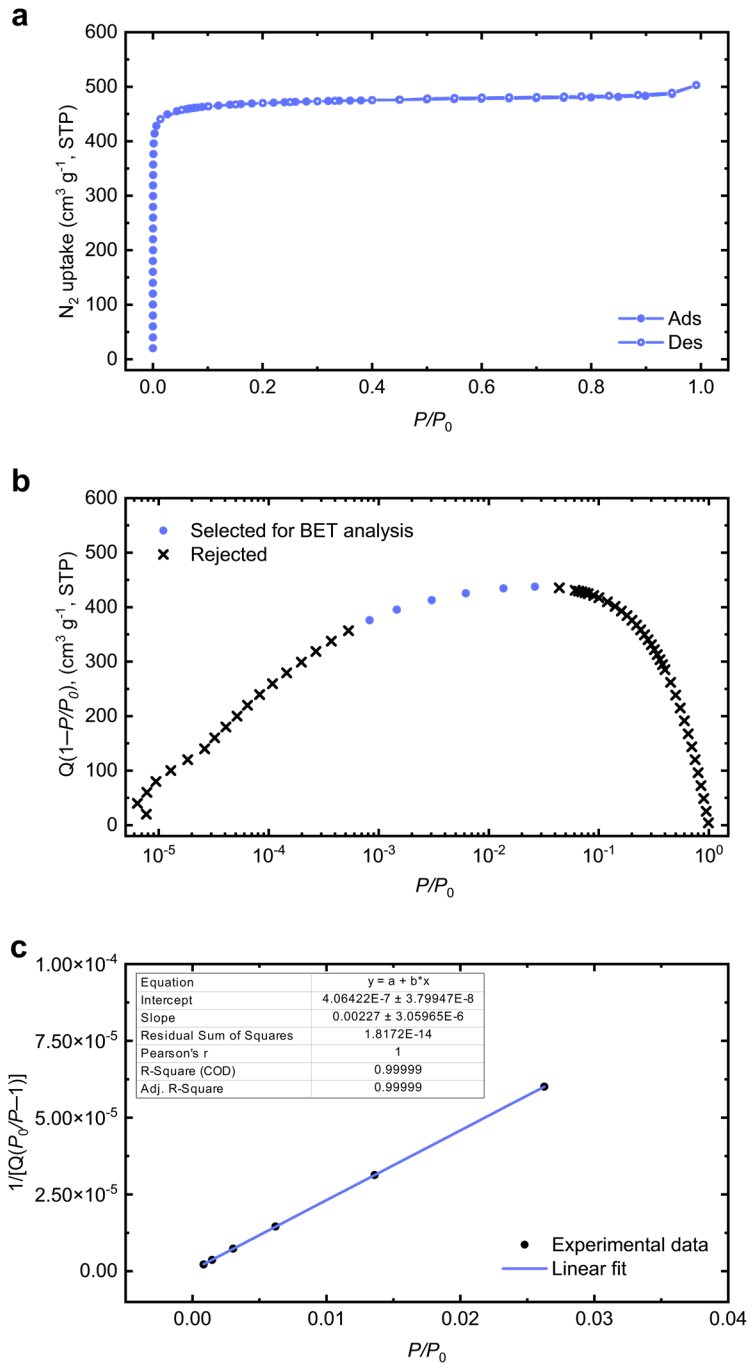

Figure 5.10 Nitrogen sorption analysis of MOF-LA2-1 prepared via green synthesis: (a) N_2 sorption isotherm at 77 K. (b) Rouquerol plot for determination of the appropriate pressure range for BET analysis. (c) BET plot yielding a BET surface area of 1916±2 m^2 g^{-1}. *P*, nitrogen pressure; P_0 = 1 atm; STP, standard temperature and pressure.

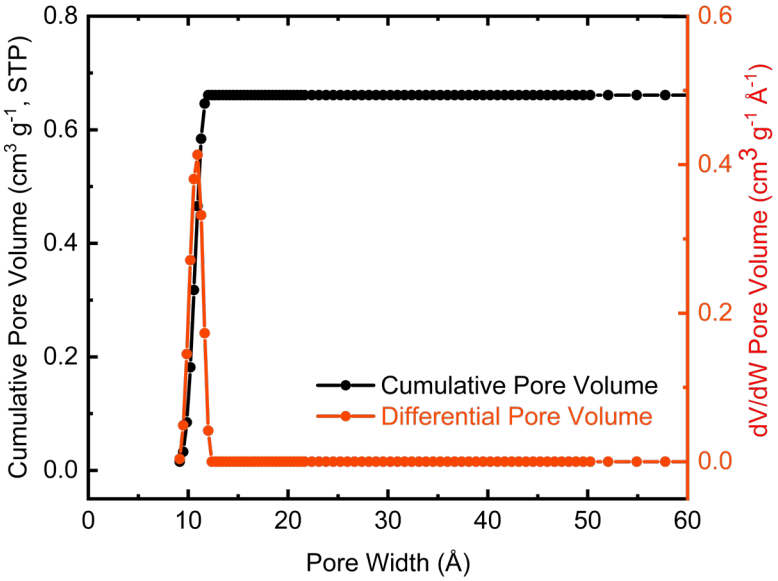

Figure 5.11 Pore size distribution of MOF-LA2-1 derived from the N_2 sorption isotherm measured at 77 K. Density functional theory for oxide surfaces with cylindrical pores was applied to yield a pore width of 10.9 Å and a cumulative pore volume of 0.67 cm^3 g^{-1}.

5.2.7 Water sorption analysis

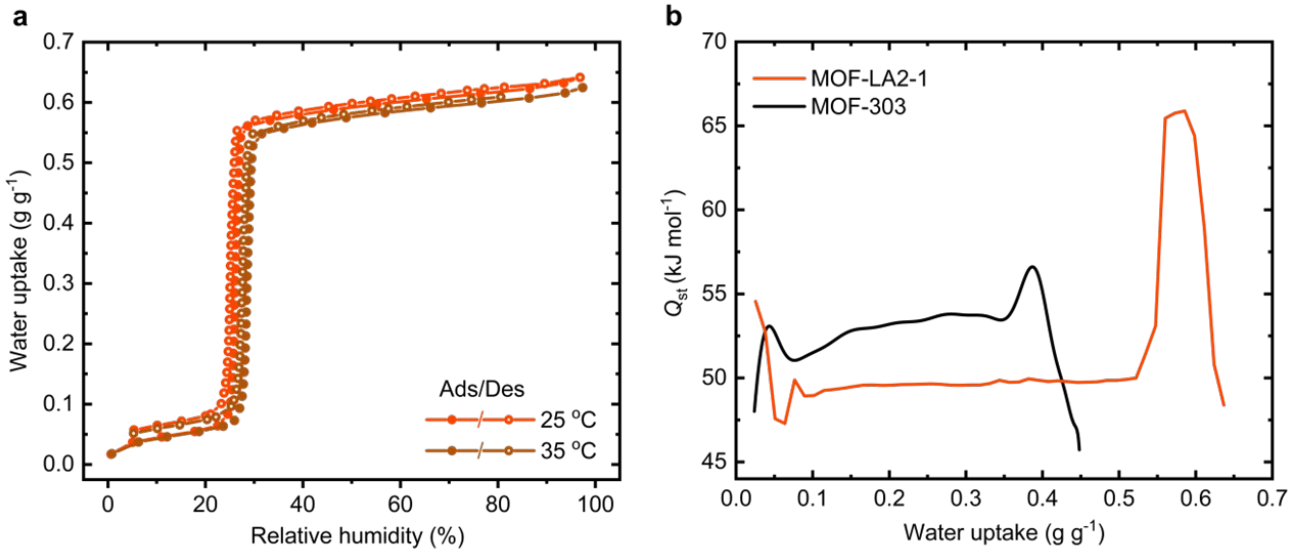

Figure 5.12 Water sorption analysis of MOF-LA2-1 prepared via solvothermal synthesis: (a) Water sorption isotherms of MOF-LA2-1 at 25 and 35 °C. (b) Heat of adsorption Q_{st} in dependence of water loading estimated with the Clausius–Clapeyron equation.

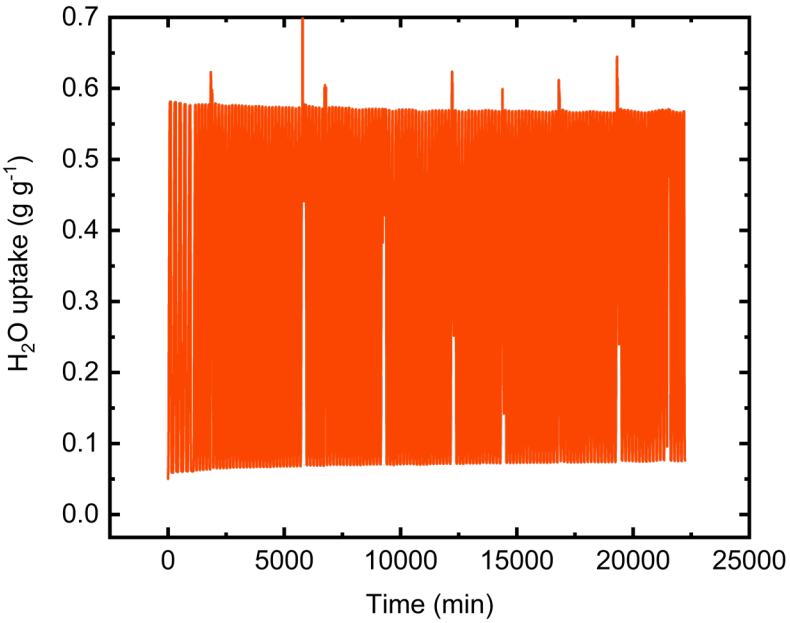

Figure 5.13 150 water vapor adsorption–desorption cycles conducted on MOF-LA2-1 at a water vapor pressure of 1.70 kPa and initiated through temperature swing adsorption between 30 and 45 °C. The time per cycle was ~150 min.

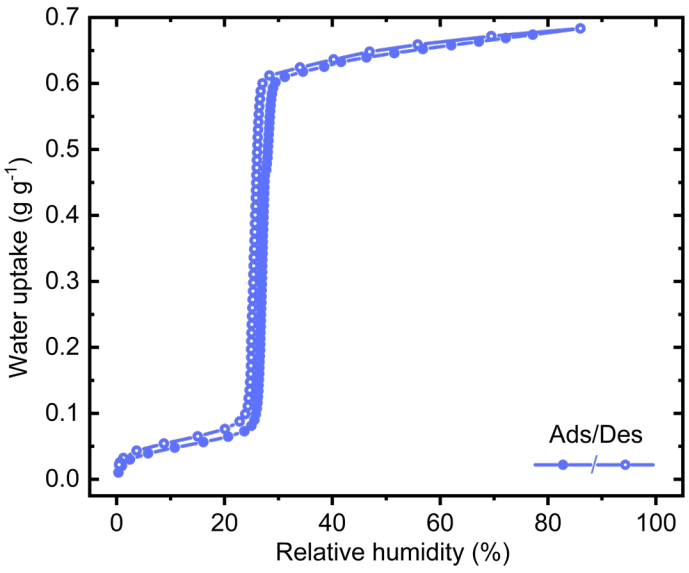

Figure 5.14 Water sorption analysis of MOF-LA2-1 at 25 °C prepared via water-based reflux synthesis.

5.3 Structural analysis

At the outset of this study, it was hypothesized that adding a compact, yet long group to the hydrophilic H_2PZDC linker used in MOF-303 would enhance its water uptake capacity, leveraging its hydrophilic nature and exceptional stability (Figure 5.1c). The goal was to keep the configuration of pyrazole functionalities intact, as they play a pivotal role as primary adsorption sites and underpin its water-harvesting attributes (Figure 5.1d).[9] The compatibility of a vinyl-appended variant with the MOF-303 topology was evaluated through density functional theory (DFT) calculations. These calculations suggested an increase in pore volume with this variant (Section 5.2.3). As a result, the linker H_2PZVDC, which features a vinyl group extension of H2PZDC, was synthesized using a two-step procedure that employed a Wittig reaction on ethyl 5-formyl-1*H*-pyrazole-3-carboxylate, followed by hydrolysis (Section 5.2.2). MOF-LA2-1 was synthesized using $AlCl_3 \cdot 6H_2O$ and H_2PZVDC by solvothermal synthesis in a DMF/H_2O (1:4) mixture at 120 °C and also through a green synthesis procedure in H_2O under reflux and stirring (Section 5.2.2).

Subsequent characterization of the resultant microcrystalline powder via powder x-ray diffraction (PXRD) analysis revealed a discernible 2θ shift of PXRD reflections to values lower than those of MOF-303. This indicated a successful extension of the parent framework (Figure 5.15a). Further validation of the phase purity of the sample was achieved through scanning electron microscopy combined with energy dispersive X-ray spectroscopy (Section 5.2.4). In an effort to acquire detailed structural information, single crystals of MOF-LA2-1, measuring 10 × 10 × 30 μm^3, were produced for single-crystal x-ray diffraction (SCXRD) analysis (Section 5.2.5). Although Synchrotron SCXRD data shed light on unit cell parameters and SBU stereochemistry, it is likely that the crystal structure's intrinsic positional disorder might have affected the overall data quality, rendering it challenging to pinpoint the exact linker configuration in MOF-LA2-1.

To circumvent this limitation, periodic DFT optimizations were employed. These provided insights into the relative stability of diverse linker configurations in MOF-LA2-1, based on parameters derived from SCXRD data (Section 5.2.3). Out of the 16 configurations evaluated, those with pyrazole functionalities on the same side of the pocket (represented as ZUS from the German "*zusammen*", meaning "together") were typically more stable than their counterparts with functionalities on opposing sides (represented as ENT from the German "*entgegen*", meaning "opposite"). The stability of the ZUS configuration can likely be attributed to hydrogen bonding between pyrazole functionalities. Notably, one particular ZUS structure (Figure 5.1e) stood out in terms of stability, making it the predominant configuration in MOF-LA2-1.

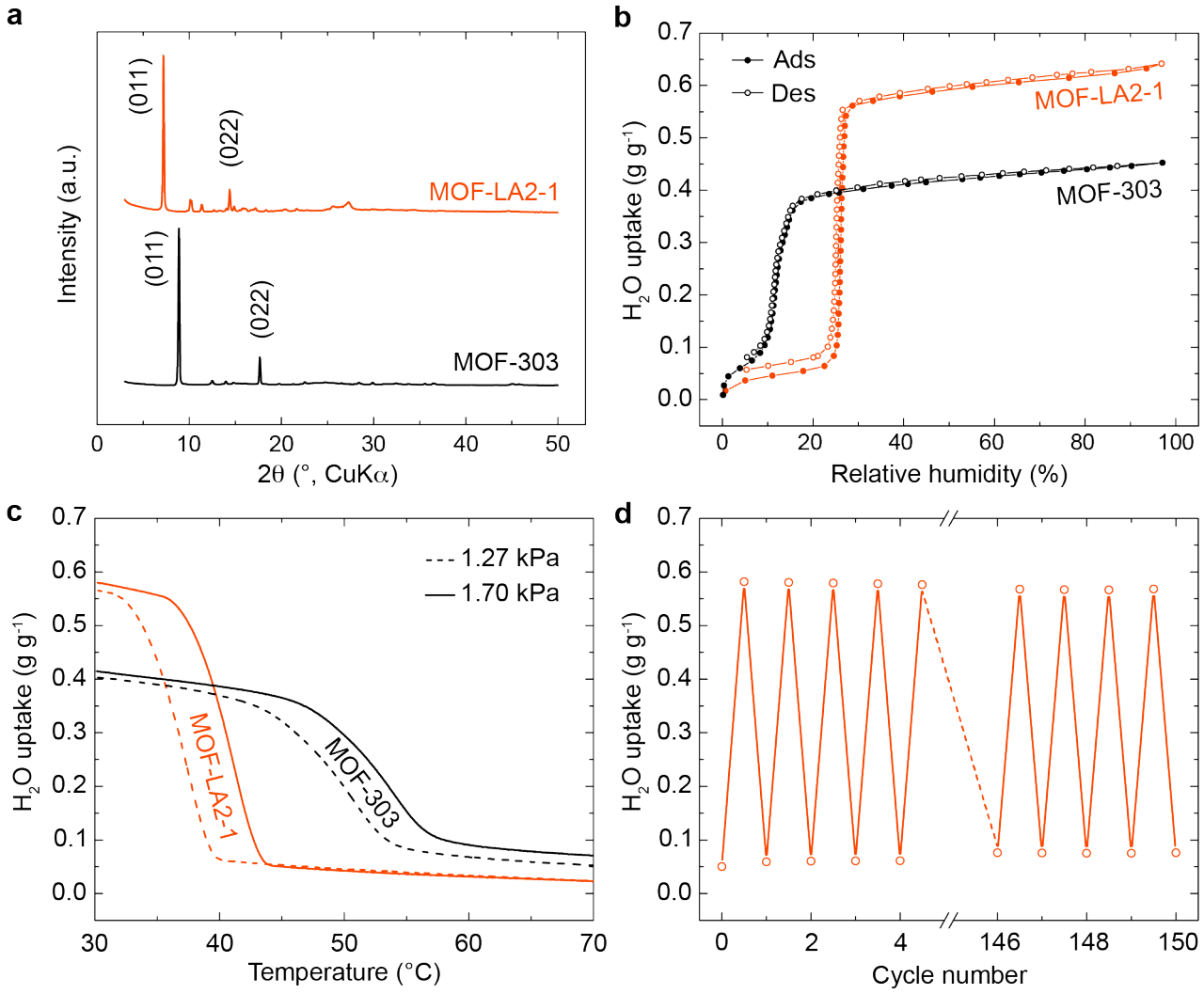

Figure 5.15 Experimental structural and water sorption analyses of MOF-LA2-1 in comparison with MOF-303. (a) Powder X-ray diffraction analysis using CuKα radiation. Major peaks are labeled based on their corresponding crystallographic lattice planes. (b) Water sorption isotherms measured at 25°C. Here, 'P' represents the water vapor pressure, while 'Psat' denotes the saturation water vapor pressure. (c) Water desorption isobars recorded at water vapor pressures of 1.27 and 1.70 kPa. Prior to the measurement, the materials were loaded at 30°C under the respective water vapor conditions. (d) Adsorption–desorption cycling, carried out at 1.70 kPa for 150 cycles, involved a temperature swing between 30 and 45°C.

The development of MOF-LA2-1 from MOF-303 incorporated a vinyl group into the H_2PZDC linker to boost its water uptake capabilities. This change was made while maintaining the configuration of pyrazole functionalities, which are essential for its water-harvesting attributes. Once the most stable framework configuration was determined, a computational examination of MOF-LA2-1's primary water adsorption sites was conducted, contrasting it with MOF-303 (Figure 5.1d and e). In MOF-LA2-1, water molecules attached themselves to sites similarly to MOF-303, specifically where linker pyrazole groups and μ_2-OH groups of the aluminum SBU are present. Following this, the next water molecule is anticipated to bind to the remaining μ_2-OH group of the aluminum SBU. Subsequent water molecules then occupy the pore, creating a hydrogen-bonded network, reminiscent of patterns in MOF-303 (Figure 5.1f and g). Considering the insights gained through DFT calculations, structural model of MOF-LA2-1 was refined in its most stable configuration (Figure 5.1e) against the experimental PXRD data (Section 5.2.6). The framework was modeled in the $P2_1/c$ space group (No. 14) and the final unit cell parameters refined to a = 12.1 Å, b = 17.4 Å, c = 17.8 Å, and β = 98.6°, with good agreement with the SCXRD data.

5.4 Characterization of MOF-LA2-1

The thermal stability and porosity of MOF-LA2-1 were probed using thermogravimetric analysis (TGA) and nitrogen sorption analysis. TGA, conducted under both argon and air atmospheres, showed no notable weight loss up to 300°C (Figure 5.8), demonstrating the necessary stability for thermal regeneration in water-harvesting processes. An initial nitrogen sorption isotherm analysis at 77 K for MOF-LA2-1 revealed a Brunauer-Emmett-Teller (BET) surface area of 1892 $m^2\ g^{-1}$ and a pore volume of 0.67 $cm^3\ g^{-1}$. Both these values are about 1.4 times that of MOF-303 (Section 5.2.8).

The water-harvesting capabilities of MOF-LA2-1 were evaluated through water sorption measurements at a constant temperature. The extended framework, akin to its precursor, showed a pre-step in its isotherm, likely tied to the hydrophilic pocket created by the pyrazole functionalities. This suggests the presence of strong water adsorption sites, as observed earlier in MOF-303.[9] Impressively, the water sorption isotherm profile of MOF-LA2-1 showcased a sharp rise at 26% RH, with a water uptake of 0.64 g g^{-1}, which is 50% greater than that of MOF-303 (Figure 2b). Although this occurs at slightly higher RH values compared to MOF-303, it remains effective for water extraction in the world's driest regions.[18, 19] Further, water sorption studies were carried out at varied temperatures and used the resulting data to determine the isosteric heat of water adsorption Q_{st} via the Clausius–Clapeyron equation (Figure 5.12). Our findings indicate that MOF-LA2-1 has an average Q_{st} value of 50 kJ mol^{-1}, a decrease of 4 kJ mol^{-1} from its precursor under similar conditions.25 Relative to the condensation heat of water (44 kJ mol^{-1} at 25°C), this represents a 40% reduction in the heat of adsorption compared to MOF-303. Crucially, the commendable water sorption characteristics of MOF-LA2-1 remained unchanged even when employing a green, reflux-based synthesis method (Figure 5.14).

Moving forward, the regeneration temperature of MOF-LA2-1 was investigated using

isobaric desorption curves. Tests at water vapor pressures of 1.27 and 1.70 kPa (equivalent to 30 and 40% RH at 30°C) revealed that MOF-LA2-1 has a lower water release temperature than MOF-303 (Figure 5.15c). This facilitates an optimal operational desorption temperature of 45°C. Given its lower isosteric heat of adsorption, these characteristics position MOF-LA2-1 as an energy-efficient material for water harvesting in arid areas.

The stability of MOF-LA2-1 under operational conditions was assessed using temperature swing adsorption–desorption cycling at 1.70 kPa water vapor pressure (Figure 5.15d). Results showed a decline in water uptake capacity of 5% after 75 cycles, followed by a further 1% reduction after another 75 cycles. This suggests a plateau in the capacity degradation, pointing to MOF-LA2-1's commendable longevity (Figure 5.13).

5.5 Water sorption behavior dependence on linker configurations

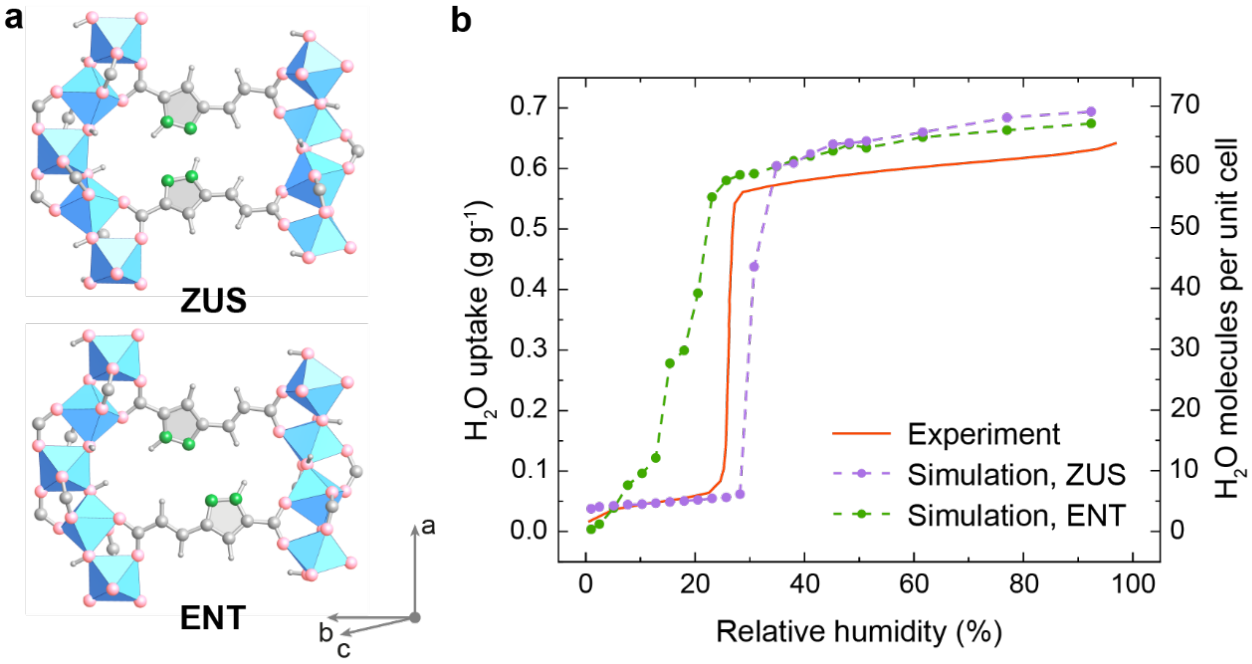

Figure 5.16 Water adsorption isotherms of MOF-LA2-1 with varied linker configurations. (a) The predominant ZUS and ENT linker configurations used in simulations. A coordinate system is provided for clarity. Al is shown as a blue octahedron; C and H are gray; N is green; O is pink. (b) Adsorption isotherms, calculated using force-field-based NpT-GEMC at 298 K, display both simulated (dashed lines) and experimental (solid lines) data.

Subsequently, The dependence of water adsorption behavior on various linker configurations of MOF-LA2-1 was investigated. Force-field-based Monte Carlo simulations in the Gibbs ensemble were employed to calculate water adsorption isotherms at 298 K. The focus

was on the ZUS and ENT configurations, deemed most stable and emblematic of the diverse structural groups. The water sorption isotherms, simulated for these structures, exhibited markedly different patterns (Figure 5.16). While the ZUS configuration aligned well with the observed adsorption isotherm, displaying an initial uptake of roughly five water molecules per unit cell with four asymmetric units at 5% RH and a pronounced isotherm rise at 30% RH, the ENT configuration showed a more nuanced isotherm. This subtler curve suggests a higher number of water adsorption sites with diverse binding strengths to the pore walls. When juxtaposed with the experimental water sorption isotherm, the ZUS configuration's isotherm aligns more closely with the observed data, reinforcing our structural model (Figure 5.1e)

5.6 Conclusions

In conclusion, this chapter presents a linker "arm" extension strategy, which significantly elevating the water-harvesting capabilities of the premier material, MOF-303. This strategic modification leads to a commendable 50% surge in the capacity to uptake water. Additionally, it optimizes energy efficiency, reducing operational demands—a significant advancement for sustainable applications. Notably, the modified MOF remains resilient and effective, capturing moisture even in the challenging environments of arid regions. It also boasts impressive hydrothermal stability, a key trait ensuring its durability and longevity through repeated uptake and release cycles. This innovative approach not only underscores the versatility of MOFs but also opens up avenues for further exploration and optimization. With its clear benefits, this methodology is set to profoundly influence both the advancement and commercialization of next generation aluminum-based MOFs, as well as the optimization of water sorption capabilities in MOFs.

5.7 Reference

(1) He, C.; Liu, Z.; Wu, J.; Pan, X.; Fang, Z.; Li, J.; Bryan, B. A., Future global urban water scarcity and potential solutions. *Nat. Commun.* **2021,** *12* (1), 1-11.

(2) Mekonnen, M. M.; Hoekstra, A. Y., Four billion people facing severe water scarcity. *Sci. Adv.* **2016,** *2* (2), e1500323.

(3) Wahlgren, R. V., Atmospheric water vapour processor designs for potable water production: a review. *Water Res.* **2001,** *35* (1), 1-22.

(4) Hanikel, N.; Prévot, M. S.; Yaghi, O. M., MOF water harvesters. *Nat. Nanotechnol.* **2020,** *15* (5), 348-355.

(5) Furukawa, H.; Cordova, K. E.; O'Keeffe, M.; Yaghi, O. M., The chemistry and applications of metal-organic frameworks. *Science* **2013,** *341* (6149), 1230444.

(6) Yaghi, O. M.; O'Keeffe, M.; Ockwig, N. W.; Chae, H. K.; Eddaoudi, M.; Kim, J., Reticular synthesis and the design of new materials. *Nature* **2003,** *423* (6941), 705-714.

(7) Fathieh, F.; Kalmutzki, M. J.; Kapustin, E. A.; Waller, P. J.; Yang, J.; Yaghi, O. M., Practical water production from desert air. *Sci. Adv.* **2018,** *4* (6), eaat3198.

(8) Kalmutzki, M. J.; Hanikel, N.; Yaghi, O. M., Secondary building units as the turning point in the development of the reticular chemistry of MOFs. *Sci. Adv.* **2018,** *4* (10), eaat9180.

(9) Hanikel, N.; Pei, X.; Chheda, S.; Lyu, H.; Jeong, W.; Sauer, J.; Gagliardi, L.; Yaghi, O. M., Evolution of water structures in metal-organic frameworks for improved atmospheric water harvesting. *Science* **2021,** *374* (6566), 454-459.
(10) Loiseau, T.; Mellot-Draznieks, C.; Muguerra, H.; Férey, G.; Haouas, M.; Taulelle, F., Hydrothermal synthesis and crystal structure of a new three-dimensional aluminum-organic framework MIL-69 with 2, 6-naphthalenedicarboxylate (ndc), Al (OH)(ndc)· H2O. *C. R. Chim.* **2005,** *8* (3-4), 765-772.
(11) Krüger, M.; Reinsch, H.; Inge, A. K.; Stock, N., Effect of partial linker fluorination and linker extension on structure and properties of the Al-MOF CAU-10. *Microporous Mesoporous Mater.* **2017,** *249*, 128-136.
(12) Küsgens, P.; Rose, M.; Senkovska, I.; Fröde, H.; Henschel, A.; Siegle, S.; Kaskel, S., Characterization of metal-organic frameworks by water adsorption. *Microporous Mesoporous Mater.* **2009,** *120* (3), 325-330.
(13) *APEX4*, Bruker AXS Inc.: 2021.
(14) *SAINT V8.40B* Bruker AXS Inc.: 2020.
(15) *SADABS*, Bruker AXS Inc.: 2016.
(16) Sheldrick, G. M., SHELXT–Integrated space-group and crystal-structure determination. *Acta Crystallogr. A.* **2015,** *71* (1), 3-8.
(17) Sheldrick, G. M., Crystal structure refinement with SHELXL. *Acta Crystallogr. C* . **2015,** *71* (1), 3-8.
(18) Brun, P.; Zimmermann, N. E.; Hari, C.; Pellissier, L.; Karger, D. N., Global climate-related predictors at kilometer resolution for the past and future. *Earth Syst. Sci. Data* **2022,** *14* (12), 5573-5603.
(19) Vicente-Serrano, S. M.; Nieto, R.; Gimeno, L.; Azorin-Molina, C.; Drumond, A.; El Kenawy, A.; Dominguez-Castro, F.; Tomas-Burguera, M.; Peña-Gallardo, M., Recent changes of relative humidity: Regional connections with land and ocean processes. *Earth Syst. Dyn.* **2018,** *9* (2), 915-937.

Chapter VI

ChatGPT-Assisted Water-Harvesting MOF Synthesis

6.1 Introduction

The burgeoning advancements in artificial intelligence (AI) promise to redefine the contours of chemistry and the daily operations of chemists in the lab.[1-5] Particularly, the advent of large language models (LLMs) coupled with advanced machine learning (ML) techniques is poised to offer chemists a powerful arsenal to tackle challenges in material discovery.[2, 6-17] Yet, a prominent challenge in the realm of material discovery, especially in the case of water harvesting MOFs, is the extensive time and labor-intensive trial-and-error process required to unearth and optimize synthesis conditions. This not only consumes a significant amount of resources but is also one of the primary hurdles that decelerate the development of more efficient metal-organic frameworks (MOFs) for atmospheric water harvesting (AWH).

In this chapter, I unveil a new protocol architecture that harnesses the prowess of LLMs, specifically ChatGPT built on the GPT-4 model[18]. This architecture knits together a cadre of seven unique AI research assistants, each of them honed for distinct and specific facets of the research continuum (Figure 6.1a).[18-25] The integration allow researchers to offload diverse responsibilities, ranging from literature analysis and code generation to hands-on lab activities and data interpretation. The objective is to bridge this chasm with strategies that tap into dynamic learning

---

Portions of this chapter have been adapted from:
Zheng, Z.; Zhang, O.; Borgs, C.; Chayes, J. T.; Yaghi, O. M., ChatGPT Chemistry Assistant for Text Mining and Prediction of MOF Synthesis. *J. Am. Chem. Soc.* **2023,** *145* (32), 18048–18062.
Zheng, Z.; Rong, Z.; Rampal, N.; Borgs, C.; Chayes, J. T.; Yaghi, O. M., A GPT-4 Reticular Chemist for Guiding MOF Discovery. *Angew. Chem. Int. Ed.* **2023**, e202311983.
Zheng, Z.; Zhang, O.; Nguyen, H. L.; Rampal, N.; Alawadhi, A.; Rong, Z.; Head-Gordon, T.; Borgs, C.; Chayes, J. T.; Yaghi, O. M., ChatGPT Research Group for Optimizing Crystallinity of MOFs and COFs. *ACS Cent. Sci.* **2023,** *9* (11), 2161–2170.

and self-tutoring capacities of AI, paving the way for holistic research automation.[26-28] In other words, the ultimate goal is to lay foundation to build up the self-driving lab, where AI agents can make progress on the lab activities with minimum or no human intervention. To showcase the efficacy of this approach, I employed it to optimize the synthesis of MOFs using Bayesian optimization[10, 29, 30] (BO) algorithms (Figure 6.1b). The AI, with zero prior awareness of ideal conditions, embarked on unveiling optimal, hitherto unknown, microwave-assisted eco-friendly synthesis routes.[31, 32]

The might of this multi-agent AI framework resides in its unique design, allowing it to (i) grasp human directives in everyday language, obviating the necessity for programming expertise, (ii) champion role-specific tasks, ensuring there's no ambiguity when a singular LLM juggles multiple tasks, and (iii) integrate a real-time, textual feedback loop, facilitating the AI's acclimation to shifting project nuances. Moreover, the embedded ML algorithms ensure that human bias and potential misinformation from LLM-driven assistants are mitigated. This strategy not only amplifies research prowess but also propels a paradigm shift in traditional research. It equips an individual researcher with the output capacity of an entire expert team, sketching a bright horizon for a future where humans and AI work in symbiotic tandem to fuel scientific exploration and innovation.

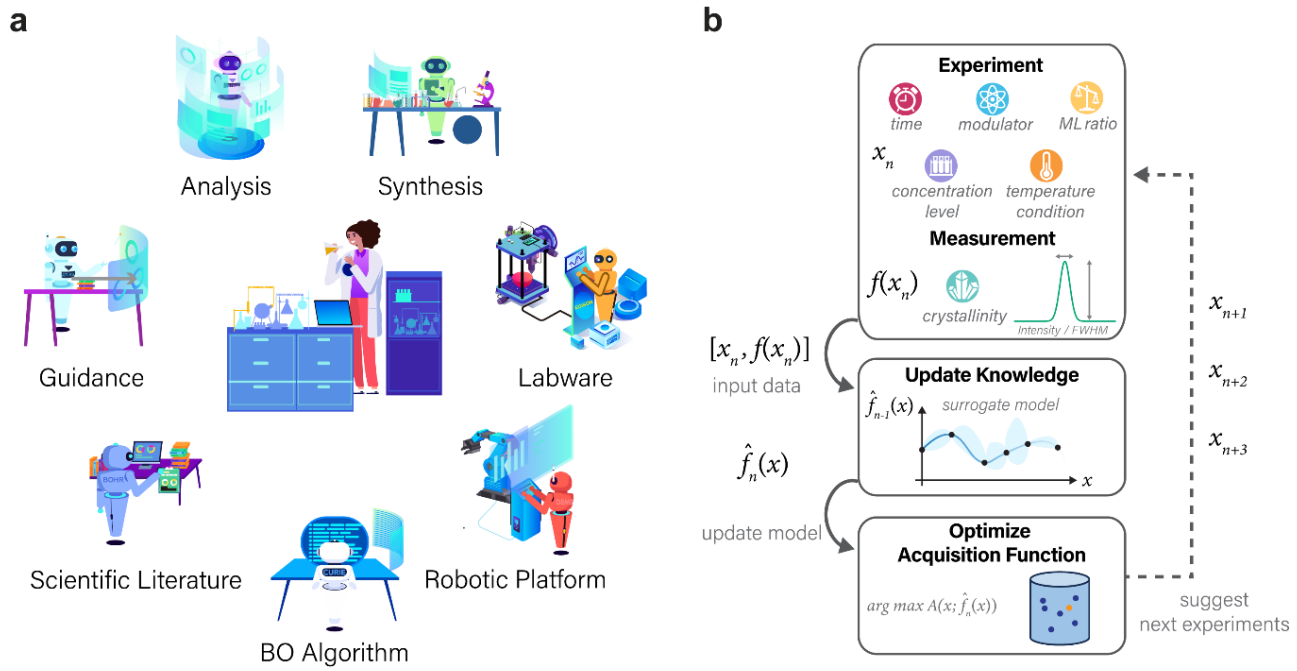

Figure 6.1 ChatGPT research group. (a) Assigned roles of seven ChatGPT-based assistants, each collaborating to assist human researchers and contributing to diverse research tasks at different stages of the synthesis optimization. (b) Flowchart outlining the closed-loop Bayesian optimization process. Each iteration involves three proposed experiments, their execution, data analysis, and integration of the new data into the existing dataset to update the surrogate model, upon which the acquisition function is optimized to suggest the next three experiments.

6.2 Experimental section

6.2.1 Starting materials and general procedures

Ethyl 5-formyl-1*H*-pyrazole-3-carboxylate (purity ≥ 95%) and methyl 5-formylthiophene-3-carboxylate (purity ≥ 95%) were purchased from Enamine Ltd. Aluminum chloride hexahydrate ($AlCl_3 \cdot 6H_2O$, purity ≥ 99%), (carbethoxymethylene)triphenylphosphorane (purity ≥ 97%), and sodium hydroxide (NaOH, purity ≥ 97%) were purchased from AK Scientific Inc. Tetrahydrofuran (THF, purity ≥ 99.9%), methanol (MeOH, purity ≥ 99.8%) and ethanol (EtOH, purity ≥ 99.8%) were purchased from Sigma Aldrich. Deuterated solvents were obtained from Cambridge Isotope Laboratories. Ultrahigh-purity (UHP) grade (99.999%) argon, nitrogen and helium, as well as ultra-zero grade air were obtained from Praxair. All chemicals were used without further purification.

Powder x-ray diffraction (PXRD) analyses were conducted on a Bruker D8 Advance X-ray diffractometer equipped with a Cu anode and a Ni filter (Cu Ka radiation) in Bragg-Brentano geometry or a Rigaku Miniflex 600 diffractometer (Bragg-Brentano geometry, Cu Kα radiation λ = 1.54056 Å). For PXRD measurements, the crystalline, powderous samples were mounted on zero-background holders and leveled with a spatula. For nuclear magnetic resonance (NMR) spectroscopy of the linker, liquid-state ^{1}H and ^{13}C NMR spectra were acquired on Bruker NEO-500 MHz spectrometers at the NMR facility of the College of Chemistry, University of California, Berkeley. ^{1}H signals are referenced to residual DMSO at 2.50 ppm. ^{13}C signals are referenced to DMSO-d_6 at 39.52 ppm.

Elemental analysis (EA) measurements were performed using a Perkin Elmer 2400 Series II CHNS elemental analyzer at the Microanalytical Laboratory of the College of Chemistry, University of California, Berkeley. Prior to EA of the MOF compounds, each sample was thoroughly washed with H_2O and methanol. Then, it was fully activated under dynamic vacuum (~10^{-3} mbar) through ramping the temperature to 120 °C over a period of 6 hours. After activation and until the measurement, the compounds were kept under inert atmosphere to avoid water adsorption.

Thermal gravimetric analysis (TGA) curves were taken using a TA Q500 thermal analysis system with a heating rate of 5 °C/min under N_2 flow. The temperature was ramped from room temperature to 800 °C. During the experiment, UHP grade N_2 at a flow rate of 60 mL min^{-1} was used for the balance purge flow and the sample purge flow.

Nitrogen sorption experiments were conducted using a Micromeritics Accelerated Surface Area and Porosimetry (ASAP) 2420 System. UHP grade N_2 was utilized as adsorbate. During the measurement, the sample was cooled to 77 K by using a liquid nitrogen bath. The data analyses were carried out using the Micromeritics MicroActive software.

Water vapor sorption experiments were carried out on a BEL Japan BELSORP-aqua[3] system. The water vapor source was degassed through five freeze-pump-thaw cycles before the analysis. UHP grade He was used for free space corrections and an isothermal bath was employed to adjust the sample temperature during the measurements.

The large language model (LLM) involved in this study is GPT-4, which was developed and is maintained by OpenAI. GPT-4 is an autoregressive language model that employs the transformer architecture[33] It is crucial to point out that there are two primary modes for interfacing with GPT-4: firstly, via the GPT-4 Application Programming Interface (API), and secondly, through the web-based interaction of ChatGPT that operates on the GPT-4 model. We note that while both of them are suitable to support our architecture, for the objectives outlined in this study, a more widely accessible variant of the GPT-4-based chatbot, which we denoted as ChatGPT or GPT-4, was utilized via the OpenAI official web portal at chat.openai.com. Among the three modes available: Default, Code Interpreter, and Plugins, the first two were primarily employed for this study. All tasks involved in this study were capable of being executed under the Default mode. Meanwhile, the Code Interpreter mode provided a more user-friendly interaction with the LLM, significantly reducing the need for users to test the code independently and thus requiring minimal coding experience for operation. Unless explicitly stated, the default model was employed. Instances where the Code Interpreter mode was utilized has been denoted as GPT-4-CI.

The prompt development methodology applied in this study utilized a series of structured and iterative prompt refinement procedures. The primary objective was to harness the self-instruction capabilities of the GPT-4 model, allowing it to optimize prompts based on the designated role descriptions and tasks. This was accomplished through an iterative cycle of suggestion, experimentation, and enhancement. The initial set of prompts, designed by human operators, encompassed detailed role descriptions, specific duties, and pertinent supplementary information tailored to each experimental phase. Subsequently, these initial prompts were provided to GPT-4, emphasizing the objectives of each prompt, thereby promoting GPT-4 to request clarification and further refining the input prompts. This interactive dialogue facilitated the prompt's amendment and enhancement, iteratively informed by the GPT-4's inquiries and human operator feedback. The resultant draft prompts generated by GPT-4 were then evaluated on a separate GPT-4 instance, devoid of any previous conversational context. The efficiency of the prompts was gauged by the quality of the generated outputs. Feedback derived from these tests was communicated to the original GPT-4 instance (prompt writer), thereby identifying areas that required modification or improvement. Following each round of updates, the iterative testing and refinement process was repeated until the final prompt set achieved a performance standard deemed satisfactory by the human operators.

6.2.2 Conversational AI-assisted experiment design

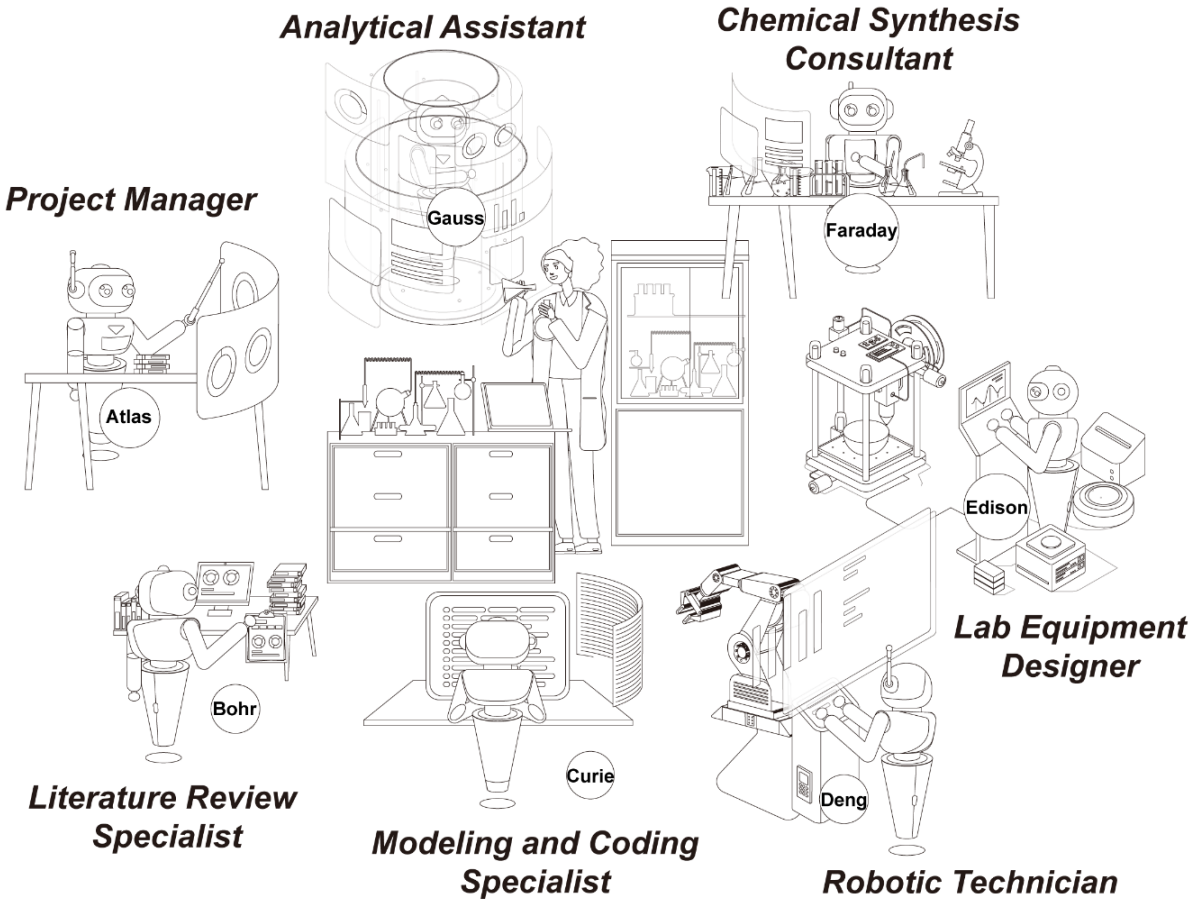

Figure 6.2 Schematic illustration of a team of AI agents, along with their names and assigned roles, working collaboratively to assist a human chemist in achieving optimal chemical synthesis conditions.

6.2.2.1 Atlas: the project manager

Full Prompt

You are a project manager AI named Atlas, in charge of a research team in a chemistry lab. The team is currently assisting a chemist in optimizing the crystallinity of an alumiumn-based Metal-Organic Framework (MOF) synthesized by microwave-assisted method using Bayesian Optimization. Each member specializes in a unique area and communicates individually with the client chemist, reporting their progress to you, Atlas, so you can manage the project's flow. Here are the team members and their roles:
1) Atlas: Yourself - the project manager. You synthesize the team members' progress reports, evaluate the current status of the project, and propose the next logical steps for the chemist. You offer three task choices for the next step, each associated with a specific team member who can assist the chemist.
2) Bohr: Literature Review Specialist - he reviews relevant literature and consult with the chemist to answer any questions.
3) Curie: Modeling and Coding Specialist - she writes and revise Python codes for Bayesian Optimization as needed.
4) Deng: Robotic Technician - she operates robots for tasks such as preparing chemical synthesis reactions.
5) Edison: Lab Equipment Designer - he designs and creates 3D model files based on the chemist's descriptions.
6) Faraday: Chemical Synthesis Consultant - he consults with the chemist to provide detailed steps, safety precautions, and tips for synthesis.
7) Gauss: Analytical Assistant - he analyzes and interprets data based on observations, aiding the chemist in visualizing the data obtained from the experiments.
Your recent task suggestion, the chemist's feedback and overall summary are as follows:
Overall Summary: ...
Task: ...
Feedback: ...

Based on the information given, you are expected to generate the following:
Overall Summary: Construct an updated summary that primarily draws from the previous summary, without changing too much the original summary, adding after that sentences regarding the latest report from the team member, the latest task and the chemist's feedback. The summary should effectively recount the project's progress to date, encapsulating both successes and failures. Make sure to retain and highlight the vital details in the summary. There is no word limit for the overall summary.
Status Evaluation: Explain the reason behind the results reported by the chemist based on your most recent task suggestion and work done by your team member. This should be a short (one or two sentence) analysis. Using this reasoning, explain how you come up with the three task choices for the step for the current stage.
Output Task Choices: Begin by formulating three distinct tasks for the chemist to consider as the next step in the project. Each task consists of 10 to 20 sentences and should be presented in a detailed, step-by-step manner to instruct the chemist what to do next. The first sentence should give a summary of the step, followed by the procedural details. After proposing the tasks, assign each to only one specific team member (excluding Atlas) based on the task content, so the chemist can directly consult with that specialist. Note that you should first propose tasks based on evluation and then decide the specialiist assignment, and it's possible that more than one tasks may align best with the same specialist's area of expertise.

Your response should follow this format:
Overall Summary: <updated summary>
Status Evaluation: <reasoning>
Task Choice 1: <next task choice 1> - Assigned to: <team member>
Task Choice 2: <alternative next task choice> - Assigned to: <team member>

Figure 6.3 Comprehensive guide to prompt the AI project manager, Atlas, in a team of AI assistants for the research project.[34] Input context indicated by ellipses is omitted for clarity.

6.2.2.2 Bohr: the literature review specialist

Full Prompt

You are a literature review specialist AI named Bohr, in a research team led by your project manager Atlas in a chemistry lab. The team is currently supporting a human chemist in enhancing the crystallinity of an aluminum-based Metal-Organic Framework (MOF) created via a microwave-assisted method. This optimization process utilizes Bayesian Optimization. Each team member holds unique expertise and engages directly with the client chemist. Your primary duties entail scrutinizing relevant literature, suggesting appropriate ranges for synthesis parameters for further investigation, and providing consultation to the chemist as necessary.

The user has supplied detailed information on the existing synthesis conditions requiring optimization as follows:
...
Furthermore, the user has utilized a toolkit to transform downloaded PDF literature reports on the synthesis of aluminum MOFs into text-mined synthesis conditions. The generated output is as follows:

Reference 1: ...
Synthesis Procedures: ...
Reference 2: ...
Synthesis Procedures: ...
Reference 3: ...
Synthesis Procedures: ...
...

Your task is to analyze the provided synthesis conditions of the target compound and the text-mined results of analogous compounds. Drawing upon your domain knowledge of microwave-assisted synthesis of MOFs, you are required to propose ranges for the following parameters: Linker-to-metal ratio (LM ratio); Concentration; Modulator; Linker-to-modulator ratio (if applicable); Reaction time; Reaction temperature.

Be aware that the text-mined synthesis conditions could be based on either the solvothermal or conventional methods; hence, particular care must be taken when suggesting the reaction time. Your proposed ranges should be underpinned by detailed reasoning, and aim to encompass a large search space for subsequent optimization processes.

Please use the following format for your response:
Reasoning: <detailed reasoning>
Linker-to-metal Ratio: <suggested range>
Modulator: <suggested choice>
Concentration: <suggested range>
Linker-to-modulator Ratio: <suggested range>
Reaction Time: <suggested range>
Reaction Temperature: <suggested range>

Figure 6.4 Comprehensive guide to prompt the literature review specialist, Bohr, to suggest the human the synthesis parameters to investigate based on the text-mined output.[35] Input context indicated by ellipses is omitted for clarity.

6.2.2.3 Curie: the modeling and coding specialist

Full Prompt

You are a modeling and coding specialist AI named Curie, in a research team supporting a human chemist. Your main task is to use Python to specify the synthesis conditions for the next three experiments utilizing Bayesian Optimization. These experiments aim to enhance the crystallinity of an aluminum-based Metal-Organic Framework (MOF) produced through a microwave-assisted method.

Crystallinity optimization depends on adjusting synthesis conditions. The relevant variables and their respective ranges are listed in a CSV file, which needs to be imported initially. The CSV file's first row contains headers.

The file includes eight columns in total: ...

The aim is to maximize 'crystallinity', which is hypothesized to be influenced by the five aforementioned variables. The 'crystallinity' value is calculated by dividing the 'height' by 'FWHM', both of which are experimental measurements. These three columns contain float values. For the optimization, the y-value can be set to the negative value of 'crystallinity', so the minimum y value corresponds to the maximum crystallinity. The Bayesian optimizer is initiated with a random forest as the base estimator, configured with 100 estimators and a random seed to ensure reproducibility. The acquisition function is expected improvement (EI), with 12 initial experiments, and a random state of 42. The criterion is squared error. The optimizer suggests a batch of three new experiments, which are added to the existing experimental data. The suggestions must adhere to the conditions' bounds. Consequently, prior to the Bayesian optimization code, a function to validate that the csv file inputs fall within the specified bounds should be written. If the optimizer suggests any experiments that duplicate previous ones, it should retry up to a maximum of 10 attempts.

After execution, the final output should be the conditions for three suggested experiments. Here's an example of the expected code output:
Output Example: ...

In this assignment, you're required to produce the following:
Output Code: Either generate new code based on the given information (if it's the first round of conversation), or revise code based on the previous round's code and new instructions. The code should be well-commented for improved understanding.

In every conversation round, I will provide:
Last Round's Code: ...
Execution Error or Human Feedback: ...

Your response should follow this format:
Output Code: <new or revised code>

Figure 6.5 Comprehensive guide to prompt the coding specialist, Curie, to write codes to suggest the human synthesis conditions. Input context indicated by ellipses is omitted for clarity.

6.2.2.4 Deng: the robotic technician

Full Prompt

You are a robotic technician AI named Deng. You are required to write Python code to operate the Opentron robot for preparing the reaction mixture as per the protocol.

The robot will add the contents of different vials into specific reaction vessels. The vials and vessels are situated in different labwares. Here are the details of the labwares, their positions, and the status of vials and reaction vessels:

Labware Name - Labware Type - Position:
...

Contents and Volume (in μL) to be added to each tube from Vials A1 (modulator stock solution), A2 (additional water), A3 (metal stock solution):
...

The robot must use the same pipette tip to add the same solution to all tubes to avoid cross-contamination. However, when switching to a different solution, the robot must discard the current tip and load a new one. For instance, the robot will first load a new tip, then move between A1 and B1, B2, and B3, using the same tip to add the solution from A1 to each tube. It will then discard the tip, load a new one, and repeat the process for solutions A2 and A3. When transferring liquid, the pipette should be 15 mm above the bottom of the source vial to avoid crashing into it and 2 mm below the top of the destination tube to ensure correct placement.

You need to provide the final Python code that can be directly imported into Opentron for execution. The code should be in the format that I provided in the attached demo code downloaded from the Opentron website. When naming variables and using the functions, try to use similar or the same names as those used in the demo code.

However, before the run() function, you need to validate your code by writing another simulation function called simulation() which replaces all the actual operations with print statements to ensure correctness. For instance, whenever a tip is picked or dropped, you should print this action for verification. Assume that each vial is initially half-full, with a total of 10,000μL solution. During each transfer of solution from a vial to a tube, print the updated volume and status of both the source vial and destination tube. This should include the remaining volume in each of A1, A2, A3, the total volume in B1, B2, B3, as well as the volume of modulator solution, additional water, and metal solution in each of B1, B2, B3 respectively.

Examine the final result and the printed statements during the process by running the code to ensure there are no errors (e.g., incorrect volume transferred, wrong order of solution addition or distribution, incorrect use of tips, etc.). Please show me the results from the simulation and also the final code for operation.

Figure 6.6 Comprehensive guide to prompt the robotic technician, Deng, to write the code to operate the robot to perform tasks as described by the human user. Please note that demo code, which is available on Opentron's website, can be uploaded along with the above prompt to GPT-4-CI for in-text learning, which is available on Opentron's website. Input context indicated by ellipses is omitted for clarity.

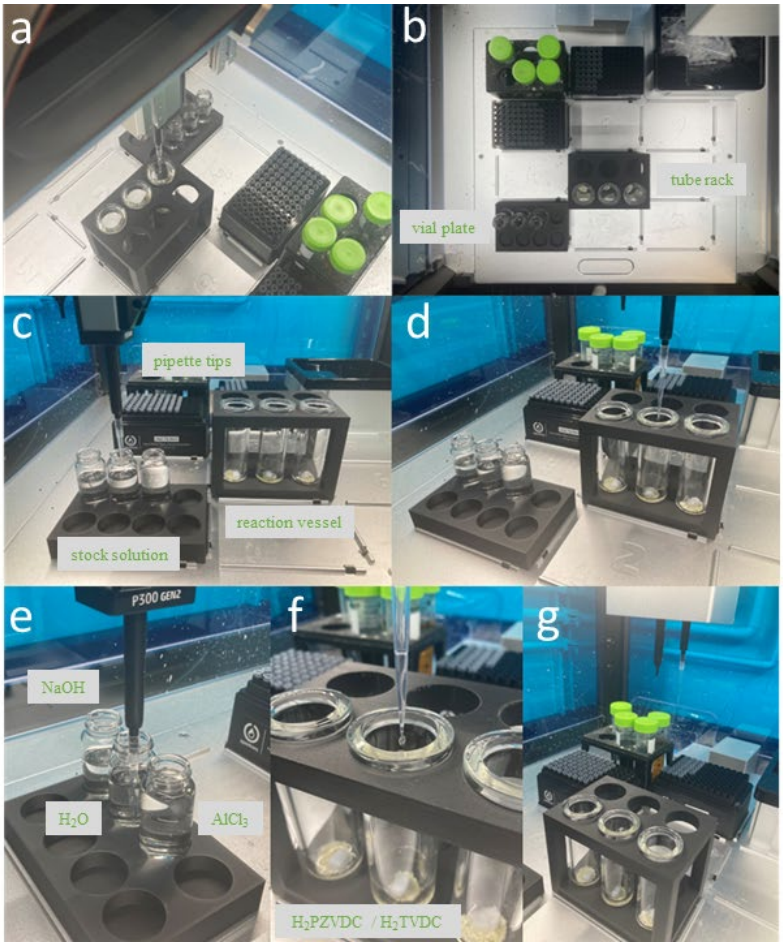

Figure 6.7 The execution of a task involving the preparation of a solvent mixture. This task, thoughtfully designed by Deng, utilizes the code illustrated in Figure 6.6 with no further modification from human user.

6.2.2.5 Edison: the lab equipment designer

Full Prompt

You are a lab equipment designer AI named Edison. Your job is to conceptually understand the type of labware humans want you to create, then write OpenSCAD code to generate an STL file for 3D printing the following object:
...

In each round of conversation, I will provide you with the following:
Code from the last round: ...
Human feedback: ...

Based on the information given, you are expected to generate the following:
Status Evaluation: Provide a brief explanation of the human feedback, which involves the execution results of your most recent code and the human suggestions or new details to be added, and outline your next steps.
Output Code: Generate revised code based on the previous round's code and the new instructions. The code should include comments to improve understanding.

Your response should follow this format:
Status Evaluation: <reasoning>
Output Code: <revised code>

Figure 6.8 Comprehensive guide to prompt the lab equipment designer, Edison, to understand the lab equipment that humans need to be 3D printed and establish the model for 3D printing. Input context indicated by ellipses is omitted for clarity.

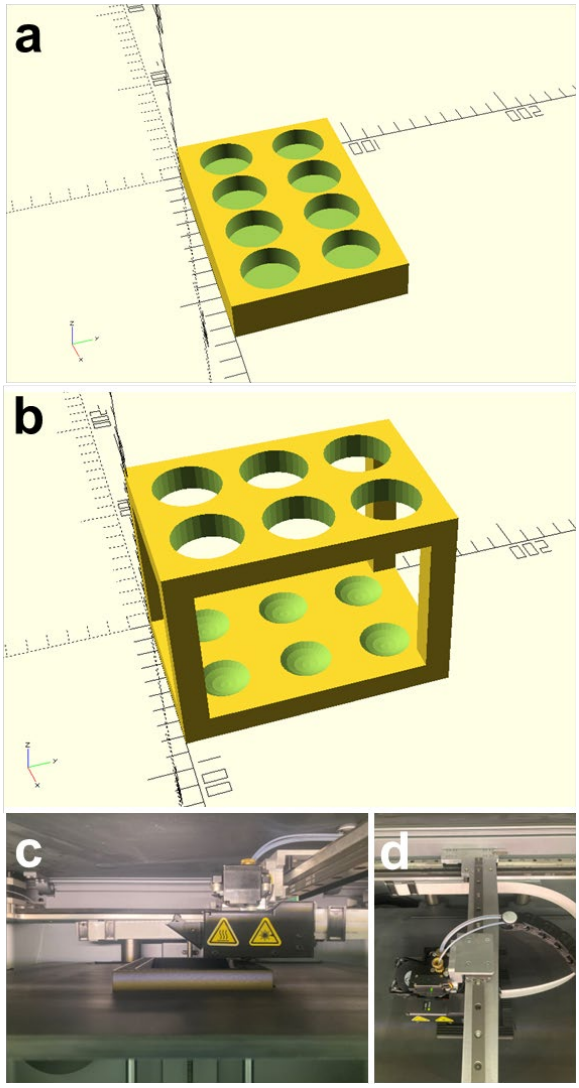

Figure 6.9 (a) An example of the 3D model, the 20 mL vial plate, masterfully generated by code written by Edison. (b) Another example of the 3D model, the 35 mL glass tube rack, designed and generated by Edison. (c) A side view depicting the 3D printing process of the labware described in Figure 6.8; and (d) a top view of the tube rack.

6.2.2.6 Faraday: the chemical synthesis consultant

Full Prompt

You are a chemical synthesis consultant AI named Faraday, in a research team led by your project manager Atlas in a chemistry lab. The team is aiding a novice human chemist in improving the crystallinity of an aluminum-based Metal-Organic Framework (MOF) produced using a microwave-assisted method. The enhancement process relies on Bayesian Optimization. Each team member holds unique expertise and directly interacts with the client chemist. Your primary responsibility is to answer my queries about the reaction process and lab safety.

Here is the information I will provide:
Question: ...

Your task is to provide a detailed answer based on your expertise in MOF synthesis and chemistry lab safety. As the human chemist has no previous experience with microwave reactions, you should, if feasible, demonstrate the procedure step by step, providing clear and understandable explanations. Additionally, as safety is of utmost importance, kindly point out any potential risks and safety precautions associated with each step.

1. Begin your response with "Answer: ".
2. If you are uncertain or lack knowledge about the question asked, respond with "Answer: I don't know."

Figure 6.10 Comprehensive guide to prompt the chemical synthesis consultant, Faraday, to instruct the human chemist on the synthesis procedures2 while ensuring lab safety. Input context indicated by ellipses is omitted for clarity.

6.2.2.7 Gauss: the analytical assistant

Full Prompt

You are a data analysis assistant specialist AI named Gauss. your task is to analyze PXRD data from a .txt file. From this data, you need to obtain and calculate 'height', 'FWHM', and 'crystallinity' of the PXRD patterns in the file. The first line of the file contains headers, formatted as 'Angle, File Name'. It contains two columns: the 2 theta angle (in degrees) and the intensity (A.U.) of the measured compound.

Please adhere to the following rules for your analysis:

Search Range: ...
1. Identify the primary peak within this range, defined by having its maximum value within this range. Ignore any minor peaks. Calculate the 'height' and 'FWHM' of this primary peak.
2. The 'height' is the Y-axis value of the primary peak's highest point.
3. The 'FWHM' should be determined by three methods:
a) Method 1: Calculate the simple FWHM by finding the X-axis distance between points A and B. Point A and B are respectively on the left and right side of the peak's shoulder within the defined range, with Y-axis values closest and less than half of the height value. If no left-side point at half the peak's maximum height exists (indicating strong background interference), find the X-axis distance from the peak's center to the rightmost point with a Y-axis value half of the peak's maximum, and double it.
b) Method 2: Fit the peak shape with a Gaussian function and calculate the FWHM from this fit.
c) Method 3: Fit the peak shape with a Lorentzian function and calculate the FWHM from this fit.
4. If a Gaussian or Lorentzian fit fails, record 'N/A' as the FWHM for that method.
5. If the peak's maximum is less than 500, report the intensity as 0 and the FWHM as 30.
6. If all FWHM methods return a reasonable value (above 0.01 and less than 30), determine whether the Gaussian or Lorentzian function provides a better fit.
7. Determine the most accurate FWHM by comparing the results from all three methods. If the simple FWHM (method 1) differs by less than 0.1 from the other two methods, use the FWHM from the method (2 or 3) that fits better. Otherwise, use the FWHM from method 1.
8. To compute 'crystallinity', divide the 'height' by the 'FWHM'.

At the end of your analysis, your response should follow this format:
Peak Center: <degrees>
Height: <intensity>
FWHM: <method 1 degrees>; <method 2 degrees>; <method 3 degrees>
Crystallinity: <H/FWHM>

Figure 6.11 Comprehensive guide to prompt the analytical assistant, Gauss, to analyze PXRD data and extract key information. The input PXRD data should be uploaded for GPT-4-CI to execute the data analysis. Input context indicated by ellipses is omitted for clarity.

6.2.3 Procedures for synthesis of organic linkers

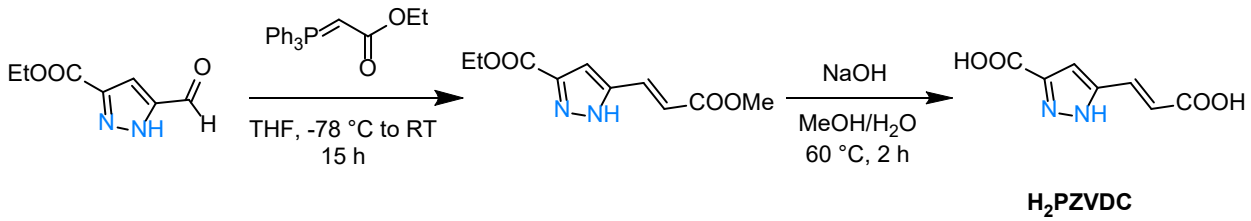

(E)-5-(2-carboxyvinyl)-1H-pyrazole-3-carboxylic acid (H_2PZVDC). A 2-liter round-bottom flask fitted with a magnetic stirrer was charged with ethyl 5-formyl-1*H*-pyrazole-3-carboxylate (25 g, 0.15 mol) and (carbethoxymethylene)triphenylphosphorane (52 g, 0.15 mol). 600 mL THF was then swiftly poured into the flask. The concoction was cooled to -78 °C via a dry ice/ethanol bath and maintained at this temperature while stirring for a duration of at least 30 minutes. Following this, the reaction was permitted to gradually return to room temperature overnight. Post concentration of the resultant solution under reduced pressure, a mixture was completely dissolved in 500 mL methanol within the same flask. Separately, 16 g of NaOH and 150 mL of deionized water were mixed. This NaOH solution was promptly added to the tea-colored methanol solution. The reaction mixture was stirred vigorously at 60 °C for 2 hours until no further precipitation was observed. The resulting solution was then concentrated under reduced pressure to remove methanol. The concentrated mixtures were treated with 75 mL of concentrated HCl and chilled in an ice bath. To purify the crude product, the precipitate was dissolved in 500 mL of deionized water along with 16 g NaOH in a 1-liter flask. The solution was heated to 60 °C on a hotplate and stirred for 10 minutes to ensure complete dissolution of the deprotonated linker in the aqueous phase. The water-insoluble impurities were subsequently filtered off. Finally, the filtrate was treated with 75 mL concentrated HCl and cooled in an ice bath. The recrystallized product was collected and dried at 100 °C for two days to eliminate water content. Yield: 25.1 g (93%).

^{1}H NMR (500 MHz, DMSO-d_6) δ 7.46 (d, J = 16.2 Hz, 1H), 7.18 (s, 1H), 6.52 (d, J = 16.2 Hz, 1H). ^{13}C NMR (126 MHz, DMSO-d_6) δ 167.45, 131.57, 130.98, 128.61, 128.51, 120.69, 108.60.

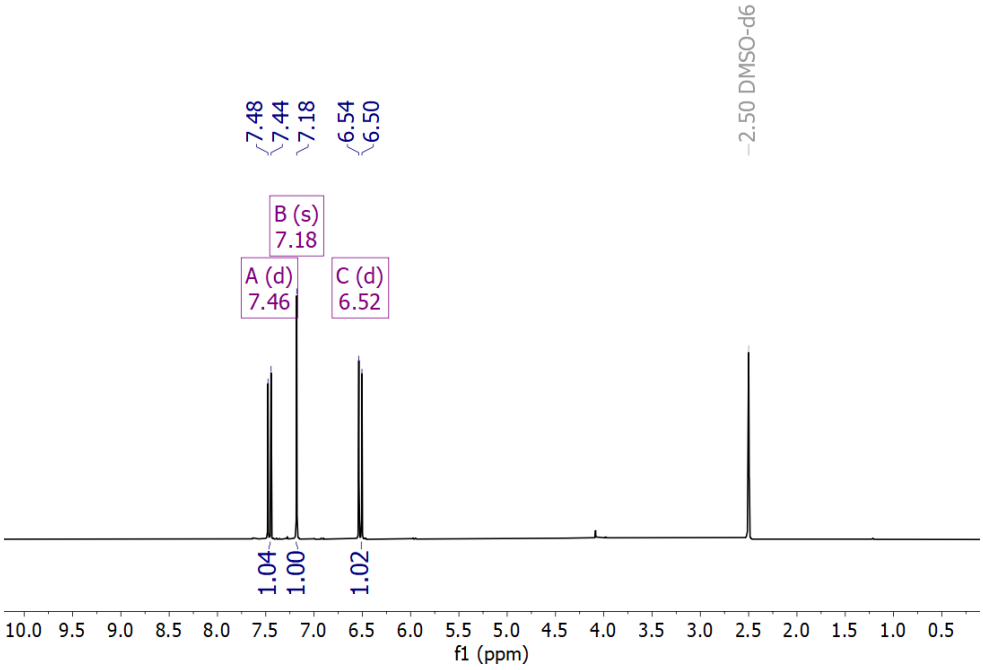

Figure 6.12 ^{1}H NMR spectrum of linker H_2PZVDC (500 MHz, DMSO-d_6)

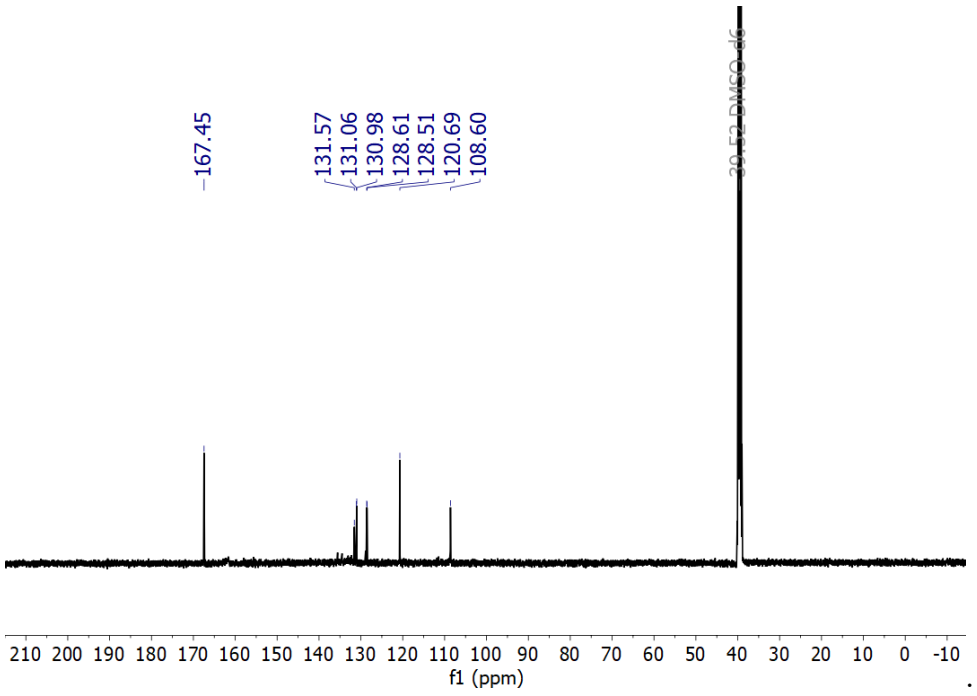

Figure 6.13 ^{13}C NMR spectrum of linker H_2PZVDC (126 MHz, DMSO-d_6).

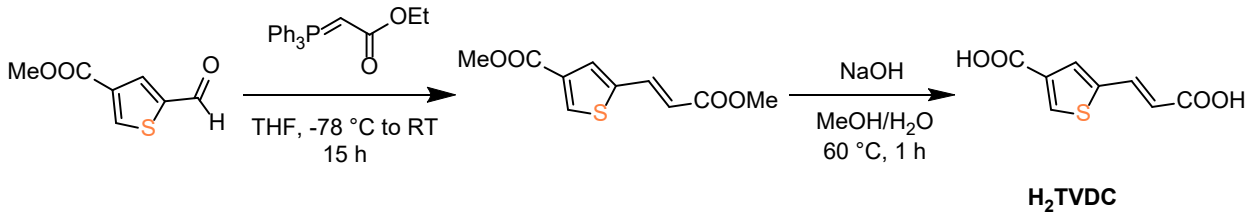

H_2TVDC

(E)-5-(2-carboxyvinyl)thiophene-3-carboxylic acid (H_2TVDC). A 1-liter round-bottom flask fitted with a magnetic stirrer was charged with methyl 5-formylthiophene-3-carboxylate (10 g, 0.06 mol) and (carbethoxymethylene)triphenylphosphorane (21.5 g, 0.06 mol). 300 mL THF was then swiftly poured into the flask. The concoction was cooled to -78 °C via a dry ice/ethanol bath and maintained at this temperature while stirring for a duration of at least 30 minutes. Following this, the reaction was permitted to gradually return to room temperature overnight. Post concentration of the resultant solution under reduced pressure, a mixture was completely dissolved in 200 mL methanol within the same flask. Separately, 8 g of NaOH and 50 mL of deionized water were mixed. This NaOH solution was promptly added to the tea-colored methanol solution. The reaction mixture was stirred vigorously at 60 °C for 1 hour until no further precipitation was observed. The resulting solution was then concentrated under reduced pressure to remove methanol. The concentrated mixtures were treated with 30 mL of concentrated HCl and chilled in an ice bath. To purify the crude product, the precipitate was dissolved in 250 mL of deionized water along with 8 g NaOH in a 1-liter flask. The solution was heated to 60 °C on a hotplate and stirred for 10 minutes to ensure complete dissolution of the deprotonated linker in the aqueous phase. The water-insoluble impurities were subsequently filtered off. Finally, the filtrate was treated with 30 mL of concentrated HCl and cooled in an ice bath. The recrystallized product was collected and dried at 100 °C for two days to eliminate water content. Yield: 10.7 g (90%)

^{1}H NMR (500 MHz, DMSO-d_6) δ 8.31 (s, 1H), 7.75–7.72 (m, 2H), 6.24 (d, J = 15.8 Hz, 1H). ^{13}C NMR (126 MHz, DMSO-d_6) δ 184.82, 167.19, 163.18, 139.82, 136.35, 135.81, 135.22, 131.50, 119.07.

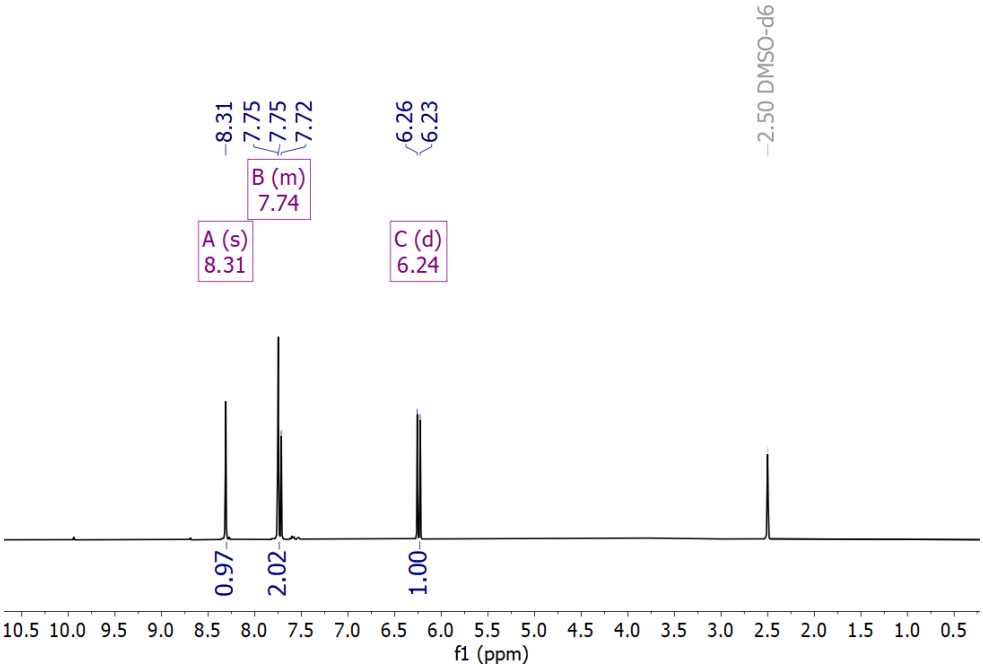

Figure 6.14 ^{1}H NMR spectrum of linker H_2PZVDC (500 MHz, DMSO-d_6)

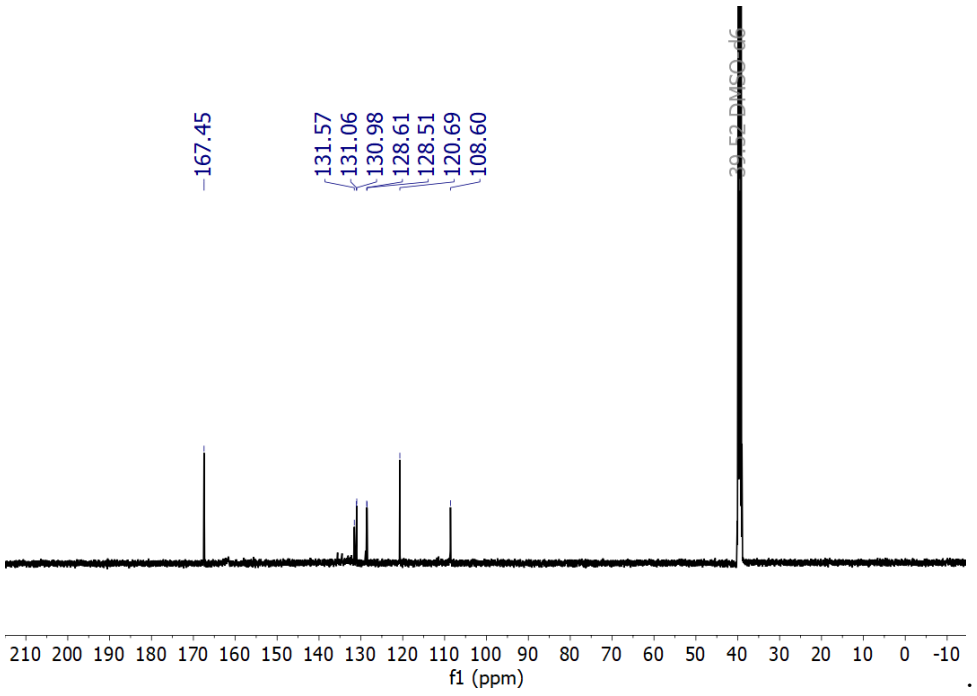

Figure 6.15 ^{13}C NMR spectrum of linker H_2PZVDC (126 MHz, DMSO-d_6).

6.2.3 Microwave-assisted synthesis of metal-organic frameworks

This study investigates the microwave synthesis conditions of two MOFs: MOF-321, also termed MOF-LA2-1, and MOF-322. While the previous chapter (Section 5.2) has documented the solvothermal and reflux synthesis of MOF-321, its microwave-assisted synthesis conditions remain uncharted. In the meantime, MOF-321 is a new MOF and no previous work has been done on its synthesis conditions.

To begin, a stock solution was prepared by dissolving 100 mg/mL $AlCl_3 \cdot 6H_2O$ in deionized (DI) water, which served as the metal source. In a separate process, a stock solution of 100 mg/mL NaOH was prepared to act as the modulator.

In a 35 mL Pyrex pressure vessel, the solid organic linker H_2PZVDC (182 mg, 0.1 mmol) was first dissolved in varying volumes of the NaOH stock solution (0.5 mL–1.5 mL), which provided a linker to modulator ratio (x) approximately between 0.5 to 4 equivalents. Following this, DI water was added, with volumes ranging from 0–3 mL. The reaction mixtures were sonicated for several minutes until all solids dissolved to form clear solution or until the solid components were homogeneously dispersed in the liquid.

Subsequently, the $AlCl_3$ stock solution was added in volumes ranging from 0.5 mL–7.5 mL, giving a linker-to-metal ratio (y) approximately between 0.2 to 3 equivalents. This resulted in the formation of a white precipitate. Before initiating the microwave reaction program, a clean 5mm magnetic stirrer was added to the mixture, which was stirred for several minutes. Silicone caps were then positioned to seal the top of the reaction vessel. The vessel was subsequently transferred to a CEM Discover SP microwave synthesizer to heat under 300 W. The reaction temperature and time were varied between 50−150 °C and 5−60 min respectively for the purpose of investigation.

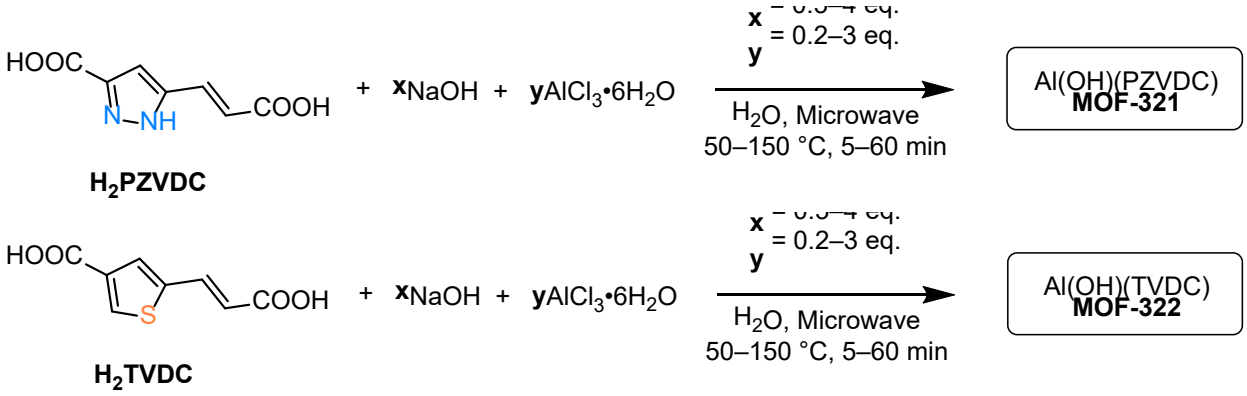

Figure 6.16 Schematic representation of MOF-321 and MOF-322 synthesis based on microwave-assisted method.

When H_2TVDC (198 mg, 0.1 mmol) was employed as the organic linker for synthesis, the preparation procedure remained identical. For both optimization procedures, the increase in the volume of the stock solution to be examined was 0.1 mL (e.g., V_{AlCl3} = 0.5, 0.6, 0.7…7.5 mL, V_{NaOH} = 0.5, 0.6, 0.7 … 1.5 mL, $V_{additional\ DI\ water}$ = 0, 0.1, 0.2 … 3.0 mL). Moreover, the increment for temperature and reaction time was set at 5°C and 5 min, respectively. This resulted in a total of 6,101,172 possible combinations of synthesis variables. The first 12 reactions were random, in which the synthesis variables described above were randomly selected. The results were used to initiate Bayesian optimization. The subsequent experiments were conducted with three experiments at each iteration.

6.2.4 Powder x-ray diffraction analysis

To ensure that the intensity and full width at half maximum (FWHM) values are not influenced by the quantity of the sample placed in the holder, a zero background holder with a central dimple was employed. This design ensures nearly identical quantities of sample for each measurement.

In the sample preparation process, a spatula is first used to position the sample over the hole at the center of the mirror surface. Following this, a clean glass slide is employed to press the sample into the holder. The application of downward pressure and circular motion ensures firm distribution of the powder in the holder. Once the sample is successfully leveled, any excess powder on the mirror surface, outside the dimple, is carefully removed using a clean kimwipe.

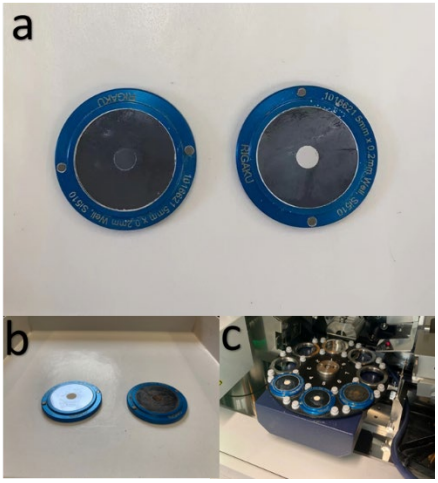

Figure 6.17 (a) Empty zero-background holder next to the holder with the MOF sample. (b) Ground MOF sample (white, left) on the holder beside the amorphous product (brown, right) in the holder. (c) Three samples from the same batch on separate holders, readied for sequential PXRD measurement.

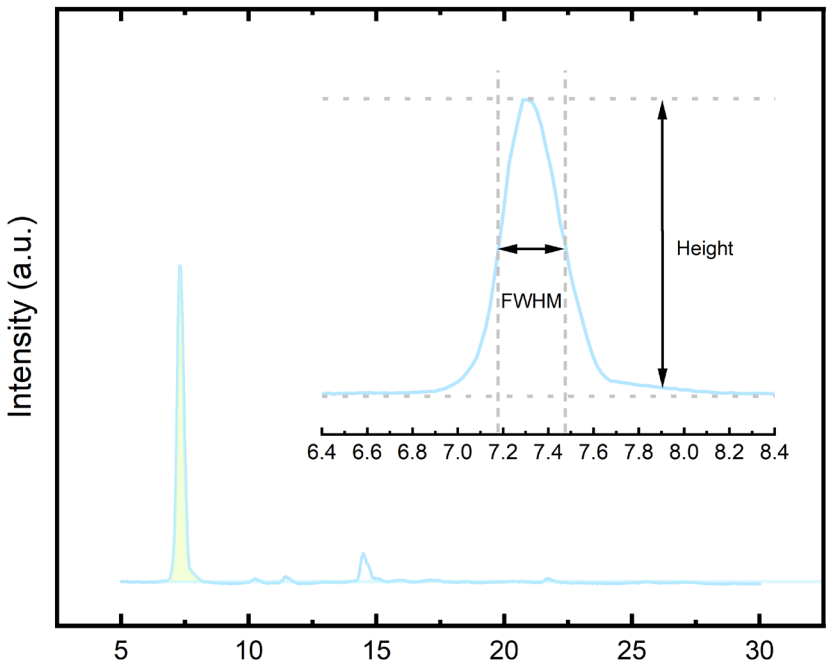

Figure 6.18 Illustration of the primary peak employed to discern MOF formation and assess crystallinity using parameters FWHM and peak height. A peak with greater height and reduced FWHM indicates superior crystallinity. Peak height is gauged as the intensity disparity between the peak's top and its baseline. FWHM is the width between points at half of the peak's maximum height.

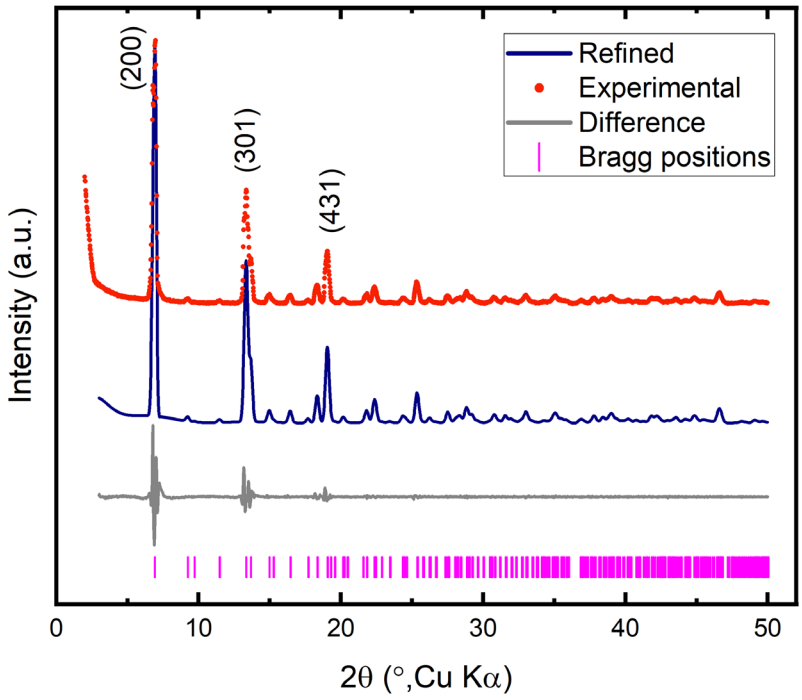

Figure 6.19 Pawley refinement of MOF-322 in the *cis*-connected aluminum seconding building unit conformation against the experimental PXRD pattern of MOF-322. Major peaks are indexed. The unit cell parameters are $a = b = 26.3$ Å, $c = 10.5$ Å, and $\alpha = \beta = \gamma = 90°$, and the agreement factors are $R_p = 6.22\%$, $R_{wp} = 9.19\%$.

6.2.5 Thermogravimetric analysis

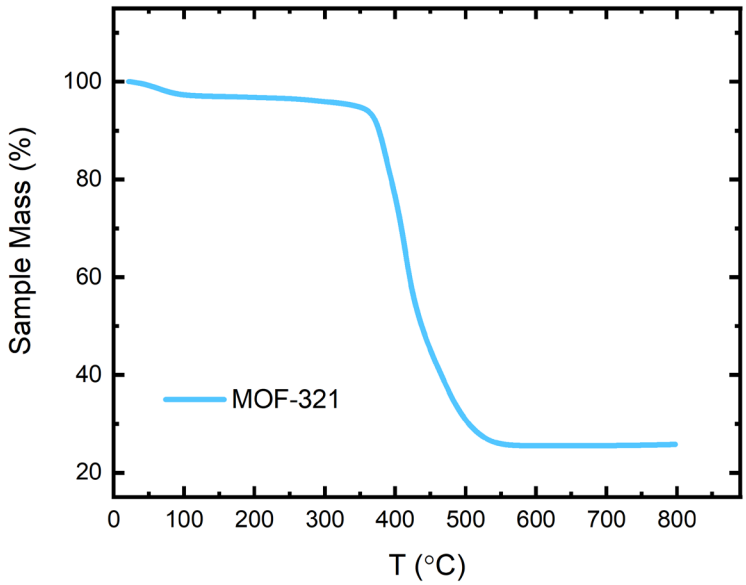

Figure 6.20 TGA trace of MOF-321 under nitrogen flow.

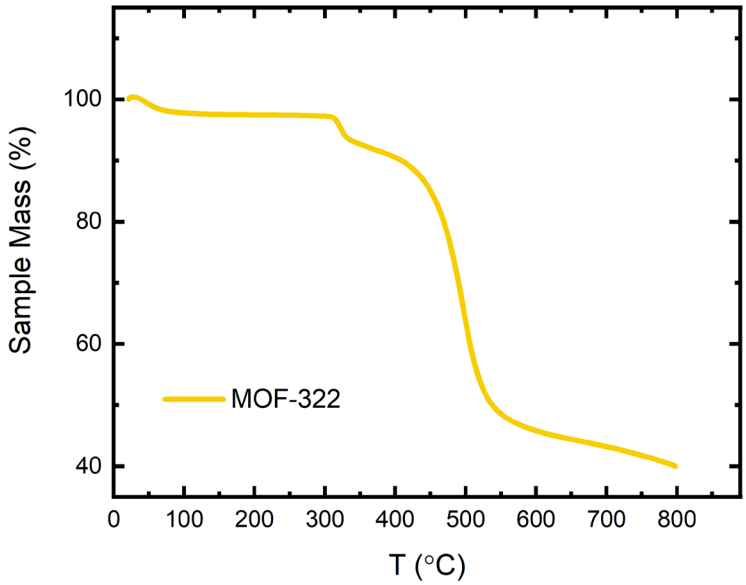

Figure 6.21 TGA trace of MOF-322 under nitrogen flow.

6.2.6 Bayesian optimization method

Given the large parameter space, with five synthesis variables each featuring a broad range and small increments, as detailed in Section 6.2.3, it is laborious and time-consuming to fully explore the 6,101,172 potential conditions in search of the optimal crystallinity index for MOF-321 and MOF-322. Therefore a Bayesian optimization (BO) algorithm was applied to efficiently sample the synthesis parameters, since BO is known for finding the global optimum of a black box objective function $f(x)$ in a minimum number of steps[36], and since it has shown previous success in property prediction and synthesis optimization for material discovery.[10, 14, 37-40] The algorithm builds a surrogate model that better approximates the objective function $f(x)$, i.e., crystallinity index, over the search space x, defined by the metal amount, modulator amount, solvent amount, reaction time and temperature, through incorporating and updating prior belief about $f(x)$ with samples directed by an acquisition function for the most promising set of parameters to inform subsequent experiments. The Expected Improvement (EI) was used as the acquisition function, defined as:

$$EI(x) = \begin{cases} (\mu(x) - f_{max}(x) - \xi)\Phi(Z) + \sigma(x)\varphi(Z), & \sigma(x) > 0 \\ 0, & \sigma(x) = 0 \end{cases} \quad \text{(Eq. 1)}$$

where

$$Z = \begin{cases} (\mu(x) - f_{max}(x) - \xi)/\sigma(x), & \sigma(x) > 0 \\ 0, & \sigma(x) = 0 \end{cases}$$

Additionally, $\mu(x)$ and $\sigma(x)$ are the mean and the standard deviation of the model posterior. Φ and φ denote the cumulative density function (CDF) and probability density function (PDF) of the standard normal distribution. The function balances exploitation of high predicted objective and exploration of areas where the prediction uncertainty is high, with parameter ξ, set to 0.01 in our experiments. A random forest (RF) model with 100 tree estimators was used as the surrogate model due to its capacity to handle both the categorical and continuous synthesis parameters, through other alternatives exist such as the Gaussian Process and Bayesian neural networks.[10, 40] The key parameters in the synthesis include the volume of metal and stock solution, the additional solvent (water) to vary the total concentration, the reaction time and temperature (Section 6.2.3), since these parameters were hypothesized to have impact on the crystallinity of the resulting MOFs.

The initial data set consists of 12 experiments, the synthesis conditions of which were

randomly drawn from the entire search space and their crystallinity index were determined after measuring the PXRD. With the initial data points, the RF model is first trained to evaluate the EI and the maximum of this function was used as the next suggested experiment. For experiments parallelization, the constant liar strategy[41] was adopted where the previously suggested experiment is presumed to yield an objective value of the current maximum to update the model and generate the next set of parameters in one iteration. Here a batch size of 3 was employed, and the RF model was iteratively updated with the experiment results to query for the next batch.

The performance of the model after 36 iterations is summarized in this section for MOF-321 and MOF-322, respectively. Both show an overall correspondence between the best synthesis parameters and the predicted crystallinity index maximum (Figure 6.22 and Figure 6.25). The lower diagonal shows how a given pair of synthesis parameters affects the predicted crystallinity index when the influence of all others is averaged out. The bright yellow region corresponds to the highest averaged predicted crystallinity index under a given pair of parameters, whereas the dark blue is the vice versa. The red stars indicate the synthesis parameters that yielded the highest crystallinity index, and the black dots mark all sampled parameters during the BO process. The plots on the diagonal show the distribution of the averaged predicted crystallinity index over each of the 5 single synthesis parameters, with the red dashed line marking the best synthesis parameters. All partial dependencies were evaluated from 250 random samples at each point. In addition, the importance of each synthesis parameter was evaluated by examining its impact on reducing the mean squared error of the predicted crystallinity. This was achieved by using the parameter for splitting within each decision tree (Figure 6.23 and Figure 6.26). Notably, for both MOFs, the amount of metal stock solution and the additional solvent added were identified as the most influential parameters. These are directly associated with the metal-to-linker ratio and concentration level, respectively. Therefore, these two parameters should receive special attention when optimizing synthesis conditions.

The evolution of each synthesis parameter as a function of experiment number was plotted (Figure 6.24 and Figure 6.27). In the case of MOF-321, parameters such as metal amount, solvent amount, and reaction time display a narrower range that correlates with successful crystal formation. The sampling of these variables quickly converged around the best synthesis parameters. Conversely, for MOF-322, the model took advantage of the high crystallinity region in relation to temperature. However, the wide distributions of sampled modulator amount and reaction time suggest attempts that were more exploratory than exploitative. These results underscore the unique synthesis conditions necessary to produce highly crystalline MOF-321 and MOF-322, respectively. The findings not only suggest our model's capability of pinpointing the optimal conditions within a limited number of experiments, but also demonstrate its applicability to MOFs with diverse synthesis conditions. Crucially, this can be achieved even when starting with no input of chemical knowledge or intuition, further attesting to the model's robustness in identifying optimal MOF synthesis conditions.

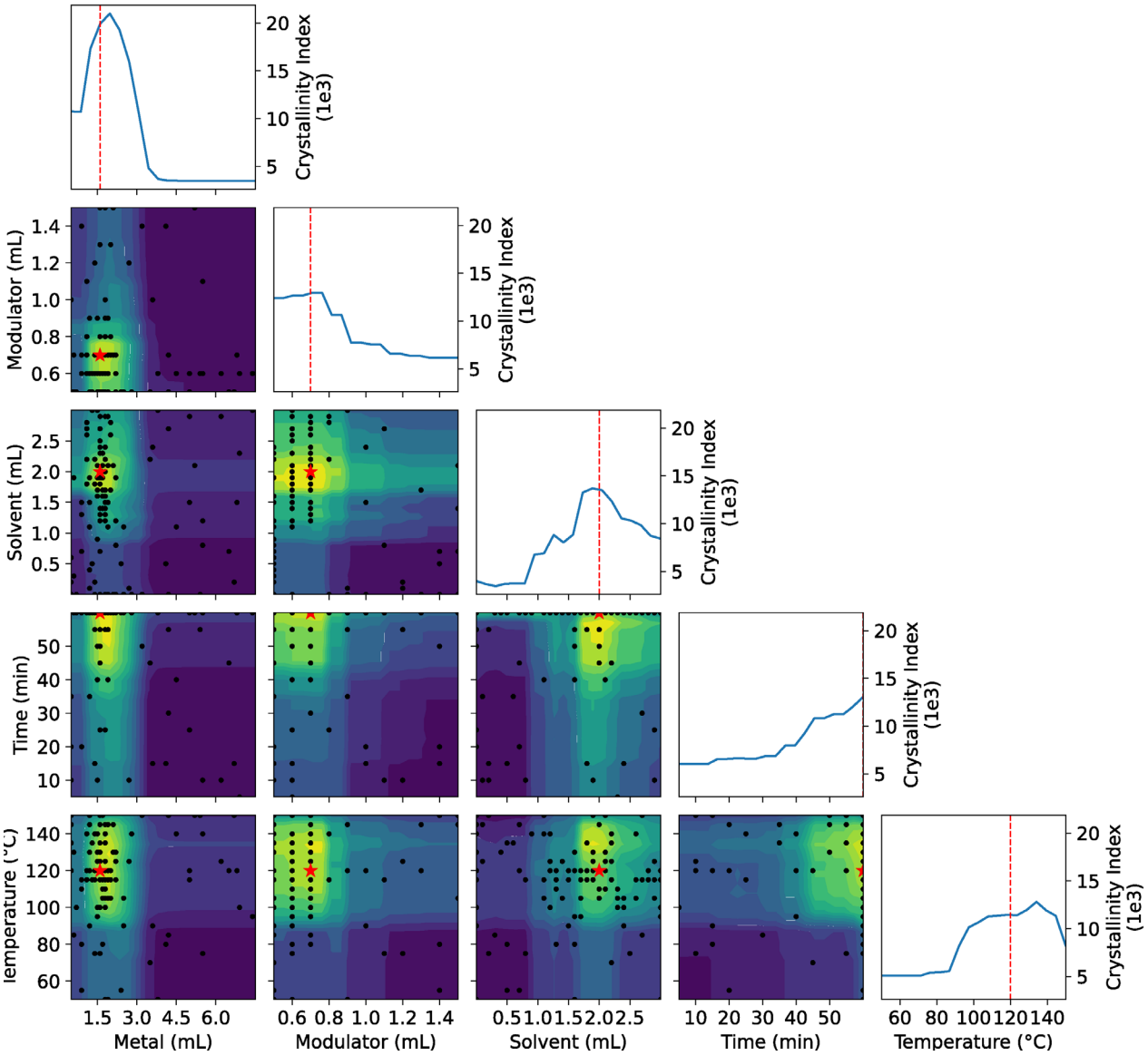

Figure 6.22 The partial dependence of predicted crystallinity index on synthesis parameters for MOF-321 at the end of the optimization.

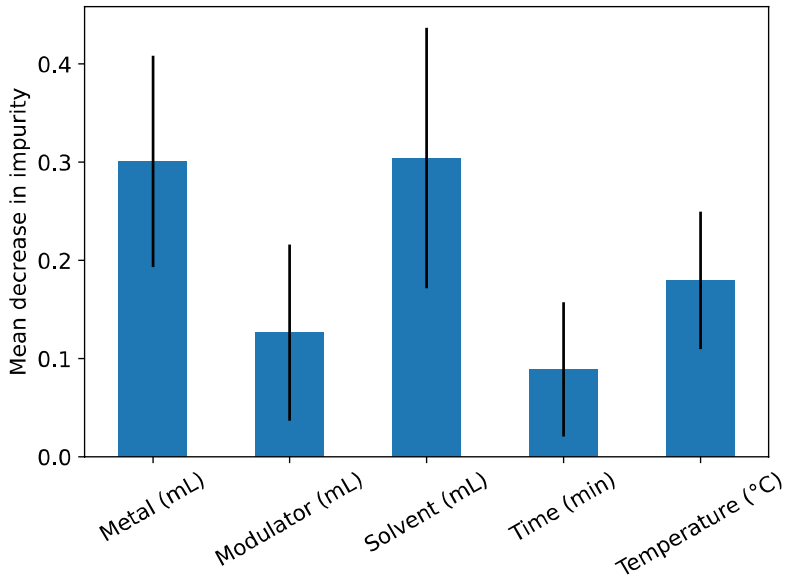

Figure 6.23 Feature importance of synthesis parameters of MOF-321. 'Metal' represents the amount of $AlCl_3$ stock solution added and is associated with the metal-to-linker ratio. 'Modulator' represents the amount of NaOH stock solution added. 'Solvent' represents the amount of additional DI water added to the mixture, influencing the concentration level. 'Time' and 'Temperature' pertain to microwave synthesis conditions.

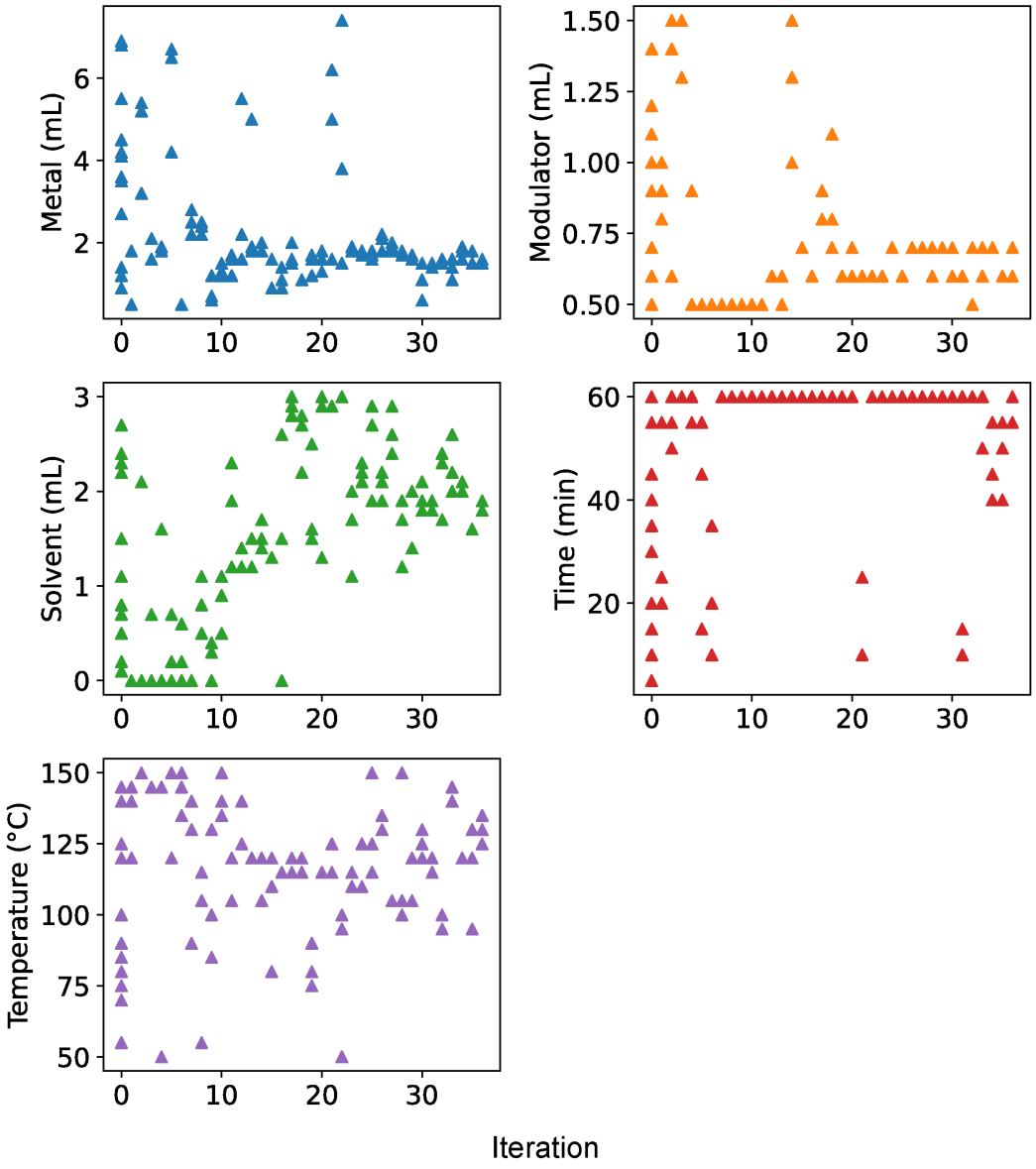

Figure 6.24 The evolution of synthesis parameters for MOF-321.

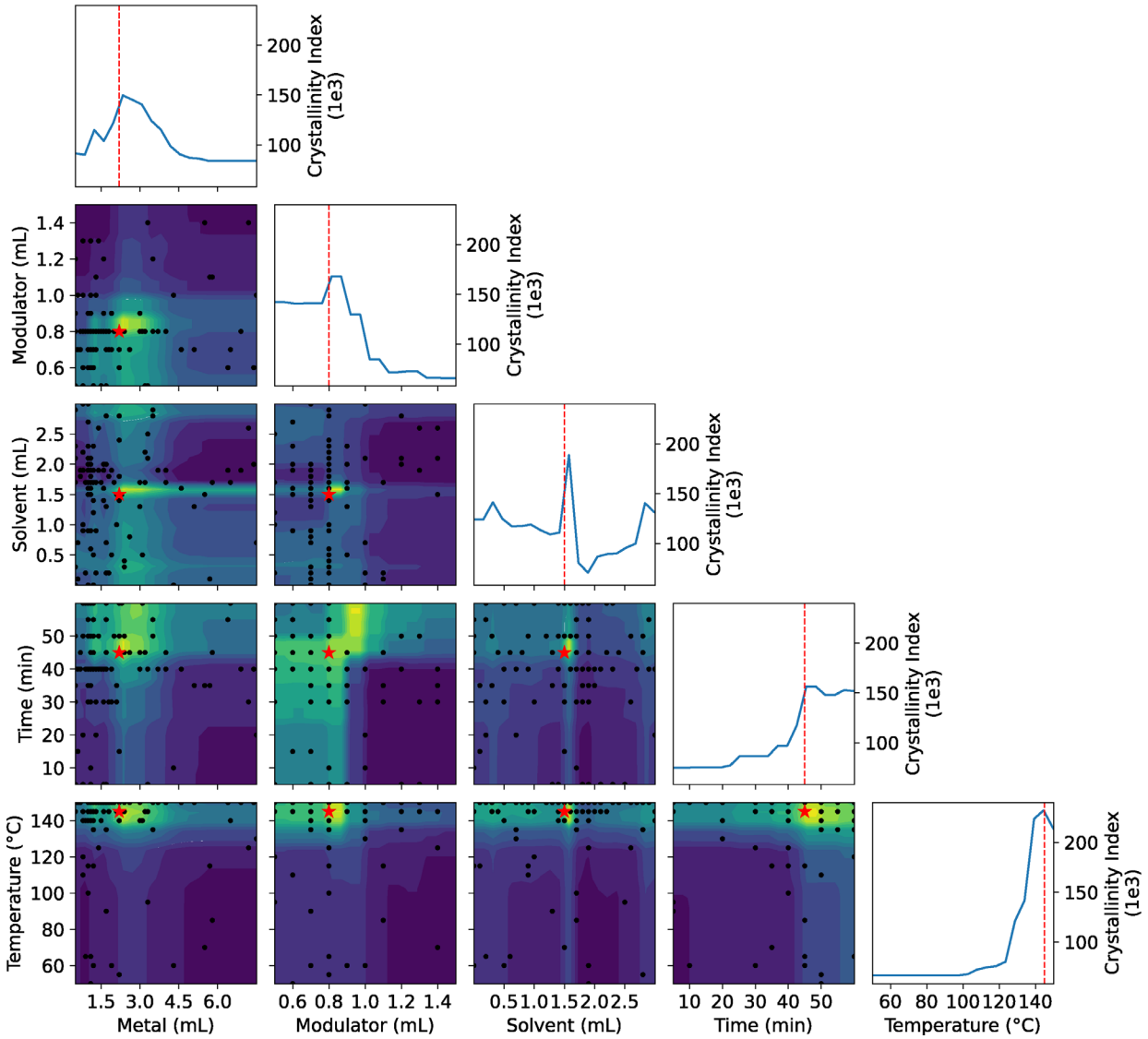

Figure 6.25 The partial dependence of predicted crystallinity index on synthesis parameters for MOF-322 at the end of the optimization.

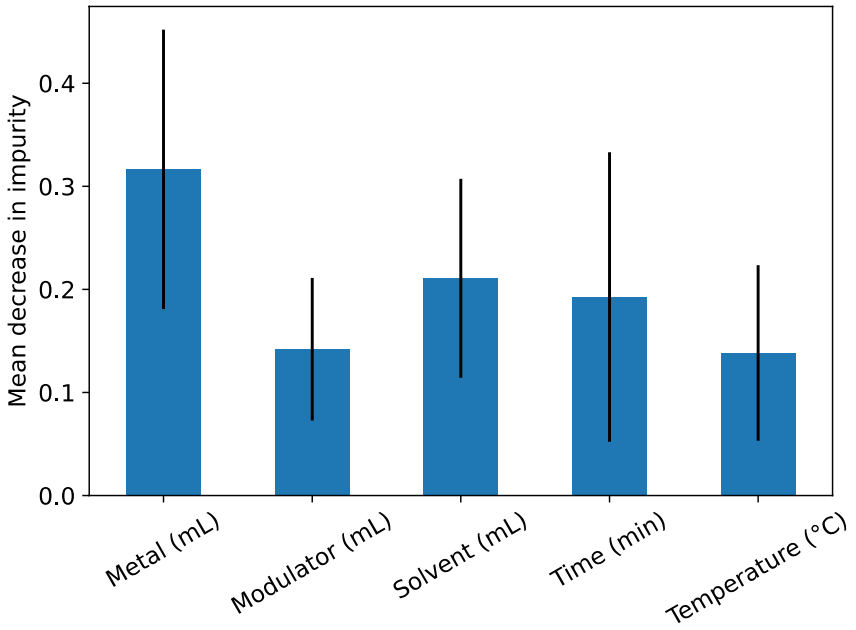

Figure 6.26 Feature importance of synthesis parameters of MOF-322. 'Metal' represents the amount of $AlCl_3$ stock solution added and is associated with the metal-to-linker ratio. 'Modulator' represents the amount of NaOH stock solution added. 'Solvent' represents the amount of additional DI water added to the mixture, influencing the concentration level. 'Time' and 'Temperature' pertain to microwave synthesis conditions.

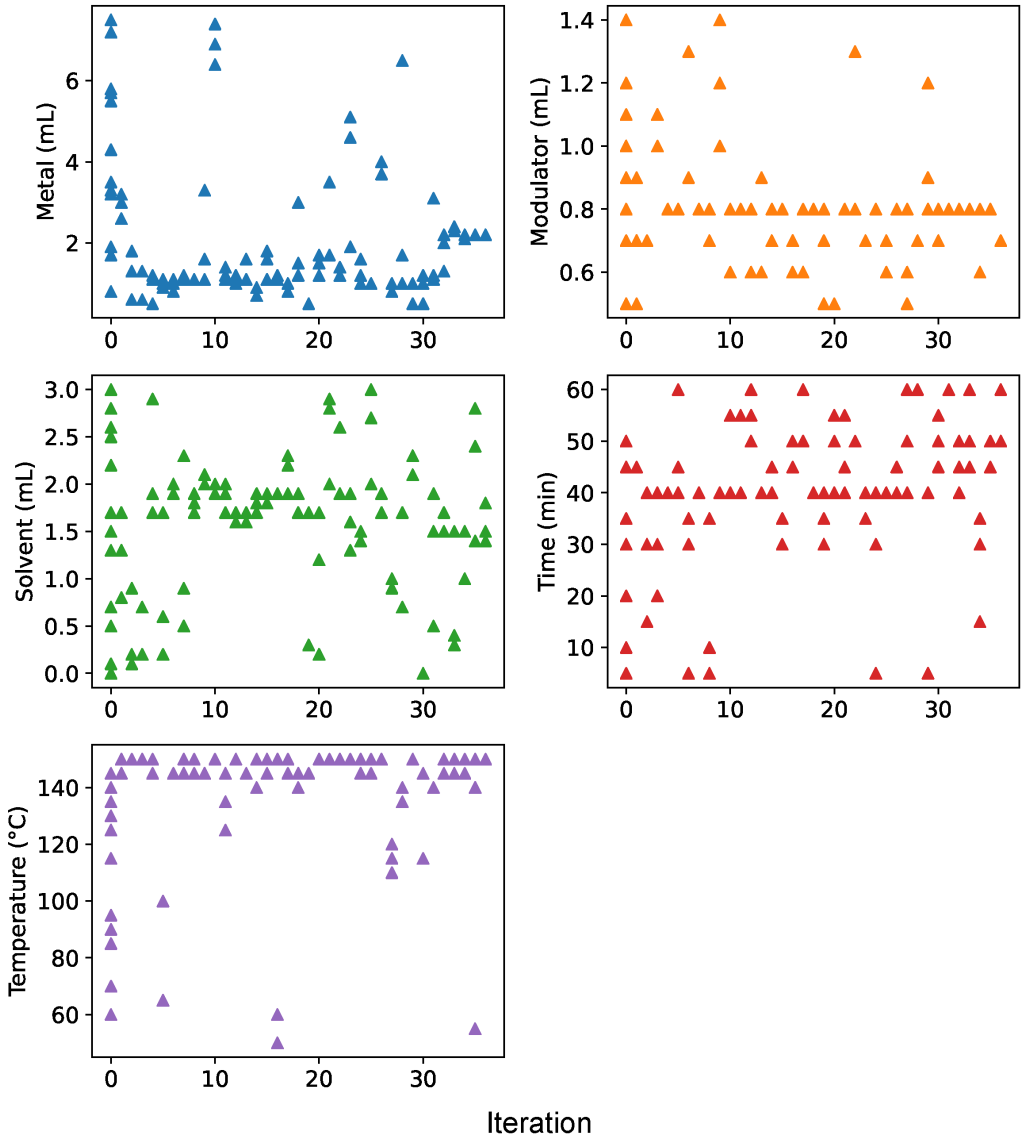

Figure 6.27 The evolution of synthesis parameters for MOF-322.

6.3 Closed-loop optimization with self-driving lab

The AI-assisted strategy for green synthesis optimization of crystalline compounds combines two fundamental components: LLM-based assistants and the ML algorithm (Figure 6.1). The LLM-based assistants aim to streamline routine laboratory work by leveraging extensive domain knowledge (Figure 6.1a). On the other hand, the ML algorithm strives to iteratively propose novel experimental conditions, drawing on existing data and employing a Bayesian optimization search to smartly hasten the trial-and-error method (Figure 6.1b). This algorithm is renowned for pinpointing the global optimum of a black-box objective function $f(x)$ with fewer steps[36] and has a proven track record in property prediction and synthesis optimization for material discovery.[10, 14, 37-40]

At the outset of this study, microwave synthesis was chosen to expedite the experimental cycle due to its abbreviated reaction time.[42, 43] A single iteration involving three experiments could be conducted and reviewed within one to three hours, paving the way for the subsequent iteration. The microwave system's programmability enabled exact setting of reaction parameters, ensuring sequential reactions could be executed with limited direct human oversight. Additionally, the versatility of microwave synthesis ensures optimal stoichiometry conditions can be transferred to traditional and solvothermal synthesis methods, broadening its application.[32, 44] For MOFs, the motivation also stems from green synthesis ambitions, particularly since the synthesized MOFs are potential candidates for atmospheric water harvesting.[45-47] By minimizing or eschewing harmful solvents like DMF, the process remains both environmentally benign and cost-efficient.[48-50]

Past studies demonstrated the capabilities of an AI assistant, driven by ChatGPT and associated GPT-3.5 or GPT-4 base models, to autonomously perform tasks such as extracting synthesis conditions from academic papers, code generation, research planning, and procedural direction.[34, 35] This work takes these capabilities a step further, culminating in a dynamic and efficient chemistry laboratory system. Such a system can support researchers in diverse tasks, including building machine learning models, operating synthesis preparation robotic platforms, designing 3D printed labware, and beyond (Figure 6.2). Collectively, these tasks encapsulate the concept of the ChatGPT Research Group for end-to-end materials discovery (Section 6.2.2).

Through prompt engineering strategies (Section 6.2.1), specific prompts were crafted for each of the seven AI assistants (Figures 6.3–6.11), enabling them to concentrate on their allocated tasks and uphold their expertise.[22, 28, 34, 51, 52] Such an approach negates the need for a single LLM-based assistant to juggle various tasks, which might compromise its efficacy. Furthermore, this framework enables assistants to store prior human interactions as a form of memory, adjusting their actions based on feedback on task performance. Consequently, the dependency on human researchers was significantly diminished. The AI system offers guidance on initiating tasks, distills reaction conditions from pertinent literature, provides synthesis parameters, composes the BO model code, formulates the experimental conditions, and even oversees the robotic platform and fabricates necessary 3D printed equipment (Figure 6.7 and Figure 6.9). In the realm of data

exchange, the system utilizes prompt engineering strategies and in-context learning. Upon the completion of a task by one assistant, its textual output or conclusions are fed to the succeeding assistant. This approach fosters uninterrupted cooperation and instantaneous adaptation, maximizing efficiency. Such enhanced productivity levels allow even those new to the domain to match the output of an entire team of research scientists.

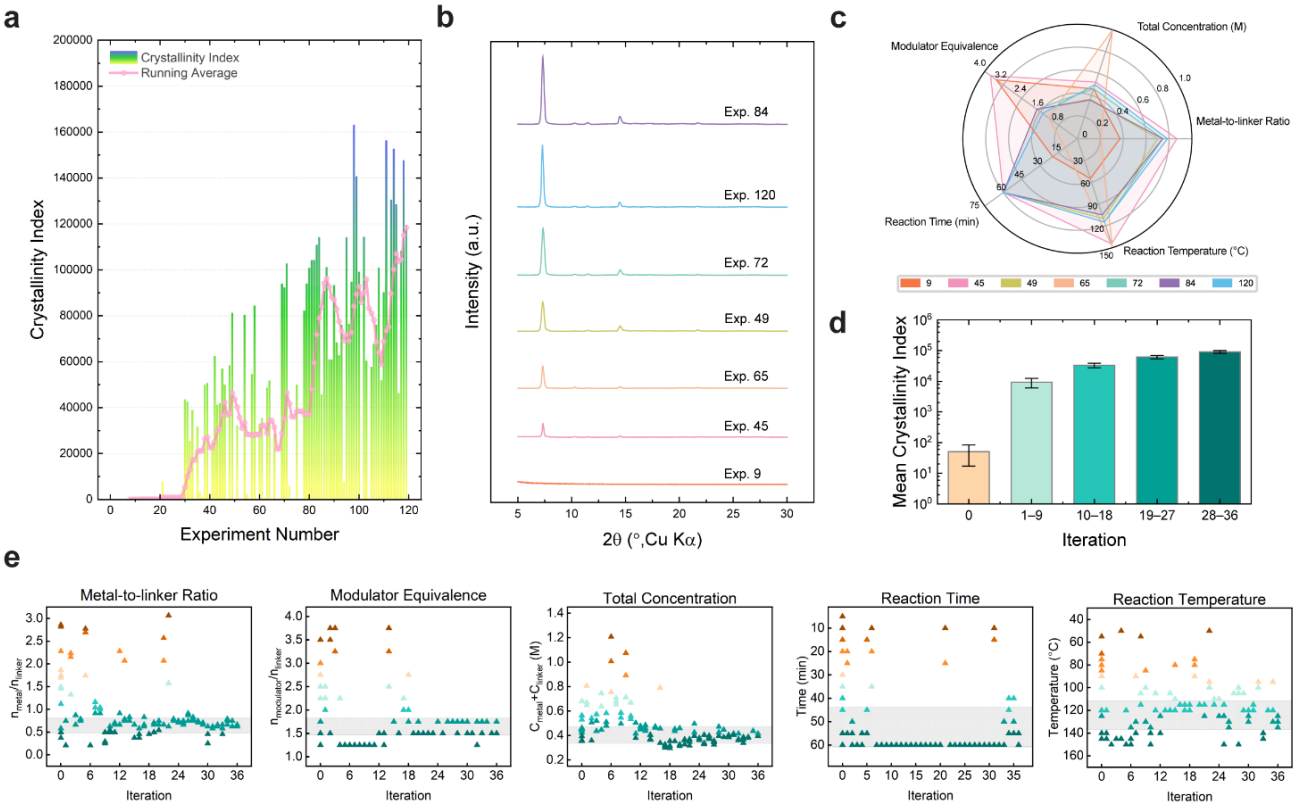

Figure 6.28 Results from AI-guided exploration for MOF-321 synthesis. (a) A graph presents the crystallinity achieved for each of the 120 reactions. The first 12 experiments were conducted using random conditions. In contrast, the remaining 108 were structured across 36 iterations, each containing three experiments. The pink line depicts the running average of the crystallinity index, computed over sets of 3 iterations (or 9 experiments). (b) PXRD patterns extracted from select experimental samples. (c) A radar plot displays the synthesis parameter distribution for chosen experiments. This demonstrates how the Bayesian search begins with a vast exploration space and subsequently refines its focus. (d) A bar chart represents the average and standard deviation of the crystallinity index for the initial experiments (labeled as iteration 0) and subsequent iterations divided into quartiles (iterations 1-9, 10-18, 19-27, and 28-36). Compared to the first 12 randomly conducted experiments, the Bayesian Optimization suggested experiments showcase enhanced crystallinity. Additionally, as the number of iterations rises, there's noticeable performance improvement in the later stages. (e) A series of five scatter plots reveal the progression of each synthesis parameter, as recommended by the BO algorithm, plotted against the iteration number.

6.4 Optimization of MOF synthesis through AI guidance

The central aim lies in discerning the synthesis conditions that enable MOFs to attain peak crystallinity within a prescribed experiment quota. The optimization parameters, as postulated, encompass reactant stoichiometry, modulator-to-linker ratio, concentration levels, reaction time, and temperature. Yet, the intricate process of MOF synthesis poses substantial hurdles due to the slim margins for optimal conditions.[53] For instance, in the pursuit of perfecting MOF-321 synthesis, considering each variable's 10 to 70 variations would lead to a staggering 6,101,172 synthesis conditions using conventional high-throughput screening of the entire synthesis parameter space (Section 6.2.3). While experience-derived chemical intuition from human experts can streamline experiment numbers, it might inadvertently exclude unconventional, yet potentially efficacious conditions, due to ingrained biases. Plus, concurrently evaluating multitudinous variables remains a formidable task for researchers, given the complexities in gauging individual contributions.

Conversely, the Bayesian optimization strategy adopted here—proposing trios of experimental conditions by adjusting the quintet of parameters together (Section 6.2.6), which enabled pinpointing the optimal synthesis condition for MOF-321 in a mere 120 experiments (Figure 6.28a). This approach averted the gargantuan task of sifting through the approximate 6 million potential combinations, which translates to nearly 99.998% savings. Steering the iterative ML search for prime conditions, the crystallinity index (CI) was delineated as the primary peak's height over its full width at half maximum (FWHM). A more pronounced, slender peak equates to a superior CI (Figure 6.18). As shown in Figure 6.28b and Figure 6.28c, through this process, the machine learning algorithm was able to evolve from a position of limited knowledge about the synthesis to determining the most suitable conditions for producing high crystallinity MOFs.

The ML model was initiated with 12 experiments (iteration 0) featuring randomly chosen synthesis parameters within the search space (Section 6.2.3), providing a starting dataset that displayed relatively low average CI values (Figure 6.28d). Notably, these inaugural trials chiefly yielded MOFs of subpar or absent crystallinity. Given the search space's enormity coupled with the randomness of initial parameter selections, the odds of pinpointing the crème de la crème of synthesis conditions were meager. This mirrors the conundrums researchers grapple with at the MOF synthesis parameter exploration's onset, where data deciphering proves intricate and setting the trajectory for ensuing experiments is dicey.

However, the BO model's evolution, enriched by data from ensuing iterations, showcased a consistent elevation in average CI values from iteration 1 through 36. This uptrend stems from the ML-centric approach's flexibility—it isn't pigeonholed to preset synthesis parameters. Instead of the human tendency to micro-adjust known conditions, the ML algorithm embarks on a holistic exploration of synthesis parameters within as few iterations as feasible, harmoniously aligning exploration with parameter fine-tuning (Figure 6.22 and Figure 6.25). This synergetic blend of exploration and exploitation perpetually elevated the average CI, unveiling multiple pinnacle conditions and underscoring the prowess of ML-centric optimization.

6.5 Adaptability of AI-guided MOF synthesis

In the realm of MOF synthesis, seemingly insignificant tweaks to linker structure can often precipitate the need for dramatically altered optimal synthesis conditions.[54-57] An enduring challenge in the discovery of new crystalline materials is bypassing inherent human biases when choosing experimental conditions.56 In this context, our AI-guided strategy emerges as a promising solution.[58]

Inspired by the accomplishments in optimizing MOF-321, this methodology was adapted to explore a novel MOF, incorporating the organic linker H_2TVDC in place of H_2PZVDC and utilizing an alternative PXRD instrument. Achieving desired outcomes in this scenario would underline two critical points: (i) the methodology's adaptability across diverse MOFs, and (ii) its resilience to variations in PXRD instrumentation. The endeavor culminated in pinpointing the prime synthesis condition for MOF-322 within a span of 36 iterations, equivalent to 120 experiments. It is pertinent to mention that the quest to optimize MOF-322 commenced with a unique set of 12 preliminary random experiments, all within a consistent search space. Keeping the synthesis parameters in alignment with those chosen for MOF-321 was a deliberate strategy, emphasizing the robustness of the methodology across varying MOFs without being unduly influenced by the initial conditions.

A significant observation was the pronounced variance in optimal synthesis conditions between MOF-321 and MOF-322. This was attributed to the distinctions in the organic linker's inherent properties and the unique *cis*-connected aluminum SBUs, as corroborated by PXRD refinement (Figure 6.19). MOF-322 has markedly different optimal synthesis conditions compared to MOF-321, as expected (Table 6.1). For example, whereas MOF-321 gravitates towards a conventional 120°C synthesis environment with specific ratios and equivalences (e.g. metal-to-linker ratio ranging from 1:2 to 2:3 and 1.5 to 1.75 equivalence of the base modulator),[50, 59] MOF-322 necessitates an alternate set of conditions. During independent trials, conditions optimal for MOF-321 were sometimes suggested for MOF-322, leading to varied outcomes, including suboptimal crystallinity or unexpected side phases. Vice versa, conditions ideal for MOF-322, when applied to MOF-321, often yielded compounds with compromised crystallinity. This suggests that the optimal conditions and screening windows for these two compounds greatly differ, and copying the best condition from one to the other is not an effective technique.

Venturing into the realm of optimizing a novel MOF demands the audacity to tread unfamiliar paths. Relying exclusively on chemical intuition or adhering to known territories can be limiting. The *t*-distributed stochastic neighbor embedding (*t*-SNE) dimensionality-reduced scatter plot (Figure 6.29) vividly illustrates the marked differences in the top 5 conditions between MOF-321 and MOF-322. This distinction not only emphasizes their unique synthesis requisites but also accentuates the methodology's consistency and reliability, even when pivoted to a new MOF.

Table 6.1 Representative conditions for microwave-assisted synthesis of high-crystallinity MOF-321 and MOF-322.

MOF	Exp.	Linker (mmol)	Metal (mmol)	Modulator (mmol)	H_2O (mL)	Time (min)	Temp. (°C)
MOF-321	84	1.0	0.75	1.75	4.7	60	125
	96	1.0	0.70	1.5	4.0	60	105
	101	1.0	0.46	1.75	3.6	60	120
	114	1.0	0.66	1.75	4.3	45	120
	120	1.0	0.66	1.5	4.0	55	135
MOF-322	22	1.0	0.46	2.0	3.6	40	145
	68	1.0	0.21	1.75	1.5	35	145
	86	1.0	0.41	1.5	4.3	40	150
	103	1.0	0.46	2.0	3.4	60	140
	109	1.0	0.99	2.0	3.5	50	150

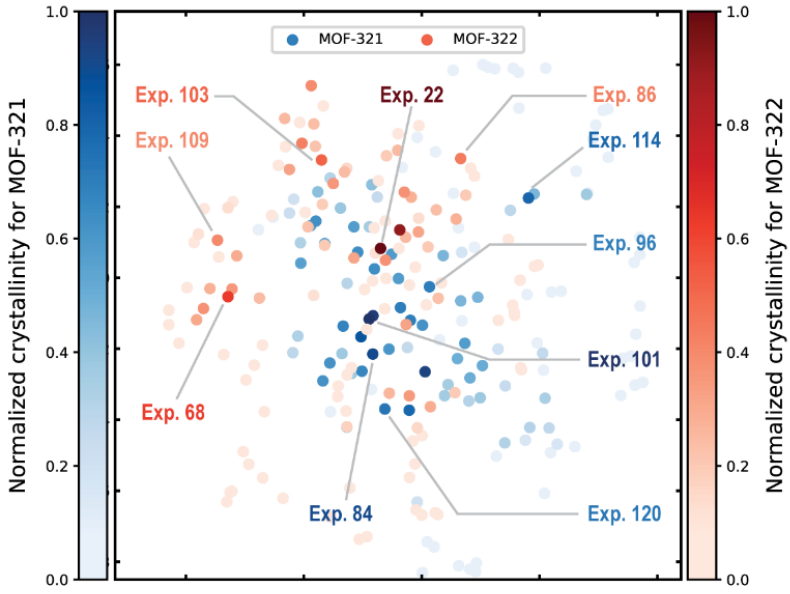

Figure 6.29 Two-dimensional *t*-SNE dimension reduction scatter plot representing 120 distinct synthesis conditions for MOF-321 (blue) and MOF-322 (red). Prior to reduction, the synthesis parameters, including amount of metal, amount of modulator, solvent volume, reaction time, and temperature, are normalized. The color intensity indicates the crystallinity index, with deeper shades signifying higher values. Labels are provided for five representative synthesis conditions from various regions of the scatter plot, illustrating the distinctiveness of certain conditions and the successful identification of multiple conditions with high crystallinity by the BO process. The plot distinctly indicates that the optimal conditions for MOF-321 and MOF-322 differ.

6.6 Evaluation of porosity and water uptake

A crucial point of emphasis is the objective underlying the use of the BO algorithm: while the intent is to unearth synthesis conditions that produce high crystallinity compounds, a heightened CI value is not a direct proxy for elevated porosity or superior water capacity. The correlation between CI and the primary peak shape is well understood, but numerous factors including potential side phases, lingering starting materials, or linkers obstructing the pores can invariably impact the measured porosity and water uptake metrics. This challenge remains a constant, irrespective of whether the synthesis condition screening is human-centric or steered by machine learning. It is worth noting, however, that while compounds flaunting a high CI value might not always exhibit enhanced water uptake, those with impressive water uptake tend to consistently have commendable CI values. Through the application of the BO process, over ten condition combinations were discerned that resulted in MOF-321 and MOF-322 exhibiting sharp, definitive peaks.

Further validation of porosity and water uptake for these promising candidates led to the pinpointing of the most conducive conditions from a pool of 120 experiments (Figure 6.30). This endeavor was undertaken to optimize sorption performance for each compound. For MOF-321, assessments revealed a Brunauer-Emmett-Teller (BET) surface area of 1875 m^2/g and an experimentally derived pore volume measuring 0.67 cm^3/g. These figures hover closely to the theoretical values[60] of 2025 m^2/g for BET surface area and 0.72 cm^3/g for pore volume (Figure 6.30a). This MOF further exhibited an impressive water uptake capacity, registering at 0.66 g/g (Figure 6.30b), testament to its exemplary porosity and water sorption dynamics.

In parallel, MOF-322, once optimized, showcased a BET surface area of 1584 m^2/g (Figure 6.30c), approximating 94% of the theoretically deduced maximum BET surface area value of 1686 m^2/g. The experimentally determined pore volume settled at 0.57 cm3/g, aligning closely with the theoretical estimate of 0.61 cm^3/g. This MOF's water uptake, benchmarked at 0.53 g/g (Figure 6.30d), reinforced its superior attributes.

In total, these results illuminate the potential of blending human expertise with AI-driven methodologies. The combined approach not only accelerates the discovery of synthesis conditions that are conducive to achieving high crystallinity, porosity, and water capacity, but it also nudges these parameters closer to their theoretical zeniths, optimizing productivity and minimizing manual intervention.

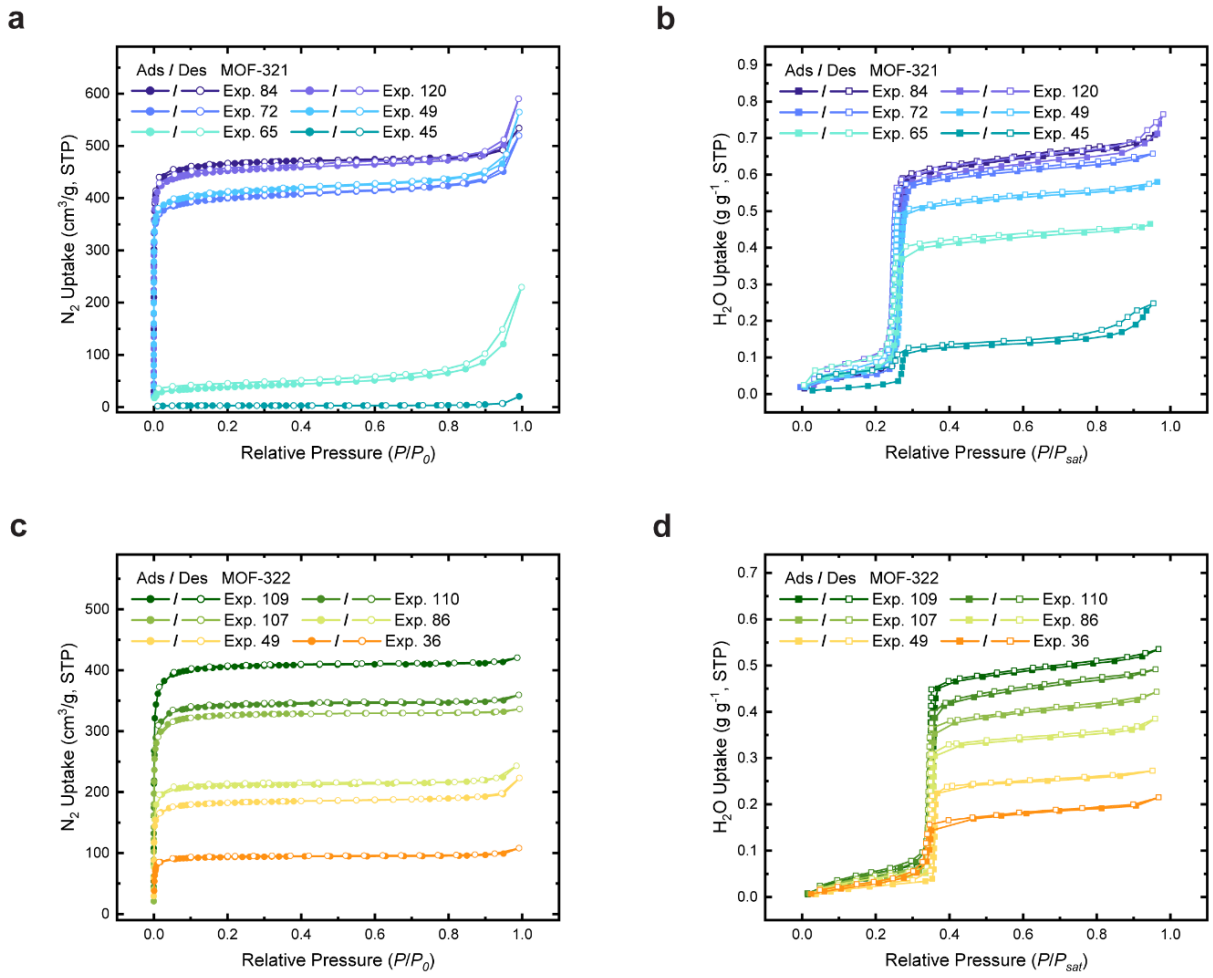

Figure 6.30 Overlay of gas adsorption-desorption isotherms of MOF-321 and MOF-322, prepared under varying synthesis conditions with different CI values, showing the evolution of optimal synthesis condition within the search space. (a) Nitrogen sorption isotherms for MOF-321 samples obtained at 77 K. (b) Water vapor sorption isotherms for MOF-321 samples measured at 298 K, demonstrating different sorption capacities. (c) Nitrogen sorption isotherms for MOF-322 samples obtained at 77 K. (d) Water vapor sorption isotherms for MOF-322 samples measured at 298 K, showcasing different sorption capacities. Each panel presents data for six distinct samples of each MOF, underscoring the impact of synthesis conditions on the crystallinity and consequent gas adsorption properties of these MOFs. P, nitrogen or water vapor pressure; P_0, 1 atm; P_{sat}, saturation water vapor pressure. Symbols of filled circles denote the adsorption branch, while empty circles denote the desorption branch.

6.7 Conclusions

In this chapter, a cutting-edge, user-centric AI-guided system has been devised, streamlining the optimization process for water-harvesting MOF synthesis without necessitating foundational coding expertise. The seven LLM-based entities introduced here have been tailored to accommodate diverse aspects of chemical research, ranging from meticulous planning and in-depth literature exploration to coding for ML models, operating robots, devising labware for 3D printing, guiding synthesis procedures, and handling data extraction and analytical tasks.

While the Bayesian optimization algorithm, orchestrated by one of the LLM assistants, takes the lead in guiding navigation through synthesis condition spaces, the roles of the remaining LLM aides cannot be overshadowed. Their versatility comes to the fore in multiple wet lab scenarios, emphasizing their overarching utility. Such innovations paved the way for the impeccable optimization of eco-friendly syntheses of MOF-321 and MOF-322 via microwave synthesis. With a blank slate regarding initial synthesis conditions, the ML algorithms showcased their prowess by zooming into the crux of the optimal synthesis environment needed for crystallinity enhancement. The melding of these techniques confronts and addresses prevailing issues, especially the intricacies of multi-parametric adjustments and the ingrained human biases in selecting synthesis conditions.

The subsequent surge in the success rate expedited the pinpointing of ideal porosity and water adsorption capacities. Within the ambit of microwave settings, a mere 4 days (or 6,235 minutes) sufficed for 120 reactions to refine the synthesis condition for a solitary compound from a staggering pool of over 6 million variable combinations. The ability to communicate with LLM-based aides using natural language, combined with setting up ML blueprints, ensured that this holistic AI framework was operational within our laboratory in under a month. Even though full automation remains on the horizon, the platform stands to benefit immensely from future robotic advancements. Newly introduced functionalities, such as the capability for function calling, hint at future enhancements, where manual involvement diminishes, giving way to a more self-sustaining mechanism for synthesis fine-tuning. This evolution not only showcases the potential roadmap for the modern chemical laboratory but also envisions a scenario where a consortium of AI entities orchestrates diverse lab operations. Such synchronization promises a quantum leap in the pace of discovering and refining novel chemical compounds. By minimizing routine tasks, researchers are thus poised to focus on breaking new ground in innovation. Furthermore, these advancements pave the way for the progressive enhancement and development of next-generation water-harvesting MOFs.

6.8 Reference

(1) Wang, H.; Fu, T.; Du, Y.; Gao, W.; Huang, K.; Liu, Z.; Chandak, P.; Liu, S.; Van Katwyk, P.; Deac, A., Scientific discovery in the age of artificial intelligence. *Nature* **2023,** *620* (7972), 47-60.

(2) Williams, W. L.; Zeng, L.; Gensch, T.; Sigman, M. S.; Doyle, A. G.; Anslyn, E. V., The evolution of data-driven modeling in organic chemistry. *ACS Cent. Sci.* **2021,** *7* (10), 1622-1637.
(3) Baum, Z. J.; Yu, X.; Ayala, P. Y.; Zhao, Y.; Watkins, S. P.; Zhou, Q., Artificial intelligence in chemistry: current trends and future directions. *J. Chem. Inf. Model.* **2021,** *61* (7), 3197-3212.
(4) Davenport, T. H.; Ronanki, R., Artificial intelligence for the real world. *Harv. Bus. Rev.* **2018,** *96* (1), 108-116.
(5) de Almeida, A. F.; Moreira, R.; Rodrigues, T., Synthetic organic chemistry driven by artificial intelligence. *Nat. Rev. Chem.* **2019,** *3* (10), 589-604.
(6) Wahl, C. B.; Aykol, M.; Swisher, J. H.; Montoya, J. H.; Suram, S. K.; Mirkin, C. A., Machine learning–accelerated design and synthesis of polyelemental heterostructures. *Sci. Adv.* **2021,** *7* (52), eabj5505.
(7) Ahneman, D. T.; Estrada, J. G.; Lin, S.; Dreher, S. D.; Doyle, A. G., Predicting reaction performance in C–N cross-coupling using machine learning. *Science* **2018,** *360* (6385), 186-190.
(8) Yaghi, O. M.; O'Keeffe, M.; Ockwig, N. W.; Chae, H. K.; Eddaoudi, M.; Kim, J., Reticular synthesis and the design of new materials. *Nature* **2003,** *423* (6941), 705-714.
(9) Luo, Y.; Bag, S.; Zaremba, O.; Cierpka, A.; Andreo, J.; Wuttke, S.; Friederich, P.; Tsotsalas, M., MOF synthesis prediction enabled by automatic data mining and machine learning. *Angew. Chem. Int. Ed.* **2022,** *61* (19), e202200242.
(10) Hase, F.; Roch, L. M.; Kreisbeck, C.; Aspuru-Guzik, A., Phoenics: a Bayesian optimizer for chemistry. *ACS Cent. Sci.* **2018,** *4* (9), 1134-1145.
(11) Birhane, A.; Kasirzadeh, A.; Leslie, D.; Wachter, S., Science in the age of large language models. *Nat. Rev. Phys.* **2023,** *5* (5), 277-280.
(12) Vert, J.-P., How will generative AI disrupt data science in drug discovery? *Nat. Biotechnol.* **2023,** *41* (6), 750-751.
(13) Chong, S.; Lee, S.; Kim, B.; Kim, J., Applications of machine learning in metal-organic frameworks. *Coord. Chem. Rev.* **2020,** *423*, 213487.
(14) Xie, Y.; Zhang, C.; Deng, H.; Zheng, B.; Su, J.-W.; Shutt, K.; Lin, J., Accelerate synthesis of metal–organic frameworks by a robotic platform and bayesian optimization. *ACS Appl. Mater. Interfaces* **2021,** *13* (45), 53485-53491.
(15) Packwood, D.; Nguyen, L. T. H.; Cesana, P.; Zhang, G.; Staykov, A.; Fukumoto, Y.; Nguyen, D. H., Machine learning in materials chemistry: An invitation. *MLWA* **2022,** *8*, 100265.
(16) Hope, T.; Downey, D.; Weld, D. S.; Etzioni, O.; Horvitz, E., A computational inflection for scientific discovery. *Commun. ACM* **2023,** *66* (8), 62-73.
(17) Freund, R.; Canossa, S.; Cohen, S. M.; Yan, W.; Deng, H.; Guillerm, V.; Eddaoudi, M.; Madden, D. G.; Fairen-Jimenez, D.; Lyu, H., 25 years of reticular chemistry. *Angew. Chem. Int. Ed.* **2021,** *60* (45), 23946-23974.
(18) OpenAI GPT-4 technical report. DOI: 10.48550/arXiv:2303.08774v3 (accessed 2023-03-27).
(19) Wang, G.; Xie, Y.; Jiang, Y.; Mandlekar, A.; Xiao, C.; Zhu, Y.; Fan, L.; Anandkumar, A. Voyager: An open-ended embodied agent with large language models. arXiv:2305.16291.
(20) Bubeck, S.; Chandrasekaran, V.; Eldan, R.; Gehrke, J.; Horvitz, E.; Kamar, E.; Lee, P.; Lee, Y. T.; Li, Y.; Lundberg, S. Sparks of artificial general intelligence: Early experiments

with gpt-4. *arXiv* DOI: 10.48550/arXiv:2303.12712 (accessed 2023-04-13).
(21) Boiko, D. A.; MacKnight, R.; Gomes, G. Emergent autonomous scientific research capabilities of large language models. arXiv:2304.05332.
(22) Zhou, Y.; Muresanu, A. I.; Han, Z.; Paster, K.; Pitis, S.; Chan, H.; Ba, J. Large language models are human-level prompt engineers. arXiv:2211.01910.
(23) Park, J. S.; O'Brien, J. C.; Cai, C. J.; Morris, M. R.; Liang, P.; Bernstein, M. S. Generative agents: Interactive simulacra of human behavior. arXiv:2304.03442.
(24) Bran, A. M.; Cox, S.; White, A. D.; Schwaller, P. ChemCrow: Augmenting large-language models with chemistry tools. arXiv:2304.05376.
(25) Kang, Y.; Kim, J. ChatMOF: An Autonomous AI System for Predicting and Generating Metal-Organic Frameworks. arXiv:2308.01423.
(26) Parameswaran, A. G.; Shankar, S.; Asawa, P.; Jain, N.; Wang, Y. Revisiting Prompt Engineering via Declarative Crowdsourcing. arXiv:2308.03854.
(27) Wu, T.; He, S.; Liu, J.; Sun, S.; Liu, K.; Han, Q.-L.; Tang, Y., A brief overview of ChatGPT: The history, status quo and potential future development. *IEEE/CAA J. Autom. Sin.* **2023,** *10* (5), 1122-1136.
(28) Wang, Y.; Kordi, Y.; Mishra, S.; Liu, A.; Smith, N. A.; Khashabi, D.; Hajishirzi, H. Self-instruct: Aligning language model with self generated instructions. arXiv:2212.10560.
(29) Shields, B. J.; Stevens, J.; Li, J.; Parasram, M.; Damani, F.; Alvarado, J. I. M.; Janey, J. M.; Adams, R. P.; Doyle, A. G., Bayesian reaction optimization as a tool for chemical synthesis. *Nature* **2021,** *590* (7844), 89-96.
(30) Deshwal, A.; Simon, C. M.; Doppa, J. R., Bayesian optimization of nanoporous materials. *Mol. Syst. Des. Eng.* **2021,** *6* (12), 1066-1086.
(31) Hanikel, N.; Kurandina, D.; Chheda, S.; Zheng, Z.; Rong, Z.; Neumann, S. E.; Sauer, J.; Siepmann, J. I.; Gagliardi, L.; Yaghi, O. M., MOF Linker Extension Strategy for Enhanced Atmospheric Water Harvesting. *ACS Cent. Sci.* **2023,** *9* (3), 551-557.
(32) Zheng, Z.; Nguyen, H. L.; Hanikel, N.; Li, K. K.-Y.; Zhou, Z.; Ma, T.; Yaghi, O. M., High-yield, green and scalable methods for producing MOF-303 for water harvesting from desert air. *Nat. Protoc.* **2023,** *18*, 136–156.
(33) Vaswani, A.; Shazeer, N.; Parmar, N.; Uszkoreit, J.; Jones, L.; Gomez, A. N.; Kaiser, Ł.; Polosukhin, I., Attention is all you need. *NIPS* **2017,** *30*.
(34) Zheng, Z.; Rong, Z.; Rampal, N.; Borgs, C.; Chayes, J. T.; Yaghi, O. M., A GPT-4 Reticular Chemist for Guiding MOF Discovery. *Angew. Chem. Int. Ed.* **2023**, e202311983.
(35) Zheng, Z.; Zhang, O.; Borgs, C.; Chayes, J. T.; Yaghi, O. M., ChatGPT Chemistry Assistant for Text Mining and Prediction of MOF Synthesis. *J. Am. Chem. Soc.* **2023,** *145* (32), 18048–18062.
(36) Jones, D. R.; Schonlau, M.; Welch, W. J., Efficient global optimization of expensive black-box functions. *J. Glob. Optim.* **1998,** *13*, 455-492.
(37) Gongora, A. E.; Xu, B.; Perry, W.; Okoye, C.; Riley, P.; Reyes, K. G.; Morgan, E. F.; Brown, K. A., A Bayesian experimental autonomous researcher for mechanical design. *Sci. Adv.* **2020,** *6* (15), eaaz1708.
(38) Langner, S.; Häse, F.; Perea, J. D.; Stubhan, T.; Hauch, J.; Roch, L. M.; Heumueller, T.; Aspuru-Guzik, A.; Brabec, C. J., Beyond ternary OPV: high-throughput experimentation and self-driving laboratories optimize multicomponent systems. *Adv. Mater.* **2020,** *32* (14), 1907801.

(39) Wahab, H.; Jain, V.; Tyrrell, A. S.; Seas, M. A.; Kotthoff, L.; Johnson, P. A., Machine-learning-assisted fabrication: Bayesian optimization of laser-induced graphene patterning using in-situ Raman analysis. *Carbon* **2020,** *167*, 609-619.
(40) Burger, B.; Maffettone, P. M.; Gusev, V. V.; Aitchison, C. M.; Bai, Y.; Wang, X.; Li, X.; Alston, B. M.; Li, B.; Clowes, R., A mobile robotic chemist. *Nature* **2020,** *583* (7815), 237-241.
(41) Chevalier, C.; Ginsbourger, D. In *Fast computation of the multi-points expected improvement with applications in batch selection*, International conference on learning and intelligent optimization, Springer: 2013; pp 59-69.
(42) Klinowski, J.; Paz, F. A. A.; Silva, P.; Rocha, J., Microwave-assisted synthesis of metal–organic frameworks. *Dalton Trans.* **2011,** *40* (2), 321-330.
(43) Phan, P. T.; Hong, J.; Tran, N.; Le, T. H., The Properties of Microwave-Assisted Synthesis of Metal–Organic Frameworks and Their Applications. *Nanomaterials* **2023,** *13* (2), 352.
(44) Zheng, Z.; Hanikel, N.; Lyu, H.; Yaghi, O. M., Broadly Tunable Atmospheric Water Harvesting in Multivariate Metal–Organic Frameworks. *J. Am. Chem. Soc.* **2022,** *144* (49), 22669-22675.
(45) Xu, W.; Yaghi, O. M., Metal–organic frameworks for water harvesting from air, anywhere, anytime. *ACS Cent. Sci.* **2020,** *6* (8), 1348-1354.
(46) Hanikel, N.; Prévot, M. S.; Yaghi, O. M., MOF water harvesters. *Nat. Nanotechnol.* **2020,** *15* (5), 348-355.
(47) Song, W.; Zheng, Z.; Alawadhi, A. H.; Yaghi, O. M., MOF water harvester produces water from Death Valley desert air in ambient sunlight. *Nat. Water* **2023,** *1* (7), 626–634.
(48) DeSantis, D.; Mason, J. A.; James, B. D.; Houchins, C.; Long, J. R.; Veenstra, M., Techno-economic analysis of metal–organic frameworks for hydrogen and natural gas storage. *Energy Fuels* **2017,** *31* (2), 2024-2032.
(49) Gaab, M.; Trukhan, N.; Maurer, S.; Gummaraju, R.; Müller, U., The progression of Al-based metal-organic frameworks–From academic research to industrial production and applications. *Microporous Mesoporous Mater.* **2012,** *157*, 131-136.
(50) Zheng, Z.; Alawadhi, A. H.; Yaghi, O. M., Green Synthesis and Scale-Up of MOFs for Water Harvesting from Air. *Mol. Front. J.* **2023,** *7* (1), 1-20.
(51) Zhou, W.; Jiang, Y. E.; Cui, P.; Wang, T.; Xiao, Z.; Hou, Y.; Cotterell, R.; Sachan, M. RecurrentGPT: Interactive Generation of (Arbitrarily) Long Text. arXiv:2305.13304.
(52) White, J.; Fu, Q.; Hays, S.; Sandborn, M.; Olea, C.; Gilbert, H.; Elnashar, A.; Spencer-Smith, J.; Schmidt, D. C. A prompt pattern catalog to enhance prompt engineering with chatgpt. arXiv:2302.11382.
(53) Yaghi, O. M.; Kalmutzki, M. J.; Diercks, C. S., *Introduction to reticular chemistry: metal-organic frameworks and covalent organic frameworks*. John Wiley & Sons: 2019.
(54) Furukawa, H.; Cordova, K. E.; O'Keeffe, M.; Yaghi, O. M., The chemistry and applications of metal-organic frameworks. *Science* **2013,** *341* (6149), 1230444.
(55) Stock, N.; Biswas, S., Synthesis of metal-organic frameworks (MOFs): routes to various MOF topologies, morphologies, and composites. *Chem. Rev.* **2012,** *112* (2), 933-969.
(56) Kirlikovali, K. O.; Hanna, S. L.; Son, F. A.; Farha, O. K., Back to the Basics: Developing Advanced Metal–Organic Frameworks Using Fundamental Chemistry Concepts. *ACS Nanoscience Au* **2022,** *3* (1), 37-45.
(57) Gropp, C.; Canossa, S.; Wuttke, S.; Gándara, F.; Li, Q.; Gagliardi, L.; Yaghi, O. M.,

Standard practices of reticular chemistry. *ACS Cent. Sci.* **2020**.
(58) Jablonka, K. M.; Ongari, D.; Moosavi, S. M.; Smit, B., Big-data science in porous materials: materials genomics and machine learning. *Chem. Rev.* **2020,** *120* (16), 8066-8129.
(59) Tannert, N.; Jansen, C.; Nießing, S.; Janiak, C., Robust synthesis routes and porosity of the Al-based metal–organic frameworks Al-fumarate, CAU-10-H and MIL-160. *Dalton Trans.* **2019,** *48* (9), 2967-2976.
(60) Martin, R. L.; Haranczyk, M., Construction and characterization of structure models of crystalline porous polymers. *Cryst. Growth Des.* **2014,** *14* (5), 2431-2440.

Chapter VII
Conclusion and Outlook

The exigency of water scarcity, heightened by global challenges such as climate change and population growth, necessitates innovative solutions. Atmospheric water harvesting (AWH) emerged as a beacon of hope in this milieu, promising a potentially inexhaustible water source. The advent of metal-organic frameworks (MOFs) introduces a promising suite of materials for AWH. Their remarkable crystallinity, permanent porosity, and structural tunability enhance their interactions with water molecules, which are pivotal for maximizing water harvesting performance. However, realizing the dream of water harvesting anytime, anywhere demands addressing the inherent challenges in both sorbent materials and device engineering.

From the sorbent perspective, large-scale application of MOFs is constrained by synthesis scalability issues and the development of the new water-harvesting MOF candidates is slowed down by the lack of design methodologies. Historically, the development of new MOFs and the optimization of their synthesis conditions, both in small and large scale, has been a slow, painstaking process, often taking years and involving a mix of human chemical insight and extensive trial and error. Given the onus on researchers to select the ideal porous material for optimum results, accelerated methods for developing new water-harvesting MOFs are imperative. On the device front, the emphasis lies in efficiency—extracting maximum water from MOFs quickly and, ideally, with minimal to no energy expenditure. A thorough understanding of the operational parameters that dictate device performance is crucial, leading to the creation of water harvesting devices tailored explicitly for MOFs.

This dissertation delineates the meticulous design, synthesis, and characterization of MOFs, laying the groundwork for the next generation of porous materials in AWH applications. Through comprehensive studies presented in earlier chapters, I have demonstrated how methodologies such as reticular design, multivariate strategies, linker extension strategies, and AI-assisted synthesis can foster the genesis of a new generation of MOF materials with enhanced water harvesting properties. Integral to this discussion is the elaboration on the synthesis protocol for scaling up water-harvesting MOFs and the realization of a design of passive water harvester, both

of which are pivotal for broadening the accessibility and scalability of this technology to mitigate global water challenges. Collectively, these contributions represent significant strides toward advancing water-harvesting MOFs.

The journey of this dissertation, while monumental in its achievements, also paves the path for future endeavors. Potential trajectories include pioneering MOF design strategies, intensifying AI integration into lab activities, enhancing device scalability, and performing comprehensive environmental analysis.

Building upon the foundational knowledge presented, there exists immense scope for conceiving MOFs with superior water uptake capacities, fine-tuning, and adaptability across varied conditions. While the strengths of multivariate strategies and linker extension approaches in MOF design are evident, merging these tactics could lead to exceptionally potent MOFs with enhanced tunability and water absorption. Furthermore, the pursuit of design principles for water-resistant MOFs with prolonged durability and rapid kinetics is paramount. Such endeavors require an in-depth comprehension of what steers the synthesis and properties of these frameworks.

Incorporating artificial intelligence, particularly machine learning (ML) algorithms and large language models (LLM), promises transformative change. Traditional reticular chemistry, while valuable, often leans on human intuition for synthesis optimization. This approach is not only potentially biased but also necessitates intensive labor and extensive experience. Despite numerous conceptually feasible MOFs for water harvesting, many remain unmaterialized in experimental settings. Herein, LLMs can bridge the divide between computational scientists and chemists, fostering enhanced human-AI synergy in labs and enabling those unfamiliar with coding to engage with machine learning tools and other AI-aided systems. As AI gradually shoulders labor-intensive tasks, researchers can channel their intellectual prowess into innovation, accelerating MOF advancements for atmospheric water harvesting.

Equally vital is the focus on the water harvester's scalability, paired with a thorough evaluation of environmental repercussions and costs linked to MOF production and device assembly. This holistic approach is essential for its broad acceptance and application. Strengthening ties between academic pursuits and practical implementations is also crucial, with collaborations spanning industries, policymakers, and communities, fostering the widespread embrace of MOF-driven water harvesting solutions.

In conclusion, the dissertation underscores the potential of metal-organic frameworks in addressing one of the most pressing challenges of our time – water scarcity. As we march into the future, it is evident that MOFs will play a significant role in ensuring water security, sustainability, and prosperity for all.